博士論文

Parametric analyses in electron linac production of ^{99}Mo/^{99m}Tc

（電子リニアックを用いた ^{99}Mo/^{99m}Tc 製造におけるパラメータ解析）

張 宰雄

Doctoral dissertation

Parametric analyses in electron linac production of ^{99}Mo/^{99m}Tc

---

by

Jaewoong Jang

Submitted to the Department of Bioengineering
in partial fulfillment of the requirements for the degree of
Doctor of Philosophy
IN THE FIELD OF BIOENGINEERING

School of Engineering
University of Tokyo
Advisor: Prof. Mitsuru Uesaka

September 2019

Parametric analyses in electron linac production of ^{99}Mo/^{99m}Tc

Jaewoong Jang <jangj@korea.ac.kr>
Department of Bioengineering
School of Engineering
University of Tokyo

This dissertation was typeset using LaTeX 2$_\varepsilon$, KOMA-Script, BibLaTeX, and biber. Figures were generated using GNUPLOT, ANGEL, GHOSTSCRIPT, MS VISIO, or their combinations.

Dedicated to my wife
for her support and encouragement

Declaration

I declare that I have authored this dissertation independently, that I have not used other than the declared sources, and that I have explicitly marked all material which has been quoted either literally or by content from the used sources.

Jaewoong Jang	August 14, 2019
Author	Date

Some of the figures and tables in this dissertation were derived from the previous publications or thesis of the author, which have been marked as follows:

(i) Figures and tables reused *without* modifications have been marked with "reproduced from ..." in their captions.

(ii) Figures and tables reused *with* modifications have been marked with "adapted from ..." in their captions.

The associated license information, if any, has also been stated in the captions. Except the above two cases, all the figures, tables, and listings presented in this dissertation are original, have been generated by the author himself, and have not been published elsewhere.

For the following published materials to be addressed as parts of this dissertation, and for this dissertation to be archived in UTokyo Repository (https://repository.dl.itc.u-tokyo.ac.jp/), written consent has been obtained from the individual coauthors.

[1] J. Jang and M. Uesaka. Influence of enriched ^{100}Mo on Mo reaction yields. *Journal of Physics Communications* **3**, 055015 (2019). DOI: 10.1088/2399-6528/ab1d6b.

[2] J. Jang, M. Yamamoto, and M. Uesaka. Design of an X-band electron linear accelerator dedicated to decentralized ^{99}Mo/^{99m}Tc supply: From beam energy selection to yield estimation. *Physical Review Accelerators and Beams* **20**, 104701 (2017). DOI: 10.1103/PhysRevAccelBeams.20.104701.

Acknowledgments

First of all, I would like to express my sincerest gratitude to my advisor, Prof. Uesaka, who patiently guided and generously supported me during my entire graduate study. My five-year stay in his laboratory was a memorable and unforgettably rewarding time. Prof. Uesaka let me conduct research on one of the most interesting and long-standing accelerator applications: production of medical radionuclides. Thanks to his expertise in accelerator science and technology, I could work on both the accelerator itself and on its applications. Also, I greatly appreciate the collaborative research he established, where I met and interacted with leading researchers from a variety of backgrounds. I am also grateful for his encouragement and support for experiments, without which the experimental works of this dissertation could not be conducted.

I am deeply indebted to Dr. Yamamoto (Accuthera Inc.) for his guidance and advice throughout my graduate research. It was Dr. Yamamoto who showed me how interpreted languages can be used in conducting research, in controlling simulation programs in particular. Inspired by his program-driven accelerator design methodology, I devised the computational approaches and programs used in this dissertation.

My sincerest appreciation goes to Prof. Ohtsuki and Dr. Sekimoto (Institute for Integrated Radiation and Nuclear Science, Kyoto University), from whom I learned the steps and skills necessary for photonuclear experiments, and to Prof. Kikunaga and Prof. Kashiwagi (Research Center for ELectron PHoton Science, Tohoku University), for providing guidance and fine-tuned electron beams during experiments. Without their guidance and help, no irradiation experiments could be conducted in this dissertation.

A large part of this dissertation addresses chemical subjects in addition to the main physical problems. In conducting chemical and radiochemical experiments, Dr. Tatenuma, Mr. Tsuguchi, Mr. Kawakami, and Ms. Natori (Kaken Inc.) kindly guided me and let me use their facilities and devices without difficulties. I would like to express my sincerest thanks to their guidance and support.

I am grateful to Dr. Tadokoro (Hitachi, Ltd.) for valuable discussions and advice. Although I could not talk with him as frequently as in my master's course, his advice has been invaluable in pursuing the research of medical radionuclide production.

The last minute of my PhD course was full of new experiences. I came to learn how preclinical testing is performed in nuclear medicine, how laboratory mice are handled, and how radiopharmaceuticals are prepared in practice. I could have these exciting experiences thanks to: Prof. Kumakura (Saitama Medical Center, Saitama Medical University), Prof. Wada, Prof. Akimitsu, Dr. Ozeki (Nakanishi), and Ms. Shiizu (Isotope Science Center, University of Tokyo). Without their guidance and support, the biodistribution studies conducted in this dissertation would not have been possible.

I would like to express my sincere appreciation to the Ministry of Education, Culture, Sports, Science and Technology (MEXT), Japan, for providing me with the tuition fees and monthly stipends during the whole period of my graduate course, and to the University of Tokyo, for recommending me to the MEXT scholarship. Thanks to this generous financial support, I could always focus on research and need not hesitate when I wanted to spend more time on research.

I also need to thank our laboratory members. I am grateful to Prof. Yamashita and a former secretary Ms. Sekiguchi for their support and guidance. I thank Y. Inoue and M. Ozeki for experimental assistance, and thank Alexa, Yu, Chen, and Michel for the random conversations and eating together that regularly reminded me of the existence of school life.

Finally, I would like to express my deepest gratitude to all my family, for their unconditional love and support.

Abstract

Technetium-99m (^{99m}Tc), the daughter radionuclide of molybdenum-99 (^{99}Mo), plays an indispensable role in diagnosing various diseases such as myocardial ischemia and bone metastasis. Recent interruptions of ^{99}Mo production reactors have prompted research into accelerator production of ^{99}Mo/^{99m}Tc, among which ^{99}Mo production using an electron linear accelerator (linac) and the ^{100}Mo(γ,n)^{99}Mo reaction is considered a promising alternative.

The key to realizing electron linac production of ^{99}Mo/^{99m}Tc lies in increasing the yield of ^{99}Mo and the radioactive concentration of ^{99m}Tc, both of which are determined by parameter choices. Therefore, identifying the parameters of importance and understanding their appropriate ranges can justify the design parameters of a newly constructed ^{99}Mo electron linac, and can make an existing electron linac available for ^{99}Mo production. Through parametric analyses, this dissertation attempts to provide a comprehensive understanding of beam and targetry parameters.

To solve simulation problems for wide ranges of parameter values, we developed three computer programs. We then carried out parametric analyses using the programs, and validated some of the results through experiments. Subsequently, we conducted modeling studies and defined a figure of merit that can quantify the influence of ^{100}Mo enrichment level on ^{99}Mo/^{99m}Tc yields. Also, we parameterized the ^{99m}Tc radioactive concentration such that it takes into account the issue of low specific activity ^{99}Mo.

In addition to the parametric analyses, we conducted small-animal biodistribution studies to test the radiopharmaceutical quality of linac-derived ^{99m}Tc. The tests showed that linac-derived ^{99m}Tc can be comparable to the conventional reactor-derived ^{99m}Tc.

The main goal of this dissertation is to provide reasonable parameter values in electron linac production of ^{99}Mo/^{99m}Tc, based on multivariate parametric analyses. The analyses consist of (i) identification of important parameters, (ii) understanding the influences of the parameters on the overall ^{99}Mo/^{99m}Tc production system, (iii) developing tools and methods for solving the identified parametric problems, (iv) and analyzing the numerical results. Based on the analyses, we suggest acceptable ranges of the identified parameters.

Contents

List of figures

List of tables

Listings

Glossary

Abbreviations

AA activated alumina

ABEC aqueous biphasic extraction chromatographic

AC activated carbon

ADC analog-to-digital converter

BBU beam breakup

CLI command-line interface

CLIC Compact Linear Collider

cpm count per minute

CT computed tomography

DCC density change coefficient

DTPA diethylenetriaminepentaacetic acid (common name: pentetic acid)

ELPH Research Center for ELectron PHoton Science, Tohoku University

EM electromagnetic

EOI end of irradiation

EOP end of postirradiation processing

FAST field-assisted sintering technique

FDG fludeoxyglucose

FWHM full width at half maximum

GDR giant dipole resonance

GUI graphical user interface

HEU highly enriched uranium

HFR High Flux Reactor

HMPAO hexamethylpropyleneamine oxime (common name: exametazime)

HSA high specific activity

IEEE Institute of Electrical and Electronics Engineers

IER ion exchange resin

ISC Isotope Science Center, University of Tokyo

ITU International Telecommunication Union

KURNS Institute for Integrated Radiation and Nuclear Science, Kyoto University

KURRI Kyoto University Research Reactor Institute

LEU low enriched uranium

linac linear accelerator

LSA low specific activity

MC Monte Carlo

MDP methylene diphosphonate (common name: medronic acid)

MRI magnetic resonance imaging

NIS sodium-iodide symporter

NRU National Research Universal

PECS pulsed electric current sintering

PET positron emission tomography

RAC radioactive concentration

RCC right circular cylinder

RF radio frequency

RMS root mean square

SCS side-coupled biperiodic structure

SMC Saitama Medical Center, Saitama Medical University

SPECT single-photon emission computed tomography

SPS spark plasma sintering

SW standing wave

TcMM Technetium Master Milker

TW traveling wave

Symbols

%ID ratio between the activity (dose) of an organ and the injected activity (dose)

%ID/g %ID divided by the weight of the organ

A activity of a radionuclide

A mass number

α_{att} attenuation constant per unit length

S specific activity of a radionuclide

B branching fraction

β normalized beam velocity

β_{wc} waveguide-to-cavity coupling coefficient

C_{A} radioactive concentration

D demand for a radionuclide

δ macropulse duty cycle

D density change coefficient

D_{org} activity (dose) of an organ

D_{tot} injected activity (dose)

E beam energy

$E_{\text{e}-}$ electron energy

E_{gain} beam energy gain

E_{γ} photon energy

$E_{\gamma,\text{th}}$ threshold energy for a photonuclear reaction

g eigenvalue

$\mathbf{X}$ eigenvector

f_{op} operating frequency

I_b average beam current (shortened to beam current in this dissertation; see Sec. 3.3.4)

$I_{b,\text{peak}}$ peak beam current (the beam current of a macropulse)

I_{γ} photon intensity

k thermal conductivity

κ fraction of ^{99}Mo/$^{99\text{m}}$Tc lost during postirradiation processing

L accelerating structure length

λ decay constant

M molar mass

m mass

$\bar{M}$ weighted-average molar mass

$\mathbf{Mo_{met}}$ Mo metal

$\mathbf{MoO_3}$ Mo(VI) oxide

m_{org} weight of an organ

n amount of substance (number of moles)

$\mathcal{N}$ number density

N_{A} Avogadro constant

N number of a radionuclide

N_r number of nuclear reactions taken place

Φ particle fluence

ψ_{conc} $^{99\mathrm{m}}$Tc concentration efficiency

$P_{\otimes}$ peak RF power fed into an accelerating structure

q_{e} elementary charge

$\mathcal{R}$ production rate of a radionuclide

ρ mass density

r_{s} effective shunt impedance per unit length

$r_{\mathrm{Tc\text{-}99m/Mo\text{-}99}}$ ratio between $^{99\mathrm{m}}$Tc and ^{99}Mo in ^{99}Mo/$^{99\mathrm{m}}$Tc

S specific yield of a radionuclide

Σ macroscopic cross section

σ microscopic cross section

σ_{h} Horizontal beam size (normal distribution)

σ_{v} Vertical beam size (normal distribution)

$t_{1/2}$ half-life of a radionuclide

T_{b} boiling point

t_{cool} cooling time

t_{dead} dead time

t_{dec} decay time

t_{del} delivery time

t_{irr} irradiation time

t_{live} live time

T_{m} melting point

t_{pro} postirradiation processing time

t_{real} real time

$\mathcal{V}$ volume

Γ total particle fluence in a given region

V accelerating voltage

ΔV_{stat} electric potential difference

w mass fraction

x amount fraction

ξ ratio between a target density and a material density

Y yield of a radionuclide

Z atomic number

Z_{eff} effective atomic number

ζ $^{99\text{m}}$Tc elution efficiency

Chapter 1

Introduction

1.1 ^{99}Mo/^{99m}Tc in nuclear medicine

Nuclear medicine is a field of medical imaging which provides a means of examining organ functions via planar scintigraphy, SPECT, and positron emission tomography (PET). Organ-specific pharmaceuticals labeled with trace amounts of radionuclides, referred to as radiopharmaceuticals, are administered to patients, and the gamma rays emitted from the radionuclides are measured by gamma cameras (Fig. 1.1). The measured uptakes of the radiopharmaceuticals are then used to assess the functions of the organs in question and, in turn, to diagnose the associated diseases. For instance, an excessive thyroid uptake can be a sign of Graves' disease, and an insufficient myocardial uptake can be a sign of myocardial ischemia[1].

Compared with the organs of interest, the surrounding anatomical structures emit much weaker radiation signals, resulting in limited amounts of anatomical information. Therefore, modern SPECT and PET machines are usually integrated with an x-ray computed tomography (CT) or magnetic resonance imaging (MRI) machine. Examples of such hybrid imaging modalities include SPECT/CT, PET/CT, and PET/MRI.

Although the number of PET scans using fluorine-18 fludeoxyglucose (^{18}F-FDG) has been on the rise, planar scintigraphy and SPECT scans using technetium-99m (^{99m}Tc) radiopharmaceuticals are still the most widespread procedures in nuclear medicine, accounting for about 80% of all nuclear medicine procedures[2,3]. Some of the commonly used ^{99m}Tc radiopharmaceuticals are listed in Table 1.1.

^{99m}Tc deexcites to ^{99}Tc with >99.9% probability, of which 90.8% is accompanied by

[1] F. A. Mettler *et al.* *Essentials of Nuclear Medicine Imaging*. 6th ed. (2012).
[2] W. C. Eckelman. *JACC Cardiovasc. Imaging* **2**, 364–368 (2009).
[3] OECD Nuclear Energy Agency. *The Supply of Medical Radioisotopes: 2018 Medical Isotope Demand and Capacity Projection for the 2018-2023 Period* (2018).

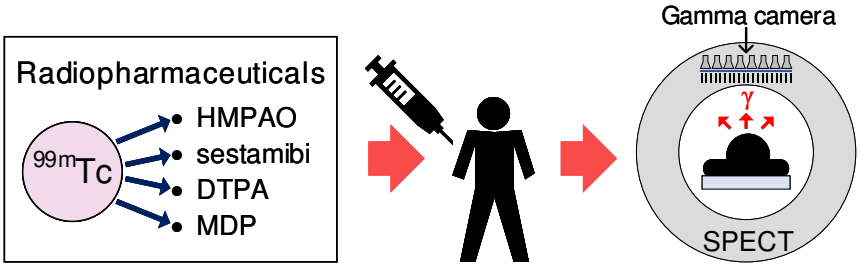

Fig. 1.1. An illustration of a SPECT imaging procedure.

Table 1.1. Commonly used ^{99m}Tc radiopharmaceuticals and their diagnostic use.

Radiopharmaceutical	Imaging protocol	Diagnostic target
^{99m}Tc-HMPAO[1]	Cerebral perfusion imaging	Ischemic stroke
^{99m}Tc-pertechnetate[2]	Thyroid uptake measurement	Thyroid function
^{99m}Tc-sestamibi	Myocardial perfusion imaging	Myocardial ischemia
^{99m}Tc-DTPA[3]	Renography	Renal function
^{99m}Tc-MDP[4]	Bone scintigraphy	Bone metastasis

[1] Hexamethylpropyleneamine oxime (common name: exametazime).
[2] Pertechnetate (TcO_4^-) is a Tc oxyanion which itself is taken up by the thyroid gland; hence, no separate pharmaceutical is required.
[3] Diethylenetriaminepentaacetic acid (common name: pentetic acid).
[4] Methylene diphosphonate (common name: medronic acid).

the emission of a 140.5-keV photon[4]. The energy window of a ^{99m}Tc gamma camera is therefore tuned to 140.5 keV[5]. ^{99m}Tc exhibits various oxidation states from -1 to $+7$[6], enabling formulation of various radiopharmaceutical complexes, and has a physical half-life of about 6 h, providing its radiopharmaceuticals with moderate effective half-lives. The 6-h physical half-life of ^{99m}Tc, however, is insufficient for its delivery to clinics and radiopharmacies; therefore, ^{99m}Tc is obtained through its longer-lived precursor, molybdenum-99 (^{99}Mo). ^{99}Mo has a half-life of about 66 h, and transmutes into ^{99m}Tc via negatron (β^-) decay with 87.5% probability.

Using a column of alumina (Al_2O_3) as the stationary phase and normal saline (0.9% w/v NaCl) as the mobile phase, ^{99m}Tc can be extracted from Al_2O_3 repeatedly until the ^{99}Mo loses most of its activity. This chromatographic method was developed at the Brookhaven National Laboratory in the 1950s[2,7], and has made ^{99}Mo one of the most important radionuclides in nuclear medicine.

[4] E. Browne *et al. Nucl. Data Sheets* **145**, 25–340 (2017).
[5] T. P. Sanders *et al. J. Nucl. Med.* **12**, 703–706 (1971).
[6] S. Liu *et al. Chem. Rev.* **99**, 2235–2268 (1999).
[7] V. J. Molinski. *Int. J. Appl. Radiat. lsot.* **33**, 811–819 (1982).

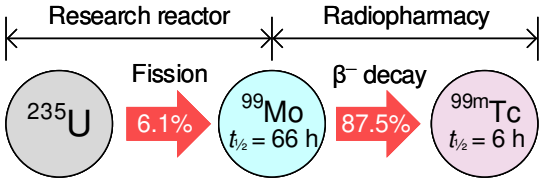

Fig. 1.2. An illustration of fission-based ^{99}Mo/^{99m}Tc supply chain.

Table 1.2. Issues involved in the fission production of ^{99}Mo.

Issue	Solution (a–d) and its disadvantages (→)
Civilian use of HEU	(a) Conversion from HEU to LEU targets → Radioactive waste from ^{235}U fission → Continued dependence on aging reactors (b) Utilizing the ^{98}Mo(n,γ)^{99}Mo reaction route → Low specific activity ^{99}Mo → Limited availability of reactors
Aging of reactors	(c) Commissioning new reactors → Public acceptance issues and high costs (d) Accelerator production of ^{99}Mo/^{99m}Tc → Low specific activity ^{99}Mo

1.2 Fission production of ^{99}Mo and its issues

Most ^{99}Mo for medical imaging is produced via the fission of uranium-235 (^{235}U) in multipurpose research reactors (Fig. 1.2). Recently, the fission-based ^{99}Mo supply chain has become unstable because of two major issues (Table 1.2): (i) the need for conversion of highly enriched uranium (HEU) to low enriched uranium (LEU) targets, and (ii) aging of the ^{99}Mo production reactors.

Naturally occurring uranium consists of three isotopes: ^{234}U (0.005%), ^{235}U (0.72%), and ^{238}U (99.27%), where ^{235}U is the only fissile nuclide. The percentages indicate the amount fractions[8]. By definition, HEU is uranium enriched to >20% by mass fraction in ^{235}U, and weapons-grade HEU is the one that has a ^{235}U enrichment level of >90%[9]. Approximately 40–50 kg of weapons-grade HEU have been supplied annually to selected research reactors for ^{99}Mo production[9,10]. Because HEU can be transformed into nuclear weapons, the international community has

[8] J. Meija *et al. Pure Appl. Chem.* **88**, 293–306 (2016).
[9] National Academies of Sciences, Engineering, and Medicine. *Molybdenum-99 for Medical Imaging* (2016).
[10] O. Reistad *et al. Nonproliferation Rev.* **15**, 265–287 (2008).

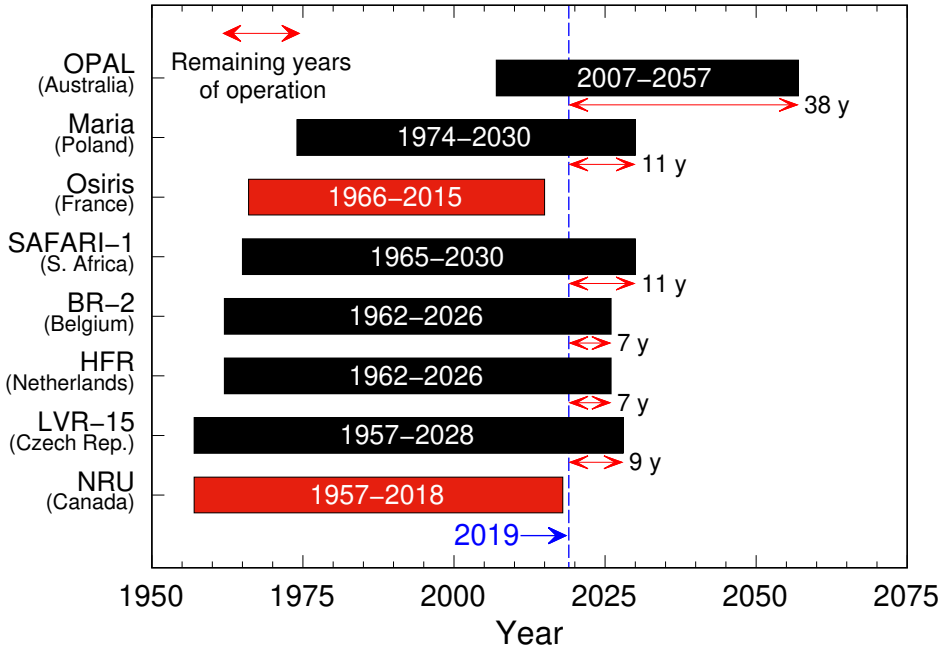

Fig. 1.3. Operation periods of major ^{99}Mo production reactors. The end years of operation can be found in [3]. Figure reproduced from our publication [15] which is licensed under CC BY 3.0.

agreed to replace HEU with LEU in civilian sectors, including the fission production of ^{99}Mo[11,12]. Some of the major ^{99}Mo suppliers have succeeded in converting their HEU targets to LEU ones and, presently, more than half the demand for ^{99}Mo is supplied using LEU targets[3].

In contrast to the HEU-to-LEU conversion issue which is being solved, the aging of the ^{99}Mo production reactors is becoming increasingly problematic. For instance, the National Research Universal (NRU) reactor and the High Flux Reactor (HFR) ceased operations simultaneously during 2009–2010[9,13], attributed to their aging. The unscheduled and prolonged shutdowns of the two major reactors led to cancellation and postponement of ^{99m}Tc-based medical procedures worldwide[9,14], which is known as the 2009–2010 global supply shortages[3,9]. Moreover, as of 2019, all but one of the reactors are planned to shut down in about 10 years (Fig. 1.3), necessitating alternative sources of ^{99}Mo/^{99m}Tc.

An alternative reactor-based solution is to produce ^{99}Mo via the neutron cap-

[11] C. Hansell. *Nonproliferation Rev.* **15**, 185–208 (2008).
[12] C. Hansell. *Nonproliferation Rev.* **15**, 289–310 (2008).
[13] B. Ponsard. In *Proceedings of the 14th International Topical Meeting on Research Reactor Fuel Management, RRFM 2010* (2010).
[14] R. Van Noorden. *Nature* **504**, 202–204 (2013).

ture reaction ^{98}Mo(n,γ)^{99}Mo. However, because the thermal cross section is only 0.13 b[16,17], the resulting ^{99}Mo exhibits low specific activity (LSA), for which the conventional Al_2O_3-based ^{99m}Tc generators cannot be used for ^{99m}Tc extraction. While this LSA problem can be solved by chemical means[18], the limited availability of reactors remains problematic. Commissioning a new research reactor may be an option, but is often unfeasible for reasons such as public acceptance issues and the prohibitive capital cost.

Because of the problems associated with the reactor approaches, accelerator-based methods of ^{99}Mo/^{99m}Tc production, which had already been known but remained unused, have been revisited and investigated extensively by various research groups.

1.3 Accelerator production of ^{99}Mo/^{99m}Tc

The unstable fission-based ^{99}Mo supply chain has prompted research into accelerator-based methods of ^{99}Mo/^{99m}Tc production (see Fig. 1.4 and Appendix B). One method is to utilize fast neutron generators and induce the ^{100}Mo(n,2n)^{99}Mo reaction. For example, a collaborative research group in Japan proposed commissioning a 40 MeV and 2 mA deuteron cyclotron[19,20], which can generate high-intensity fast neutrons by bombarding deuterons with carbon atoms. Colliding with a Mo target, the fast neutrons can then induce the ^{100}Mo(n,2n)^{99}Mo reaction. Also, several other research groups[21–23] proposed utilizing fusion neutron sources in inducing the ^{100}Mo(n,2n)^{99}Mo reaction.

Direct production of ^{99m}Tc via the ^{100}Mo(p,2n)^{99m}Tc reaction is also a promising alternative. This approach utilizes 18–24 MeV proton cyclotrons, originally commissioned for positron emitter production, in inducing the ^{100}Mo(p,2n)^{99m}Tc reaction. Therefore, if a clinic is equipped with a PET cyclotron, ^{99m}Tc can also become available. Although the method has been known since the early 1970s[26], it was not until the 2009–2010 ^{99}Mo shortages that the direct production of ^{99m}Tc was reconsidered and

[16] International Atomic Energy Agency. *Fission Molybdenum for Medical Use* (1989).
[17] National Research Council (US). *Medical Isotope Production Without Highly Enriched Uranium* (2009).
[18] A. Dash *et al. Nucl. Med. Biol.* **40**, 167–176 (2013).
[19] Y. Nagai *et al. J. Phys. Soc. Jpn.* **82**, 064201 (2013).
[20] K. Tsukada *et al. J. Phys. Soc. Jpn.* **87**, 043201 (2018).
[21] K.-N. Leung *et al. Appl. Radiat. Isot.* **137**, 23–27 (2018).
[22] M. Capogni *et al. Molecules* **23**, 1872 (2018).
[23] M. Ohta *et al. Nucl. Mater. Energy* **15**, 261–266 (2018).
[26] J. E. Beaver *et al. J. Nucl. Med.* **12**, 739–741 (1971).

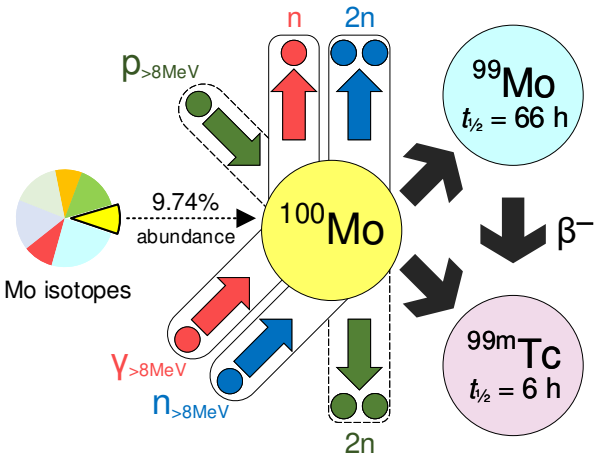

(a)

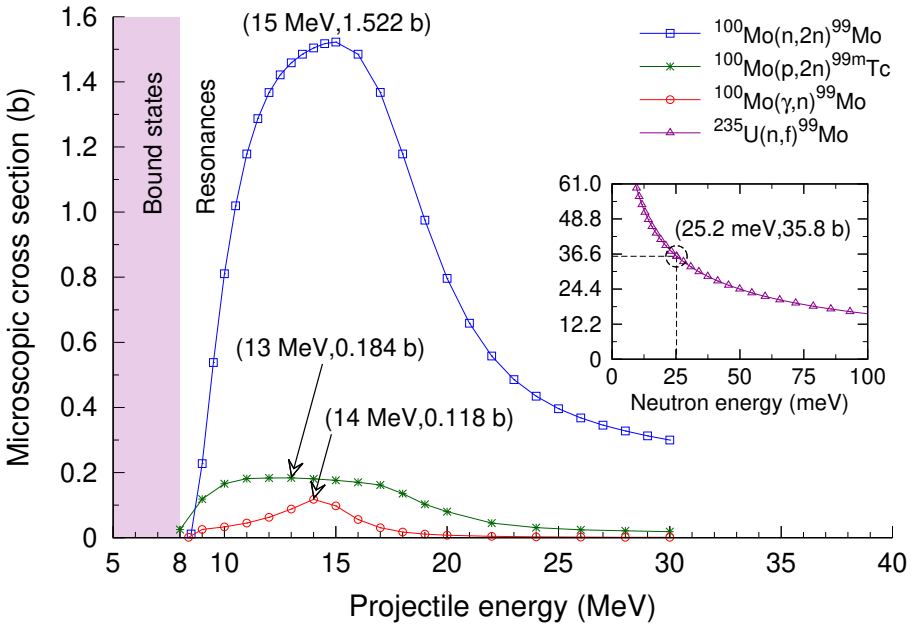

(b)

Fig. 1.4. (a) A diagram of accelerator- and ^{100}Mo-based production of ^{99}Mo/^{99m}Tc and (b) the associated excitation functions. The nonfission excitation functions are from TENDL-2017 [24], and the fission one is from ENDF/B-VIII.0 [25] multiplied by the 6.1% fission yield for ^{99}Mo. The individual excitation functions are also plotted in Appendix C. Figure (a) reproduced from our publication [15] which is licensed under CC BY 3.0.

investigated extensively[15,27–38]. Significant advancements have been made thus far[39], and clinical routine use of cyclotron-derived ^{99m}Tc is expected in the near future.

Another method is to utilize 20–50 MeV electron linacs that can generate high-energy photons. The high-energy photons, generated via electron collisions with a high-Z material, are used to induce the photonuclear reaction ^{100}Mo(γ,n)^{99}Mo. Bennett and his colleagues conducted pioneering and comprehensive research in the late 1990s[40], which has been revisited after the 2009–2010 ^{99}Mo shortages[15,41–52]. This electron linac approach is the subject of this dissertation, and will be elaborated in the following section.

1.4 Electron linac production of ^{99}Mo/^{99m}Tc

Electron linacs can be commissioned in multiple regions, by which ^{99}Mo can be produced in a decentralized fashion (Fig. 1.5). Decentralized ^{99}Mo production can stabilize the ^{99}Mo supply chain, in that an interrupted production facility can be backed up by the others. In addition, the giant dipole resonance (GDR) of ^{100}Mo(γ,n)^{99}Mo

[15] J. Jang *et al. J. Phys. Commun.* **3**, 055015 (2019).
[27] T. Ruth. *Nature* **457**, 536–537 (2009).
[28] A. Celler *et al. Phys. Med. Biol.* **56**, 5469–5484 (2011).
[29] X. Hou *et al. Phys. Med. Biol.* **57**, 1499–1515 (2012).
[30] K. Gagnon *et al. Appl. Radiat. Isot.* **70**, 1685–1690 (2012).
[31] K. Gagnon *et al. Nucl. Med. Biol.* **39**, 923–925 (2012).
[32] J. Esposito *et al. Sci. Technol. Nucl. Ins.* **2013**, 972381 (2013).
[33] S. M. Qaim *et al. Appl. Radiat. Isot.* **85**, 101–113 (2014).
[34] X. Hou *et al. Phys. Med. Biol.* **61**, 8199–8213 (2016).
[35] J. D. Andersson *et al. Nucl. Med. Biol.* **60**, 63–70 (2018).
[36] P. Martini *et al. Appl. Radiat. Isot.* **139**, 325–331 (2018).
[37] N. M. Uzunov *et al. Phys. Med. Biol.* **63**, 185021 (2018).
[38] L. Meléndez-Alafort *et al. Med. Phys.* **46**, 1437–1446 (2019).
[39] International Atomic Energy Agency. *Cyclotron Based Production of Technetium-99m* (2017).
[40] R. G. Bennett *et al. Nucl. Technol.* **126**, 102–121 (1999).
[41] C. Ross *et al. Phys. Can.* **66**, 19–24 (2010).
[42] R. Galea *et al. Phys. Med. Biol.* **58**, 2737–2750 (2013).
[43] B. Szpunar *et al. Nucl. Instrum. Methods Phys. Res. A* **729**, 41–50 (2013).
[44] V. N. Starovoitova *et al. Appl. Radiat. Isot.* **85**, 39–44 (2014).
[45] K. Mang'era *et al. J. Radioanal. Nucl. Chem.* **305**, 79–85 (2015).
[46] N. P. Dikiy *et al. Appl. Radiat. Isot.* **114**, 7–13 (2016).
[47] A. Tsechanski *et al. Nucl. Instrum. Methods Phys. Res. B* **366**, 124–139 (2016).
[48] S. Sekimoto *et al. J. Radioanal. Nucl. Chem.* **311**, 1361–1366 (2017).
[49] T. M. Martin *et al. J. Radioanal. Nucl. Chem.* **314**, 1051–1062 (2017).
[50] J. Jang *et al. Phys. Rev. Accel. Beams* **20**, 104701 (2017).
[51] T. Takeda *et al. J. Radioanal. Nucl. Chem.* **318**, 811–821 (2018).
[52] D. V. Fedorchenko *et al. Nucl. Instrum. Methods Phys. Res. B* **438**, 6–13 (2019).

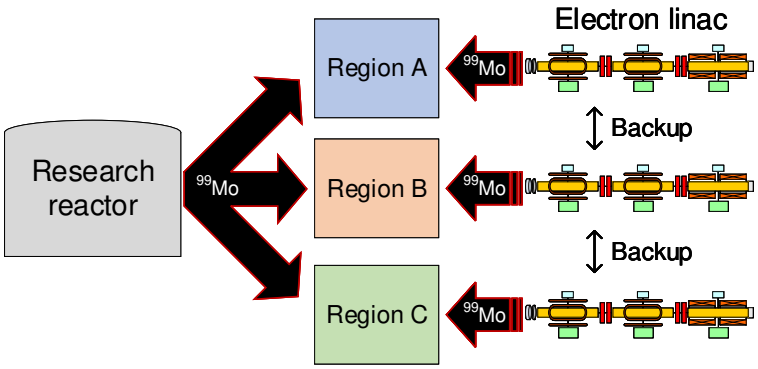

Fig. 1.5. A schematic comparison of the reactor- and linac-based ^{99}Mo supply chains.

can be utilized in improving the ^{99}Mo yield. Other advantages include reduction in radioactive waste.

The electron linac approach can be compared with the two cyclotron approaches introduced in Sec. 1.3: (i) 40 MeV deuteron and (ii) 18–24 MeV proton cyclotrons.

Compared with the 40 MeV deuteron cyclotron, 20–50 MeV electron linacs can reduce the radiation damage of targetry components, because the stopping power of electrons is much lower than that of deuterons for similar beam energies. Also, considering the abilities of the involved particles to interact with nuclei[53], reduction in the induced activity of beamline and targetry components are expected in the electron linac approach, making the shielding design simpler.

Induced activity refers to the activity emitted from accelerator components that became radioactive by incident radiation.

Compared with the proton cyclotrons, on the other hand, electron linacs can retain the advantage of ^{99}Mo/^{99m}Tc over ^{99m}Tc, namely the 11 times longer half-life of ^{99}Mo (Sec. 1.1); by the presence of ^{99}Mo, the short-lived ^{99m}Tc can be stockpiled in the form of ^{99}Mo/^{99m}Tc, and can therefore be delivered to countries where particle accelerators are unavailable.

Electron linac production of ^{99}Mo/^{99m}Tc consists of multiple branches of science, including physics, chemistry, and biomedical sciences (Fig. 1.6). The research subjects involved in the respective disciplines are introduced below.

1.4.1 Physical step

It is the design of an electron linac and its target system that dictates the overall integrity of ^{99}Mo production cycle. In a broad sense, electron linac design includes determination of the operating beam energy and beam current taking into account both

[53] A. H. Sullivan. *A guide to radiation and radioactivity levels near high energy particle accelerators* (1992).

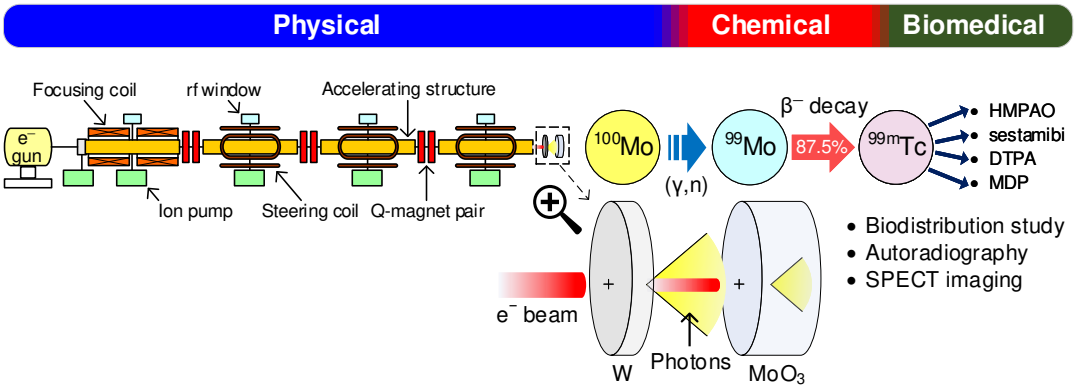

Fig. 1.6. Research topics in the electron linac production of ^{99}Mo/^{99m}Tc.

the ^{99}Mo production and engineering perspectives. These tasks cannot be excluded even in cases where custom-made electron linacs can be purchased or existing electron linacs can be utilized. Once the beam energy and current are determined, the next step is to secure an electron linac that can provide high-quality electron beams in a stable manner. Failure of this step will lead to failure of the entire ^{99}Mo/^{99m}Tc production system.

The operating beam energy can be determined based on the ^{99}Mo production efficiency[50], and typically lies in the range of 20–50 MeV[41–46,48–52]. MC simulation and analysis of ^{99}Mo/^{99m}Tc yields can be useful in determining the ^{99}Mo production efficiency[50].

An electron linac can be designed and commissioned from scratch, or can be purchased from an accelerator development company. As for existing electron linacs, their use is more appropriate for experimental ^{99}Mo production, because the linac specifications are not necessarily optimal for ^{99}Mo production. Parametric investigation of a ^{99}Mo production electron linac will be addressed in Chap. 3.

Accelerated electron beams are transported to ^{99}Mo production targetry and their kinetic energy is converted into bremsstrahlung photons. Inefficient conversion means that part of the electron beam energy is wasted that would otherwise be available for the ^{100}Mo(γ,n)^{99}Mo reaction. Accordingly, ^{99}Mo production targetry should be designed such that the given electron beams are utilized to the greatest extent possible, which can be accomplished by parametric analysis. The parametric studies of ^{99}Mo production targetry and their experimental validation will be addressed in Chaps. 4 and 5, respectively.

1.4.2 Chemical step

As explained in Sec. 1.1, ^{99m}Tc is supplied to clinics and radiopharmacies in the form of a chromatographic device referred to as a ^{99m}Tc generator. A ^{99m}Tc generator is a lead-shielded container for a column of Al_2O_3, where $[^{99}Mo]MoO_4^{2-}$ is loaded and constantly decays to $[^{99m}Tc]TcO_4^-$. Because the affinity of MoO_4^{2-} for the Al_2O_3 polar stationary phase is greater than that of TcO_4^-, a saline mobile phase can separate $[^{99m}Tc]TcO_4^-$ from $[^{99}Mo]MoO_4^{2-}$.

The specific activity of linac ^{99}Mo is lower than that of fission ^{99}Mo by three orders of magnitude[54] and, therefore, the former and latter are referred to as LSA and high specific activity (HSA), respectively. Because of the LSA characteristic of linac ^{99}Mo, alumina can no longer be used for ^{99m}Tc elution, requiring new separation methods.

Reversed-phase chromatography is considered a promising solution to the LSA issue. In contrast to the conventional ^{99m}Tc generator, reversed-phase chromatography employs a nonpolar stationary phase. Because of this polarity inversion, hydrophobic TcO_4^- ions now adsorb to the nonpolar stationary phase, while hydrophilic MoO_4^{2-} ions are more attracted to the polar mobile phase. As a result, sufficient radioactive concentration (RAC) of ^{99m}Tc can be obtained from LSA ^{99}Mo. Our collaborative research group has been working on AC chromatography[48,55], which is essentially reversed-phase chromatography. Parametric studies for the AC chromatography and its experimental verification will be explained in Chap. 7.

1.4.3 Biomedical step

After all, ^{99m}Tc obtained from linac ^{99}Mo must be able to be used for medical imaging. The quality of such linac-derived ^{99m}Tc as a radiopharmaceutical must be assured through a series of quality controls, preclinical testing, and clinical trials. Below we introduce preclinical testing methods.

Biodistribution studies can be useful in assessing the radiopharmaceutical quality of linac-derived ^{99m}Tc in a quantitative manner. In early-phase biodistribution studies, ^{99m}Tc radiopharmaceuticals are administered to small animals such as mice or rats, and the pharmacokinetics is investigated by comparing the gamma-ray intensities of dissected organs. The gamma counts collected from the organs can then be used for a quantitative assessment of the ^{99m}Tc radiopharmaceutical.

[54] International Atomic Energy Agency. *Non-HEU Production Technologies for Molybdenum-99 and Technetium-99m* (2013).
[55] H. Kawamura *et al.* Jpn. Pat. 5569834 (2014).

It is the images that are most often used by nuclear medicine physicians to diagnose diseases and, accordingly, imaging studies should also be performed in the biomedical step. Compared with the biodistribution studies, imaging studies can be considered as a qualitative assessment of linac-derived ^{99m}Tc. Autoradiography and small-animal SPECT imaging are one of the imaging studies available in the preclinical phase. In autoradiography, animals are administered with ^{99m}Tc radiopharmaceuticals and sacrificed, and frozen sections of the organs of interest are obtained and imaged. The distribution of ^{99m}Tc compounds can then be examined through the relative pixel intensities of the image. Small-animal SPECT imaging, on the other hand, can be thought of as miniaturized human SPECT imaging.

We conducted biodistribution studies using ^{99m}Tc obtained from linac ^{99}Mo and AC chromatography. The experimental methods and results will be presented in Chap. 8.

1.5 Dissertation objectives and outline

Because of its multidisciplinary nature, electron linac production of ^{99}Mo/^{99m}Tc requires analyses of various interdependent parameters. Through parametric analyses, this dissertation attempts to provide parameter values that are scientifically reasonable and practically achievable. Computer programs were developed for solving the parameter problems, and some of the findings were validated through irradiation experiments.

The dissertation consists of nine chapters. In this chapter, we introduced the background and objectives of the dissertation work. In Chap. 2, the computational approaches we employed in the parametric analyses will be explained. Chaps. 3 and 4 are dedicated to the parametric studies of a ^{99}Mo production electron linac and its targetry, respectively, for which the developed programs were used. The experimental part of Chap. 4 has been addressed separately in Chap. 5 because of its large volume. Subsequently, Chap. 6 will address a physical parameter we defined for studying enriched ^{100}Mo, which was also calculated by one of the developed programs. Chap. 7 will delve into the LSA issue, and will derive parameterized RAC and its experimental verification. Chap. 8 is reserved for the biomedical research topics introduced in Sec. 1.4.3, which is not a parametric study but is intended for testing the clinical value of linac-derived ^{99m}Tc. Finally, Chap. 9 provides the conclusion and future work of the dissertation.

Chapter
2

Computational approaches

Abstract

Physical and chemical problems involved in electron linac production of ^{99}Mo require a broad range of simulation tasks and dedicated tools that can control the simulation runs. We developed and used three such programs throughout this dissertation work. The fundamental concepts of the programs are introduced in this chapter.

2.1 The need for dedicated computer programs

Research tasks involved in electron linac production of ^{99}Mo, such as parametric analysis, require a wide spectrum of independent simulation runs and postprocessing. Typically, more than hundreds of simulation runs are necessary for one research task and, therefore, existing simulation tools may no longer be handled manually. For instance, examining only 10 beam energies and 50 target thicknesses will require 500 simulation runs, each of which necessitates parameter modifications according to the simulation setup in question (Fig. 2.1). Therefore, developing computer programs dedicated to individual research topics is necessary, particularly for designing an electron linac and its targetry.

We developed three computer programs for this dissertation work (Fig. 2.2): (i) `phitar`, (ii) `enrimo`, and (iii) `actdyn`, all of which are written in PERL (Perl 5), heavily commented, and are available in open-source repositories[56–58]. The PERL language was chosen because of its robust and user-friendly regular expression engine. Many of the datasets presented in this dissertation have been generated using the programs (i)–(iii), either by direct use or as the frontend programs of other existing simulation

[56] J. Jang. `phitar` - A PHITS wrapper for targetry design (v1.03) (2019).
[57] J. Jang. `enrimo` - Investigate the influence of an enriched Mo isotope (v1.05) (2019).
[58] J. Jang. `actdyn` - A Mo-99/Tc-99m activity dynamics simulator (v2.31) (2019).

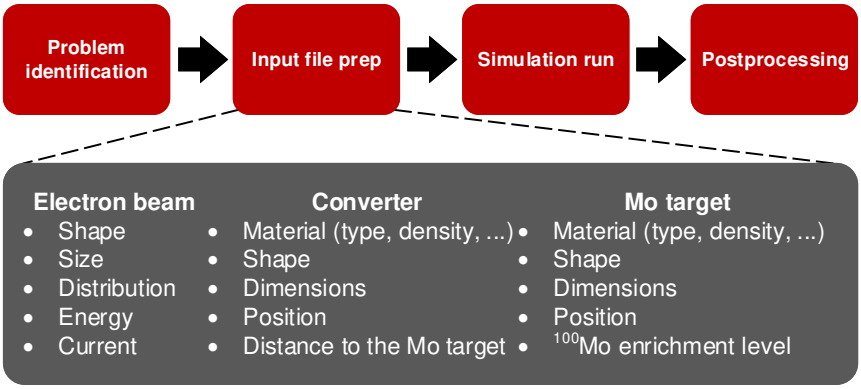

Fig. 2.1. A diagram describing the workflow of multivariate simulation.

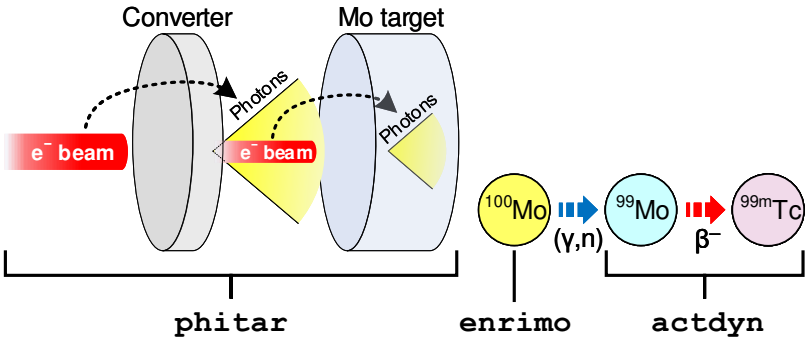

Fig. 2.2. Computer programs developed in this dissertation work and their roles.

programs. Where appropriate, the use of the programs will be mentioned in chapters addressing specific topics. In this chapter, some of the core concepts and algorithms of the programs will be explained.

2.2 `phitar`: A PHITS wrapper for targetry design

The multivariate yield of the ^{100}Mo(γ,n)^{99}Mo reaction can be expressed as[15,50]

$$\begin{aligned} Y_{\text{Mo-99}}(t_{\text{irr}}, w_{\text{Mo-100}}) = {} & [1 - \exp(-\lambda_{\text{Mo-99}} t_{\text{irr}})]\, \mathcal{V}_{\text{Mo-tar}} I_{\text{e}^-} \\ & \times \left[\frac{w_{\text{Mo-100}} w_{\text{Mo}}(w_{\text{Mo-100}}) \rho_{\text{Mo-tar}}}{M_{\text{Mo-100}}} N_{\text{A}} \right] \\ & \times \int_{E_{\gamma,\text{th}}}^{\infty} \Phi_{\text{Mo-tar}}(E_\gamma) \sigma(E_\gamma)\, \mathrm{d}E_\gamma, \end{aligned} \tag{2.1}$$

[15] J. Jang *et al. J. Phys. Commun.* **3**, 055015 (2019).
[50] J. Jang *et al. Phys. Rev. Accel. Beams* **20**, 104701 (2017).

where $\lambda_{\text{Mo-99}}$ is the decay constant of ^{99}Mo, t_{irr} the irradiation time, $\mathcal{V}_{\text{Mo-tar}}$ the volume of a Mo target, $I_{\text{e}-}$ the electron beam current, w the mass fraction, $\rho_{\text{Mo-tar}}$ the mass density of the Mo target, $M_{\text{Mo-100}}$ the molar mass of ^{100}Mo, N_{A} the Avogadro constant, $E_\gamma = E_\gamma(E_{\text{e}-})$ the photon beam energy, $\Phi_{\text{Mo-tar}}$ the particle fluence in the Mo target, and σ the microscopic cross section. The target density $\rho_{\text{Mo-tar}}$ in Eq. (2.1) is related to the material density by

$$\rho_{\text{Mo-tar}} = \xi \rho_{\text{Mo-mat}}, \tag{2.2}$$

where $\xi \leq 1$ is the ratio between the target and material densities, which we refer to as a density ratio.

When designing ^{99}Mo production targetry, MC simulations need to be performed with the following parameters of Eq. (2.1) varied over ranges: t_{irr}, $\mathcal{V}_{\text{Mo-tar}}$ (via the Mo target dimensions), $w_{\text{Mo-100}}$, $\rho_{\text{Mo-tar}}$, σ, $E_{\text{e}-}$, the material types of converter and Mo targets, the distance between the two materials, and the shape and size of electron beams. Because of this multivariate characteristics, performing MC simulations for Eq. (2.1) in a manual fashion is often impractical. In order to enable such multivariate simulation, we developed a wrapper program of the PHITS MC simulation platform[59], called `phitar`. Accepting the user requests via its input parser, `phitar` generates and runs PHITS input files, and performs postprocessing in an automated manner. `phitar` is an object-oriented program written using the `Moose` ecosystem of PERL. A simplified diagram of `phitar` is shown in Fig. 2.3.

Essentially, the multivariate simulation of `phitar` is performed by two iterator routines: (i) an outer iterator that runs over ranges of electron beam parameters, and (ii) an inner iterator that runs over ranges of targetry materials and dimensions. When a range of beam parameters set by the user is passed to the outer iterator, the other beam parameters are automatically determined. Next, ranges of geometric parameters also set by the user are sequentially passed to the inner iterator.

Part of the outer iterator is presented in Listing 2.1, showing how the inner iterator is invoked. The scalar variables `$src_nrg` and `$src_size` contain beam parameter values that are to be varied or fixed, and the control variable `$_` is passed to the inner iterator for the whole range of the varying dimension of a given material. Such iterative invocations are performed for the following target material:

(i) `@{$bconv->iteration_geoms}` for a cylindrical-shaped converter
(ii) `@{$motar_rcc->iteration_geoms}` for a cylindrical-shaped Mo target
(iii) `@{$motar_trc->iteration_geoms}` for a frustum-shaped Mo target

[59] T. Sato *et al. J. Nucl. Sci. Technol.* **55**, 684–690 (2018).

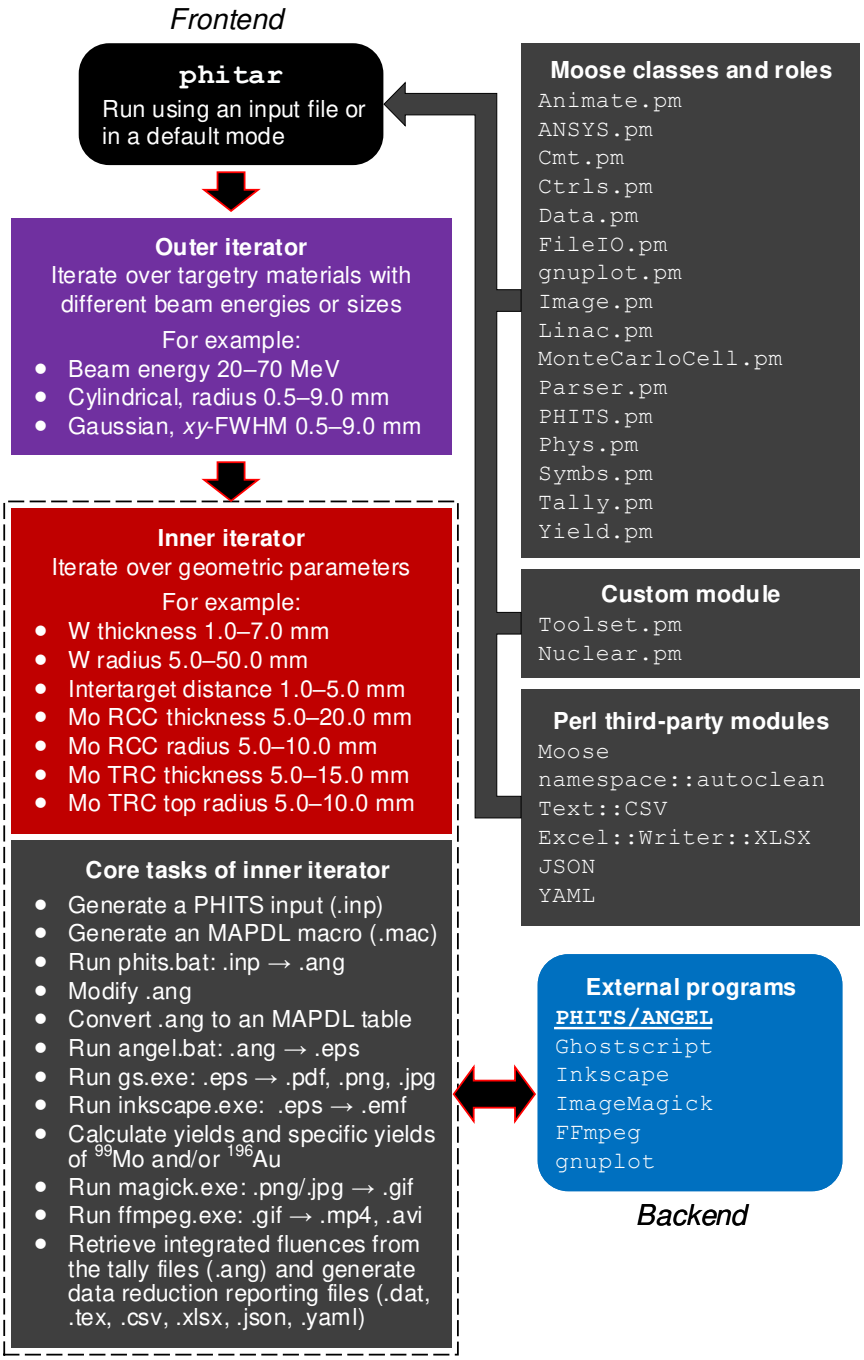

Fig. 2.3. A simplified diagram of `phitar`.

```
        # Invoke the inner iterator for a range of varying geometric
    parameter
        # of a target material, with the set of source parameters
    specified
        # at the beginning of this outer iterator.
        inner_iterator(
            $prog_info_href,
            $run_opts_href,
            $src_nrg,
            $src_size,
            $bconv,
            $_,
        ) for @{$bconv->iteration_geoms};
        inner_iterator(
            $prog_info_href,
            $run_opts_href,
            $src_nrg,
            $src_size,
            $motar_rcc,
            $_,
        ) for @{$motar_rcc->iteration_geoms};
        inner_iterator(
            $prog_info_href,
            $run_opts_href,
            $src_nrg,
            $src_size,
            $motar_trc,
            $_,
        ) for @{$motar_trc->iteration_geoms};
```

Listing 2.1: Part of the outer iterator of `phitar`.

Data reduction and postprocessing are automatically performed on the calculation results and, as a result, the following types of outputs are obtained: columnar data (`.dat`), LaTeX 2ε tabular environment (`.tex`), comma-separated values (`.csv`), MS EXCEL (`.xlsx`), JAVASCRIPT Object Notation (`.json`), YAML (`.yaml`), ANSYS MAPDL table (`.tab`), vector graphics formats (`.pdf`, `.emf`, and `.wmf`), and rasterized images (`.png` and `.jpg`) and their animated videos (`.gif`, `.avi`, and `.mp4`). These files are intended to improve the readability of the calculation results and to facilitate data exchange.

The output types can be designated by the user.

The explanations and diagrams given above are the minimum amount of information necessary to understand the core tasks and algorithm of `phitar`. As of v1.03[56], `phitar` consists of 19,745 lines of code and 4,308 lines of comments; by the relatively

large number of comment lines, the implementation details are self-contained in the source code. The usage instructions of `phitar` are provided in Appendix A.1. The parametric and design studies of ^{99}Mo production targetry, which will be addressed in Chap. 4 and Chap. 5, were conducted using `phitar`. Also, in Chap. 3, `phitar` was used to simulate particle tracks and heat distributions in target materials as functions of target dimensions and electron beam energy.

2.3 `enrimo`: A DCC calculator

In accelerator production of ^{99}Mo, the use of enriched ^{100}Mo is considered necessary, and in cyclotron production of ^{99m}Tc, the use of enriched ^{100}Mo is required[15]. In order to facilitate determining the ^{100}Mo enrichment level and the $^{92,94–98}$Mo depletion levels, we defined a figure of merit called a DCC. The concept of DCC encompasses all of the ^{100}Mo(γ,n)^{99}Mo, ^{100}Mo(n,2n)^{99}Mo, ^{100}Mo(p,2n)^{99m}Tc reaction routes (see Fig. 1.4), and will be addressed as a separate topic in Chap. 6. In this section, some subtle concepts of the DCC and their implementation in code will be explained.

2.3.1 Molybdenum oxide and density quantities

The number density of ^{100}Mo in a given Mo material can be written as[15]

$$\mathcal{N}_{\text{Mo-100}} = \frac{\rho_{\text{Mo-100}}}{M_{\text{Mo-100}}} N_{\text{A}} = \frac{w_{\text{Mo-100}}\rho_{\text{Mo}}}{M_{\text{Mo-100}}} N_{\text{A}} = \frac{w_{\text{Mo-100}} w_{\text{Mo}}(w_{\text{Mo-100}})\xi\rho_{\text{Mo-mat}}}{M_{\text{Mo-100}}} N_{\text{A}}, \quad (2.3)$$

of which the parameters were explained in Eq. (2.1). To reiterate, ρ, w, and M denote the mass density, mass fraction, and molar mass, respectively, and N_{A} is the Avogadro constant. For explanation purposes, we will assume $\xi = 1$ and thereby $\rho_{\text{Mo-tar}} = \rho_{\text{Mo-mat}}$ (see Eq. (2.2)).

By multiplying Eq. (2.3) by the volume of a Mo target $\mathcal{V}_{\text{Mo-tar}}$, we, in effect, calculate the total number of ^{100}Mo nuclides contained in the Mo target:

$$\begin{aligned}\mathcal{N}_{\text{Mo-100}}\mathcal{V}_{\text{Mo-tar}} &= \left(\frac{\text{number of } ^{100}\text{Mo nuclides}}{\text{cm}^3}\right)\left(\text{cm}^3\right) \\ &= \text{number of } ^{100}\text{Mo nuclides}.\end{aligned}$$

Clearly, when a Mo oxide is used as the Mo target, in holds that $w_{\text{Mo}} \neq 1$ and

therefore $\rho_{\text{Mo}} \neq \rho_{\text{Mo-tar}}$. We then need to calculate w_{Mo} using

$$w_{\text{Mo}} = \frac{n_{\text{Mo}}\bar{M}_{\text{Mo}}}{n_{\text{Mo}}\bar{M}_{\text{Mo}} + n_{\text{O}}\bar{M}_{\text{O}}}, \tag{2.4}$$

where n is the amount of substance, and $\bar{M}$ is the weighted-average molar mass. For instance, a target of MoO_2 results in

$$w_{\text{Mo}} = \frac{(1)(95.949\,\text{g mol}^{-1})}{(1)(95.949\,\text{g mol}^{-1}) + (2)(15.999\,\text{g mol}^{-1})} \approx 0.7500, \tag{2.5}$$

and hence

$$\rho_{\text{Mo}} = w_{\text{Mo}}\rho_{\text{MoO}_2} = (0.7500)(6.47\,\text{g cm}^{-3}) \approx 4.85\,\text{g cm}^{-3}, \tag{2.6}$$

and for a MoO_3 target, we have

$$w_{\text{Mo}} = \frac{(1)(95.949\,\text{g mol}^{-1})}{(1)(95.949\,\text{g mol}^{-1}) + (3)(15.999\,\text{g mol}^{-1})} \approx 0.66656, \tag{2.7}$$

which follows that

$$\rho_{\text{Mo}} = w_{\text{Mo}}\rho_{\text{MoO}_3} = (0.66656)(4.69\,\text{g cm}^{-3}) \approx 3.13\,\text{g cm}^{-3}. \tag{2.8}$$

As can be seen from Eqs. (2.6) and (2.8), a Mo oxide affects two terms that constitute the mass density of a Mo element: (i) the mass fraction of Mo in its associated Mo material, and (ii) the mass density of the Mo material. As a result, the mass densities of Mo elements in Mo oxides are always smaller than that of a Mo metal; that is, the Mo mass density in metallic Mo is given by

$$w_{\text{Mo}} = \frac{(1)(95.949\,\text{g mol}^{-1})}{(1)(95.949\,\text{g mol}^{-1}) + (0)(15.999\,\text{g mol}^{-1})} = 1.0000,$$

leading to

$$\rho_{\text{Mo}} = w_{\text{Mo}}\rho_{\text{Mo}_{\text{met}}} = (1.0000)(10.28\,\text{g cm}^{-3}) = 10.28\,\text{g cm}^{-3} = \rho_{\text{Mo}_{\text{met}}}.$$

The Mo mass densities in Mo metal and oxides are summarized in Table 2.1.

Now, we consider cases where ^{100}Mo is artificially enriched. We begin with the

Table 2.1. Mass densities of Mo elements in different Mo materials.

Mo material	$\rho_{\text{Mo-mat}} = \rho_{\text{Mo-tar}}$[1] ($\mathrm{g\,cm^{-3}}$)	w_{Mo}	ρ_{Mo} ($\mathrm{g\,cm^{-3}}$)
Mo	10.28	1.0000	10.28
MoO_2	6.47	0.7500	4.85
MoO_3	4.69	0.66656	3.13

[1] $\xi = 1$ is assumed for simplicity; see Eq. (2.2).

molar mass of a Mo element, which is calculated as a weighted mean:

$$\bar{M}_{\text{Mo}} = \sum_A x_{\text{Mo-}A} M_{\text{Mo-}A} = 95.949\,\mathrm{g\,mol^{-1}}, \tag{2.9}$$

where A represents the mass numbers of $^{92,94\text{–}98,100}$Mo that make up naturally occurring Mo, and x denotes the amount fraction. Eq. (2.9) suggests that when a Mo target is enriched to 99% in ^{100}Mo, the weighted-average molar mass of Mo is modified:

$$\bar{M}_{\text{Mo}} = (0.9900)(99.907\,\mathrm{g\,mol^{-1}}) + \sum_{A\neq 100} x_{\text{Mo-}A} M_{\text{Mo-}A} \approx 99.887\,\mathrm{g\,mol^{-1}}. \tag{2.10}$$

The changed $\bar{M}_{\text{Mo}}$ then affects its corresponding mass fraction (see Eq. (2.4)). Namely, the Mo mass fraction in MoO_2 will become

$$w_{\text{Mo}} = \frac{(1)(99.887)}{(1)(99.887) + (2)(15.999)} \approx 0.75738,$$

and that in MoO_3 will become

$$w_{\text{Mo}} = \frac{(1)(99.887)}{(1)(99.887) + (3)(15.999)} \approx 0.67544,$$

both of which differ from Eqs. (2.5) and (2.7), respectively. This led to the function notation $w_{\text{Mo}}(w_{\text{Mo-100}})$ in Eqs. (2.1) and (2.3).

Consequently, when Mo is enriched in ^{100}Mo, the mass density of ^{100}Mo is increased not only by the increase in $w_{\text{Mo-100}}$, but also by the increased w_{Mo}. In developing the DCC concept, (i) identifying this subtle change and (ii) implementing them in computer code were the main research tasks, the latter of which will be explained in the following subsection. On the other hand, rigorous definitions and explanations of the DCC will be addressed in Chap. 6.

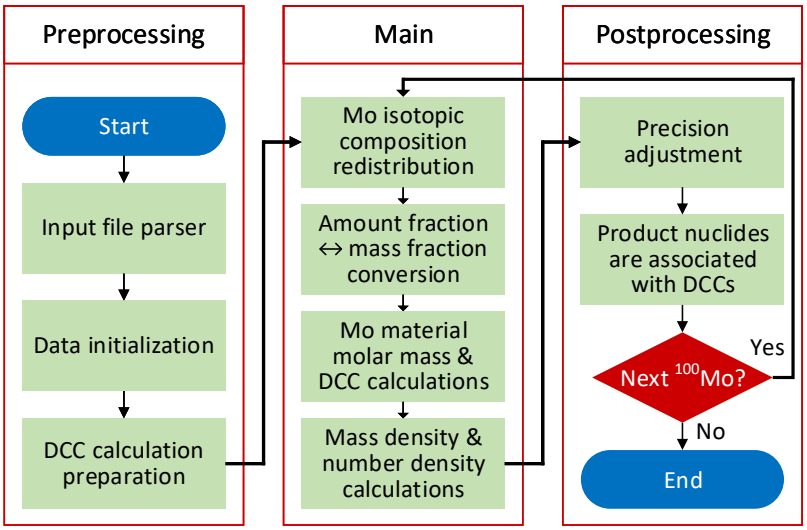

Fig. 2.4. A simplified flowchart of enrimo. Figure reproduced from our publication [15] which is licensed under CC BY 3.0.

2.3.2 DCC calculation algorithm

In order to automate the DCC calculation and facilitate data exchange, we developed a PERL program called enrimo. Because of the interdependence between DCC variables shown in Eqs. (2.4) and (2.10), emphasis was put on improving the program modularity and structuring the routine calls. The algorithm of enrimo is schematically described in Fig. 2.4.

The key tasks of enrimo are to redistribute the fraction quantities of $^{92,94–98}$Mo according to the ^{100}Mo enrichment level under consideration, and to calculate Eq. (2.10) and subsequently Eq. (2.3). The lines of code that execute some core routines of enrimo are shown in Listing 2.2. The presented code snippet is in the third layer down from the outermost one, and the invoked functions enri and enri_postproc are subdivided into multiple routine calls. In effect, the DCC calculation is performed by the sequential calls of the routines placed inside enri.

Besides, enrimo is not confined to ^{100}Mo; all of the naturally occurring Mo isotopes can be examined in place of ^{100}Mo. For example, the influence of ^{98}Mo enrichment level on Mo reaction yields can be investigated, which can then be used for studies of the ^{98}Mo(n,γ)^{99}Mo reaction (see Sec. 1.2). The source code of enrimo is available in an online repository[57], and the usage instructions are given in Appendix A.2.

```
1    # (1)--(5)
```

```
    # Redistribute the fraction quantities of Mo isotopes and
    # calculate DCCs.
    my $is_exit = enri(      # e.g.
        $chem_hrefs,         # {o => %o, mo => \%mo, momet => \%momet,
    ...}
        $mat,                # momet, moo2, moo3, ...
        $enri_nucl_elem,     # mo
        $enri_nucl_mass_num, # '100', '98', ...
        $enri_lev,           # 0.9739, 0.9954, ...
        $enri_lev_type,      # 'amt_frac'
        $depl_order,         # 'ascend'
        $is_verbose,
    );
    return if $is_exit;

    # (6)--(7)
    # Adjust the numbers of decimal places and associate
    # product nuclides with nuclear reactions and DCCs.
    enri_postproc(
        $chem_hrefs,
        $mat,
        $enri_nucl,
        $enri_lev,
        $enri_lev_range_first,
        $enri_lev_range_last,
        $enri_lev_type,
        $depl_order,
        $out_path,
        $projs,
        $precision_href,
        $is_verbose,
    );
```

Listing 2.2: Part of the inner layer of `enrimo`.

2.4 `actdyn`: A ^{99}Mo/^{99m}Tc activity model simulator

Understanding the activities of ^{99}Mo/^{99m}Tc is crucial in assessing the feasibility of electron linac production of ^{99}Mo. However, because the activities of linac-produced ^{99}Mo/^{99m}Tc depend on multiple parameters and vary with multiple time regimes, the activity calculation can be error-prone and time-consuming. For instance, the activity of a ^{99m}Tc eluate depends on the (i) decay time, (ii) ^{99}Mo activity present, (iii) elution

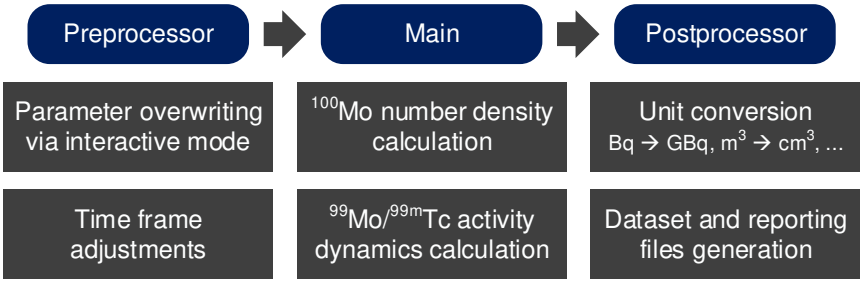

Fig. 2.5. A diagram of actdyn describing its ^{99}Mo/^{99m}Tc activity calculation.

efficiency, (iv) number of elution runs, and (v) elution intervals[50]. The detailed equations will be addressed in Sec. 3.4.

The program actdyn was developed for simulating the activities of linac-produced ^{99}Mo/^{99m}Tc we modeled[50,60]. By calculating the equations of peri-irradiation and postirradiation activities, actdyn generates ^{99}Mo/^{99m}Tc activity data. actdyn is an object-oriented program written using the Class::Struct module of PERL, which emulates the struct data type of the C language. Interactive mode is the basic run mode, via which simulation parameters can be specified (Fig. 2.5).

One of the characteristic features of actdyn is its coherent handling of time frames. Part of the commands calculating the postirradiation ^{99m}Tc activity is presented in Listing 2.3. The time frame objects such as $t_del and $t_elu are all bound to the object of total time frame $t_tot and, therefore, time frames such as times of irradiation, postirradiation processing, and delivery can be adjusted interactively. In addition, because each of these time frames can be customized via the interactive mode, simulations can be performed for various time scenarios.

```
                #   (1 - $tc99m_gen->elu_eff)
                if ($t == $t_del->to) { # e.g. $t == 96
                    # Tc-99m elute
                    $tc99m->act->elu($tc99m->act->dec * $tc99m_gen->
    elu_eff);

                    # Remnant Tc-99m activity that boosts
                    # its growth toward the Mo-99 activity
                    # > Later stored into
                    #   $tc99m->act->dec_arr->[$_nrg][$t_del->to]
                    $tc99m->act->dec(
                        $tc99m->act->dec - $tc99m->act->elu
                    );
```

[60] J. Jang. *Study on decentralized production of medical radionuclides by compact X-band electron linear accelerators*. Master's thesis. University of Tokyo, Tokyo, Japan (2017).

Table 2.2. Summary of the developed programs.

Program	Purpose	Use in the dissertation
`phitar`	Targetry design	Chaps. 3, 4, and 5
`enrimo`	Analysis of enriched ^{100}Mo	Chap. 6
`actdyn`	^{99}Mo/^{99m}Tc activity simulation	Chap. 3

```
13
14                  # Increment the elution ordinal count from 1 to 2.
15                  $tc99m_gen->elu_ord_count($tc99m_gen->elu_ord_count +
    1);
16              }
17
18              # After the EOD
19              if ($t > $t_del->to) { # e.g. $t > 96
20                  $tc99m->act->dec(
21                      # Terms signifying the decay of Tc-99m
22                      $tc99m->act->dec_arr->[$_nrg][
23                          # 96
24                          $t_del->to + (
25                              # 0, 1, 2, ...
26                              ($tc99m_gen->elu_ord_count - 2)
27                              # 0*24, 1*24, 2*24, ...
28                              * $tc99m_gen->elu_itv
29                          )
30                      ] # 96, 120, 144, ...
31                      * exp(-$tc99m->dec_const * $t_elu->from)
32
33                      # Terms signifying the production of
34                      # Tc-99m by the negatron decay of Mo-99
35                      + $mo99->negatron_dec_2->branching_fraction * (
```

Listing 2.3: Part of the activity calculation subroutine of `actdyn`.

The source code of `actdyn` can be found in an online repository[58], and the usage instructions are provided in Appendix A.3.

2.5 Summary

We developed three PERL programs dedicated to research tasks involved in the electron linac production of ^{100}Mo(γ,n)^{99}Mo. In order to facilitate data exchange and to improve the data transparency, the programs have been made available in open-source

repositories[56–58]. A summary of the programs is presented in Table 2.2. All these programs were used throughout this dissertation work, and will be mentioned where appropriate.

Chapter
3

Parametric analysis of a ^{99}Mo production electron linac

Abstract

The parametric requirements of a ^{99}Mo production electron linac differ greatly from those of other types of linacs such as radiation therapy and pulse radiolysis linacs. In this chapter, we explore linac parameters preferable for ^{99}Mo production, and present a radioactivity model that can be used to assess the ^{99}Mo/^{99m}Tc production capacity of an electron linac. The design concerns of a linac facility are also discussed.

3.1 Declaration

3.2 Overview

The kinetic energy of a charged particle gained through an electric potential difference ΔV_{stat} is given by[62]

$$E_{\text{gain}} = |q_{\text{e}}|\Delta V_{\text{stat}}, \tag{3.1}$$

where q_{e} is the elementary charge of the particle. Eq. (3.1) determines the accelerating voltages of electrostatic accelerators such as the Cockcroft-Walton generators, Van de

[50] J. Jang *et al. Phys. Rev. Accel. Beams* **20**, 104701 (2017).
[61] Creative Commons. Attribution 4.0 International (CC BY 4.0).
[62] T. P. Wangler. *RF Linear Accelerators*. 2nd ed. (2008).

Graaff generators, and tandem accelerators. Because ΔV_{stat} is typically a few MV at most, the accelerating voltages of electrostatic accelerators are limited to a few MV[62]. This limitation prompted the development of RF linacs.

Coupled-cavity linacs are a type of RF linacs, and can be classified into standing-wave (SW) and traveling-wave (TW) types[62]. For an SW linac, the energy gain can be expressed as

$$E_{\text{gain,SW}} = |q_{\text{e}}| \sum_i V_{\text{SW},i},$$

where $V_{\text{SW},i}$ is the accelerating voltage of an ith SW structure. For an SW structure, the steady-state and beam-loaded V_{SW} is given by[50,62,63]

$$V_{\text{SW}} = \sqrt{P_{\otimes} r_{\text{s}} L} \frac{2\sqrt{\beta_{\text{wc}}}}{1+\beta_{\text{wc}}} - \frac{I_b r_{\text{s}} L}{1+\beta_{\text{wc}}}, \tag{3.2}$$

The coupling coefficient β_{wc} should not be confused with the normalized beam velocity β.

where $P_{\otimes}$ is the peak RF power fed into the SW structure, r_{s} the effective shunt impedance per unit length, L the structure length, β_{wc} the waveguide-to-cavity coupling coefficient, and I_b the beam current. The first term of the right-hand side, which increases the accelerating voltage, denotes the voltage generated by the RF source. The second term, which decreases the accelerating voltage, is a representation of the voltage induced by the moving electron bunches, an effect known as the beam loading[62].

Similarly, the energy gain of charged particles in a TW linac can be expressed as

$$E_{\text{gain,TW}} = |q_{\text{e}}| \sum_i V_{\text{TW},i},$$

where the steady-state and beam-loaded V_{TW} is given by[64,65]

$$V_{\text{TW}} = \sqrt{P_{\otimes} r_{\text{s}} L \left[1 - \exp(-2\alpha_{\text{att}} L)\right]} - \frac{I_b r_{\text{s}} L}{2} \left[1 - \frac{2\alpha_{\text{att}} L \exp(-2\alpha_{\text{att}} L)}{1 - \exp(-2\alpha_{\text{att}} L)}\right], \tag{3.3}$$

with the symbol α_{att} denoting the attenuation constant per unit length.

In the field of electron linac production of ^{99}Mo, designing an electron linac involves a series of processes to increase the accelerating voltage and beam current to the greatest extent possible for a given RF power, in which Eqs. (3.2) and (3.3) play important roles. In addition, the two equations provide conceptual understanding of

[63] D. H. Whittum. In *Reviews of Accelerator Science and Technology* vol. 2, 63–92 (2009).
[64] S. Takeda. Fundamentals of linear accelerators (in Japanese) (1991).
[65] M. Yamamoto. Examination of a high-power X-band accelerator system for nuclear medicine RI production (in Japanese). Report No. EM-15013B (2015).

the beam energies and currents of the respective accelerating structures.

Recently, we have designed an X-band electron linac for production of medical radionuclides[50,60,66,67] (Fig. 3.1). The design study consisted of RF analysis based on POISSON SUPERFISH[68], and beam dynamics analysis based on GPT[69]. In our previous thesis[60], we addressed the (i) RF analysis, (ii) accelerating structure design, (iii) calculation of the beam energy and current, and (iv) beam dynamics analysis. The focus was on the electron linac itself and on maximizing its average beam current for the given X-band RF power. This chapter expands on the study of the X-band linac, with emphasis on the accelerator and beam parameters. The overall process of the design study and parametric analysis are schematically shown in Fig. 3.2.

3.3 Parametric analysis

3.3.1 Operating frequency

The effective shunt impedance per unit length r_s greatly affects the accelerating voltage and beam current (see Eqs. (3.2) and (3.3)). On top of that, r_s is proportional to the square root of the operating frequency of an electron linac f_{op}[50,70]; that is,

$$r_s \propto \sqrt{f_{op}}. \tag{3.4}$$

Therefore, f_{op} must be selected prior to designing or purchasing an electron linac. Options for f_{op} include L-, S-, C-, and X-band RFs (Table 3.1) which, in fact, represent *radar* bands[71]. The S-band RF is the most commonly used operating frequencies of industrial, medical, and research electron linacs[70,72–74].

[60] J. Jang. *Study on decentralized production of medical radionuclides by compact X-band electron linear accelerators*. Master's thesis. University of Tokyo, Tokyo, Japan (2017).
[66] J. Jang *et al.* In *Proceedings of the 7th International Particle Accelerator Conference, IPAC 2016*, 1917–1920 (2016).
[67] J. Jang *et al.* In *Proceedings of the 14th Annual Meeting of Particle Accelerator Society of Japan, PASJ 2017*, 740–742 (2017).
[68] J. H. Billen *et al.* In *Proceedings of the 1993 Particle Accelerator Conference, PAC 1993*, 790–792 (1993).
[69] S. B. van der Geer *et al.* In *Proceedings of the 5th European Particle Accelerator Conference, EPAC 1996*, 1245–1247 (1996).
[70] S. M. Hanna. In *Proceedings of the 1999 Particle Accelerator Conference, PAC 1999*, 2516–2518 (1999).
[71] M. I. Skolnik. In *Radar Handbook* (1990).
[72] M. Uesaka *et al. Nucl. Instrum. Methods Phys. Res. A* **657**, 82–87 (2011).
[73] S. Hanna. *RF Linear Accelerators for Medical and Industrial Applications* (2012).
[74] J. Shao *et al. Phys. Rev. ST Accel. Beams* **16**, 090102 (2013).

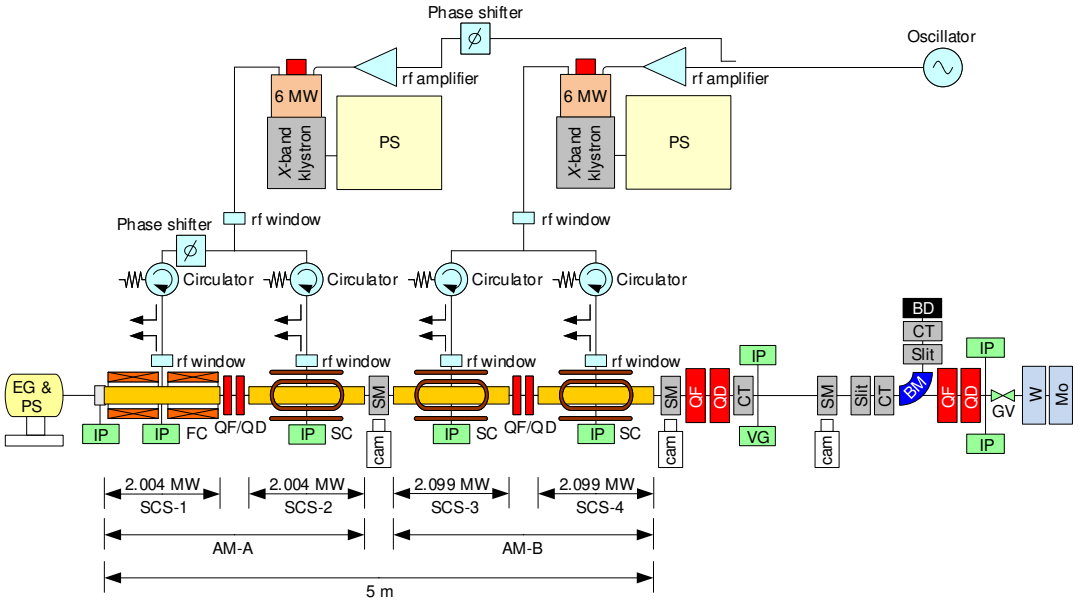

Fig. 3.1. The X-band electron linac we have previously designed. AM: accelerating module, BD: beam dump, BM: bending magnet, cam: camera, CT: current transformer, EG: electron gun, FC: focusing coil, GV: gate valve, IP: ion pump, PS: power supply, QF: focusing Q-magnet, QD: defocusing Q-magnet, SC: steering coil, SCS: side-coupled structure, SM: screen monitor, VG: vacuum gauge, W: tungsten converter, and Mo: molybdenum target. Figure reproduced from our publication [50] and previous thesis [60], the former of which is licensed under CC BY 4.0.

As can be seen from Eq. (3.4), utilizing a high RF band such as C- and X-band RFs can provide a higher accelerating gradient than their subharmonic RF bands. A higher accelerating gradient can provide the C- or X-band electron linacs with structural compactness, and such downsizing is suitable for the concept of decentralized production of ^{99}Mo (see Fig. 1.5). For this reason, we decided to design an X-band electron linac for ^{99}Mo production. The linac was designed based on two 6-MW klystrons operating at 11.9942 GHz (X-band)[75], the operating frequency of the Compact Linear Collider (CLIC)[76,77]. The maximum beam energy and average current of were calculated to be 35 MeV and 260 μA, respectively[50,60,66].

Another option is to use an S-band RF, for which various types of high-power RF sources are commercially available[73]. Because high-power RF sources can lead to

[75] T. Anno *et al.* In *Proceedings of the 12th Annual Meeting of Particle Accelerator Society of Japan, PASJ 2015*, 1129–1132 (2015).
[76] R. Tomás. *Phys. Rev. ST Accel. Beams* **13**, 014801 (2010).
[77] H. Braun *et al.* CLIC 2008 parameters. Report No. CLIC-Note-764 (2008).

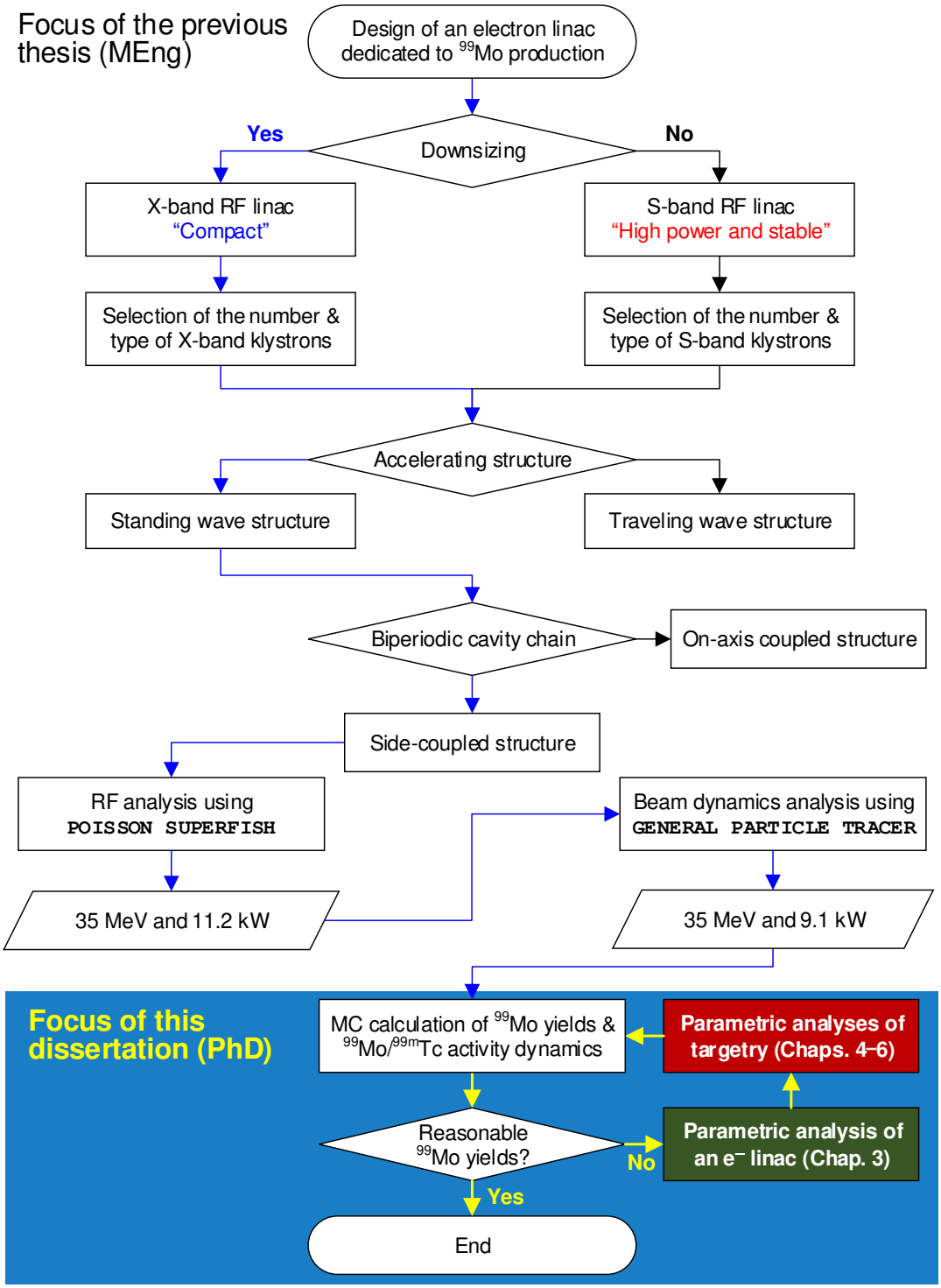

Fig. 3.2. A flowchart for the design of ^{99}Mo production electron linacs. Emphasis is put on the X-band electron linac. Figure adapted from our previous thesis [60].

Table 3.1. Examples of RF bands[1] which can be use for electron linacs. Table adapted from our previous thesis [60].

Band	Frequency (GHz)	Wavelength (mm)	Common applications[2]
L	1–2	150–300	• Long-range air surveillance radar • Global positioning system • Airport surveillance radar
S	2–4	75–150	• Wi-Fi • Microwave oven
C	4–8	37.5–75	• Wi-Fi
X	8–12	25–37.5	• Military weapon tracking radar

[1] To be more precise, the radio bands shown here are the *radar* bands designated by the Institute of Electrical and Electronics Engineers (IEEE). Different radio band designations also exist such as the International Telecommunication Union (ITU) radio bands.
[2] See [71] for more details.

high ^{99}Mo yields, our group has recently designed another electron linac that operates at 2.856 GHz (S-band RF)[78,79].

3.3.2 Accelerating structure

Although the relative advantages of SW and TW structures can be interpreted in different ways[80], here we try to compare the two structures from the standpoint of ^{99}Mo production.

An SCS shown in Fig. 3.3 is a common type of SW structure. An SCS operates at the $\pi/2$ mode, which provides field stability, and exhibits a high shunt impedance, which is characteristic of the π mode[62,63,81]. As explained in Sec. 3.3.1, we designed an X-band electron linac in the interest of downsizing ^{99}Mo production linacs. Because an SCS can also provide structural compactness via its high shunt impedance, the X-band electron linac was designed as an SCS linac. This shows that an SW structure, an SCS in particular, can be preferable if the emphasis is put on the accelerator compactness.

In general, a TW structure is less expensive than an SW structure, partly because circulators (see Fig. 3.1) are not used. If, therefore, the overall system cost is prioritized and a sufficient space is available for the linac, a TW structure can be a reasonable

[78] Y. Inoue. *Study on basic design of S-band electron linear accelerator system for ^{99}Mo/^{99m}Tc production (in Japanese)*. Master's thesis. University of Tokyo, Tokyo, Japan (2019).
[79] M. Yamamoto. Electron beam acceleration characteristics of AIST accelerating structures and examination of an accelerator system (in Japanese). Report No. EM-18034A (2018).
[80] R. H. Miller. In *Proceedings of the 1986 International Linac Conference*, 200–205 (1986).
[81] E. A. Knapp *et al. Rev. Sci. Instrum.* **39**, 979–991 (1968).

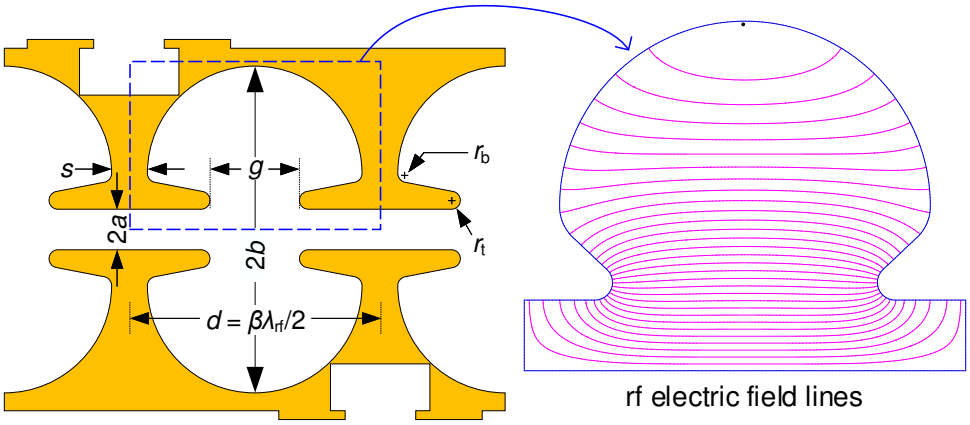

Fig. 3.3. An accelerating cavity of SCS and its time-varying electric fields calculated for 11.99-GHz X-band RF using SUPERFISH (magnetic fields are not shown). $2a$: beam aperture diameter, $2b$: cavity diameter, d: cavity length, g: gap length, r_t: nose cone tip radius, r_b: nose cone base radius, s: disk thickness, β: normalized beam velocity, and λ_{rf}: RF wavelength. Figures adapted from our publication [50] and previous thesis [60], the former of which is licensed under CC BY 4.0.

choice.

3.3.3 Beam energy

Electron beam energies determine the photon energies and thereby greatly affect the yields of Mo photonuclear reactions, including the ^{100}Mo(γ,n)^{99}Mo reaction. To investigate the dependence of ^{99}Mo yields on electron beam energies, we rewrite Eq. (2.1) as

$$Y_{\text{Mo-99}}(t_{\text{irr}}, E_{e-}) = [1 - \exp(-\lambda_{\text{Mo-99}} t_{\text{irr}})]\, \mathcal{V}_{\text{Mo-tar}} I_{e-} \times \int_{E_{\gamma,\text{th}}}^{\infty} \Phi_{\text{Mo-tar}}(E_\gamma)\, \Sigma(E_\gamma)\, \mathrm{d}E_\gamma, \tag{3.5}$$

where the macroscopic cross section is related to the microscopic one by (see Eq. (2.3))

$$\Sigma(E_\gamma) \equiv \mathcal{N}_{\text{Mo-100}} \sigma(E_\gamma) = \left[\frac{w_{\text{Mo-100}} w_{\text{Mo}}(w_{\text{Mo-100}})\, \rho_{\text{Mo-tar}}}{M_{\text{Mo-100}}} N_A\right] \sigma(E_\gamma).$$

To calculate ^{99}Mo yields using Eq. (3.5), we obtained $\Phi_{\text{Mo-tar}}(E_\gamma)$ for various electron beam energies using PHITS v2.88[59] and EGS5[82] MC simulation programs, with

[59] T. Sato *et al. J. Nucl. Sci. Technol.* **55**, 684–690 (2018).
[82] H. Hirayama *et al. The* EGS5 *code system* (2005).

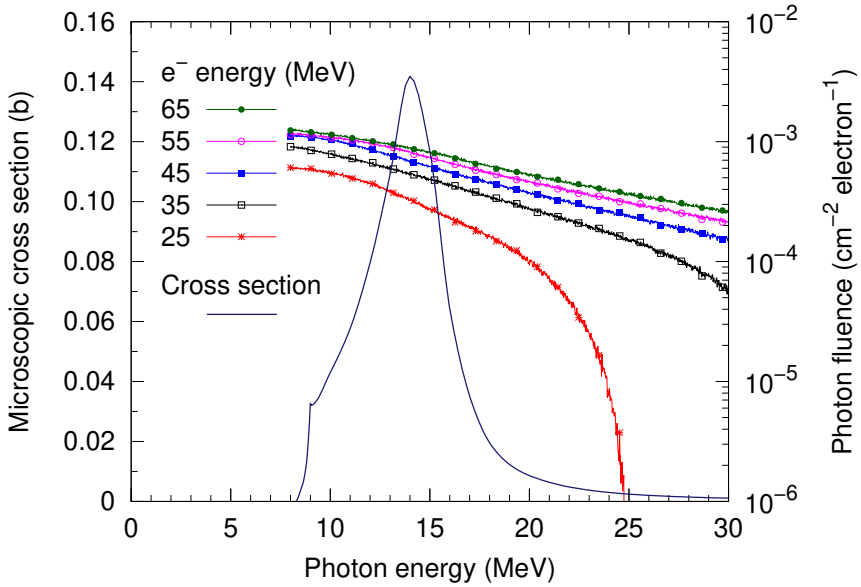

Fig. 3.4. The excitation function for ^{100}Mo(γ,n)^{99}Mo contained in TENDL-2009 [24] (solid line, associated with the left-hand side y-axis) and photon fluences calculated for various electron beam energies (lines with points, associated with the right-hand side y-axis). The W converter thickness was 1 mm, and the Mo target volume was 0.495 cm^3. Figure adapted from our publication [50] which is licensed under CC BY 4.0.

`actdyn` (Sec. 2.4) used as the frontend program. The obtained fluences are plotted in Fig. 3.4, and the calculated ^{99}Mo yields in Figs. 3.5 and 3.6.

In Fig. 3.5, the ^{99}Mo yields are plotted as groups of different irradiation times. The slopes of the ^{99}Mo yield groups show that as the electron beam energy increases, the dependence of the ^{99}Mo yield on the irradiation time also increases; in other words, increasing the irradiation time will increase the ^{99}Mo yield more effectively at higher beam energies.

The relations between ^{99}Mo yields, irradiation times, and beam energies are further explained in Fig. 3.6. The bottommost contour represents ^{99}Mo yield of 0.25 GBq μA^{-1}, and the contours are spaced by 0.25 GBq μA^{-1}. The curvature of each contour signifies how much irradiation time can be reduced by increasing electron beam energies in obtaining the same ^{99}Mo yields. For instance, to obtain the ^{99}Mo yield of 1.25 GBq μA^{-1}, which corresponds to the fifth contour from the bottom, $E_{e^-} = 20$ MeV requires $t_{irr} = 273$ h, whereas $E_{e^-} = 35$ MeV requires $t_{irr} = 39$ h. In other words, increasing the electron beam energy from 20 MeV to 35 MeV can reduce the irradiation time by a factor of 273 h/39 h = 7. On the other hand, the decrease

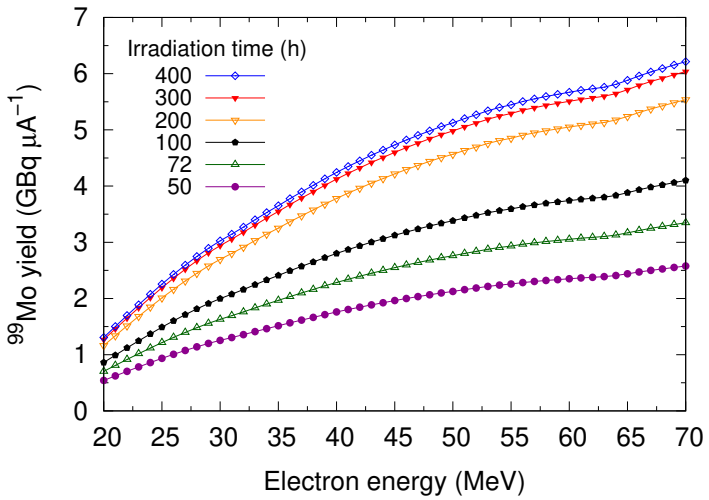

Fig. 3.5. ^{99}Mo yields calculated as functions of beam energy for various irradiation times. Figure adapted from our publication [50] which is licensed under CC BY 4.0.

in irradiation time was not significant between $E_{e^-} = 35$ MeV and $E_{e^-} = 50$ MeV. Namely, the irradiation time for $Y_{\text{Mo-99}}(E_{e^-} = 50\,\text{MeV}) = 1.25\,\text{GBq}\,\mu\text{A}^{-1}$ was 26 h, meaning that increasing the electron beam energy from 35 MeV to 50 MeV can reduce the irradiation time by a factor of only 39 h/26 h = 1.5.

Increasing an electron beam energy can lead to opening of Mo reaction channels other than ^{100}Mo(γ,n)^{99}Mo and thereby increased amounts of impurity radionuclides. More importantly, an increased electron beam energy is accompanied by a decreased electron beam current for a fixed input RF power, as can be seen from Eqs. (3.2) and (3.3). Accordingly, the beam energy of a ^{99}Mo production electron linac should be determined such that (i) the ^{99}Mo production efficiency can be improved while (ii) a sufficient electron beam current is secured. Considering the two aspects, we concluded that a beam energy of 35 MeV could be an appropriate choice[50].

To help understanding the dependence of electron and photon fluences and thereby ^{99}Mo yields on the electron beam energy, we present electron tracks calculated for different beam energies in Fig. 3.7, and photon tracks in Fig. 3.8. The calculations were performed using PHITS v3.02, EGS5, and `phitar` (Sec. 2.2).

3.3.4 Beam current

Because the ^{99}Mo yield is directly proportional to the beam current (see Eq. (3.5)), a large *average* beam current is required for the mass production of ^{99}Mo. For pulsed

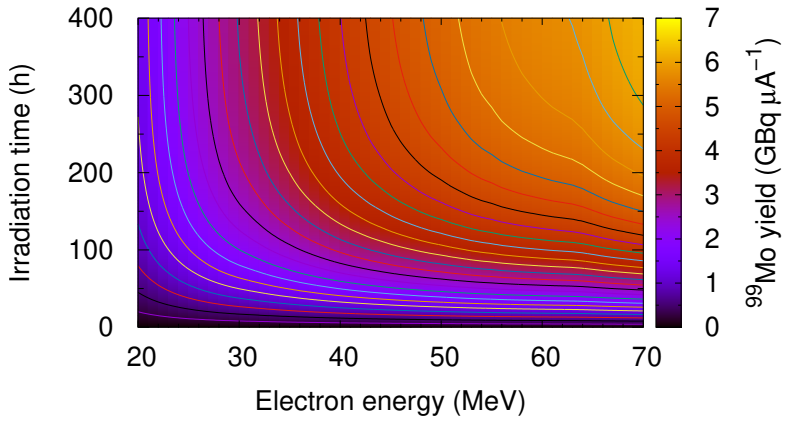

Fig. 3.6. ^{99}Mo yields calculated as functions of beam energy and irradiation time. Figure adapted from our publication [50] which is licensed under CC BY 4.0.

linacs, the average beam current is given by the product of the macropulse duty cycle δ and the peak beam current $I_{b,\mathrm{peak}}$:

$$I_b = \delta I_{b,\mathrm{peak}},$$

where the duty cycle is given by

$$\delta = \text{macropulse length} \times \text{macropulse repetition}.$$

For instance, the peak beam current of the designed X-band electron linac was calculated to be $I_{\mathrm{e}^-,\mathrm{peak}} = 130\,\mathrm{mA}$, and the duty cycle was $\delta = 5\,\mu\mathrm{s} \times 400\,\mathrm{pps} = 0.002$ determined by the klystrons used; the corresponding average beam current was thus $I_{\mathrm{e}^-} = 0.002 \times 130\,\mathrm{mA} = 260\,\mu\mathrm{A}$[50]. Unless otherwise stated, the beam current in this dissertation refers to an average beam current.

An average beam current is greatly affected by two factors: (i) beam loading and (ii) the availability of RF source. As explained in Eq. (3.2), increasing a beam current is accompanied by a decrease in the accelerating voltage, and vice versa (Fig. 3.9), attributed to the beam loading. Consequently, the extent to which an average beam current can be increased at a fixed beam energy is dictated by the available RF power. Because accelerator RF sources are expensive, the type and number of RF source machines should be chosen considering the overall system cost. For this reason, we set two 6 MW X-band klystrons as the RF source of the X-band electron linac[50], and set two 7.5 MW S-band klystrons as the RF source of the S-band electron linac[78,79].

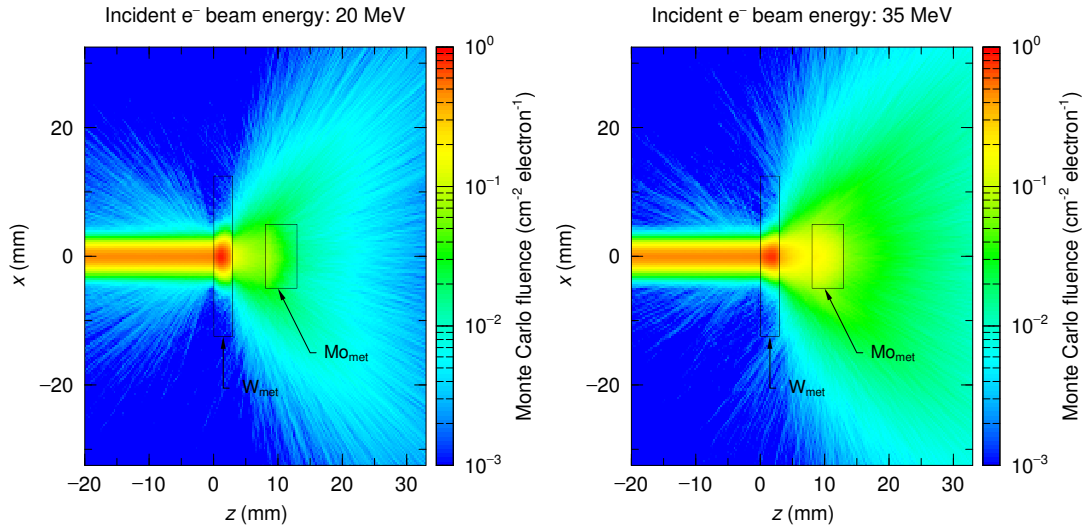

Fig. 3.7. Electron tracks calculated for (a) 20-MeV and (b) 35-MeV electron beams. The transverse electron beam size was 3 mm in FWHM.

3.3.5 Beam size

Unless otherwise specified, the beam size in this dissertation refers to an *electron* beam size in the *transverse* plane. A small beam size is required in some fields of linac applications such as pulse radiolysis[83]. By contrast, the beam size of a ^{99}Mo production electron linac should not be too small, because a highly focused beam can result in focused heat accumulation in a bremsstrahlung converter. If the cooling rate is insufficient, the focused thermal energy can lead to melting or evaporation of the converter.

The beam size of the designed X-band electron linac was about 1.5 mm in FWHM at the beam exit (Fig. 3.10), which is considered to be too small from the viewpoint of focused heat load. Beam sizes greater than 2 mm in FWHM, for instance 4.5-mm FWHM, are preferable. The dependence of thermal energy concentration on the beam size can be seen in Figs. 3.11 and 3.12.

3.3.6 Beam emittance

When accelerated, charged particle bunches unavoidably gain different momenta and are dispersed over phase space, the extent of which depends on various accelerator components. Beam emittance is a measure of the particle coordinate spread and is

[83] J. Yang *et al. Nucl. Instrum. Methods Phys. Res. A* **629**, 6–10 (2011).

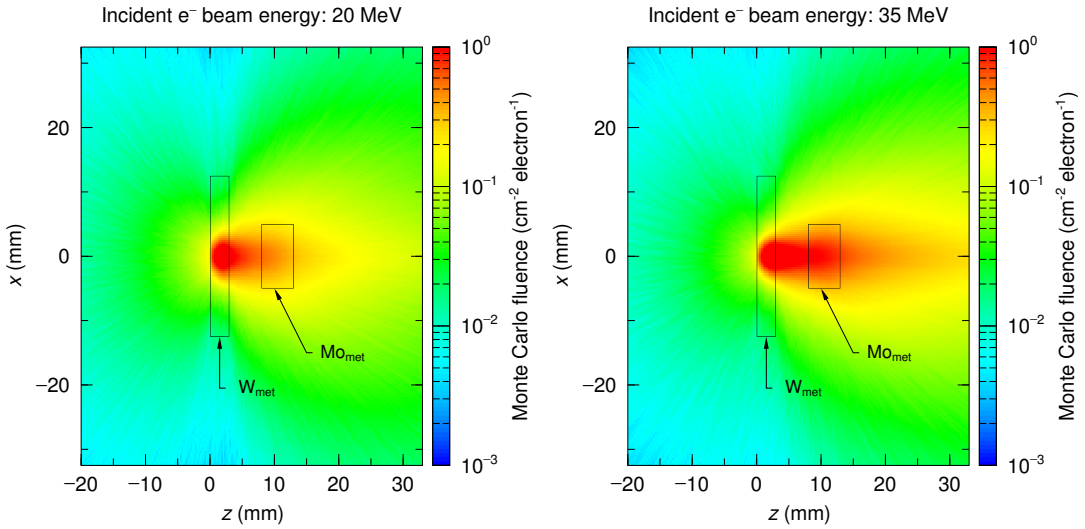

Fig. 3.8. Photon tracks calculated for (a) 20-MeV and (b) 35-MeV electron beams. The transverse electron beam size was 3 mm in FWHM.

expressed in position-momentum phase space[62]. In many fields of linac applications, beam emittance is one of the most important design parameters; examples include the e^+e^- collider experiments[76] and pulse radiolysis[83]. In the former, minimization of wakefields and fine-tuned beam energies are required, and in the latter, the beams should be confined within the intended focal points. All these requirements are characterized by small beam emittance[62].

When the electromagnetic (EM) field of a charged particle bunch is scattered by some subcomponents of an accelerating structure, the scattered field, referred to as a wakefield, can act on the trailing bunches. The wakefields can lead to beam-breakup instabilities (BBU) and thereby the growth of beam emittance[62]. The increased beam emittance can then result in beam loss and radioactivation of the accelerator, affecting its operational stability and availability.

Because ^{99}Mo must be produced and supplied on a regular basis, the operational stability of an electron linac is of paramount importance. Accordingly, although the required emittance reduction is less strict than those in other linac applications such as e^+e^- collider experiments, restricting the beam emittance to a certain extent is still necessary. Fig. 3.13 shows the normalized root mean square (RMS) emittance of the designed X-band electron linac, which is considered acceptably small.

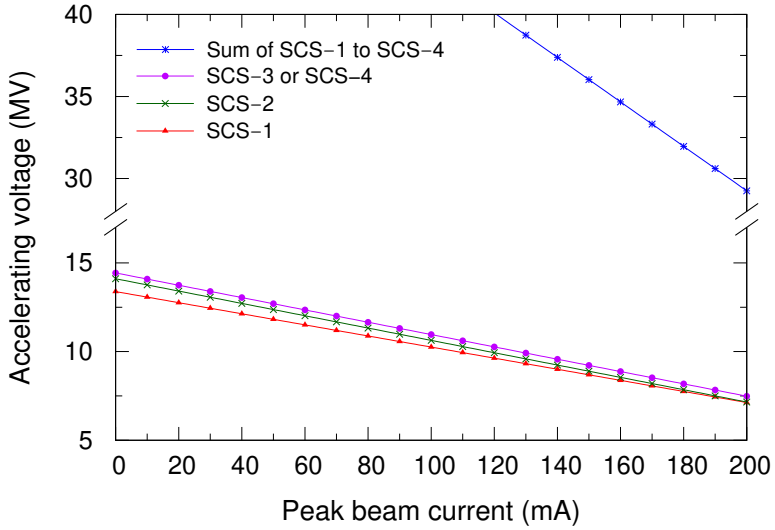

Fig. 3.9. Calculation results of Eq. (3.2). Detailed calculation conditions are given in [50]. Figure adapted from our publication [50] which is licensed under CC BY 4.0.

3.4 ^{99}Mo/^{99m}Tc activity model

To justify the determined linac and beam parameters, we have previously developed a mathematical model that can estimate ^{99}Mo/^{99m}Tc activities *during and after* Mo target irradiation. The model was addressed separately in our previous thesis[60] and publication[50]; in the former, we presented two derivation methods with the detailed processes shown and, in the latter, we presented a refined derivation method but with some processes omitted. To describe the model in a more consistent manner and to help understanding its physical meaning, below we rederive the modeled activities.

For a radionuclide i that is the decay product of another radionuclide $i-1$, the production and decay rates of i can be described by a Bateman equation[84,85]:

The model for this differential equation was formulated by E. Rutherford[84].

$$\frac{\mathrm{d}N_i(t)}{\mathrm{d}t} = \underbrace{-\lambda_i N_i(t)}_{\text{decay of } i} \underbrace{+\lambda_{i-1} N_{i-1}(t)}_{\text{production of } i}, \tag{3.6}$$

where N denotes the number of radionuclides.

Taking into account the branching fraction of $i-1$ to i, or $B_{i-1\to i}$, we rewrite

[84] E. Rutherford. *Radio-activity*. 2nd ed. (1905).
[85] H. Bateman. *Proc. Cambridge Philos. Soc.* **15**, 423–427 (1910).

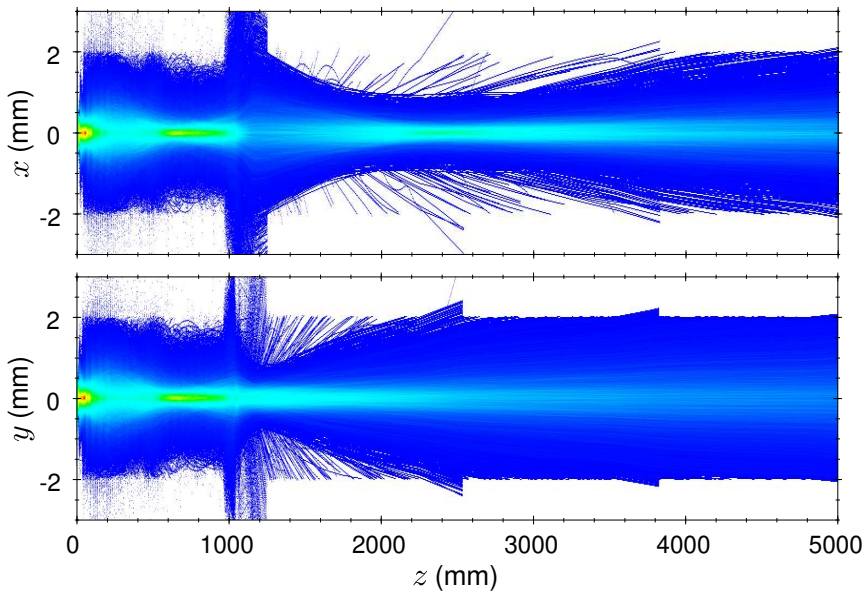

(a)

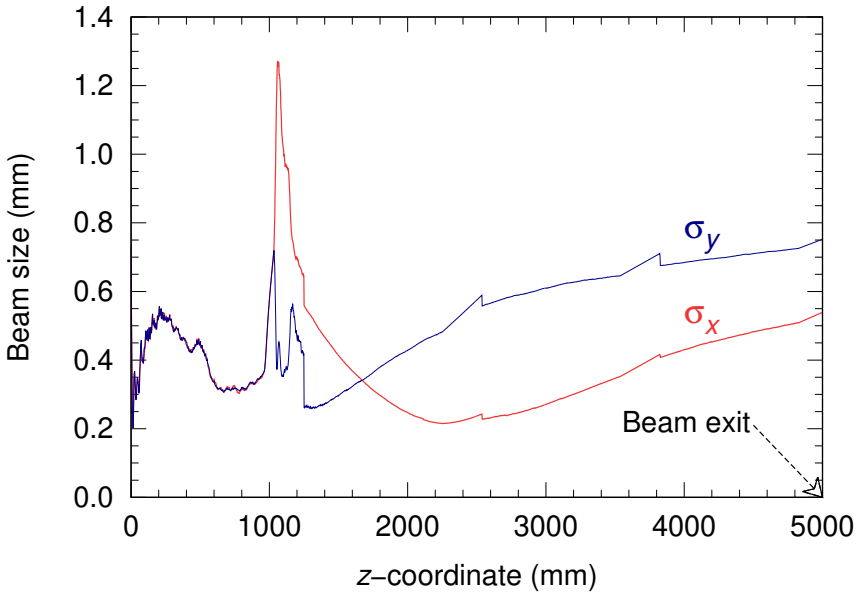

(b)

Fig. 3.10. The transverse beam size of the designed X-band electron linac. (a) Electron tracks in the xz- and yz-planes and (b) their two-dimensional representations. The beam exit is at $z = 5000$ mm. Figures adapted from our publication [50] and previous thesis [60], the former of which is licensed under CC BY 4.0.

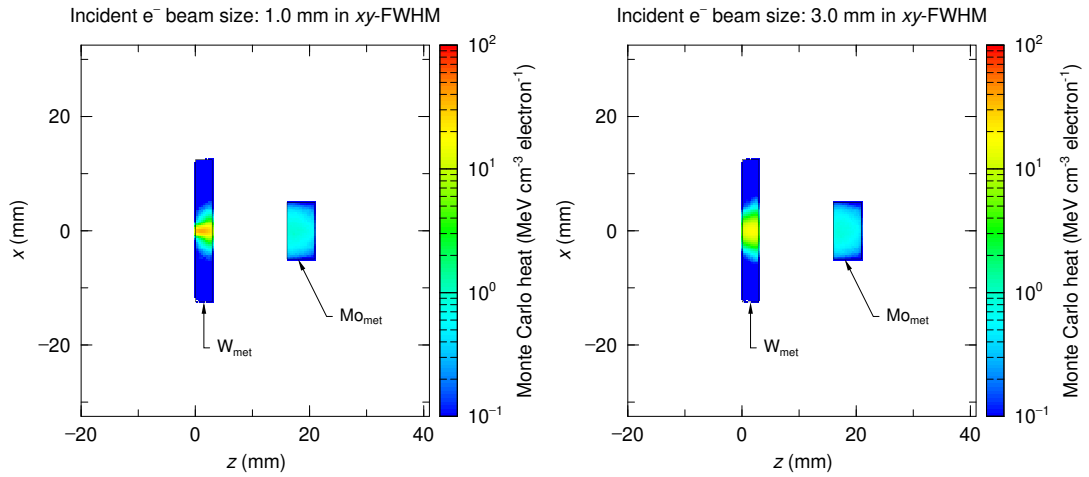

Fig. 3.11. *xz*-plane heat distribution in target materials calculated using PHITS v3.02, EGS5, and `phitar`. The transverse electron beam sizes were (a) 1-mm and (b) 3-mm in FWHM.

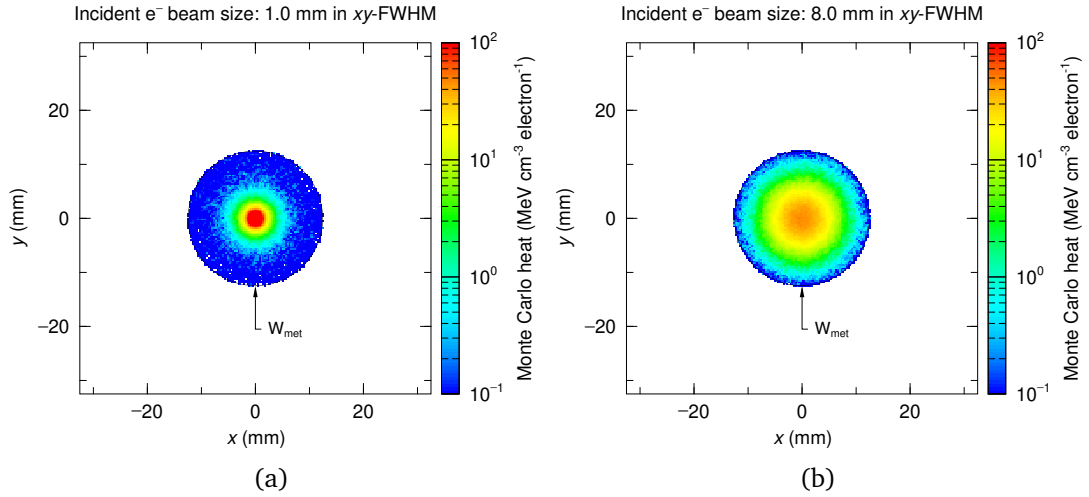

Fig. 3.12. *xy*-plane heat distribution in a W converter calculated using PHITS v3.02, EGS5, and `phitar`. The transverse electron beam sizes were (a) 1-mm and (b) 8-mm in FWHM.

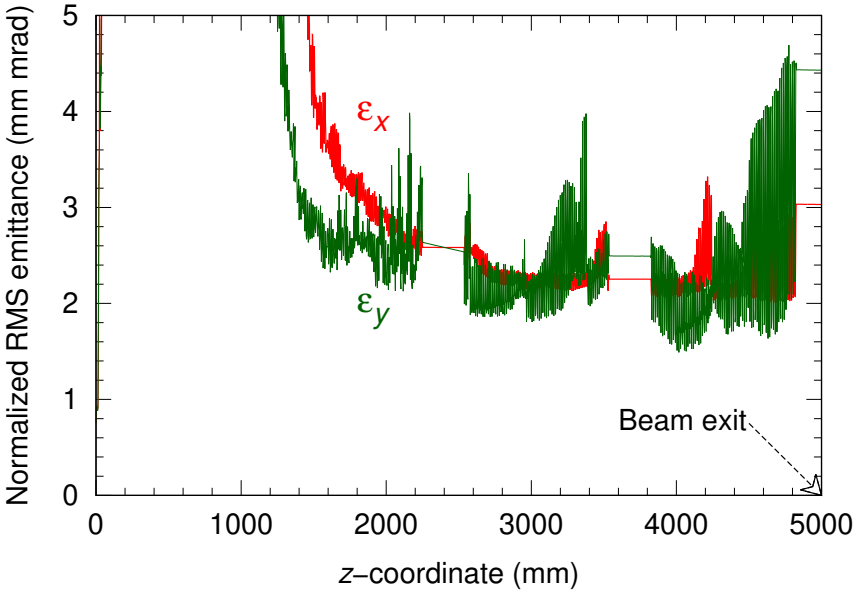

Fig. 3.13. Emittance of the designed X-band electron linac[50]. Figure adapted from our previous thesis [60].

Eq. (3.6) as

$$\frac{\mathrm{d}N_i(t)}{\mathrm{d}t} = -\lambda_i N_i(t) + B_{i-1\to i}\lambda_{i-1}N_{i-1}(t)\,. \tag{3.7}$$

On the other hand, if the radionuclide of interest is produced by a means other than radioactive decay, for instance a particle-induced nuclear reaction, Eq. (3.6) should be modified as

$$\frac{\mathrm{d}N_i(t)}{\mathrm{d}t} = -\lambda_i N_i(t) + \mathcal{R}_i, \tag{3.8}$$

where $\mathcal{R}_i$ denotes the production rate of i. Note that because $\mathcal{R}_i$ is a nonzero constant, the differential equation is no longer homogeneous. We refer to Eq. (3.8) as a *modified* Bateman equation[50].

By solving Eq. (3.7) or Eq. (3.8), or a combination of the two, ^{99}Mo/^{99m}Tc activity equations can be obtained for various scenarios. In setting and solving the equations, two cases must be considered separately: ^{99}Mo/^{99m}Tc activities being produced and lost during irradiation (peri-irradiation), and ^{99}Mo/^{99m}Tc activities being lost after the end of irradiation (postirradiation). The two cases will be addressed in the following subsections.

3.4.1 Peri-irradiation activities

For linac-produced ^{99}Mo, the production rate term in Eq. (3.8) is given by the rate of ^{99}Mo production obtained via the ^{100}Mo(γ,n)^{99}Mo reaction, $\mathcal{R}_{\text{Mo-99}}$ (see Eq. (3.5)):

$$\begin{aligned}\frac{\mathrm{d}N_{\text{Mo-99}}(t)}{\mathrm{d}t} &= \underbrace{-\lambda_{\text{Mo-99}}N_{\text{Mo-99}}(t)}_{\text{decay of Mo-99}} \underbrace{+\mathcal{V}_{\text{Mo-tar}}I_{\text{e}-}\int_{E_{\gamma,\text{th}}}^{\infty}\Phi_{\text{Mo-tar}}(E_\gamma)\,\Sigma(E_\gamma)\,\mathrm{d}E_\gamma}_{\text{production of Mo-99}} \\ &= -\lambda_{\text{Mo-99}}N_{\text{Mo-99}}(t) + \mathcal{R}_{\text{Mo-99}}. \end{aligned} \tag{3.9}$$

For ^{99m}Tc produced as a decay product of ^{99}Mo, on the other hand, Eq. (3.7) is used as

$$\frac{\mathrm{d}N_{\text{Tc-99m}}(t)}{\mathrm{d}t} = \underbrace{-\lambda_{\text{Tc-99m}}N_{\text{Tc-99m}}(t)}_{\text{decay of Tc-99m}} \underbrace{+B_{\text{Mo-99}\to\text{Tc-99m}}\lambda_{\text{Mo-99}}N_{\text{Mo-99}}(t)}_{\text{production of Tc-99m}}. \tag{3.10}$$

Representing ^{99}Mo and ^{99m}Tc as p and d, respectively, the system of Eqs. (3.9) and (3.10) can be expressed as

$$\begin{aligned}\begin{bmatrix}N_p'(t)\\ N_d'(t)\end{bmatrix} &= \begin{bmatrix}-\lambda_p & 0\\ B_{p\to d}\lambda_p & -\lambda_d\end{bmatrix}\begin{bmatrix}N_p(t)\\ N_d(t)\end{bmatrix} + \begin{bmatrix}\mathcal{R}_{\text{Mo-99}}\\ 0\end{bmatrix} \\ \mathbf{N}' &= \mathbf{A}\mathbf{N} + \mathbf{F}, \end{aligned} \tag{3.11}$$

where $\mathbf{N}'$ represents the column vector of derivatives, $\mathbf{A}$ the coefficient matrix, $\mathbf{N}$ the solution vector, and $\mathbf{F}$ the column vector contributing to the nonhomogeneity.

In order to assure a correct set of solutions is obtained, we solved Eq. (3.11) using two different approaches, namely (i) an eigenvalue-eigenvector problem and (ii) Laplace transforms, and verified whether the same set of solutions are obtained.

Solutions by eigenvalues and eigenvectors

By solving the eigenvalue-eigenvector problem of Eq. (3.11), the solutions will be given in the form of

$$\begin{aligned}\mathbf{N} = \begin{bmatrix}N_p(t)\\ N_d(t)\end{bmatrix} &= \mathbf{N}_{\text{general}} + \mathbf{N}_{\text{particular}} \\ &= (C_p\mathbf{N}_p + C_d\mathbf{N}_d) + \mathbf{N}_{\text{particular}} \\ &= [C_p\mathbf{X}_p\exp(g_pt) + C_d\mathbf{X}_d\exp(g_dt)] + \mathbf{N}_{\text{particular}}, \end{aligned} \tag{3.12}$$

where g denotes an eigenvalue of $\mathbf{A}$, and $\mathbf{X}$ the eigenvector corresponding to g.

From the relation

$$\begin{aligned} \mathbf{A}\mathbf{X} &= g\mathbf{X} \\ (\mathbf{A} - g\mathbf{I})\,\mathbf{X} &= \mathbf{O} \end{aligned} \tag{3.13}$$

where $\mathbf{X}$ is a nonzero vector, it follows that

$$|\mathbf{A} - g\mathbf{I}| = \begin{vmatrix} -\lambda_p - g & 0 \\ B_{p\to d}\lambda_p & -\lambda_d - g \end{vmatrix} = 0,$$

where we find the eigenvalues

$$g_p = -\lambda_p, \qquad g_d = -\lambda_d. \tag{3.14}$$

For $g_p = -\lambda_p$, Eq. (3.13) becomes

$$\begin{bmatrix} 0 & 0 \\ B_{p\to d}\lambda_p & \lambda_p - \lambda_d \end{bmatrix} \begin{bmatrix} a \\ b \end{bmatrix} = \begin{bmatrix} 0 \\ 0 \end{bmatrix},$$

where we obtain

$$b = B_{p\to d}\frac{\lambda_p}{\lambda_d - \lambda_p}a,$$

yielding the eigenvector

$$\mathbf{X}_p = \begin{bmatrix} 1 \\ B_{p\to d}\frac{\lambda_p}{\lambda_d - \lambda_p} \end{bmatrix}. \tag{3.15}$$

Subsequently, inserting $g_d = -\lambda_d$ into Eq. (3.13) gives

$$\begin{bmatrix} \lambda_d - \lambda_p & 0 \\ B_{p\to d}\lambda_p & 0 \end{bmatrix} \begin{bmatrix} c \\ d \end{bmatrix} = \begin{bmatrix} 0 \\ 0 \end{bmatrix},$$

where

$$c = 0.$$

Because $\mathbf{X}_d$ is not a null vector, a free variable m can be used as

$$\begin{bmatrix} c \\ d \end{bmatrix} = \begin{bmatrix} 0 \\ m \end{bmatrix} = m \begin{bmatrix} 0 \\ 1 \end{bmatrix},$$

leading to

$$\mathbf{X}_d = \begin{bmatrix} 0 \\ 1 \end{bmatrix}. \tag{3.16}$$

Next, to obtain the particular solution, we put $\mathbf{N}_{\text{particular}} = \begin{bmatrix} e \\ f \end{bmatrix}$ and plug it into Eq. (3.11), obtaining

$$\begin{bmatrix} 0 \\ 0 \end{bmatrix} = \begin{bmatrix} -\lambda_p & 0 \\ B_{p\to d}\lambda_p & -\lambda_d \end{bmatrix} \begin{bmatrix} e \\ f \end{bmatrix} + \begin{bmatrix} \mathcal{R}_{\text{Mo-99}} \\ 0 \end{bmatrix},$$

from which it follows that

$$e = \frac{\mathcal{R}_{\text{Mo-99}}}{\lambda_p}, \qquad f = \frac{B_{p\to d}\mathcal{R}_{\text{Mo-99}}}{\lambda_d},$$

and therefore

$$\mathbf{N}_{\text{particular}} = \begin{bmatrix} \frac{\mathcal{R}_{\text{Mo-99}}}{\lambda_p} \\ \frac{B_{p\to d}\mathcal{R}_{\text{Mo-99}}}{\lambda_d} \end{bmatrix}. \tag{3.17}$$

Finally, we insert Eqs. (3.14), (3.15), (3.16), and (3.17), into Eq. (3.12), and find

$$\begin{bmatrix} N_p(t) \\ N_d(t) \end{bmatrix} = \left\{ C_p \begin{bmatrix} 1 \\ B_{p\to d}\frac{\lambda_p}{\lambda_d-\lambda_p} \end{bmatrix} \exp(-\lambda_p t) + C_d \begin{bmatrix} 0 \\ 1 \end{bmatrix} \exp(-\lambda_d t) \right\} + \begin{bmatrix} \frac{\mathcal{R}_{\text{Mo-99}}}{\lambda_p} \\ \frac{B_{p\to d}\mathcal{R}_{\text{Mo-99}}}{\lambda_d} \end{bmatrix},$$

that is,

$$N_p(t) = C_p \exp(-\lambda_p t) + \frac{\mathcal{R}_{\text{Mo-99}}}{\lambda_p}, \tag{3.18}$$

$$N_d(t) = C_p B_{p\to d}\frac{\lambda_p}{\lambda_d - \lambda_p}\exp(-\lambda_p t) + C_d \exp(-\lambda_d t) + \frac{B_{p\to d}\mathcal{R}_{\text{Mo-99}}}{\lambda_d}. \tag{3.19}$$

Eq. (3.18) represents the number of ^{99}Mo nuclides lost by their radioactive decay and produced by Mo target irradiation. Likewise, Eq. (3.19) represents the number of ^{99m}Tc nuclides lost by their radioactive decay and produced by the decay of ^{99}Mo that is being lost and produced. To make the solution complete, the constants need to be determined. First, we set $t = 0$ in Eq. (3.18), finding

$$C_p = N_p(0) - \frac{\mathcal{R}_{\text{Mo-99}}}{\lambda_p}. \tag{3.20}$$

Plugging Eq. (3.20) into Eq. (3.18) then yields

$$N_p(t) = N_p(0)\exp(-\lambda_p t) + [1-\exp(-\lambda_p t)]\,\frac{\mathcal{R}_{\text{Mo-99}}}{\lambda_p},$$

or, by the relation $A_p = \lambda_p N_p$,

$$A_p(t) = \underbrace{A_p(0)\exp(-\lambda_p t)}_{\text{decay of } p} + \underbrace{[1-\exp(-\lambda_p t)]\,\mathcal{R}_{\text{Mo-99}}}_{\text{production of } p}. \tag{3.21}$$

Eq. (3.21) is the solution of Eq. (3.11) corresponding to the differential equation for $N_p'(t)$.

Next, to determine the constant C_d in Eq. (3.19), we rewrite Eq. (3.18) as

$$C_p\exp(-\lambda_p t) = N_p(t) - \frac{\mathcal{R}_{\text{Mo-99}}}{\lambda_p},$$

and insert it into Eq. (3.19). We then obtain

$$N_d(t) = \left[N_p(t) - \frac{\mathcal{R}_{\text{Mo-99}}}{\lambda_p}\right] B_{p\to d}\frac{\lambda_p}{\lambda_d-\lambda_p} + C_d\exp(-\lambda_d t) + \frac{B_{p\to d}\mathcal{R}_{\text{Mo-99}}}{\lambda_d},$$

which can be rearranged as

$$N_d(t) = \frac{B_{p\to d}N_p(t)\,\lambda_p}{\lambda_d-\lambda_p} + C_d\exp(-\lambda_d t) - \frac{B_{p\to d}\mathcal{R}_{\text{Mo-99}}\lambda_p}{\lambda_d\,(\lambda_d-\lambda_p)}.$$

Setting $t = 0$, the constant becomes

$$C_d = N_d(0) - \frac{B_{p\to d}N_p(0)\,\lambda_p}{\lambda_d-\lambda_p} + \frac{B_{p\to d}\mathcal{R}_{\text{Mo-99}}\lambda_p}{\lambda_d\,(\lambda_d-\lambda_p)}. \tag{3.22}$$

We now plug Eqs. (3.20) and (3.22) into Eq. (3.19), and find

$$\begin{aligned} N_d(t) = {} & \left[\frac{\lambda_p N_p(0) - \mathcal{R}_{\text{Mo-99}}}{\lambda_d-\lambda_p}\right] B_{p\to d}\exp(-\lambda_p t) \\ & + \left[N_d(0) + \frac{B_{p\to d}\mathcal{R}_{\text{Mo-99}}\lambda_p - B_{p\to d}\lambda_p\lambda_d N_p(0)}{\lambda_d\,(\lambda_d-\lambda_p)}\right]\exp(-\lambda_d t) \\ & + \frac{B_{p\to d}\mathcal{R}_{\text{Mo-99}}}{\lambda_d}. \end{aligned}$$

Multiplying both sides by λ_d, we obtain

$$\begin{aligned} A_d(t) = &\left[\frac{A_p(0) - \mathcal{R}_{\text{Mo-99}}}{\lambda_d - \lambda_p}\right] B_{p\to d}\lambda_d \exp(-\lambda_p t) \\ &+ \left[A_d(0) + \frac{B_{p\to d}\mathcal{R}_{\text{Mo-99}}\lambda_p - B_{p\to d}\lambda_d A_p(0)}{\lambda_d - \lambda_p}\right] \exp(-\lambda_d t) \\ &+ B_{p\to d}\mathcal{R}_{\text{Mo-99}}. \end{aligned}$$

Factoring out $B_{p\to d}\mathcal{R}_{\text{Mo-99}}$ gives

$$\begin{aligned} A_d(t) = &\frac{B_{p\to d}\lambda_d A_p(0)\exp(-\lambda_p t)}{\lambda_d - \lambda_p} \\ &+ A_d(0)\exp(-\lambda_d t) - \frac{B_{p\to d}\lambda_d A_p(0)\exp(-\lambda_d t)}{\lambda_d - \lambda_p} \\ &+ B_{p\to d}\mathcal{R}_{\text{Mo-99}}\left[1 + \frac{\lambda_p \exp(-\lambda_d t) - \lambda_d \exp(-\lambda_p t)}{\lambda_d - \lambda_p}\right], \end{aligned}$$

and factoring out $B_{p\to d}\frac{\lambda_d}{\lambda_d - \lambda_p}A_p(0)$ leads to:

$$\begin{aligned} A_d(t) = &\underbrace{A_d(0)\exp(-\lambda_d t)}_{\text{decay of } d} \\ &\underbrace{+B_{p\to d}\frac{\lambda_d}{\lambda_d - \lambda_p}A_p(0)\left[\exp(-\lambda_p t) - \exp(-\lambda_d t)\right]}_{\text{production of } d \text{ via decay of } p \text{ existing at } t=0} \\ &\underbrace{+B_{p\to d}\mathcal{R}_{\text{Mo-99}}\left[1 + \frac{\lambda_p \exp(-\lambda_d t) - \lambda_d \exp(-\lambda_p t)}{\lambda_d - \lambda_p}\right]}_{\text{production of } d \text{ via decay of } p \text{ produced at } t}. \end{aligned} \tag{3.23}$$

Eq. (3.23) is the solution of Eq. (3.11) corresponding to the differential equation for $N'_d(t)$.

Solutions by Laplace transforms

Taking the Laplace transform on Eq. (3.9), we obtain

$$\begin{aligned} \mathcal{L}\left\{N'_p(t) + \lambda_p N_p(t)\right\} &= (s + \lambda_p)\, N_p(s) - N_p(t)\,|_{t=0}, \\ \mathcal{L}\left\{\mathcal{R}_{\text{Mo-99}}\right\} &= \frac{\mathcal{R}_{\text{Mo-99}}}{s}, \end{aligned}$$

that is,

$$N_p(s) = \frac{N_p(t)\,|_{t=0}}{s+\lambda_p} + \frac{\mathcal{R}_{\text{Mo-99}}}{s\,(s+\lambda_p)}. \tag{3.24}$$

The inverse Laplace transform is

$$\mathcal{L}^{-1}\left\{N_p(s)\right\} = N_p(t) = N_p(0)\exp(-\lambda_p t) + \frac{[1-\exp(-\lambda_p t)]}{\lambda_p}\mathcal{R}_{\text{Mo-99}}.$$

Multiplying both sides by λ_p yields

$$A_p(t) = A_p(0)\exp(-\lambda_p t) + [1-\exp(-\lambda_p t)]\,\mathcal{R}_{\text{Mo-99}}. \tag{3.25}$$

Eq. (3.25) is the solution of Eq. (3.11) corresponding to the differential equation for $N_p'(t)$, and is exactly the same as Eq. (3.21) which was obtained by solving the eigenvalue-eigenvector problem.

Similarly, we take the Laplace transform on Eq. (3.10), obtaining

$$N_d(s) = \frac{N_d(t)\,|_{t=0}}{s+\lambda_d} + \frac{B_{p\to d}\lambda_p N_p(s)}{s+\lambda_d}.$$

Replacing the term $N_p(s)$ by Eq. (3.24), we find

$$N_d(s) = \underbrace{\frac{N_d(t)\,|_{t=0}}{s+\lambda_d}}_{\text{(i)}} \underbrace{+\frac{B_{p\to d}\lambda_p N_p(t)\,|_{t=0}}{(s+\lambda_p)\,(s+\lambda_d)}}_{\text{(ii)}} \underbrace{+\frac{B_{p\to d}\lambda_p \mathcal{R}_{\text{Mo-99}}}{s\,(s+\lambda_p)\,(s+\lambda_d)}}_{\text{(iii)}}. \tag{3.26}$$

The inverse Laplace transform of (i) is

$$N_d(t)\,|_{t=0}\mathcal{L}^{-1}\left\{\frac{1}{s+\lambda_d}\right\} = N_d(0)\exp(-\lambda_d t)\,.$$

For (ii), the inverse Laplace transform is

$$B_{p\to d}\lambda_p N_p(t)\,|_{t=0}\mathcal{L}^{-1}\left\{\frac{1}{(s+\lambda_p)\,(s+\lambda_d)}\right\} = B_{p\to d}A_p(0)\left[\frac{\exp(-\lambda_p t)-\exp(-\lambda_d t)}{\lambda_d-\lambda_p}\right].$$

Lastly, the inverse Laplace transform of (iii) is

$$B_{p\to d}\lambda_p \mathcal{R}_{\text{Mo-99}}\mathcal{L}^{-1}\left\{\frac{1}{s\,(s+\lambda_p)\,(s+\lambda_d)}\right\} = B_{p\to d}\mathcal{R}_{\text{Mo-99}} \times\left[\frac{1}{\lambda_d}+\frac{\exp(-\lambda_p t)}{\lambda_p-\lambda_d}+\frac{\lambda_p\exp(-\lambda_d t)}{\lambda_d\,(\lambda_d-\lambda_p)}\right].$$

Table 3.2. Solutions of the system of modified and original Bateman equations obtained by different methods.

	Solution for $N'_p(t)$	Solution for $N'_d(t)$
Eigenvalue-eigenvector problem	Eq. (3.21)	Eq. (3.23)
Laplace transform	Eq. (3.25)	Eq. (3.27)

Consequently, the inverse Laplace transform of Eq. (3.26) is given by

$$\begin{aligned}\mathcal{L}^{-1}\left\{N_d(s)\right\} = N_d(t) = N_d(0)\exp(-\lambda_d t) \\ + B_{p\to d}A_p(0)\left[\frac{\exp(-\lambda_p t)-\exp(-\lambda_d t)}{\lambda_d-\lambda_p}\right] \\ + B_{p\to d}\mathcal{R}_{\text{Mo-99}}\left[\frac{1}{\lambda_d}+\frac{\exp(-\lambda_p t)}{\lambda_p-\lambda_d}+\frac{\lambda_p\exp(-\lambda_d t)}{\lambda_d(\lambda_d-\lambda_p)}\right].\end{aligned}$$

Multiplying by λ_d, we arrive at

$$\begin{aligned}A_d(t) =& A_d(0)\exp(-\lambda_d t) \\ &+ B_{p\to d}\frac{\lambda_d}{\lambda_d-\lambda_p}A_p(0)\left[\exp(-\lambda_p t)-\exp(-\lambda_d t)\right] \\ &+ B_{p\to d}\mathcal{R}_{\text{Mo-99}}\left[1+\frac{\lambda_d\exp(-\lambda_p t)-\lambda_p\exp(-\lambda_d t)}{\lambda_p-\lambda_d}\right].\end{aligned} \tag{3.27}$$

Eq. (3.27) is the solution of Eq. (3.11) corresponding to the differential equation for $N'_d(t)$, and is exactly the same as Eq. (3.23) obtained from their eigenvalues and eigenvectors.

Comparison

The solutions of the system of modified and original Bateman equations solved by two methods, namely the eigenvalue-eigenvector problem and the Laplace transform, were the same (Table 3.2), corroborating that the solutions are in correct form.

3.4.2 Postirradiation activities

We now consider ^{99}Mo/^{99m}Tc activities after the end of irradiation, during which the activities are not newly produced but are only lost by their radioactive decay. In this case, the term for ^{99}Mo production rate in Eq. (3.9) becomes zero and Eq. (3.10)

remains the same, resulting in another system of Bateman equations:

$$\begin{bmatrix} N_p'(t) \\ N_d'(t) \end{bmatrix} = \begin{bmatrix} -\lambda_p & 0 \\ B_{p\to d}\lambda_p & -\lambda_d \end{bmatrix} \begin{bmatrix} N_p(t) \\ N_d(t) \end{bmatrix}. \tag{3.28}$$

Note that Eq. (3.28) is simply Eq. (3.11) with the nonhomogeneity column vector **F** *excluded*. Accordingly, the Laplace transforms of Eqs. (3.24) and (3.26) and their inverse transforms can be reused just by removing the terms containing the ^{99}Mo production rate. Namely, the Laplace transforms of Eq. (3.28) are

$$\begin{aligned} N_p(s) &= \frac{N_p(t)\,|_{t=0}}{s+\lambda_p}, \\ N_d(s) &= \frac{N_d(t)\,|_{t=0}}{s+\lambda_d} + \frac{B_{p\to d}\lambda_p N_p(t)\,|_{t=0}}{(s+\lambda_p)\,(s+\lambda_d)}, \end{aligned}$$

and their inverse transforms are

$$\begin{aligned} &\mathcal{L}^{-1}\left\{N_p(s)\right\} = N_p(t) = N_p(0)\exp(-\lambda_p t)\,, \\ &\mathcal{L}^{-1}\left\{N_d(s)\right\} = N_d(t) = N_d(0)\exp(-\lambda_d t) + B_{p\to d}A_p(0)\left[\frac{\exp(-\lambda_p t)-\exp(-\lambda_d t)}{\lambda_d-\lambda_p}\right]. \end{aligned}$$

Using the relation $A_i = \lambda_i N_i$, we obtain the postirradiation ^{99}Mo/^{99m}Tc activities:

$$A_p(t) = A_p(0)\exp(-\lambda_p t)\,, \tag{3.29}$$

$$A_d(t) = A_d(0)\exp(-\lambda_d t) + B_{p\to d}\frac{\lambda_d}{\lambda_d-\lambda_p}A_p(0)\left[\exp(-\lambda_p t)-\exp(-\lambda_d t)\right]. \tag{3.30}$$

3.4.3 Modeling the solutions

For describing the ^{99}Mo/^{99m}Tc activities, the solutions need to be modeled with respect to several time frames and chemical parameters. Namely, we consider the following four time domains:

(i) t_{irr}, the time during which a Mo target is irradiated
(ii) t_{pro}, the time during which the irradiated [^{99}Mo]Mo target is chemically processed and the processed ^{99}Mo is loaded onto a ^{99m}Tc generator
(iii) t_{del}, the time during which the ^{99m}Tc generator is delivered to a clinic
(iv) t_{dec}, the time during which the ^{99m}Tc generator is used in the clinic

We also consider the following two chemical parameters:

(i) κ, the fraction of ^{99}Mo/^{99m}Tc activities lost during t_{pro}

(ii) ζ, the ^{99m}Tc elution efficiency of a ^{99m}Tc generator

We begin with t_{irr}. In general, no ^{99}Mo activity is present before a Mo target is irradiated, from which it follows that $A_p(0) = A_d(0) = 0$, and that

$$A_p(t_{\text{irr}}) = \left[1 - \exp(-\lambda_p t_{\text{irr}})\right] \mathcal{V}_{\text{Mo-tar}} I_{\text{e}^-} \int_{E_{\gamma,\text{th}}}^{\infty} \Phi_{\text{Mo-tar}}(E_\gamma)\, \Sigma(E_\gamma)\, \mathrm{d}E_\gamma, \tag{3.31}$$

$$\begin{aligned} A_d(t_{\text{irr}}) = B_{p\to d} &\left[1 + \frac{\lambda_d}{\lambda_p - \lambda_d} \exp(-\lambda_p t_{\text{irr}}) + \frac{\lambda_p}{\lambda_d - \lambda_p} \exp(-\lambda_d t_{\text{irr}})\right] \\ &\times \mathcal{V}_{\text{Mo-tar}} I_{\text{e}^-} \int_{E_{\gamma,\text{th}}}^{\infty} \Phi_{\text{Mo-tar}}(E_\gamma)\, \Sigma(E_\gamma)\, \mathrm{d}E_\gamma, \end{aligned} \tag{3.32}$$

where the ^{99}Mo production rate is written in its original form (Eq. (3.9)). Note that Eq. (3.31) results from Eq. (3.21) or Eq. (3.25), and Eq. (3.32) results from Eq. (3.23) or Eq. (3.27).

On the other hand, the ^{99}Mo activity in the postirradiation time frames, namely t_{pro}, t_{del}, and t_{dec}, are governed by Eq. (3.29). Denoting the ^{99m}Tc elution ordinal number as n, then, Eq. (3.29) in the postirradiation regime can be written as

$$A_p\left(t_{\text{dec},n}\right) = \begin{cases} A_p(0) \exp\left(-\lambda_p t_{\text{del}}\right), & n = 1 \\ A_p(0) \exp\left(-\lambda_p t_{\text{dec},n}\right), & n \geq 2. \end{cases} \tag{3.33}$$

For ^{99m}Tc, Eq. (3.30) can be used as

$$A_d\left(t_{\text{dec},n}\right) = \begin{cases} A_d(0) \exp\left(-\lambda_d t_{\text{del}}\right) \\ \quad + B_{p\to d} \dfrac{\lambda_d}{\lambda_d - \lambda_p} A_p(0) \left[\exp\left(-\lambda_p t_{\text{del}}\right) - \exp\left(-\lambda_d t_{\text{del}}\right)\right], & n = 1 \\ A_d(0) \exp\left(-\lambda_d t_{\text{dec},n}\right) \\ \quad + B_{p\to d} \dfrac{\lambda_d}{\lambda_d - \lambda_p} A_p(0) \left[\exp\left(-\lambda_p t_{\text{dec},n}\right) - \exp\left(-\lambda_d t_{\text{dec},n}\right)\right], & n \geq 2, \end{cases} \tag{3.34}$$

where $t_{\text{dec},n}$ is the decay time between ^{99m}Tc elution runs $n-1$ and n, and t_{del} is the time during which ^{99}Mo-loaded ^{99m}Tc generators are delivered to clinics. Using the chemical parameters, the initial conditions are given by

$$A_p\left(t_{\text{dec},n} = 0\right) = \begin{cases} (1 - \kappa)\, A_p\left(t_{\text{EOP}}\right), & n = 1 \\ A_p\left(t_{\text{dec},n-1}\right), & n \geq 2, \end{cases}$$

$$A_p(t_{\text{EOP}}) = A_p(t_{\text{EOI}}) \exp\left(-\lambda_p t_{\text{pro}}\right),$$

$$A_d(t_{\mathrm{dec},n}=0) = \begin{cases} (1-\kappa)\,A_d(t_{\mathrm{EOP}})\,, & n=1 \\ (1-\zeta)\,A_d(t_{\mathrm{dec},n-1})\,, & n\geq 2, \end{cases}$$
$$A_d(t_{\mathrm{EOP}}) = A_d(t_{\mathrm{EOI}})\exp(-\lambda_d t_{\mathrm{pro}}) + B_{p\to d}\frac{\lambda_d}{\lambda_d-\lambda_p}A_p(t_{\mathrm{EOI}})\left[\exp(-\lambda_p t_{\mathrm{pro}})-\exp(-\lambda_d t_{\mathrm{pro}})\right], \quad (3.35)$$

where t_{EOI} denotes the time at the end of irradiation (EOI), and t_{EOP} the time at the end of postirradiation processing (EOP).

With Eq. (3.31)–(3.35), the revisiting of our ^{99}Mo/$^{99\mathrm{m}}$Tc activity model is completed. In the following subsection, the actual calculation and use of the developed model will be presented.

3.4.4 Use of the developed activity model

Hereafter, the abbreviations for ^{99}Mo and $^{99\mathrm{m}}$Tc, namely p and d, respectively (see Sec. 3.4.1), are replaced by their original symbols. Fig. 3.14 plots the modeled ^{99}Mo/$^{99\mathrm{m}}$Tc activities calculated using Eq. (3.31)–(3.35). The calculation was performed using our program `actdyn` (Sec. 2.4) with the following parameters:

(i) $\mathcal{V}_{\text{Mo-tar}} = 0.495\,\mathrm{cm}^3$ used in the linac design study[50] (Fig. 3.4)
(ii) $I_{\mathrm{e}^-} = 260\,\mu\mathrm{A}$ obtained from the beam dynamics study[50,60,66]
(iii) $\Phi_{\text{Mo-tar}}(E_\gamma)$ at $E_{\mathrm{e}^-} = 35\,\mathrm{MeV}$ obtained using PHITS v2.88 and EGS5 (Fig. 3.4)
(iv) $\Sigma(E_\gamma)$ contained in the TENDL-2009 library
(v) $B_{\text{Mo-99}\to\text{Tc-99m}} = 0.875$, a known value
(vi) $\kappa = 0.2$ assumed based on $\kappa \leq 0.15$ of the fission ^{99}Mo production scheme[17]
(vii) $\zeta = 0.7$ based on $\zeta > 0.8$ of a LSA $^{99\mathrm{m}}$Tc generator[48,86,87]

Although different values can be found in other literatures, in most cases $B_{\text{Mo-99}\to\text{Tc-99m}}$ lies in the range of 0.85–0.88.

In order to avoid underestimation, we set higher κ and lower ζ than those of the respective reference values. In addition, the following parameters need to be specified: t_{irr}, $t_{\mathrm{dec},n}$, and the maximum value of n. Their values and reasons are provided below.

The time of Mo target irradiation was set to be $t_{\mathrm{irr}} = 72\,\mathrm{h}$, in which case two ^{99}Mo production runs can be performed per week with one day secured for maintenance inspections. More importantly, the 72-h long irradiation can produce about half the

[17] National Research Council (US). *Medical Isotope Production Without Highly Enriched Uranium* (2009).
[48] S. Sekimoto *et al. J. Radioanal. Nucl. Chem.* **311**, 1361–1366 (2017).
[86] K. Tatenuma *et al. RADIOISOTOPES* **63**, 501–513 (2014).
[87] J. Jang *et al.* Photonuclear production of Mo-99/Tc-99m using molybdenum trioxide and activated carbon (2017).

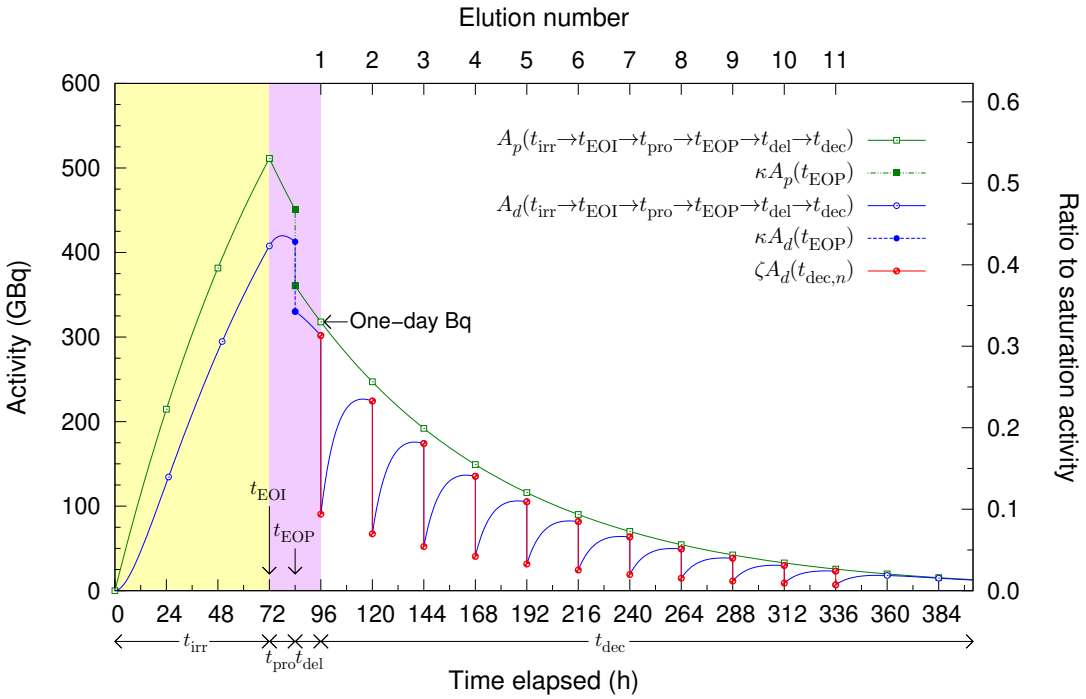

Fig. 3.14. Activities of ^{99}Mo (A_p) and ^{99m}Tc (A_d) produced from an electron linac. Our program `actdyn` was used for the calculation. Figure adapted from our publication [50] and previous thesis [60], the former of which is licensed under CC BY 4.0.

saturation yield of ^{99}Mo:

$$\frac{1-\exp\left(\ln 2/t_{1/2}^{\text{Mo-99}}\times 1.09 t_{1/2}^{\text{Mo-99}}\right)}{1-\lim_{t_{\text{irr}}\to+\infty}\exp(-\lambda_{\text{Mo-99}}t_{\text{irr}})}\approx 0.53,$$

which can be derived using Eq. (3.31), and is seen in Fig. 3.14 as the $y2$-axis. The symbol $t_{1/2}$ denotes the physical half-life.

The ^{99m}Tc elution interval can be chosen by comparing the equilibrium activity of ^{99m}Tc. Assuming that the initial ^{99m}Tc activity is zero, division of Eq. (3.30) by Eq. (3.29) gives

$$\frac{A_{\text{Tc-99m}}(t)}{A_{\text{Mo-99}}(t)}=B_{\text{Mo-99}\to\text{Tc-99m}}\frac{\lambda_{\text{Tc-99m}}}{\lambda_{\text{Tc-99m}}-\lambda_{\text{Mo-99}}}\frac{[\exp(-\lambda_{\text{Mo-99}}t)-\exp(-\lambda_{\text{Tc-99m}}t)]}{\exp(-\lambda_{\text{Mo-99}}t)}.$$

Considering the business hours and the exponential growth of ^{99m}Tc activity, the useful

elution intervals can be 3 h, 6 h, or 24 h. For instance, setting $t = 3\,\mathrm{h}$ results in

$$\frac{A_{\text{Tc-99m}}(3\,\mathrm{h})}{A_{\text{Mo-99}}(3\,\mathrm{h})} = (0.875)\,(1.1)\,\frac{\left[\exp\left(-0.0105\,\mathrm{h}^{-1}\times 3\,\mathrm{h}\right) - \exp\left(-0.1155\,\mathrm{h}^{-1}\times 3\,\mathrm{h}\right)\right]}{\exp\left(-0.0105\,\mathrm{h}^{-1}\times 3\,\mathrm{h}\right)}$$
$$\approx 0.260,$$

meaning that the ^{99m}Tc activity can grow to 26% of of its equilibrium state. By the same token, setting $t = 6\,\mathrm{h}$ gives

$$\frac{A_{\text{Tc-99m}}(6\,\mathrm{h})}{A_{\text{Mo-99}}(6\,\mathrm{h})} = (0.875)\,(1.1)\,\frac{\left[\exp\left(-0.0105\,\mathrm{h}^{-1}\times 6\,\mathrm{h}\right) - \exp\left(-0.1155\,\mathrm{h}^{-1}\times 6\,\mathrm{h}\right)\right]}{\exp\left(-0.0105\,\mathrm{h}^{-1}\times 6\,\mathrm{h}\right)}$$
$$\approx 0.450,$$

and with $t = 24\,\mathrm{h}$, we have

$$\frac{A_{\text{Tc-99m}}(24\,\mathrm{h})}{A_{\text{Mo-99}}(24\,\mathrm{h})} = (0.875)\,(1.1)\,\frac{\left[\exp\left(-0.0105\,\mathrm{h}^{-1}\times 24\,\mathrm{h}\right) - \exp\left(-0.1155\,\mathrm{h}^{-1}\times 24\,\mathrm{h}\right)\right]}{\exp\left(-0.0105\,\mathrm{h}^{-1}\times 24\,\mathrm{h}\right)}$$
$$\approx 0.885, \tag{3.36}$$

which implies that increasing the elution interval above 24 h will not lead to a significant growth of the ^{99m}Tc activity. We chose the last option, namely $t_{\text{dec},n} = 24\,\mathrm{h}$, to increase the RAC of ^{99m}Tc eluate. For the same eluent volume, low column activity of ^{99m}Tc leads to low RAC, which can result in insufficient gamma signals. The RAC issue will be addressed in detail in Chap. 7.

Besides, it should be noted that the actual value of $A_{\text{Tc-99m}}(24\,\mathrm{h})/A_{\text{Mo-99}}(24\,\mathrm{h})$ slightly differs from Eq. (3.36). In practice, the initial ^{99m}Tc activity for an elution run is nonzero, because the elution efficiency cannot be 100%. In other words, it holds in Eq. (3.35) that $\zeta < 1$, making $A_{\text{Tc-99m}}(t_{\text{dec},n} = 0) \neq 0$. Therefore, the term $A_{\text{Tc-99m}}(0)\exp(-\lambda_{\text{Tc-99m}}t)$ of Eq. (3.30) should also be taken into account in comparing the equilibrium activities of ^{99m}Tc and ^{99}Mo. Under the condition of $\zeta = 0.7$ explained in the parameter list (vii) above, the condition $A_{\text{Tc-99m}}(t_{\text{dec},n} = 0) \neq 0$ results in $A_{\text{Tc-99m}}(24\,\mathrm{h})/A_{\text{Mo-99}}(24\,\mathrm{h}) \approx 0.91$[50], which is greater than Eq. (3.36).

The last parameter to be determined is the maximum value of n. A reasonable choice is to assume that the shelf-life of a ^{99m}Tc generator is 240 h, after which the

loaded ^{99}Mo will lose most of its initial activity:

$$\exp\left(-\frac{\ln 2}{t_{1/2}^{\text{Mo-99}}}3.64t_{1/2}^{\text{Mo-99}}\right)A_{\text{Mo-99}}\left(t_{\text{dec},1}\right) \approx 0.08A_{\text{Mo-99}}\left(t_{\text{dec},1}\right),$$

which can be obtained using Eq. (3.33). With the elution interval $t_{\text{dec},n} = 24\,\text{h}$, the 240-h generator life results in the greatest elution ordinal number $n = 11$.

The elution number begins at 1 (see Fig. 3.14).

Using the set of parameters explained above, the ^{99m}Tc activity that can be obtained from one electron linac per week was calculated as

$$A_{\text{Tc-99m,wk}} = 2\left[\sum_{n=2}^{11}\zeta A_{\text{Tc-99m}}\left(t_{\text{dec},n}\right)\right] \approx 1.3\,\text{TBq}\,\text{wk}^{-1}, \tag{3.37}$$

where $n = 2$ means that the first ^{99m}Tc eluate is not scored. Containing a substantial amount of ^{99}Tc which functions as an impurity nuclide, the initial ^{99m}Tc eluate can or should be discarded to improve the radiopharmaceutical quality of ^{99m}Tc.

Combined with the demand for ^{99m}Tc in a country of interest, Eq. (3.37) can be used to estimate the number of electron linacs that can meet the ^{99m}Tc demand. In our published paper[50], we assumed that 1 million ^{99m}Tc scans are performed annually in Japan, which is the 2002 figure[88]. Although recent figures are smaller than 0.7 million[89], we used the 2002 figure in preparation for the recovery of ^{99m}Tc use frequency. Assuming that the average ^{99m}Tc dose is 740 MBq, then, the corresponding weekly ^{99m}Tc demand is

$$D_{\text{Tc-99m}} = 14.2\,\text{TBq}\,\text{wk}^{-1},$$

leading to

$$\left\lceil\frac{D_{\text{Tc-99m,wk}}}{A_{\text{Tc-99m,wk}}}\right\rceil = \left\lceil\frac{14.2\,\text{TBq}\,\text{wk}^{-1}}{1.3\,\text{TBq}\,\text{wk}^{-1}}\right\rceil = 11,$$

where the ceiling function is used for avoiding underestimation. This means that for the specified ^{99m}Tc demand, 11 of the 35 MeV and 260 μA X-band electron linacs can provide ^{99}Mo/^{99m}Tc self-sufficiency. Such supply-demand calculations can be easily performed using the dedicated program `actdyn` (Sec. 2.4), in which the developed activity model is fully implemented.

[88] Science Council of Japan. On the stable supply system of radioisotope in Japan (in Japanese) (2008).
[89] T. Yamashita. Estimate of Japan's post-2016 demand for ^{99m}Tc (2013).

3.5 Facility requirements

In addition to the linac and beam parameters, facility requirements must also be considered for ^{99}Mo production. This is especially true if the handling of unsealed radionuclides is controlled by laws or regulations of the country in question.

In Japan, for example, electron linac production of radionuclides is allowed only if the facility is equipped with subsystems that satisfy the regulatory standards. Examples include (i) radiation shielding and monitoring systems, (ii) ventilation system, (iii) decontamination system, (iv) fireproof system, and (v) evacuation system.

The electron beam energy affects not only the electron and photon distributions in targetry components (Figs. 3.7 and 3.8), but also the energy and amount of photoneutrons. Neutron outputs of different electron beam energies are shown in Fig. 3.15. In an electron accelerator, induced activity can result not only from photonuclear reactions, but also from the nucleons liberated by the photonuclear reactions[90,91]. Therefore, targetry shielding design should be performed considering the beam energy of the linac and the resulting neutron and proton generation.

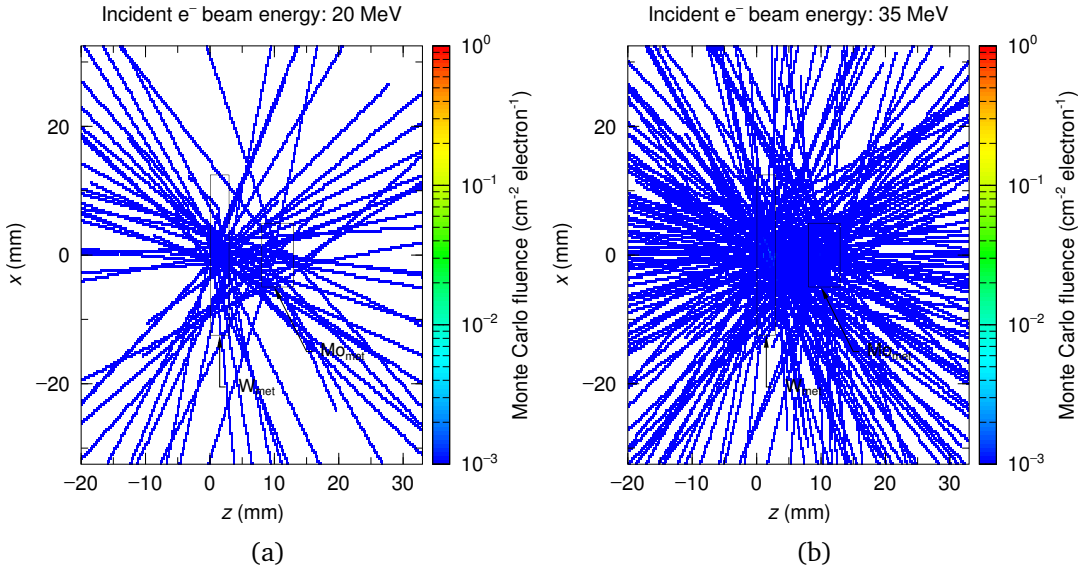

(a) (b)

Fig. 3.15. Neutron tracks calculated for (a) 20-MeV and (b) 35-MeV electron beams. PHITS v3.02, EGS5, and `phitar` were used for the calculations. The transverse electron beam size was 3 mm in FWHM.

[90] International Atomic Energy Agency. *Radiological Safety Aspects of the Operation of Electron Linear Accelerators* (1979).

[91] A. Fassò *et al.* Radiation problems in the design of the large electron-positron collider (LEP). Report No. CERN 84-02 (1984).

3.6 Summary

In this chapter, we investigated parameters of an electron linac and its beams with emphasis on ^{99}Mo/^{99m}Tc production. First, two options are available for the operating frequency: (i) C- or X-band RFs which can provide structural compactness, and (ii) an S-band RF, which can provide a high beam power and thereby a high ^{99}Mo yield. By the same token, an SW structure, an SCS in particular, can be preferable if the linac should be downsized.

Based on MC simulations and analysis of its results, we found that a beam energy of 35 MeV can be a reasonable choice for ^{99}Mo production. A high beam current is preferable for ^{99}Mo production, but is limited by the available RF power or project budget; a reasonable compromise should be made accordingly.

To alleviate the heat load on target materials, a beam size greater than 2 mm, for instance 4.5 mm, is necessary. On the other hand, the beam emittance should be reduced to the extent to which it does not affect the operational stability of the linac.

Our parameterized ^{99}Mo/^{99m}Tc activity model and its calculation program `actdyn` can be useful in assessing the feasibility of electron linac production of ^{99}Mo/^{99m}Tc. For instance, 11 of the designed X-band electron linacs can meet one million annual scans of ^{99m}Tc.

The investigated parameters and their roles, and possible options are summarized in Table 3.3. These findings can be useful in commissioning actual ^{99}Mo production electron linacs.

Table 3.3. Linac parameters and their roles in ^{99}Mo production.

Parameter	Role	Option
Operating frequency	Overall linac design	L- to X-band RFs
Accelerating structure	Size of linac	SW or TW structures
Beam energy	^{99}Mo yield and specific yield	20–50 MeV
Beam current	^{99}Mo yield and specific yield	As large as possible
Beam size	Heat load on targetry	2–8 mm, Gaussian
Beam emittance	Operational stability of linac	Moderate

Chapter
4

Parametric analysis of ^{99}Mo production targetry

Abstract

Parametric analysis of ^{99}Mo production targetry is necessary for both new and existing electron linacs: for a newly designed electron linac, investigations of targetry parameters can justify the design parameters of the linac. For an existing electron linac, it is the targetry parameters that can exploit the available beam energy and power to the greatest extent achievable, and can thereby turning the electron linac to a ^{99}Mo production machine. In this chapter, we analyze targetry parameters via a series of MC calculations using PHITS, EGS5, and `phitar`.

4.1 Overview

Accelerator targetry is a system where the accelerated beams collide with materials (i) to generate other types of particles or (ii) to obtain information from the beam-material interactions. Depending on the application, such a target system can consist of a single or multiple materials.

In the field of electron linac production of ^{99}Mo, the majority of target systems is comprised of two materials. The first material is placed near the beam exit, and is used to convert the kinetic energy of electron beams into bremsstrahlung photons (Fig. 4.1). Because it seems as though one particle is converted to another, the first material is referred to as a converter, converter target, or radiator, the first of which is used in this dissertation. High-Z materials such as W and Pt are used as the converter.

The second material is placed such that the converter-generated photons impinge on its surface, enabling the photonuclear reaction ^{100}Mo(γ,n)^{99}Mo to take place. The

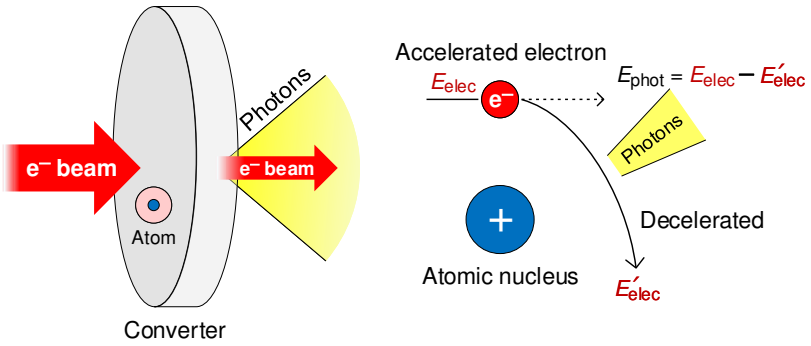

Fig. 4.1. An illustration of bremsstrahlung generation at a converter.

second material is therefore referred to as a Mo target, or simply a target. The two widely used Mo target materials are Mo metal and Mo(VI) oxide (MoO_3). Hereafter, we will refer to Mo metal as Mo_{met} to distinguish it from the Mo element.

The targetry of an electron linac is illustrated in Fig. 4.2, and the candidate materials are listed in Table 4.1. In Chap. 3, we addressed several important linac and beam parameters, including the beam energy and current. We also explained that the maximum beam current is essentially dictated by the available RF power. Because an electron linac is commissioned based on a specifically designed RF system, it can be challenging to raise the maximum beam current after linac installation. This does not, however, mean that the ^{99}Mo yields can no longer be changed; the design of targetry can greatly affect the yield and specific yield of ^{99}Mo. This also means that if an existing electron linac should be used for ^{99}Mo production, the targetry should be redesigned so that the available beam power can be utilized to the greatest extent possible.

Research on targetry requires a broad range of simulation runs, to the extent to which existing simulation tools on their own are insufficient. We therefore developed computer programs that provide means of parameter-varying and multivariate simulation runs, and automated postprocessing (Chap. 2). The programs have been designed as (i) *frontend*, (ii) *customizable*, (iii) *copyleft*, and (iv) *scalable* programs; because of the aspects (i) and (ii), the user need not know how the program works, but still can examine as much simulation variables as necessary. If the user wants to upgrade or expand the program, the aspects (iii) and (iv) allow to do so. As mentioned in Chap. 2, the programs are all written in PERL (Perl 5), and are available in open-source repositories[56–58]. Brief user manuals of the programs are found in Appendix A.

[56] J. Jang. `phitar` - A PHITS wrapper for targetry design (v1.03) (2019).
[57] J. Jang. `enrimo` - Investigate the influence of an enriched Mo isotope (v1.05) (2019).
[58] J. Jang. `actdyn` - A Mo-99/Tc-99m activity dynamics simulator (v2.31) (2019).

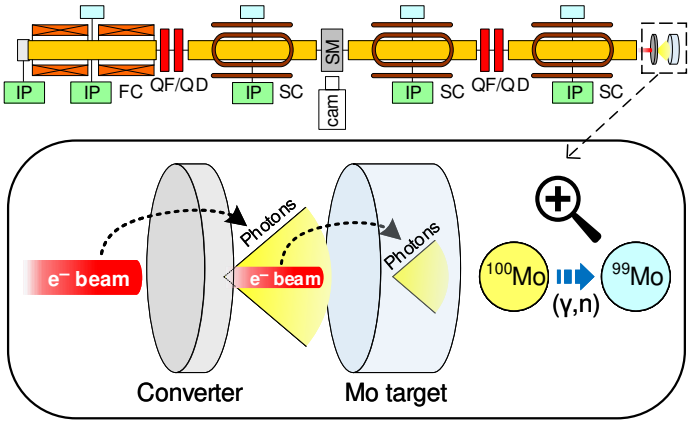

Fig. 4.2. An illustration of electron linac targetry.

Table 4.1. Roles and candidate materials of targetry components.

	Converter	Mo target
Role	γ generation via (e^-,γ)	^{99}Mo production via ^{100}Mo(γ,n)^{99}Mo
Material	Mo,[1] Ta, W, Ir, Pt, Au	Mo, MoO_3
	Naming conventions	
By function	Converter, radiator	Target
By shape	Foil, plate	Foil, plate, pellet

[1] When used as a converter, Mo also function as a Mo target; namely, electron beams are converted into bremsstrahlung photons inside Mo, and these photons induce the ^{100}Mo(γ,n)^{99}Mo reaction within that Mo [47, 52].

4.2 Integrated and separated targetry

Target systems can be classified according to the number of component materials: (i) integrated targetry, where Mo is used as both a converter and a Mo target, and (ii) separated targetry, where a separate converter is used and Mo functions only as a Mo target. The configurations of the two target systems are shown in Fig. 4.3. In this section, we compare the two target systems considering ^{99}Mo mass production.

4.2.1 ^{99}Mo specific activity

Studies[47,52] showed that under certain conditions, the ^{99}Mo specific activity of an integrated Mo target system is higher than that of a separated target system. They attributed the results to the saving of bremsstrahlung photons, which could otherwise

[47] A. Tsechanski *et al. Nucl. Instrum. Methods Phys. Res. B* **366**, 124–139 (2016).
[52] D. V. Fedorchenko *et al. Nucl. Instrum. Methods Phys. Res. B* **438**, 6–13 (2019).

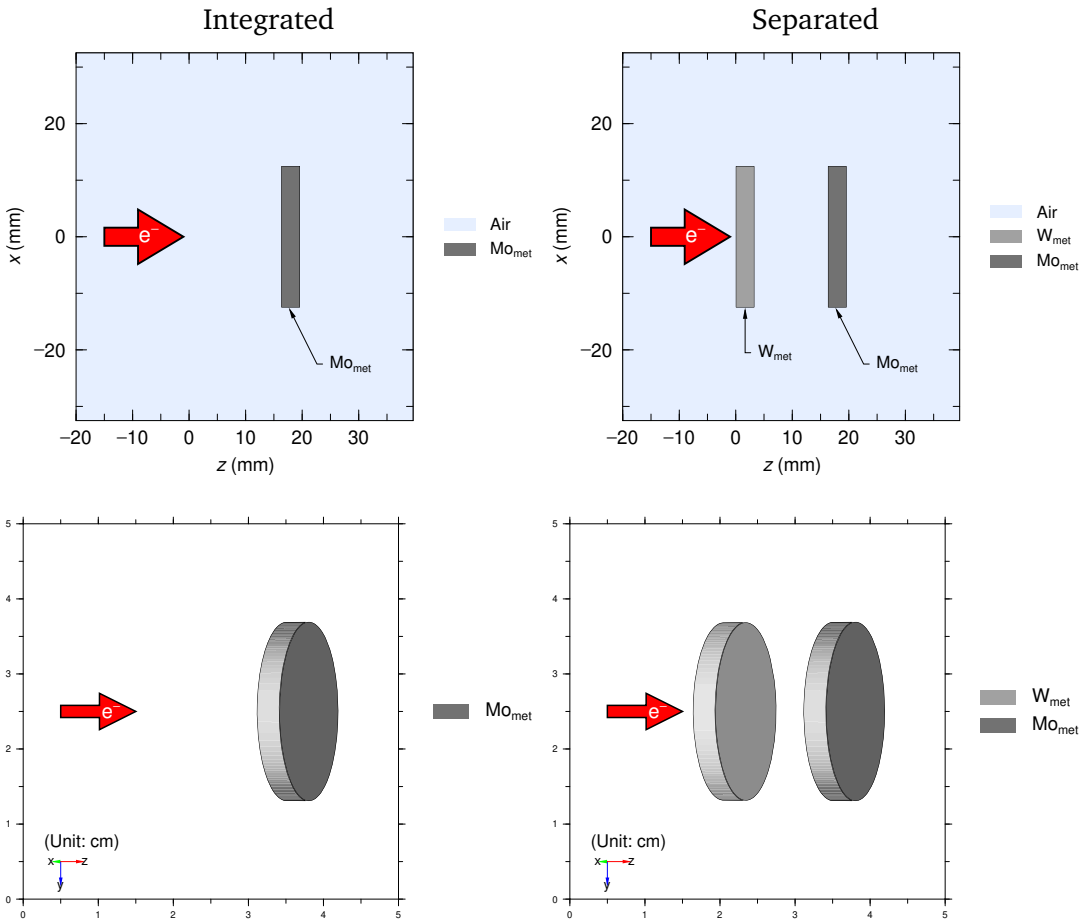

Fig. 4.3. (left) Integrated and (right) separated targetry. (top row) two- and (bottom row) three-dimensional representations.

be attenuated in a converter.

To examine if the ^{99}Mo specific activity is generally higher in an integrated target system than in a separated one, we performed MC simulations using PHITS v3.02[59] and EGS5[82], with our program `phitar` (Sec. 2.2) used as the frontend and automation programs. Electron beams of 20–50 MeV at the interval of 15 MeV were simulated. The beam size was 4.5 mm in FWHM in the x and y directions. The converter and Mo target materials were metallic W and Mo, respectively. Both W and Mo were disk-shaped and were 25 mm in diameter and 3.3 mm in thickness. Dry air was assumed to be the ambient gas of the targetry.

Simulation results of the 35 MeV case are presented in Fig. 4.4. The second row of

[59] T. Sato *et al. J. Nucl. Sci. Technol.* **55**, 684–690 (2018).
[82] H. Hirayama *et al. The* EGS5 *code system* (2005).

the figure shows that at least for 4.5-mm electron beams, photons are more homogeneously distributed over the Mo target, resulting in a higher fluence in the target, and thereby higher yield and specific yield of ^{99}Mo. For 5-min irradiation, the ^{99}Mo specific activity of the integrated targetry was calculated to be 5.44 kBq Mo-g^{-1} μA^{-1}, and that of the separated targetry to be 14.6 kBq Mo-g^{-1} μA^{-1}. This suggests that the dependence of ^{99}Mo specific activity on the multiplicity of target materials is affected by other variables such as the beam size and target dimensions. Therefore, selection between integrated and separated target systems should not be made based on the ^{99}Mo specific activity.

4.2.2 Heat load on Mo targets

Considering the heat load and cooling efficiency, a separated target system can be more useful than an integrated one. As we showed in Chap. 3, a great portion of the kinetic energy of electron beams is converted into the heat energy; from the viewpoint of a Mo target, a converter can be seen as a "heat absorber". On top of that, a converter exhibiting a high melting point and a high thermal conductivity can provide efficient cooling of the targetry. The heat distributions in a Mo target and a converter are plotted in Fig. 4.5, showing that the heat load is greatly alleviated if separated targetry is used. The use of a separate converter can also reduce the radiation damage of the Mo target.

For the reasons explained above, separated targetry is used more widely than the integrated one; studies using the separated targetry include[40–44,48–51]. This dissertation also uses a separated target system; accordingly, the converters and Mo targets will be explored separately.

4.3 Converters

A converter is the first material with which the accelerated electron beams interact. Impinging on a converter material, a moving electron beam loses its kinetic energy via

[40] R. G. Bennett *et al. Nucl. Technol.* **126**, 102–121 (1999).
[41] C. Ross *et al. Phys. Can.* **66**, 19–24 (2010).
[42] R. Galea *et al. Phys. Med. Biol.* **58**, 2737–2750 (2013).
[43] B. Szpunar *et al. Nucl. Instrum. Methods Phys. Res. A* **729**, 41–50 (2013).
[44] V. N. Starovoitova *et al. Appl. Radiat. Isot.* **85**, 39–44 (2014).
[48] S. Sekimoto *et al. J. Radioanal. Nucl. Chem.* **311**, 1361–1366 (2017).
[49] T. M. Martin *et al. J. Radioanal. Nucl. Chem.* **314**, 1051–1062 (2017).
[50] J. Jang *et al. Phys. Rev. Accel. Beams* **20**, 104701 (2017).
[51] T. Takeda *et al. J. Radioanal. Nucl. Chem.* **318**, 811–821 (2018).

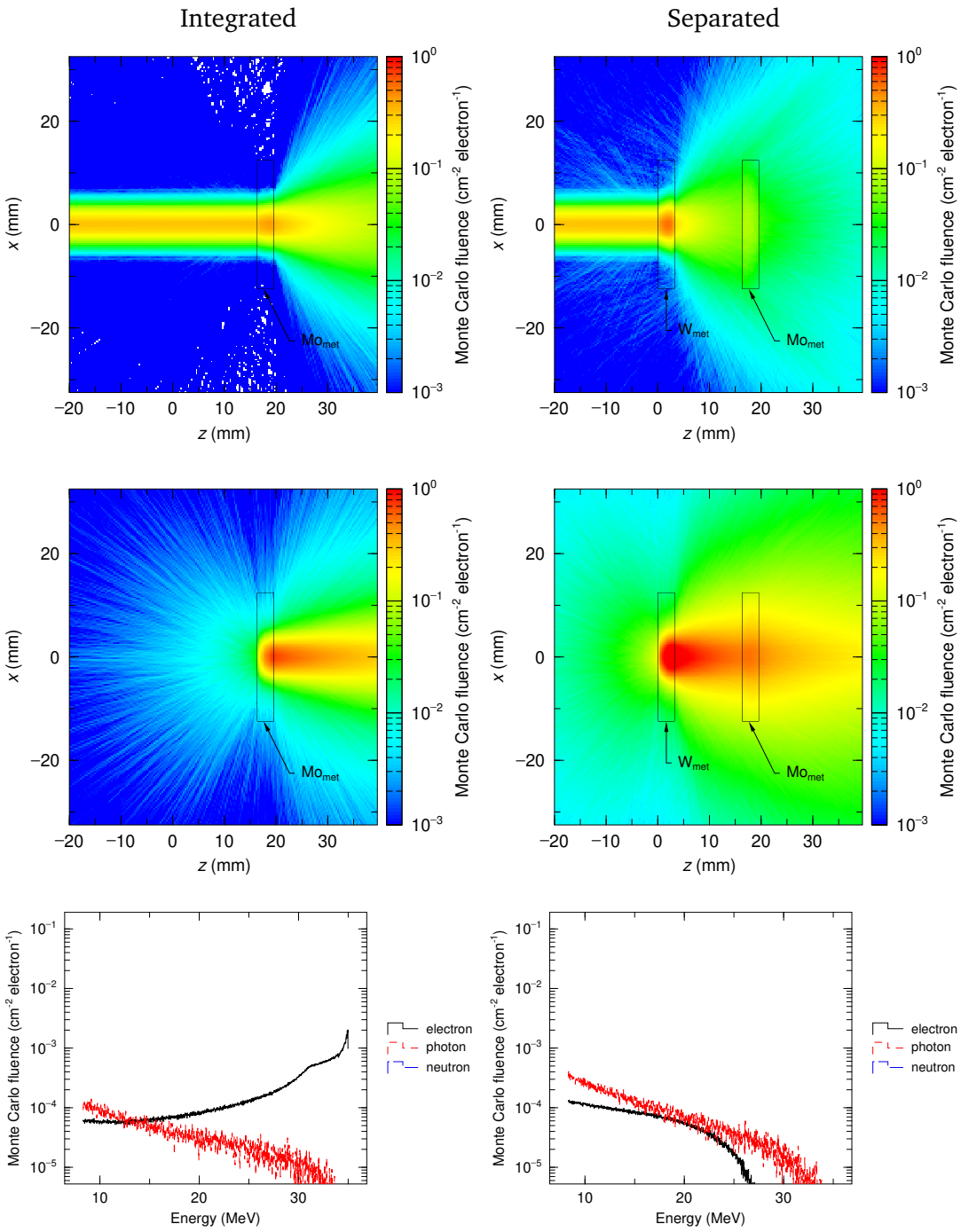

Fig. 4.4. (left column) Integrated and (right column) separated targetry. (top row) electron and (middle row) photon tracks, and (bottom row) their spectra in Mo targets. The energy and size of the incident electron beams were 35 MeV and 4.5 mm in *xy*-FWHM, respectively.

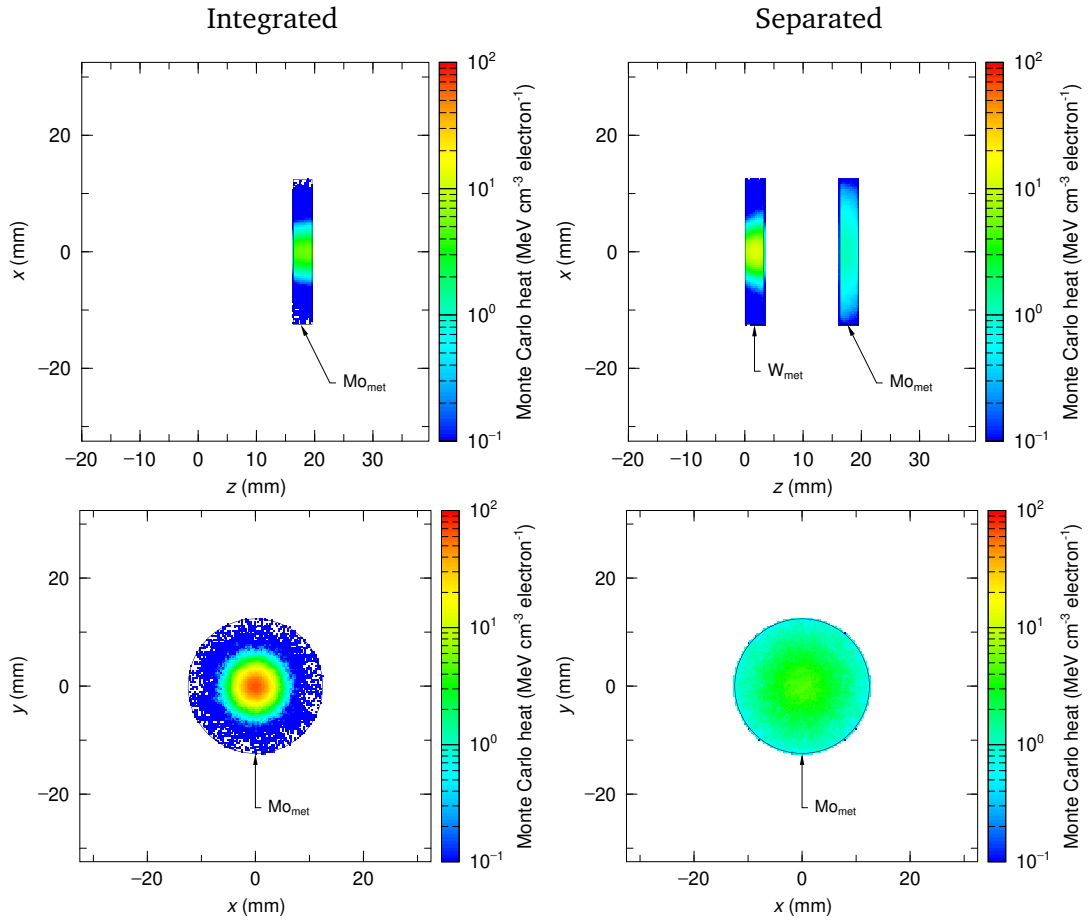

Fig. 4.5. (left column) Integrated and (right column) separated targetry. (top row) *xz*- and (bottom row) *yx*-plane heat distributions. The energy and size of the incident electron beams were 35 MeV and 4.5 mm in *xy*-FWHM, respectively.

(i) collisions with the orbital electrons or with the nucleons, or (ii) deceleration by the nucleus. By the interaction (i), the kinetic energy is converted into thermal energy, resulting in heat load on the converter. On the other hand, the kinetic energy lost by the interaction (ii) is converted into the kinetic energy of bremsstrahlung (Fig. 4.1), which we use in inducing the ^{100}Mo(γ,n)^{99}Mo reaction. In this section, we discuss what aspects should be considered in designing converters, and what materials can be used as converters.

4.3.1 Design considerations

The spectral intensity of bremsstrahlung can be approximated as[92,93]

$$I_\gamma(E_\gamma) = CZ\left(E_{e^-} - E_\gamma\right)^\alpha, \tag{4.1}$$

where C and α are constants, Z is the atomic number of the material on which electrons impinge, and E_{e^-} and E_γ are the energies of electrons and bremsstrahlung photons, respectively. Because of Eq. (4.1), high-Z materials are used as converters. If the converter consists of multiple elements, the effective atomic number Z_{eff} should be used in place of Z. Detailed explanations for the proportionality between $I_\gamma(E_\gamma)$ and Z can be found in[94,95].

The efficiency of bremsstrahlung generation depends, in addition to the atomic number, on the dimensions of the converter. In contrast to the atomic number, which is solely determined by the chemical composition of the material, the geometrical shapes of the converter can be modified to improve bremsstrahlung efficiency.

MC simulation programs can be used for finding the converter dimensions optimal for ^{99}Mo production. When running MC simulations, multiple variables should be examined independently. This is because the interactions of electrons and photons are governed by multiple physics models and factors. Examples include (i) the electron beam energy which affects the bremsstrahlung efficiency and distribution, (ii) electron beam size which affects the bremsstrahlung distribution, and (iii) Mo target dimensions and intertarget distance which affect the bremsstrahlung distribution in the Mo target (Fig. 4.6). Accordingly, designing a converter or its target system requires development of a customized wrapper program. We have developed such a program, which will be addressed later.

[92] G. H. McCall. *J. Phys. D* **15**, 823–831 (1982).
[93] N. A. Dyson. *Proc. Phys. Soc.* **73**, 924–936 (1959).
[94] A. H. Compton *et al. X-Rays in Theory and Experiment*. 2nd ed. (1967).
[95] J. K. Shultis *et al. Fundamentals of Nuclear Science and Engineering*. 3rd ed. (2017).

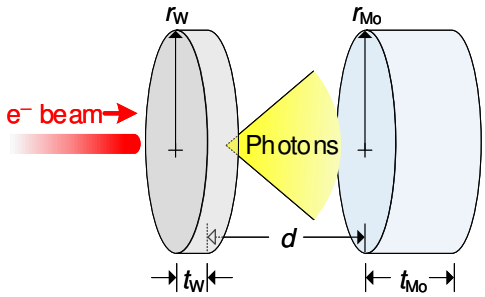

Fig. 4.6. Dimensional parameters of W-Mo targetry. t, r, and d denote the thickness, radius, and intertarget distance, respectively.

4.3.2 Materials options and comparison

The candidate converter materials are tabulated in Table 4.2. Except for Mo, which can be used as an integrated target[47,52], all of the listed materials are transition metals of the period 6. In order to determine which material is most suitable as a converter for ^{99}Mo production, we performed MC simulations using PHITS v3.02, EGS5, and `phitar`. The simulation conditions were as follows:

(i) Converter materials: Ta, W, Ir, Pt, and Au (varying parameter)
(ii) Converter shape: right circular cylinder (RCC)
(iii) Converter radius: 12.5 mm
(iv) Converter thicknesses: 1.0–7.0 mm at the interval of 0.1 mm (varying parameter)
(v) Electron beam energies: 20–50 MeV at the interval of 5 MeV (varying parameter)
(vi) Electron beam size: 3.0 mm in *xy*-FWHM
(vii) The distance between a converter and a Mo target: 1.3 mm
(viii) Mo target materials: Mo_{met} and MoO_3 (varying parameter)
(ix) Mo target shape: RCC
(x) Mo target radius: 5.0 mm
(xi) Mo target thickness: 5.0 mm

Mo as a converter material was not simulated because our target system consists of a separate converter and Mo target.

The MC photon fluences at $E_{e-} = 20$, 35, 50 MeV are plotted in Figs. 4.7 and 4.8. No significant differences in the photon fluence and thereby ^{99}Mo yield (Figs. 4.9 and 4.10) were found between the converter materials. Accordingly, a converter material should be selected based on other properties such as thermal characteristics. Exhibiting the highest melting and boiling points and the second highest thermal conductivity (Table 4.2), W can be preferable as a converter material. Beside, the low

Table 4.2. Candidate converter materials and their properties relevant to ^{99}Mo production. Z: atomic number, ρ: mass density, T_{m}: melting point, T_{b}: boiling point, and k: thermal conductivity. The greatest values in each column are highlighted by the underscore.

Material	Z	ρ (g cm^{-3})	T_{m} (K)	T_{b} (K)	k (W m^{-1} K^{-1})	Price[1](USD kg^{-1})
Mo	42	10.28	2,896	4,912	138	30
Ta	73	16.69	3,290	5,731	57.5	300–800
W	74	19.25	3,695	6,203	173	20–500
Ir	77	22.56	2,719	4,403	147	48,000
Pt	78	21.45	2,041	4,098	71.6	27,000
Au	79	19.3	1,337	3,243	318	42,000

[1] The market prices of precious and industrial metals depend on a number of factors, including (i) the processed forms such as the plate and rod, (ii) the political circumstances of the countries possessing the majority of the ores in question, and (iii) advents of new technologies that use the metals of interest. The prices listed in this table are based on multiple and uncitable webpages and, accordingly, should be seen only as examples.

cost of W can be useful in its timely exchange and relatively easier maintenance. Our target system therefore uses W as the converter.

Converter materials can be purchased from vendors. In the experimental stage, disk- or plate-shaped pure metals can be directly used as converters. For a full-fledged ^{99}Mo production system, on the other hand, the converter material may be alloyed, and should be processed and machined according to the targetry housing and cooling system.

4.4 Mo targets

To increase the ^{99}Mo yield, as many ^{100}Mo isotopes as possible should interact with bremsstrahlung photons of $>$8 MeV, the threshold for the ^{100}Mo(γ,n)^{99}Mo reaction. Hereafter, we will refer to the photons of $>$8 MeV as hyperthreshold photons. Designing Mo targets is essentially a series of parametric studies with the goal of increasing the frequency of ^{100}Mo(γ,n)^{99}Mo reaction.

4.4.1 Design considerations

Two aspects should be considered when designing Mo targets (Fig. 4.11). The first one is from the viewpoint of particle beams, and is concerned with how to increase the amount of hyperthreshold photons entering a Mo target. MC simulation and analysis

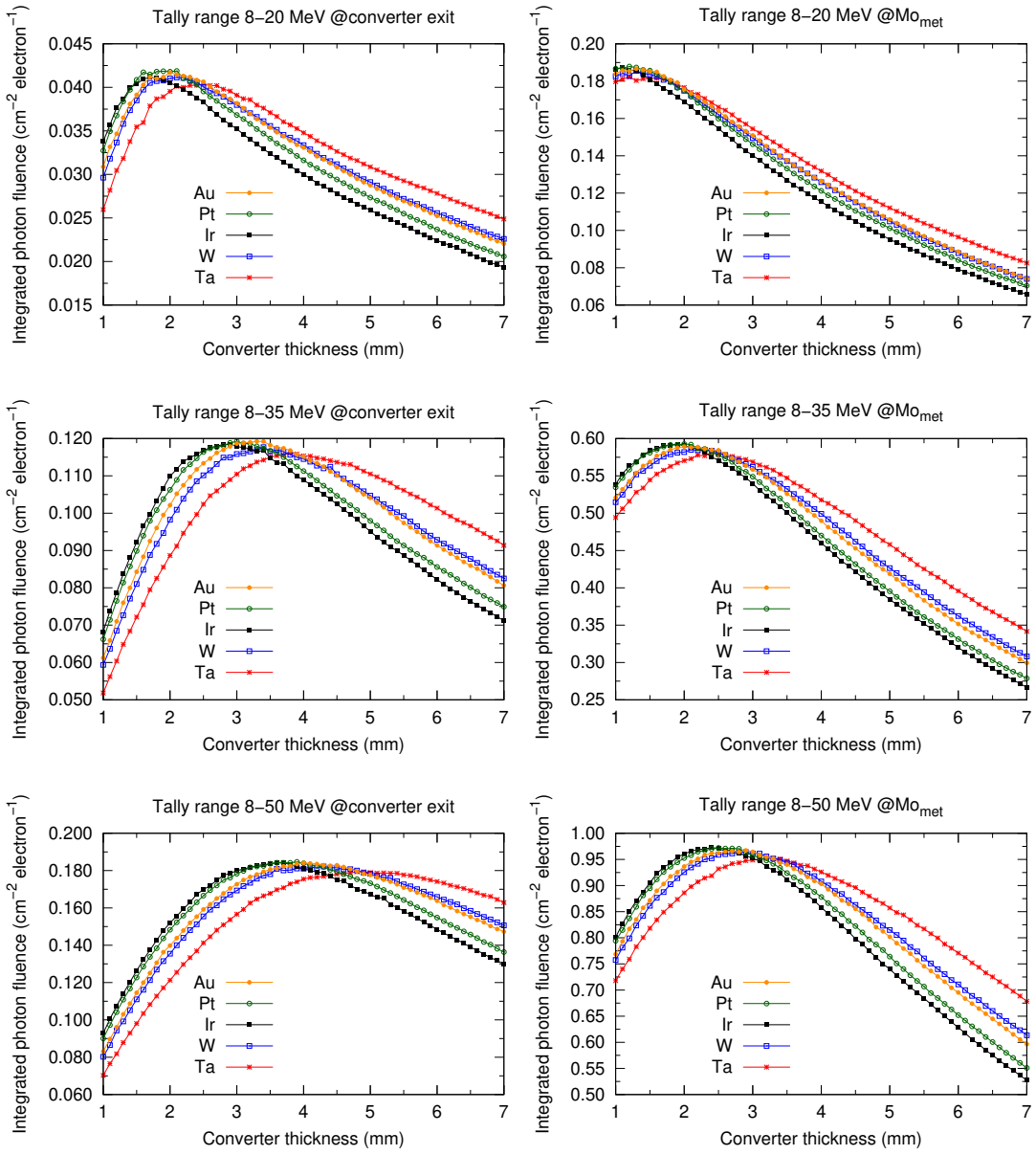

Fig. 4.7. MC photon fluences (left column) at converter exits and (right column) in the associated Mo_{met} targets, integrated over the respective energy ranges. Electron beams of 3 mm in *xy*-FWHM were transported for 10^5 times using PHITS v3.02, EGS5, and `phitar`. The electron beam energies were (top row) 20 MeV, (middle row) 35 MeV, and (bottom row) 50 MeV. The distances between converters and Mo_{met} targets were 1.3 mm.

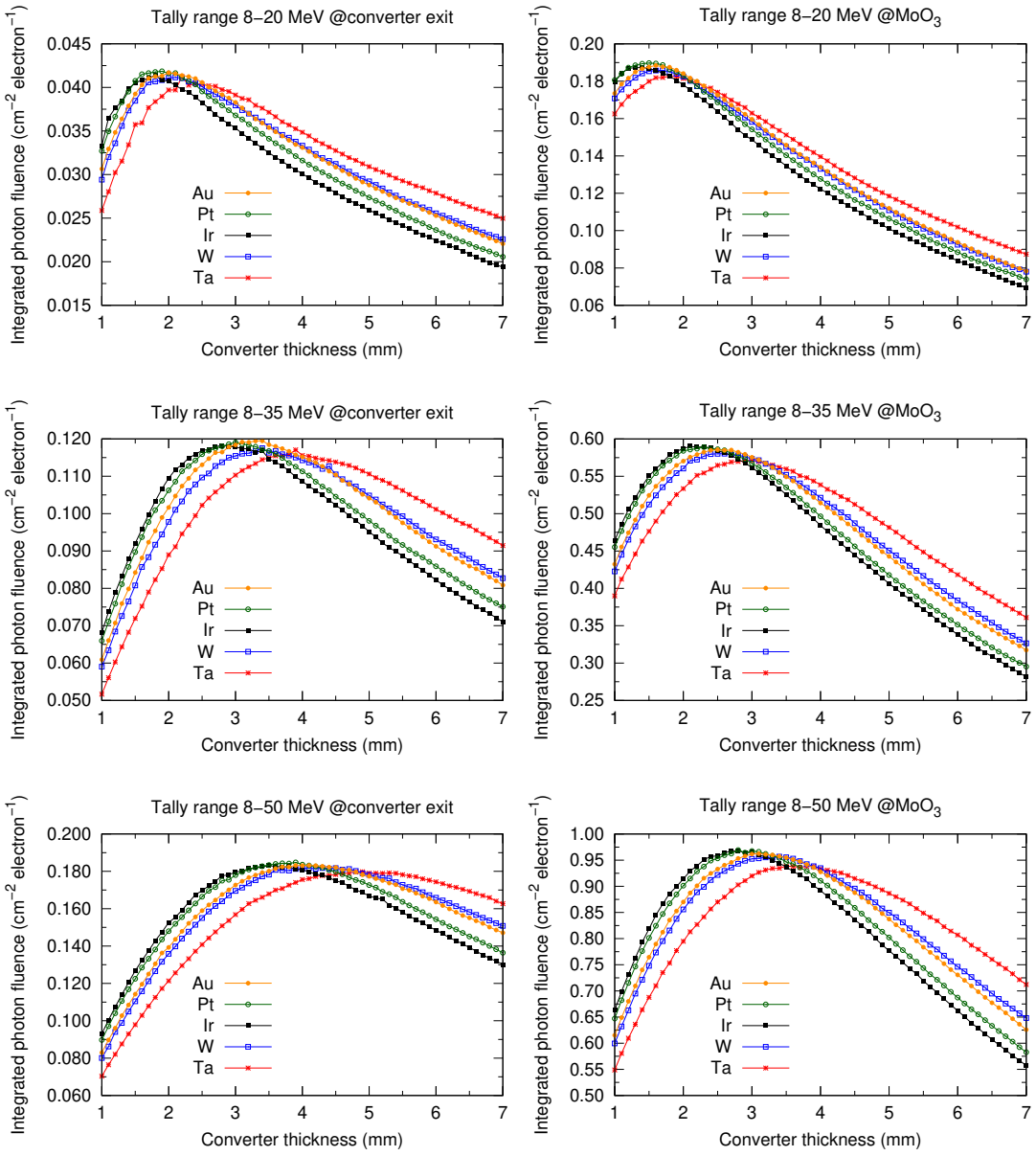

Fig. 4.8. MC photon fluences (left column) at converter exits and (right column) in the associated MoO_3 targets, integrated over the respective energy ranges. Electron beams of 3 mm in *xy*-FWHM were transported for 10^5 times using PHITS v3.02, EGS5, and `phitar`. The electron beam energies were (top row) 20 MeV, (middle row) 35 MeV, and (bottom row) 50 MeV. The distances between converters and MoO_3 targets were 1.3 mm.

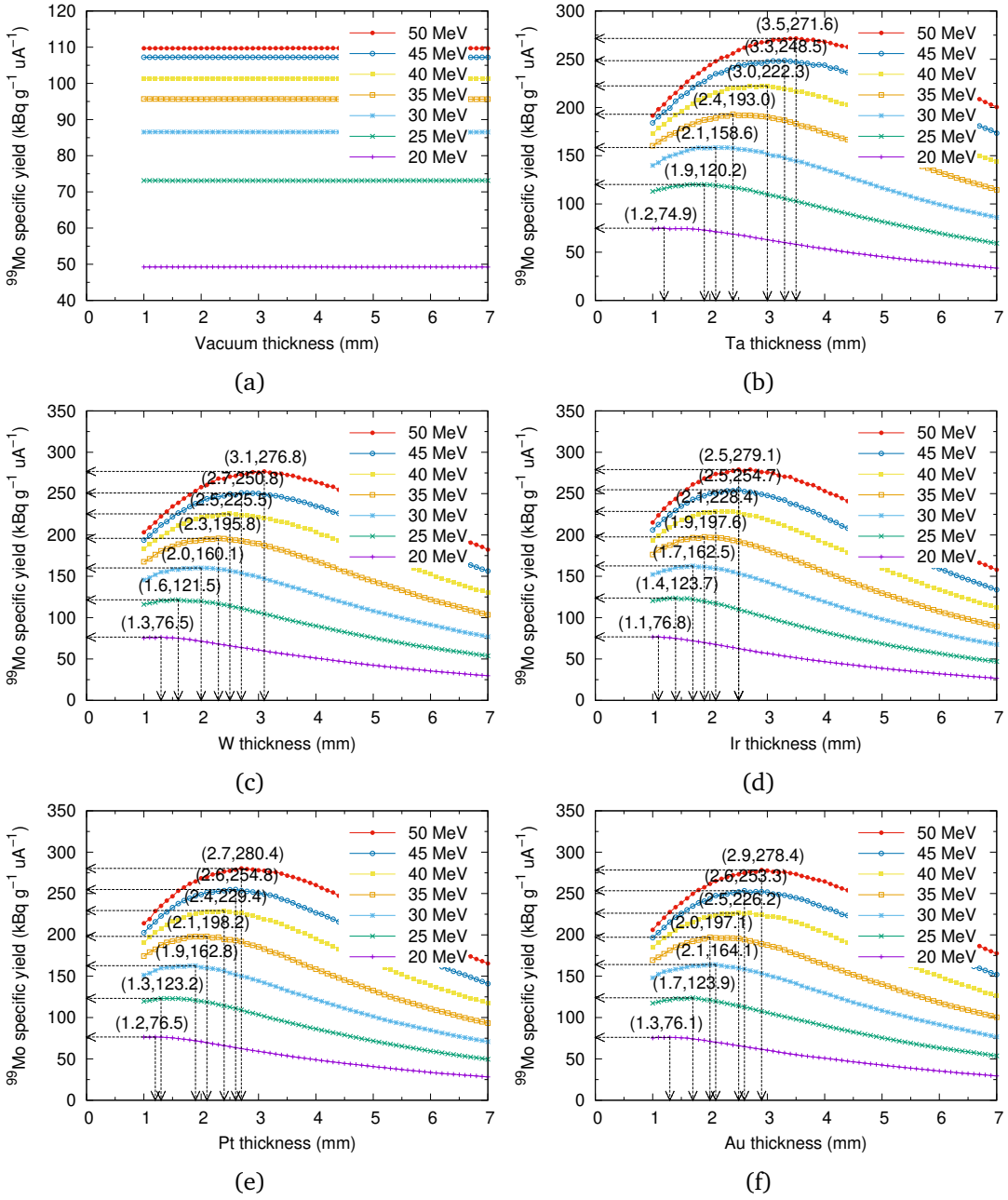

Fig. 4.9. ^{99}Mo yields of *nonenriched* Mo_{met} calculated using `phitar` for (a) void, (b) Ta, (c) W, (d) Pt, (e) Ir, and (f) Au converters. The distances between converters and Mo_{met} targets were 1.3 mm. The photon fluences in Mo_{met} targets were obtained using PHITS v3.02, EGS5, and `phitar`; electron beams having transverse beam size of 3 mm in FWHM were transported for 10^5 times. The ^{100}Mo(γ,n)^{99}Mo excitation function contained in the TENDL-2015 nuclear data library[24] was used for the yield calculation. The irradiation time was set to be 10 min.

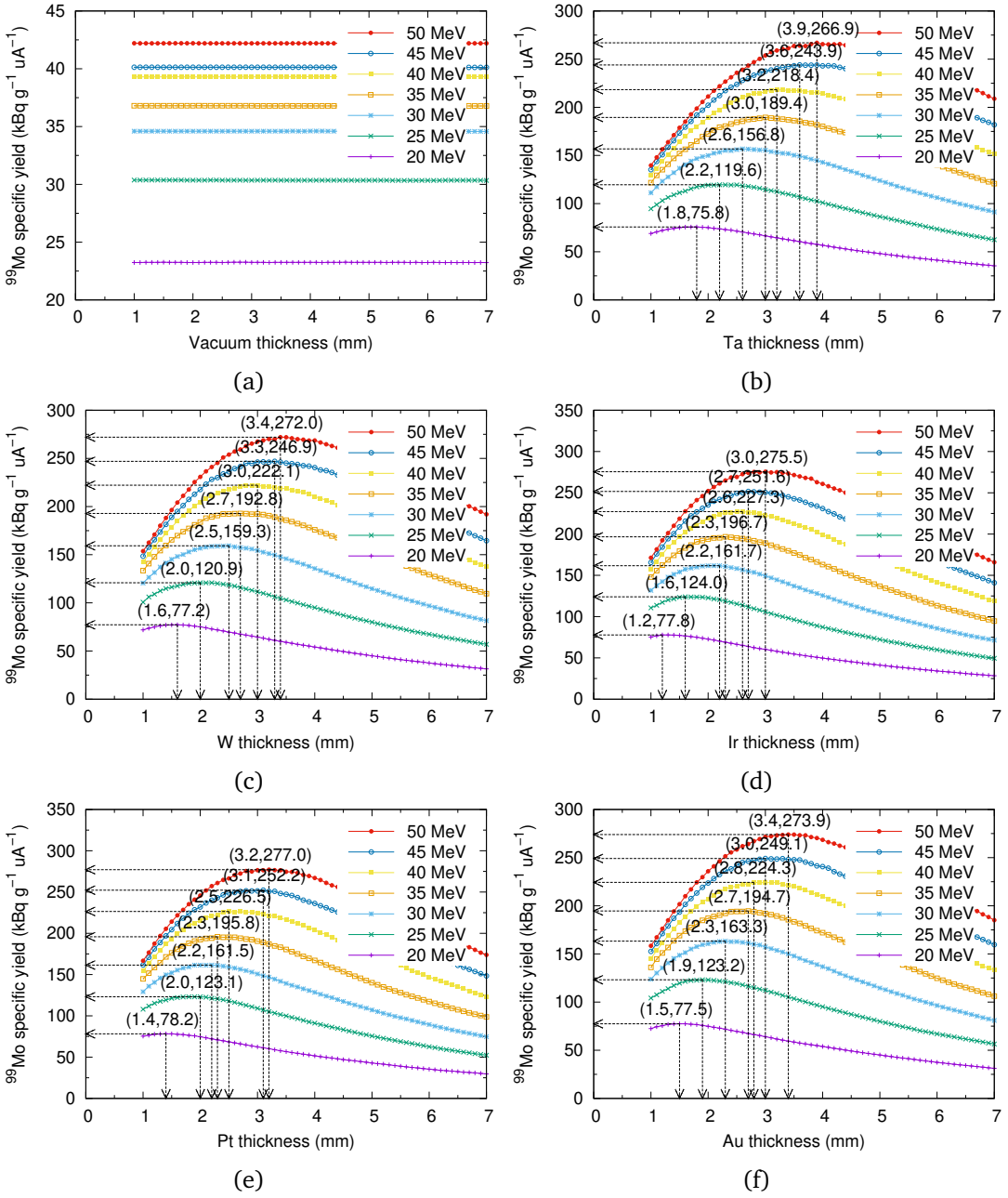

Fig. 4.10. ^{99}Mo yields of *nonenriched* MoO_3 calculated using `phitar` for (a) void, (b) Ta, (c) W, (d) Pt, (e) Ir, and (f) Au converters. The distances between converters and MoO_3 targets were 1.3 mm. The photon fluences in MoO_3 targets were obtained using PHITS v3.02, EGS5, and `phitar`; electron beams having transverse beam size of 3 mm in FWHM were transported for 10^5 times. The ^{100}Mo(γ,n)^{99}Mo excitation function contained in the TENDL-2015 nuclear data library was used for the yield calculation. The irradiation time was set to be 10 min.

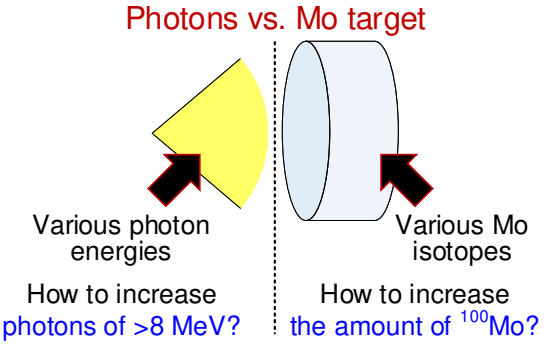

Fig. 4.11. Two aspects of Mo target design.

can be used for this purpose. The other one is from the viewpoint of the Mo target, and is about how to increase the amount of ^{100}Mo isotopes in the Mo target. The natural abundance of ^{100}Mo in naturally occurring Mo is 9.74%[8,96], which can be artificially increased by isotopic enrichment. The topic of ^{100}Mo enrichment encompasses all of the ^{100}Mo(γ,n)^{99}Mo, ^{100}Mo(n,2n)^{99}Mo and ^{100}Mo(p,2n)^{99m}Tc reaction routes, and will be addressed separately in Chap. 6. In this section, we will focus on the aspect of hyperthreshold photon.

4.4.2 Materials options and comparison

Mo_{met} and MoO_3 are the two widely used Mo materials. Because the mass density of Mo_{met} is greater than that of MoO_3 by a factor of $\frac{10.28\,g\,cm^{-3}}{4.69\,g\,cm^{-3}} \approx 2.2$, and because no other element is involved in Mo_{met}, the amount of ^{100}Mo isotopes is greater in Mo_{met} than in MoO_3 by factors of 3.2–3.3 for the same target volume[15]. Therefore, if the ^{99}Mo yield is the primary concern, Mo_{met} can be preferable to MoO_3. Other advantages of using Mo_{met} include its high melting point and high thermal conductivity (Table 4.3). The phase diagram of Mo-O system[97,98], can be useful for understanding the thermal properties of Mo_{met} and MoO_3.

Considering the postirradiation processing, on the other hand, MoO_3 can be useful because of its relatively simple dissolution reaction:

$$MoO_3(s) + 2NaOH(aq) \rightarrow Na_2MoO_4(aq) + H_2O(l). \quad (4.2)$$

[8] J. Meija *et al. Pure Appl. Chem.* **88**, 293–306 (2016).
[96] A. J. Mayer *et al. J. Anal. At. Spectrom.* **29**, 85–94 (2014).
[15] J. Jang *et al. J. Phys. Commun.* **3**, 055015 (2019).
[97] L. Brewer *et al. Bull. Alloy Phase Diagr.* **1**, 85–89 (1980).
[98] F. Predel. In *Phase Equilibria, Crystallographic and Thermodynamic Data of Binary Alloys*, 81–81 (2016).

Table 4.3. Candidate Mo target materials and their properties relevant to ^{99}Mo production [15]. The symbols $\rho_{\text{Mo-mat}}$, ρ_{Mo}, and $\rho_{\text{Mo-100}}$, denote the mass densities of Mo material, Mo element, and ^{100}Mo, respectively. Naturally isotopic composition of Mo is assumed.

Material	T_{m} (K)	T_{b} (K)	$\rho_{\text{Mo-mat}}$ (g cm^{-3})	ρ_{Mo} (g cm^{-3})	$\rho_{\text{Mo-100}}$ (g cm^{-3})
Mo_{met}	2,896	4,912	10.28	10.28	1.043
MoO_3	1,075	1,428	4.69	3.126	0.3173

Because processing irradiated Mo targets is a critical step for ^{99m}Tc extraction and should be as simple and fast as possible, the use of Eq. (4.2) can be a significant advantage in the overall production chain. For this reason, we use MoO_3 as our Mo target material. In the following, we will explore the preparation and dissolution of a MoO_3 target.

4.4.3 PECS for MoO_3 target preparation

MoO_3 targets used for experiments in this dissertation were all prepared using spark plasma sintering (SPS). The actual preparation procedures will be explained in Sec. 5.3.1. Here, we introduce the principle of SPS.

Sintering is a process during which the intergrain pores of a powder compact is shrunken and consolidated by thermal energy, without involvement of liquefaction. Characterized by a rapid heating rate (up to around 1000°C min^{-1}), SPS has been among the most effective sintering techniques[99,100]. SPS passes a pulsed direct current (DC) to a graphite die, inside which a powder specimen is placed and across which a uniaxial pressure is applied simultaneously[100]. Because of the Joule heating provided by the on-off DC, the specimen can be sintered at a rapid rate under a low temperature[99]. For example, a MoO_3 compact can be sintered at around 550°C in less than 10 min[48,55].

The long-standing term SPS, however, may be a misnomer: Hulbert and his colleagues[99] experimentally showed that at the typical operating voltage of SPS ($\leq$5 V), none of plasma, spark, or arc is observed. Some researchers have therefore begun referring to the SPS method using its alternative names, such as the field-assisted sintering technique (FAST)[101] and PECS[100]. In this dissertation, we will use the

[99] D. M. Hulbert *et al. J. Appl. Phys.* **104**, 033305 (2008).
[100] Z. A. Munir *et al. J. Mater. Sci.* **41**, 763–777 (2006).
[55] H. Kawamura *et al.* Jpn. Pat. 5569834 (2014).
[101] O. Guillon *et al. Adv. Eng. Mater.* **16**, 830–849 (2014).

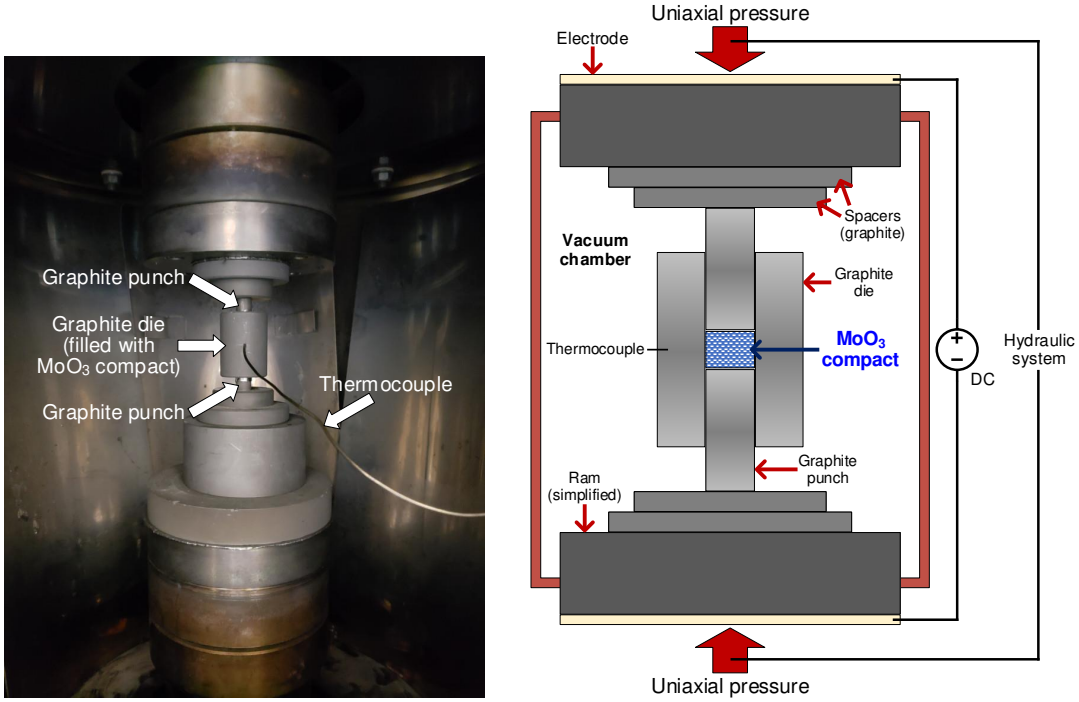

(a) (b)

Fig. 4.12. (a) An interior view of a commercial PECS machine (SPS1050, Izumi Technology, Japan) and (b) its cutaway illustration.

term PECS, as we find it more self-explanatory. The interior view of a PECS machine and its cutaway illustration are shown in Figs. 4.12(a) and 4.12(b), respectively.

4.4.4 Experimental MoO_3 dissolution and titration

The dissolution of MoO_3(s) in NaOH(aq), or Eq. (4.2), is essentially an acid-base reaction[86], a weak acid-strong base reaction in particular. In order to examine the acid-base reaction property of Eq. (4.2), we dissolved MoO_3(s) and titrated its solution in the following order (Fig. 4.13).

① 2.88 g, or $\frac{2.88\,\mathrm{g}}{143.94\,\mathrm{g\,mol^{-1}}} \approx 20.0$ mmol, of MoO_3(s) was put into a 300-mL beaker.

② To make the MoO_3(s) a liquid analyte for titration, 100 mL of distilled water was added into the beaker. As a result, a small fraction of the MoO_3(s) was hydrated in the form of molybdic acid ($H_2MoO_4{\cdot}H_2O$), and the liquid became a mixture of $H_2MoO_4{\cdot}H_2O$, MoO_3(s), and H_2O(l). The pH of the mixture was measured using a pH meter.

[86] K. Tatenuma *et al.* *RADIOISOTOPES* **63**, 501–513 (2014).

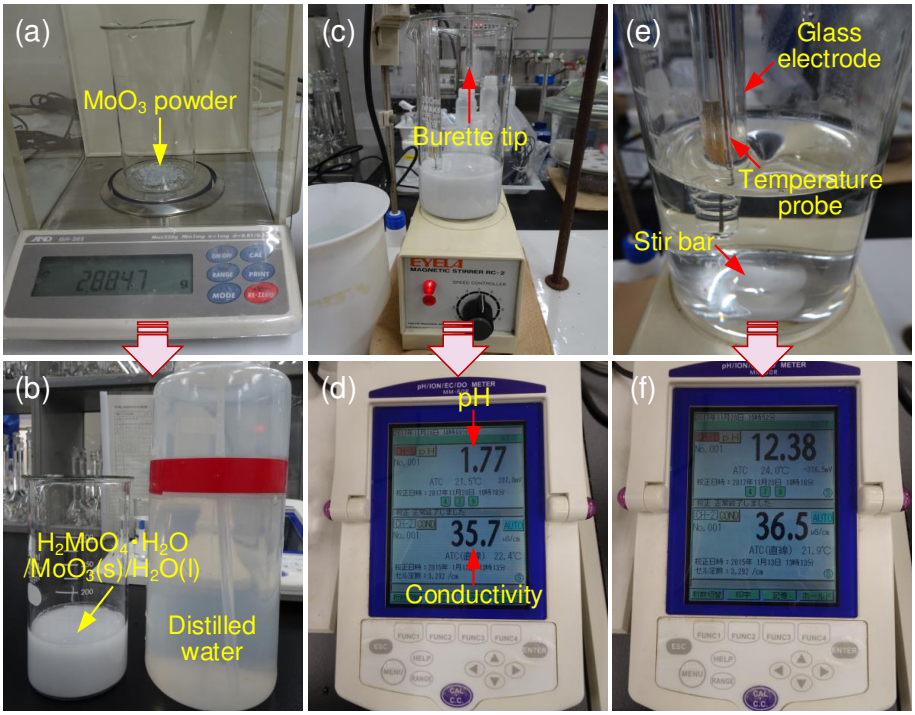

Fig. 4.13. Titration of MoO_4^{2-} using 1.00-*M* NaOH(aq). (a) Weighing MoO_3 powder (the scale indicates 2.8847 g). (b) A mixture of $H_2MoO_4{\cdot}H_2O$, MoO_3(s), and H_2O(l), resulting from the MoO_3 powder mixed with 100-mL distilled water. (c) The mixture placed on a magnetic stirrer before titration and (d) its pH, 1.77. (e) A Na_2MoO_4(aq) solution resulting from the complete dissolution of the MoO_3 powder and (f) its pH, 12.38 (past the equivalence point).

③ A 1.00-*M* NaOH(aq) titrant was prepared by dissolving 4.00 g, or $\frac{4.00\,\text{g}}{40.0\,\text{g mol}^{-1}} \approx$ 100 mmol, of NaOH(s) in 100-mL distilled water.

④ 40.0 mL of the 1.00-*M* NaOH(aq) titrant, or 40.0 mmol of NaOH(aq), was added to the beaker (see Eq. (4.2) and the step (i) above) at intervals of 0.25–2.00 mL. The time intervals between titrant additions were 2–3 min, during which the mixture was stirred by a magnetic stirrer to speed up the dissolution reaction.

The MoO_3 dissolution and titration was performed two times, the results of which are plotted in Fig. 4.14. By simple visual inspection, the pH at the stoichiometric or equivalence point was found to be 9.18, and the corresponding titrant volume was between 41.25 mL and 41.50 mL. This is in accordance with the characteristics of a weak acid-strong base titration[102]:

[102] S. S. Zumdahl *et al.* *Chemistry*. 9th ed. (2014).

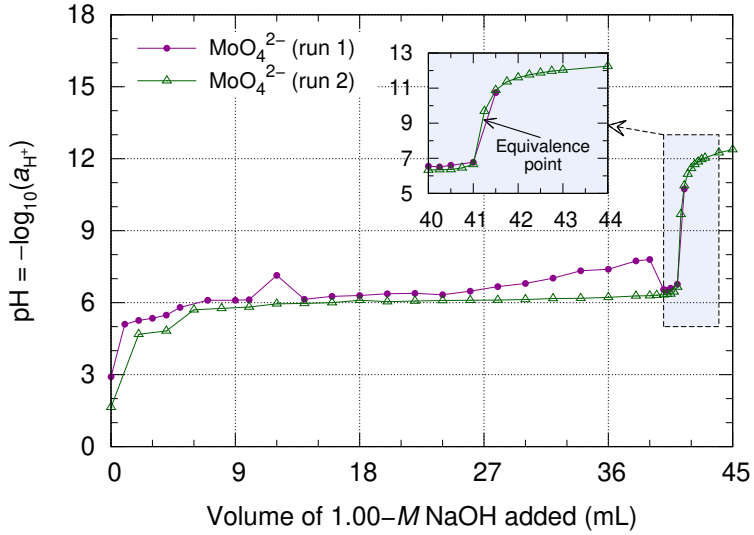

Fig. 4.14. Experimentally obtained titration curves of $MoO_4{}^{2-}$.

(1) The pH increases at a rapid rate at the beginning of titration, but is slowed down near the halfway point because of the buffering effect.
(2) The pH at the equivalence point is greater than 7 at room temperature (25°C). This property is distinguished from that of a strong acid-strong base reaction, where the pH at the equivalence point is 7 at room temperature. Also, the vertical line at around the equivalence point of a weak acid-strong base reaction is relatively short compared with that of a strong acid-strong base reaction.

The two characteristics can be observed in Fig. 4.14.

4.5 Summary

Parametric analyses of integrated and separated targetry showed that depending on their geometries, either of them can results in a higher ^{99}Mo specific activity. Therefore, other factors should be considered to compare the two target systems. For instance, a separate target system can alleviate the heat load and radiation damage of the Mo target.

The period 6 transition metals were compared as candidate converter materials. MC calculations showed that the amount of bremsstrahlung generation does not differ between the converter materials. We therefore compared the thermal properties and market prices of the candidate metals, and found that W can be suitable for ^{99}Mo production.

Two chemical forms of Mo are most widely used as Mo targets: Mo_{met} and MoO_3.

The advantages of using Mo_{met} is its higher melting point, higher thermal conductivity, and higher mass density. MoO_3, on the other hand, can be useful considering the postirradiation target dissolution. MoO_3 targets can be prepared using PECS, and can be dissolved using NaOH(aq). We experimentally confirmed that the MoO_3 dissolution reaction (Eq. (4.2)) is a weak acid-strong base reaction.

The next chapter will address detailed parametric analysis of W converter thicknesses and its experimental validation.

4.6 Acknowledgment

We are grateful to Dr. Tatenuma (Kaken) for guiding the MoO_3 dissolution experiments.

Chapter
5

Optimal converter thicknesses

Abstract

The converter thickness is one of the most important parameters which affect the ^{99}Mo production yield. In order to find the optimal converter thicknesses for ^{99}Mo production, we performed MC simulations and analyzed the results. The results were subsequently validated by irradiation experiments.

5.1 Overview

From the perspective of ^{99}Mo production, the bremsstrahlung efficiency can be defined as the amount of hyperthreshold photons interacting with a Mo target divided by the amount of electrons entering a converter (Fig. 5.1). A high bremsstrahlung efficiency, and thereby a high ^{99}Mo yield, (Eq. (3.5)) can be achieved when the sum of

(i) the amount of hyperthreshold photons generated at and leaving the converter (the "primary" photons) and

(ii) the amount of hyperthreshold photons generated at and remaining in the Mo target (the "secondary" photons)

is increased for given electron beams.

To quantitatively express the above claim, we label a photon fluence with its generated and measured regions:

$$\Phi_{\text{gen}\to\text{meas}}(E_\gamma).$$

The photon fluence in a Mo target can then be written as

$$\Phi_{\text{Mo-tar}}(E_\gamma) = \Phi_{\text{conv}\to\text{Mo-tar}}(E_\gamma) + \Phi_{\text{Mo-tar}\to\text{Mo-tar}}(E_\gamma). \tag{5.1}$$

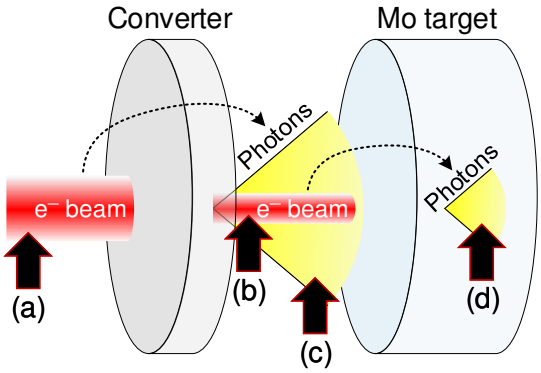

Fig. 5.1. Electron interaction with targetry materials and the resulting photon generation. (a) Electrons entering a converter; (b) electrons passing through the converter; (c) photons generated from (a) and entering a Mo target; and (d) photons generated from (b) and remaining in the Mo target. The bremsstrahlung efficiency can then be given by $\frac{(c)+(d)}{(a)}$.

Integrating Eq. (5.1) over $E_\gamma \geq E_{\gamma,\mathrm{th}}$, we obtain the total fluence of hyperthreshold photons in the Mo target:

$$\Gamma_{\text{Mo-tar}} \equiv \int_{E_{\gamma,\mathrm{th}}}^{\infty} \Phi_{\text{conv}\to\text{Mo-tar}}(E_\gamma)\,\mathrm{d}E_\gamma + \int_{E_{\gamma,\mathrm{th}}}^{\infty} \Phi_{\text{Mo-tar}\to\text{Mo-tar}}(E_\gamma)\,\mathrm{d}E_\gamma. \tag{5.2}$$

Parameters largely affecting Eq. (5.2) are the electron beam energy and converter thickness. The distance between a converter and a Mo target is also an important parameter, but its modification is often limited by the cooling system[43]. On the other hand, the influence of beam size on the bremsstrahlung efficiency becomes more important with an increasing intertarget distance.

In order to quantify the dependence of ^{99}Mo yield on the converter thickness, we performed a series of MC simulations using `phitar` (Sec. 2.2). This section is devoted to the parametric analysis of converter thicknesses and its experimental validation.

5.2 MC simulations via `phitar`

A series of MC simulations similar to that of Sec. 4.3.2 was performed using PHITS v3.02[59], EGS5[82], and `phitar` (Sec. 2.2), with a different beam size and different intertarget distance used. Namely, the transverse beam size in this section was 4.5 mm in FWHM, and the intertarget distance was 13 mm. The 13-mm distance was the

[43] B. Szpunar *et al. Nucl. Instrum. Methods Phys. Res. A* **729**, 41–50 (2013).
[59] T. Sato *et al. J. Nucl. Sci. Technol.* **55**, 684–690 (2018).
[82] H. Hirayama *et al. The* EGS5 *code system* (2005).

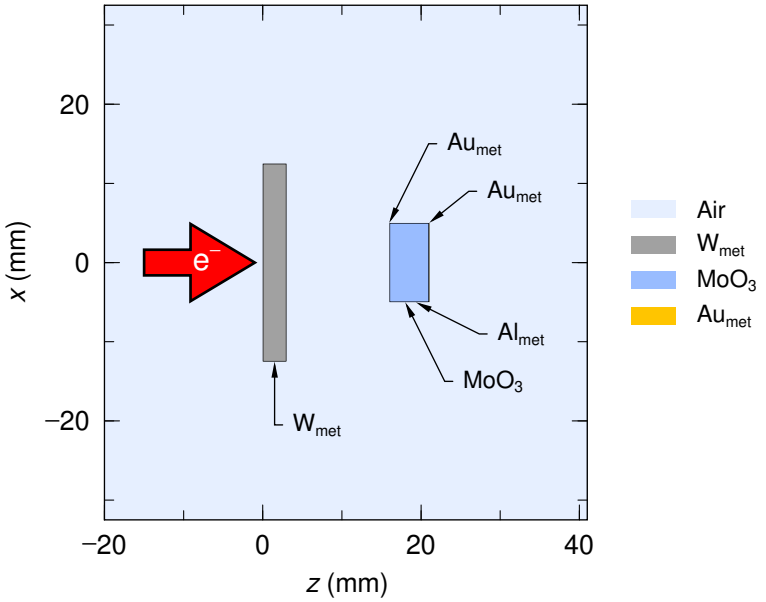

Fig. 5.2. A targetry configuration to be used in experiments.

intertarget distance of the target holder used for experiments. In addition, the MoO_3 target was now wrapped with a 12-μm thick Al foil, and 50-μm thick Au foils were placed at the front and back surfaces of the MoO_3 target for measuring the photon flux (Fig. 5.2). As with the intertarget distance, this Mo target setup was the one we planned to use in experiments.

Parts of the particle tracking results of different W thicknesses are presented in Figs. 5.3 and 5.4, which provide a qualitative understanding of the dependence of photon distributions on the W thickness. On the other hand, the quantitative fluence variations with W thicknesses are presented in Fig. 5.5, and the resulting ^{99}Mo yields are plotted in Fig. 5.6.

As shown in Eq. (3.5), it is the product of $\Phi_{\text{Mo-tar}}(E_\gamma)$ and $\Sigma(E_\gamma)$ integrated over $E_\gamma \geq E_{\gamma,\text{th}}$ that will represent the total number of ^{100}Mo(γ,n)^{99}Mo reactions taken place, or

$$N_{\text{Mo-99@Mo-tar}} = \int_{E_{\gamma,\text{th}}}^{\infty} \Phi_{\text{Mo-tar}}(E_\gamma)\Sigma(E_\gamma)\,\mathrm{d}E_\gamma. \tag{5.3}$$

A question then arises as to whether Eq. (5.2), instead of Eq. (5.3), can represent the dependence of ^{99}Mo yield on the converter thickness. This question can be answered by analyzing Figs. 5.5(d) and 5.7, the former of which plots Eq. (5.2) for $E_{e^-} = 35$ MeV and MoO_3 and the latter of which plots Eq. (5.3) under the same conditions.

Fig. 5.7 shows that the greatest $N_{\text{Mo-99@MoO}_3}$, or 2.75×10^{-5} cm^{-3} electron^{-1}, is

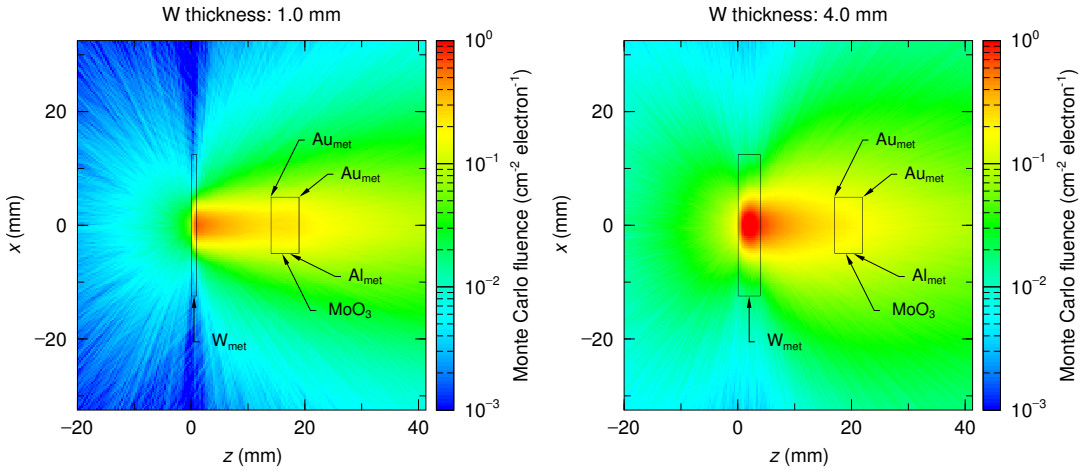

(a) (b)

Fig. 5.3. Photon tracks calculated for (a) 1-mm and (b) 4-mm thick W converters. The energy and transverse size of electron beams were 20 MeV and 4.5 mm in FWHM, respectively.

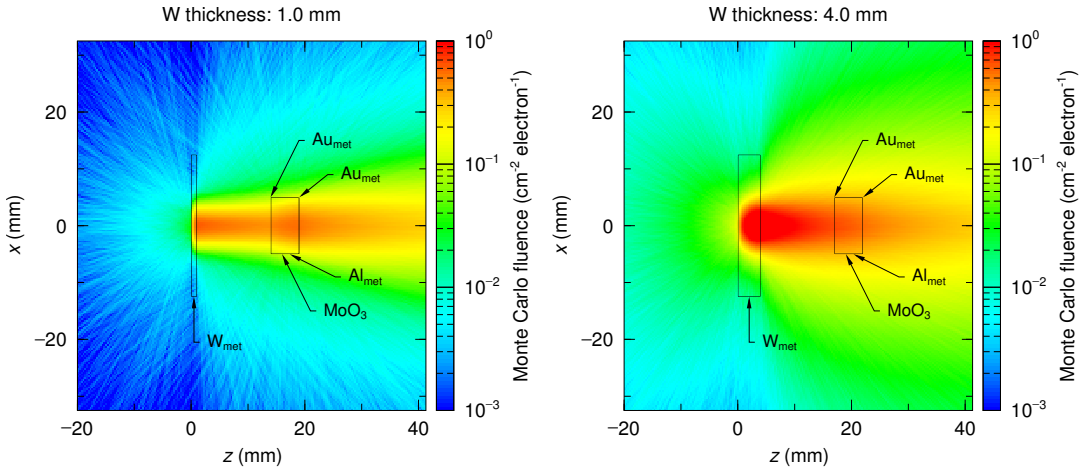

(a) (b)

Fig. 5.4. Photon tracks calculated for (a) 1-mm and (b) 4-mm thick W converters. The energy and transverse size of electron beams were 50 MeV and 4.5 mm in FWHM, respectively.

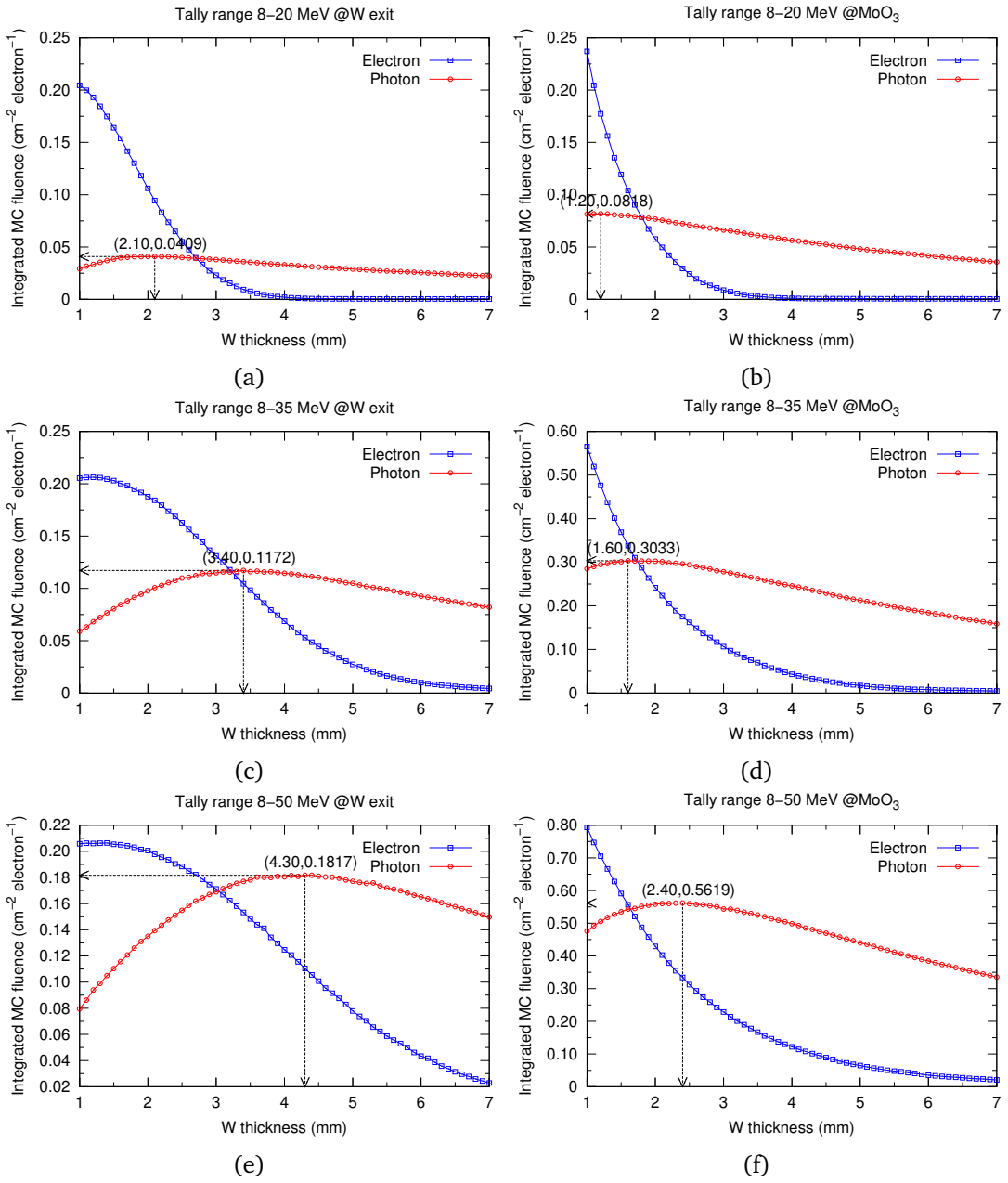

Fig. 5.5. Integrated particle fluences measured at (left column) W exits and in (right column) MoO_3 targets. The intertarget distances were 13 mm. Incident electron beam energies were (top row) 20 MeV, (middle row) 35 MeV, and (bottom row) 50 MeV. PHITS v3.02, EGS5, and `phitar` were used for the calculations. Electron beams having transverse sizes of 4.5 mm in FWHM were transported for 10^5 times.

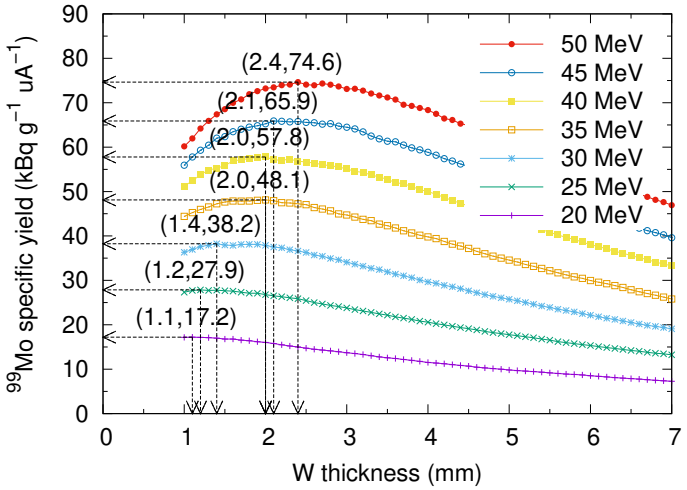

Fig. 5.6. ^{99}Mo yields of nonenriched MoO_3 calculated for W converters of different thicknesses. The photon fluences in MoO_3 targets were obtained using PHITS v3.02, EGS5, and `phitar`. The intertarget distance was 13 mm, and the transverse electron beam size was 4.5 mm in FWHM. The ^{100}Mo(γ,n)^{99}Mo excitation function was retrieved from the TENDL-2015 nuclear data library [24]. The irradiation time was set to be 5 min.

found at $t_W = 2$ mm. On the other hand, Fig. 5.5(d) shows that the greatest Γ_{MoO_3} is obtained at $t_W = 1.6$ mm. Although they are not exactly the same, the plateau of Γ_{MoO_3} in Fig. 5.5(d) implies that the fluence does not vary around $t_W = 2.0$ mm. On top of that, the t_W at which Γ_{MoO_3} is maximized in Figs. 5.5(b) and 5.5(f) are almost the same as those in Fig. 5.6. Therefore, Eq. (5.2), which is much simpler than Eq. (5.3), can represent the approximate dependence of ^{99}Mo yield on the parameter. Still, however, the ^{99}Mo/^{99m}Tc activities must always be calculated from Eq. (5.3), not from Eq. (5.2).

In order to validate the findings of Fig. 5.6, we conducted irradiation experiments using W converters.

5.3 Experimental validation

5.3.1 Materials

Target holder

To enable converter thickness adjustments, an order-made target holder was purchased (Mimasu, Japan), shown in Figs. 5.8 and 5.9. Converter thicknesses could be adjusted

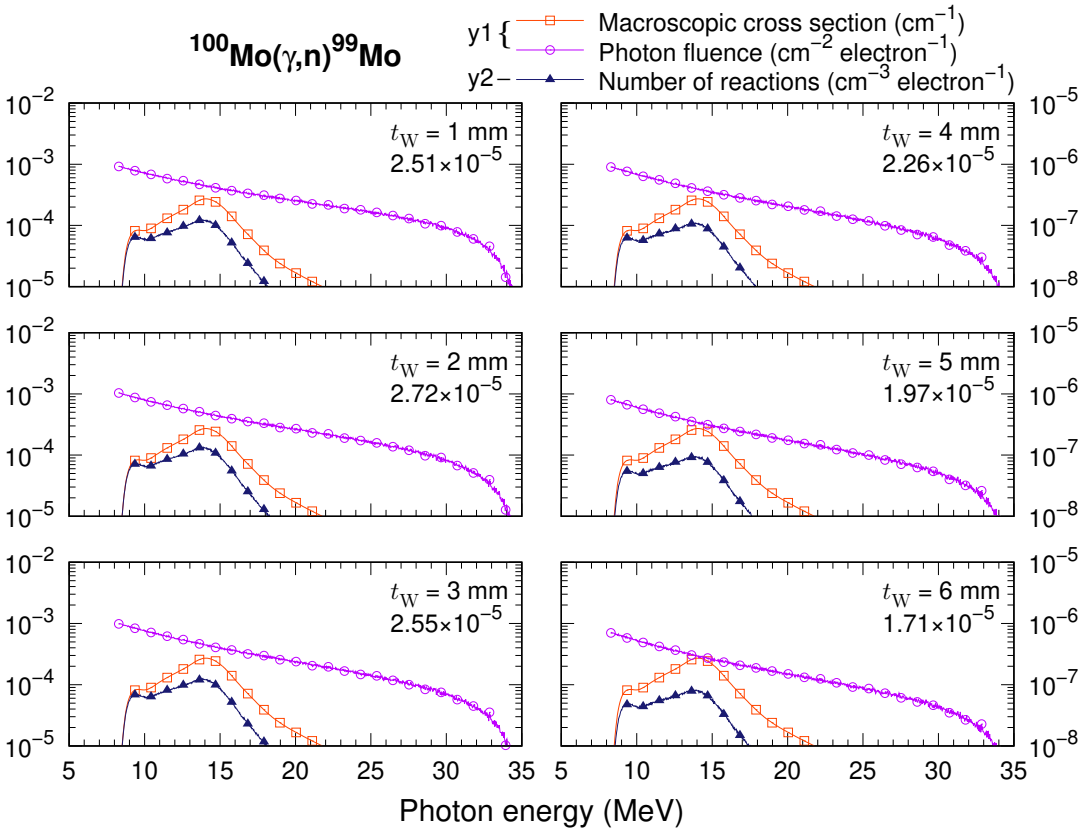

Fig. 5.7. Eq. (5.3) calculated for electron beam energy $E_{e^-} = 35$ MeV and W thicknesses $t_W = 1$–6 mm. The numbers under t_W are the calculation results. $\Phi_{MoO_3}(E_\gamma)$ and $\Sigma(E_\gamma)$ are associated with the left-y axis (y1), and their products with the right-y axis (y2).

by placing converters of different thicknesses as a whole against the backrest. The backrest was 3 mm in thickness and its distance to the MoO_3 target saddle was 10 mm, effectively resulting in an intertarget distance of 13 mm (Figs. 5.2 and 5.8).

W converters

W plates having nominal thicknesses of 0.5–2.0 mm were purchased (>99.9% purity, nominal area 50 mm × 50 mm, Nilaco Corp., Japan), shown in Fig. 5.10(a). The W plates were then weighed, and the actual dimensions were measured. Table 5.1 tabulates the resulting density ratios (Eq. (2.2)), which were used in MC simulations rerun with respect to experimental conditions. The desired W thickness was obtained by stacking the W plates.

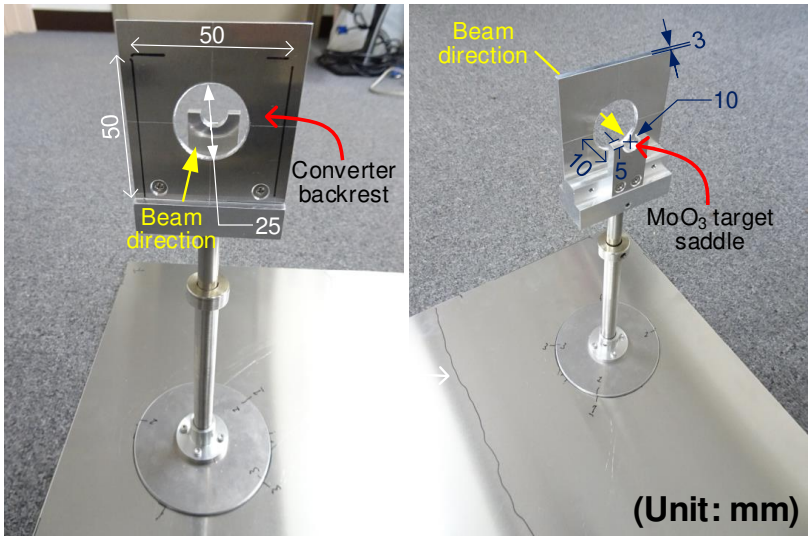

Fig. 5.8. An order-made target holder. The converter backrest is the plane against which a stack of converters leans. The MoO_3 target saddle is a support on which a MoO_3 target is put.

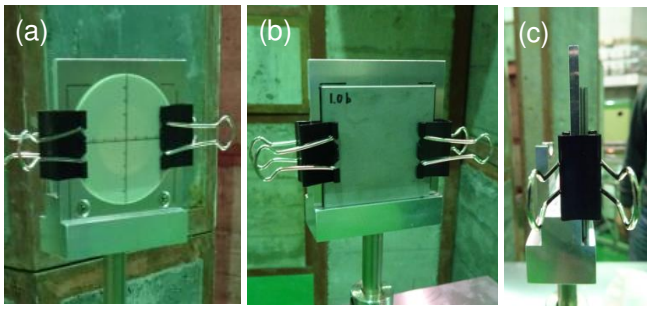

Fig. 5.9. The target holder (a) loaded with a BeO fluorescent screen, and (b) loaded with a set of W converters and (c) its side view.

MoO_3 targets

The MoO_3 targets were prepared by sintering *nonenriched* MoO_3 powder (99.99% purity, Kojundo Chemical Laboratory Co., Ltd., Japan) using a PECS machine (Sec. 4.4.3) at Kaken Inc., Hokota, Japan.

The target preparation process is shown in Fig. 5.11. The goal diameter and thickness of a MoO_3 target were 10 mm and 5 mm, respectively. When graphite sheets were removed from the surface of a MoO_3 target using sandpaper, a portion of the MoO_3 mass was unavoidably lost. As a result, the diameter and thickness of a MoO_3 target differed from their intended values. The resulting masses and volumes of the prepared MoO_3 targets are shown in Table 5.2. On the other hand, the density ratios of

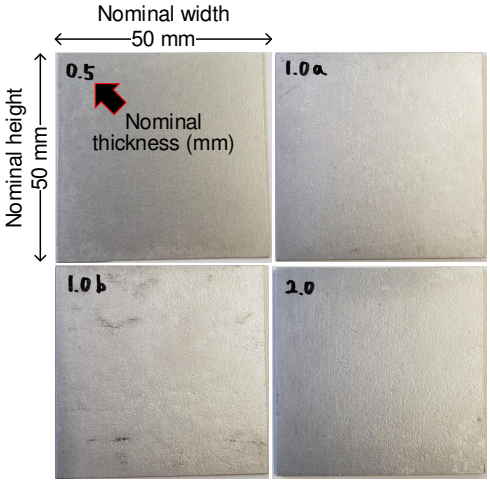

(a)

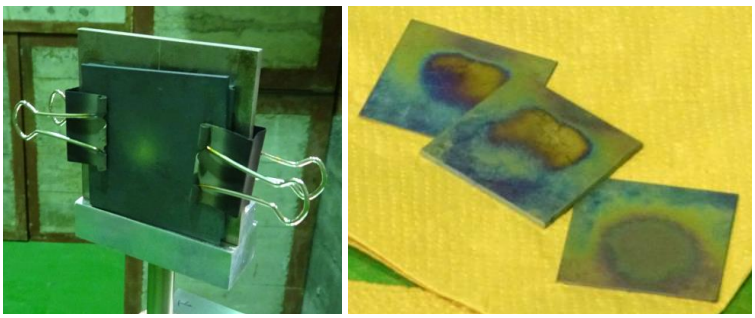

(b)

Fig. 5.10. (a) W plates of 0.5, 1.0, and 2.0 mm in nominal thickness. The nominal widths and heights were 50 mm and 50 mm, respectively. (b) W plates after irradiated by electron beams.

MoO_3 targets, which were primarily determined by their sintering efficiencies, ranged from 0.835 to 0.916. Later on, the density ratios of the MoO_3 targets were used in MC simulations rerun with respect to experimental conditions.

Au foils

In irradiation experiments using electron linacs, Au foils are often used to measure the photon flux via the ^{197}Au(γ,n)^{196}Au reaction (Fig. C.5). In our experiments, Au foils were used as a supplement to the MoO_3 targets: because the natural abundance of ^{197}Au is 100% and the excitation function for the ^{197}Au(γ,n)^{196}Au reaction is well defined, the activities of ^{196}Au could be use to assess the photon fluence and flux at the front and back surfaces of a MoO_3 target.

Table 5.1. W converters used for the irradiation (Irr.) experiments.

Energy (MeV)	Irr. No.	Combination[1]	Thickness[2](mm)	Density ratio[3]
	1	0.5	0.45	0.9565
20	2	0.5 + 1.0a	1.48	0.9683
	3	0.5 + 1.0a + 1.0b	2.53	0.9721
	4	0.5 + 1.0a	1.48	0.9683
35	5	0.5 + 2.0	2.58	0.9687
	6	0.5 + 2.0 + 1.0a	3.61	0.9725
	7	2.0	2.13	0.9809
50	8	2.0 + 1.0a	3.16	0.9805
	9	2.0 + 1.0a + 1.0b	4.21	0.9803

[1] The numbers in this column represent nominal thicknesses expressed in mm.
[2] The actual thicknesses measured using vernier calipers (0.01-mm precision).
[3] The ratio to the material density of W, 19.25 g cm^{-3}.

Table 5.2. MoO_3 targets used for the irradiation (Irr.) experiments.

Energy (MeV)	Irr. No.	Target No.	Mass (g)	Volume (cm^3)	Density ratio[1]
	1	181213-1	1.6216	0.3941	0.8773
20	2	181213-2	1.6146	0.3975	0.8661
	3	181213-3	1.6382	0.3961	0.8819
	4	181213-4	1.6309	0.3866	0.8994
35	5	181213-5	1.6294	0.3819	0.9096
	6	181213-6	1.5862	0.3783	0.8940
	7	181213-7	1.5979	0.3721	0.9157
50	8	181213-8	1.5771	0.3754	0.8958
	9	181213-9	1.4366	0.3669	0.8348

[1] The ratio to the material density of MoO_3, 4.69 g cm^{-3}.

A 50-μm thick Au foil was purchased (>99.9% purity, 50 mm × 50 mm, Nilaco Corp., Japan) and cut into circular foils of 10 mm in diameter (Fig. 5.12) using a high-precision handheld punch cutter (Nogamigiken Co., Ltd., Japan). Subsequently, the circular Au foils were weighed and their density ratios were calculated (Table 5.3). The density ratios of the Au foils were later used in MC simulations rerun with respect to experimental conditions.

Wrapping a MoO_3 target with a pair of Au foils

Finally, the MoO_3 targets were held together with pairs of Au foils using 12-μm thick Al foils (Fig. 5.13). This Al foil was thin enough to ignore its interactions with the

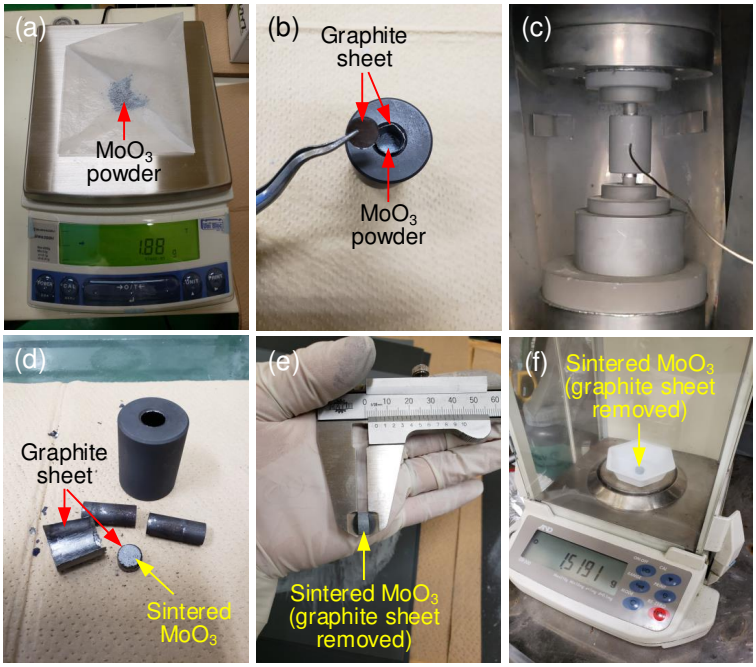

Fig. 5.11. MoO_3 preparation using PECS. (a) Weighing MoO_3 powder (the scale indicates 1.88 g). (b) Loading the MoO_3 powder wrapped with graphite sheets into a graphite die. (c) Sintering the MoO_3 compact using a PECS machine (see Fig. 4.12 for details). (d) Sintered MoO_3 prior to removal of the graphite sheets. (e) Measuring the dimensions of the MoO_3 target (with the graphite sheet removed, MoO_3 can now be called a MoO_3 target). (f) Weighing the MoO_3 target (the scale indicates 1.5191 g).

MeV-level incident radiation.

5.3.2 Irradiation

Irradiation was carried out using an S-band high-intensity electron linac at the Research Center for ELectron PHoton Science (ELPH), Tohoku University[103], for nine sets of a beam energy and a W thickness (Table 5.4).

Before beginning the first irradiation run of each beam energy (irradiation numbers 1, 4, and 7 in Table 5.4), the following preprocessing tasks were performed:

① The center of irradiation was adjusted using a BeO fluorescent screen (Fig. 5.9(a) and Fig. 5.14(b)). This was because changing the electron beam energy was accompanied by a change in the irradiation center.

[103] F. Hinode *et al.* In *Proceedings of the 15th Annual Meeting of Particle Accelerator Society of Japan*, 1326–1328 (2018).

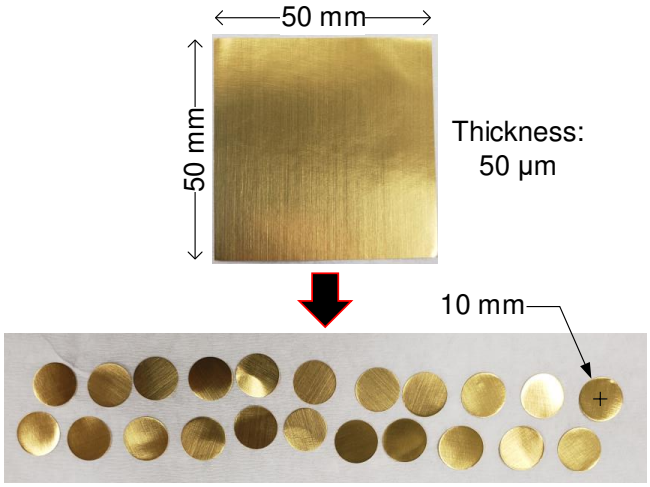

Fig. 5.12. Au foils of 50-μm thickness cut into circular foils of 10 mm in diameter.

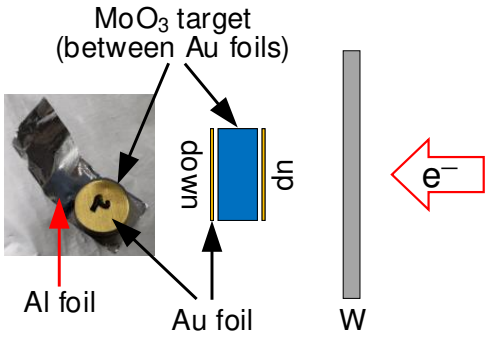

Fig. 5.13. Au foils (shown in Fig. 5.12) and a MoO_3 target (shown in Fig. 5.11) wrapped with a 13-μm thick Al foil.

② The transverse beam profile (σ_h and σ_v) was measured using screen monitors (see Fig. 3.1). Besides, the transverse beam profiles are also reflected in the burnt areas of W plates shown in Fig. 5.10(b).

③ The background beam current was measured, which was later subtracted from the actual beam current.

Fig. 5.14 shows targetry setups at the beam exit of the electron linac. The downstream plane, or the plane through which electron and photon beams exit, was marked with the plus sign (+), so that the Au foils wrapped inside the Al foil could be placed correctly (Fig. 5.13).

Upon completion of the irradiation runs, the [^{99}Mo]MoO_3 targets and [^{196}Au]Au foils were put in a radioisotope storage room to let short-lived radionuclides decay away. Subsequently, the [^{99}Mo]MoO_3 targets were sent to Kaken Inc., Mito, Japan, and the [^{196}Au]Au foils to the Institute for Integrated Radiation and Nuclear Science,

Table 5.3. Au foils used for the irradiation (Irr.) experiments.

Energy (MeV)	Irr. No.	Foil No.	Mass (g)	Density ratio[1]
20	1	1	0.07129	0.9406
		2	0.07094	0.9360
	2	3	0.07179	0.9472
		4	0.07139	0.9419
	3	5	0.07135	0.9414
		6	0.07115	0.9388
35	4	7	0.07150	0.9434
		8	0.07125	0.9401
	5	9	0.07170	0.9460
		10	0.07169	0.9459
	6	11	0.07133	0.9411
		12	0.07105	0.9374
50	7	13	0.07125	0.9401
		14	0.07129	0.9406
	8	15	0.07087	0.9351
		16	0.07131	0.9409
	9	17	0.07150	0.9434
		18	0.07119	0.9393

[1] The ratio to the material density of MoO_3, 19.3 g cm^{-3}.

Kyoto University (KURNS). The gamma rays of the MoO_3 targets and Au foils were then measured using the respective germanium detectors.

5.3.3 Gamma-ray spectrometry

Introduction

Gamma-ray spectrometry can be performed using a semiconductor detector, such as a high-purity germanium detector. The detection efficiency depends on multiple factors, including the shape, size, and position of the radioactive sample and, more importantly, the gamma-ray energies of the involved radionuclides. The dependence of detection efficiency on the gamma-ray energy is represented by a plot called the efficiency curve, which can be obtained using a gamma reference source. Using the efficiency curve, gamma counts summed over a peak area are converted to radioactivity.

On the other hand, the real time of the detector electronics is given by

$$t_{\mathrm{real}} = t_{\mathrm{live}} + t_{\mathrm{dead}},$$

Table 5.4. Irradiation (Irr.) conditions. The symbols σ_h and σ_v denote the horizontal and vertical Gaussian beam sizes, respectively.

Energy (MeV)	Irr. No.	Beam size (mm) σ_h	σ_v	Average beam current (μA)	Irradiation time (min)
	1			15.8±1.7	
20	2	10.8	3.2	15.7±1.4	10
	3			17.1±0.4	
	4			17.7±0.3	
35	5	4.4	4.8	18.1±1.2	5
	6			18.7±0.4	
	7			19.4±0.6	
50	8	4.8	2.5	20.3±0.5	5
	9			20.7±0.5	

where only the live time t_{live} leads to the formation of gamma counts; during the dead time t_{dead}, the input gate to the analog-to-digital converter (ADC) is closed, and the subsequent pulses are not measured[104]. If the activity of a radioactive sample is too high, only t_{dead} increases, and the gamma rays are not counted. In such cases, the activity concentration of the sample should be diluted or should decay for a certain cooling time t_{cool}. A combination of the two methods can also be used.

Measurement of irradiated MoO_3

The activities of MoO_3 targets were measured at Kaken Inc., Mito, Japan, in the following order (Fig. 5.15).

① Each [^{99}Mo]MoO_3 target was put into a preweighted 20-mL vial, to which a 6-*M* NaOH solution was added thereafter. The molar amount of NaOH in each 6-*M* NaOH solution was twice that of the [^{99}Mo]MoO_3 target in question (see Eq. (4.2) and Table 5.5).

② The vials were put on a laboratory hot plate for two hours. The heating temperature was 80°C. The [^{99}Mo]MoO_3 targets were then completely dissolved, resulting in Na_2[^{99}Mo]MoO_4 solutions.

③ Each Na_2[^{99}Mo]MoO_4 solution was diluted with distilled water. The dilution was performed based on the mass; to be specific, the mass of each Na_2[^{99}Mo]MoO_4 solution was adjusted to 10.00 g by adding distilled water.

④ A preweighted U-8 container was filled with 99.00 g of distilled water. As many U-8 containers as the vials were prepared.

[104] G. Gilmore. *Practical Gamma-ray Spectrometry*. 2nd ed. (2008).

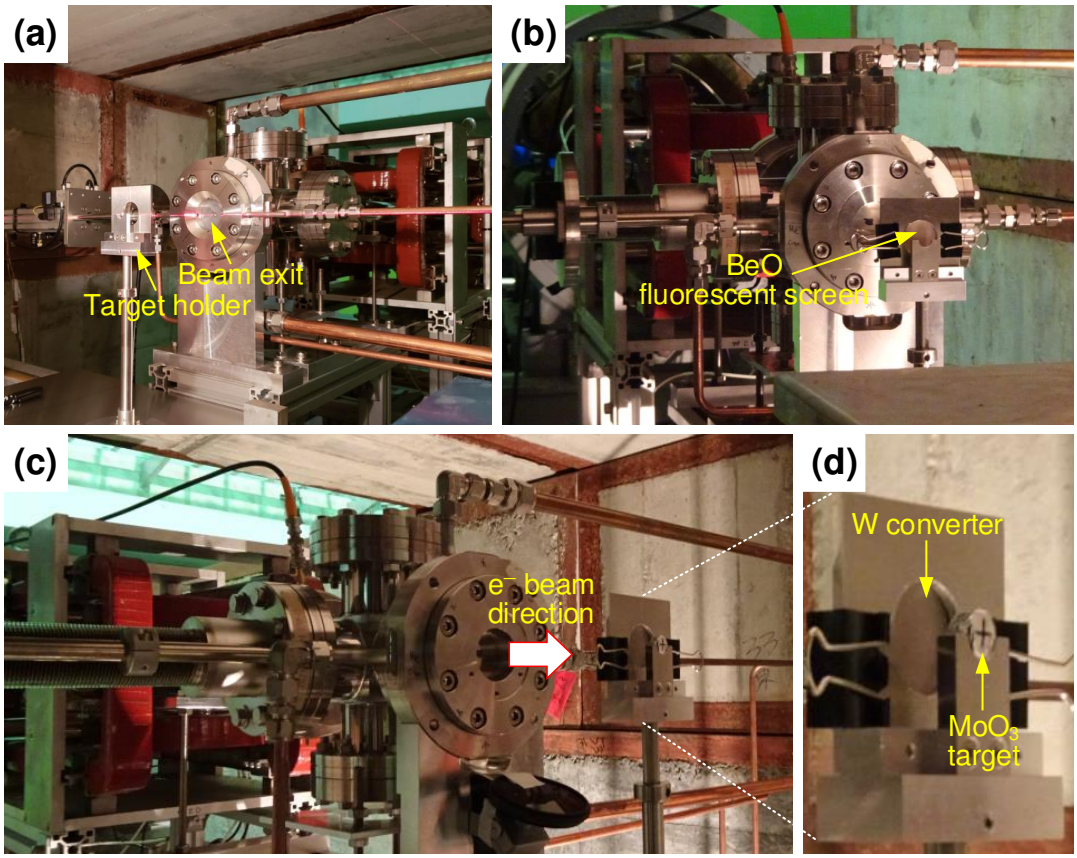

Fig. 5.14. (a) Adjusting the position of the target holder using laser. (b) Adjusting the beam irradiation center using a BeO fluorescent screen placed at the converter position. (c) Targetry set up for irradiation and (d) its enlarged view.

⑤ 1.00 g of each 10.00-g $Na_2[^{99}Mo]MoO_4$ solution obtained in ③ above, effectively representing its 10% radioactivity, was added to the U-8 container prepared in ④ above. This resulted in a 100.00-g liquid sample contained in a U-8 container, to which an efficiency curve of the germanium detector of Kaken Inc. (ORTEC GEM, Seiko EG&G) had been obtained (Fig. D.1(a)).

⑥ The gamma rays of the 100.00-g liquid samples were measured for $t_{\mathrm{live}} = 1200$ s, 1800 s, or 3600 s. Using the available efficiency curve, the gamma counts of ^{99}Mo were converted to activities.

⑦ Each measured ^{99}Mo activity was multiplied by 10 (see ⑤ above) and decay-corrected to the end of the corresponding irradiation run. Consequently, the original ^{99}Mo activities of the MoO_3 targets were obtained.

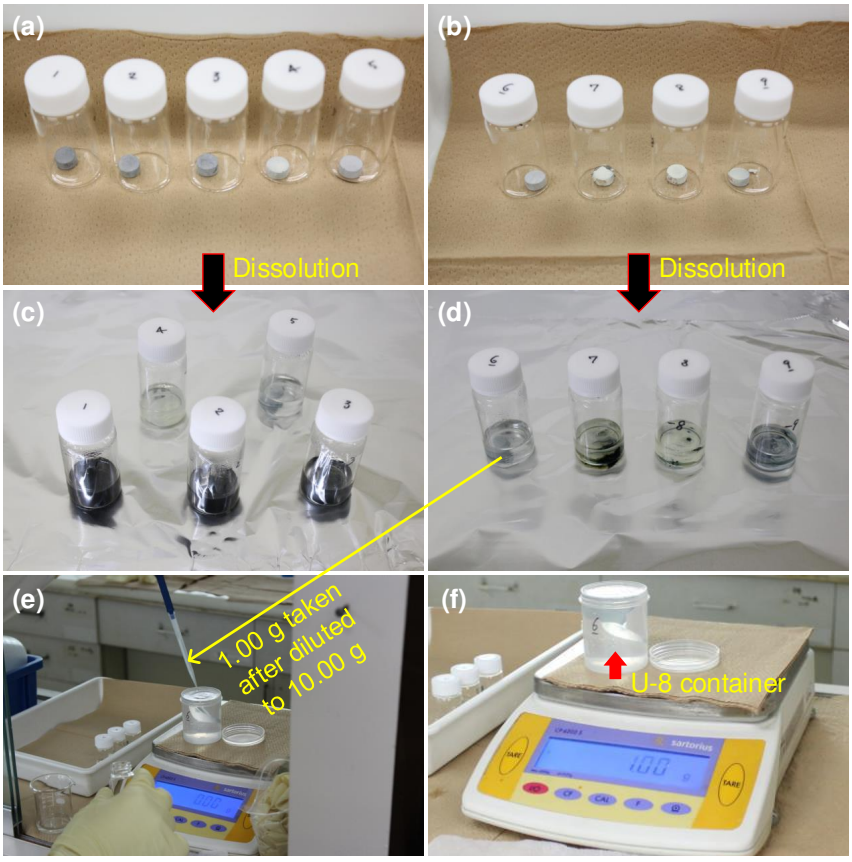

Fig. 5.15. Preparations for ^{99}Mo gamma-ray spectrometry. (a–b) [^{99}Mo]MoO_3 targets and (c–d) their dissolution in 6-*M* NaOH solutions on a laboratory hot plate, resulting in Na_2[^{99}Mo]MoO_4 solutions. (e) Before and (f) after 1.00 g of a Na_2[^{99}Mo]MoO_4 solution (which had been diluted to 10.00 g with distilled water) was added to 99.00 g of distilled water in a U-8 container.

Measurement of irradiated Au

The activities of Au foils were measured using a germanium detector (ORTEC GEM) at the KURNS in the following order. No separate chemical treatment was performed prior to the measurement.

① An efficiency curve was obtained by measuring the gamma rays of a gamma reference source, of which the activities of the involved radionuclides are known, for t_{real} = 1800 s (Fig. D.1(b)).

② The gamma rays of each Au foil were measured for t_{real} = 600 s, 900 s, 1200 s, or 3600 s.

③ Using the obtained efficiency curve, the gamma counts of ^{196}Au were converted to activities.

Table 5.5. MoO_3 dissolution conditions.

	MoO_3		NaOH	
No.	Mass (g)	Amount (mmol)	Amount (mmol)	Volume for 6 M (mL)
181213-1	1.6216	11.265	22.531	3.755
181213-2	1.6146	11.217	22.433	3.739
181213-3	1.6382	11.381	22.761	3.794
181213-4	1.6309	11.330	22.660	3.777
181213-5	1.6294	11.319	22.639	3.773
181213-6	1.5862	11.019	22.039	3.673
181213-7	1.5979	11.101	22.201	3.700
181213-8	1.5771	10.956	21.912	3.652
181213-9	1.4366	9.980	19.960	3.327

④ The measured ^{196}Au activities were decay-corrected to the end of the corresponding irradiation runs, and the original ^{196}Au activities were obtained.

Activity unit adjustment

The units of the ^{99}Mo and ^{196}Au activities were adjusted to kBq g^{-1} μA^{-1}, so that the W thickness becomes the only variable under the same beam energy. This was because

(i) the masses of MoO_3 targets and Au foils were not uniform (Tables 5.2 and 5.3), and
(ii) the beam currents for a given beam energy, 20 MeV for example, were also not uniform (Table 5.4).

Simulation rerun

To reflect the actual dimensions and mass densities of the W converters, MoO_3 targets, and Au foils, and to reflect the actual electron beam sizes, we reran the MC simulations addressed in Sec. 5.2, with respect to the actual experimental conditions shown in Tables 5.1, 5.2, 5.3, and 5.4. The simulation results were then compared with the experimental data.

5.3.4 Results and discussion

Fig. 5.16 shows a set of gamma-ray spectra for the irradiation number 2. In total, nine such sets of spectra were obtained. Because our MoO_3 targets were not enriched in

^{100}Mo, various photonuclear reactions were induced on the naturally occurring Mo isotopes other than ^{100}Mo, or $^{92,94–98}$Mo, resulting in the formation of Nb radionuclides (Fig. 5.16(a)). The relevant reactions can be found in Table B.1.

The calculated and experimentally obtained ^{99}Mo activities are plotted in Fig. 5.17. For the beam energies of 20 MeV and 35 MeV, the W thicknesses at which the greatest ^{99}Mo activities are obtained were the same between the calculation and experimental results:

Table F.2 (p. 181)

⇒ Greatest $S_{\text{Mo-99}}(20\,\text{MeV})$ calculated: 12.91 kBq g^{-1} μA^{-1} at $t_{\text{W}} = 1.48$ mm
⇒ Greatest $S_{\text{Mo-99}}(20\,\text{MeV})$ measured: 6.14 kBq g^{-1} μA^{-1} at $t_{\text{W}} = 1.48$ mm
⇒ Greatest $S_{\text{Mo-99}}(35\,\text{MeV})$ calculated: 26.80 kBq g^{-1} μA^{-1} at $t_{\text{W}} = 2.58$ mm
⇒ Greatest $S_{\text{Mo-99}}(35\,\text{MeV})$ measured: 32.29 kBq g^{-1} μA^{-1} at $t_{\text{W}} = 2.58$ mm

For the beam energy of 50 MeV, however, the optimal W thicknesses differed between the calculation and experimental results:

⇒ Greatest $S_{\text{Mo-99}}(50\,\text{MeV})$ calculated: 50.50 kBq g^{-1} μA^{-1} at $t_{\text{W}} = 3.16$ mm
⇒ Greatest $S_{\text{Mo-99}}(50\,\text{MeV})$ measured: 52.25 kBq g^{-1} μA^{-1} at $t_{\text{W}} = 2.13$ mm

As for the absolute ^{99}Mo specific activities, the differences between calculation and experimental results were factors of 1.94–2.50 in 20 MeV, 1.03–1.24 in 35 MeV, and 1.06–1.11 in 50 MeV. The differences are attributed to the following factors:

(i) *Beam energy spread*. In the MC simulation runs, monoenergetic electron beams were transported. In the irradiation experiments, however, the electron beams exhibited energy spread. Considering the relatively large differences observed in $E_{\text{e}-} = 20$ MeV, The actual energies of the 20-MeV electron beams could be distributed over a wider energy range compared with those of the 35-MeV and 50-MeV electron beams.

(ii) *Beam current fluctuation*. The average beam currents shown in Table 5.4 are actually the means of average beam currents measured over irradiation times. As can be seen from the standard deviations in Table 5.4, some of the irradiation runs were accompanied by beam current fluctuations, which could affect the absolute values of experimental ^{99}Mo specific activities.

The average beam current refers to a peak beam current multiplied by the macropulse duty cycle; see Sec. 3.3.4.

(iii) *Accuracy of the excitation function*. The ^{99}Mo activities were calculated using the ^{100}Mo(γ,n)^{99}Mo excitation function contained in the TENDL-2015 nuclear data library. The accuracy of the excitation function could affect the ^{99}Mo activity calculations.

(iv) *Irradiation center deviation*. There could be slight deviations of the beam irradiation centers. In the MC simulations, the coordinate of the irradiation center was exactly the same as that of the converter center. Although the irradiation centers were adjusted to the converter centers at each beam energy (Fig. 5.14(b)), there could be slight misalignment between the two.

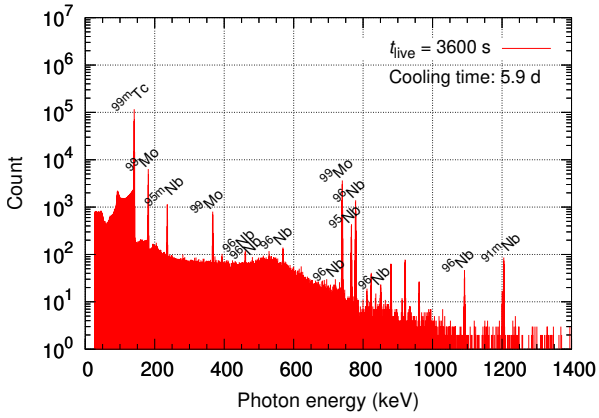

(a)

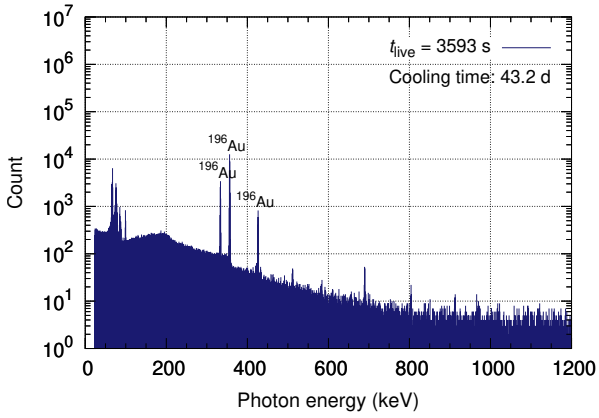

(b)

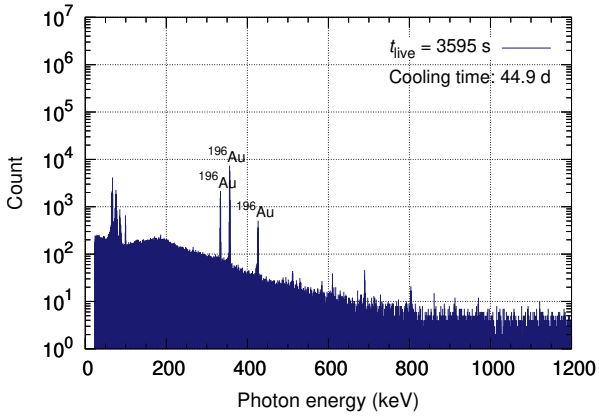

(c)

Fig. 5.16. Gamma-ray spectra measured for the (a) MoO_3 target, and (b) upstream and (b) downstream Au foils of the irradiation number 2. Radionuclides with $\geq$20 counts are annotated. The gamma-ray spectra of MoO_3 targets for the irradiation numbers 1, 3, and 4–9 are provided in Appendix E.

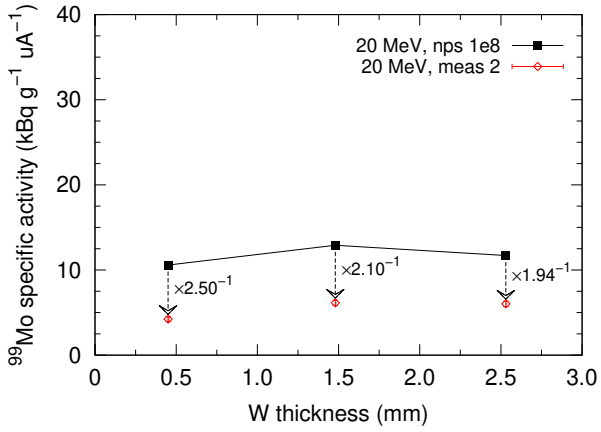

(a)

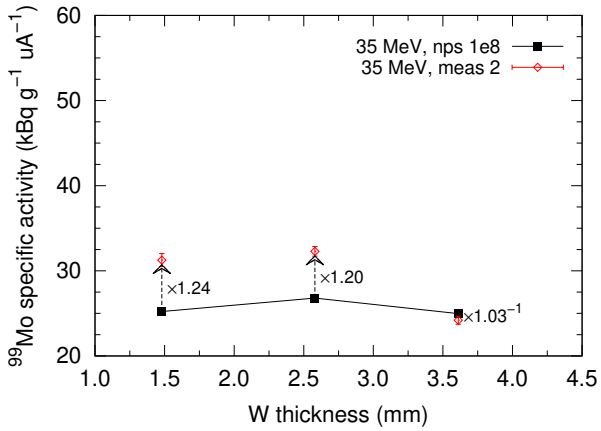

(b)

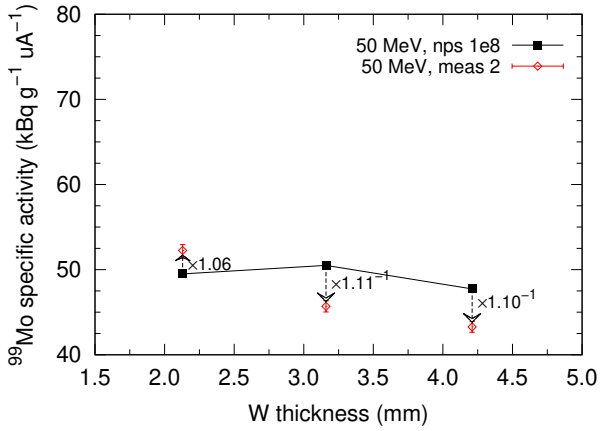

(c)

Fig. 5.17. ^{99}Mo specific activities calculated (labeled with "nps") and experimentally obtained (labeled with "meas") for electron beams of (a) 20 MeV, (b) 35 MeV, and (c) 50 MeV. The irradiation times were 10 min in (a), and 5 min in (b) and (c). The exact values are listed in Table F.2.

(v) *Errors during gamma-ray spectrometry*. As explained in Sec. 5.3.3, the irradiated MoO_3 targets were dissolved and the ^{99}Mo activity concentrations were diluted before measurement. Errors could be made during the dissolution and dilution processes.

Considering, however, similar comparisons made by other researchers[48], the factors 1.03–2.50 are deemed to be acceptable differences. The discussion continues on to the ^{196}Au specific activities.

The ^{196}Au specific activities of the upstream Au foils are plotted in Fig. 5.18, and those of the downstream Au foils in Fig. 5.19. By the terms upstream and downstream, we mean the positions of the Au foils relative to the direction of beam propagation; an upstream Au foil is the one placed near the beam exit of the electron linac, and a downstream Au foil is the one placed at the opposite side (see Fig. 5.13).

In the upstream Au foils, the W thicknesses at which the greatest ^{196}Au activities are obtained agreed between the calculation and experimental results:

⇒ Greatest $S_{\text{Au-196}}(20\,\text{MeV})$ calculated: 104.34 kBq g^{-1} μA^{-1} at $t_W = 1.48$ mm
⇒ Greatest $S_{\text{Au-196}}(20\,\text{MeV})$ measured: 74.08 kBq g^{-1} μA^{-1} at $t_W = 1.48$ mm
⇒ Greatest $S_{\text{Au-196}}(35\,\text{MeV})$ calculated: 210.60 kBq g^{-1} μA^{-1} at $t_W = 2.58$ mm
⇒ Greatest $S_{\text{Au-196}}(35\,\text{MeV})$ measured: 248.18 kBq g^{-1} μA^{-1} at $t_W = 2.58$ mm
⇒ Greatest $S_{\text{Au-196}}(50\,\text{MeV})$ calculated: 395.38 kBq g^{-1} μA^{-1} at $t_W = 3.16$ mm
⇒ Greatest $S_{\text{Au-196}}(50\,\text{MeV})$ measured: 366.92 kBq g^{-1} μA^{-1} at $t_W = 3.16$ mm

Table F.3 (p. 182)

The absolute activity differences were factors of 1.41–1.81 in 20 MeV, 1.07–1.18 in 35 MeV, and 1.08–1.55 in 50 MeV.

For the downstream Au foils, the W thicknesses at which the greatest ^{196}Au specific activities are obtained were different between the calculations and experiments:

⇒ Greatest $S_{\text{Au-196}}(20\,\text{MeV})$ calculated: 85.21 kBq g^{-1} μA^{-1} at $t_W = 0.45$ mm
⇒ Greatest $S_{\text{Au-196}}(20\,\text{MeV})$ measured: 54.00 kBq g^{-1} μA^{-1} at $t_W = 1.48$ mm
⇒ Greatest $S_{\text{Au-196}}(35\,\text{MeV})$ calculated: 178.01 kBq g^{-1} μA^{-1} at $t_W = 1.48$ mm
⇒ Greatest $S_{\text{Au-196}}(35\,\text{MeV})$ measured: 204.45 kBq g^{-1} μA^{-1} at $t_W = 2.58$ mm
⇒ Greatest $S_{\text{Au-196}}(50\,\text{MeV})$ calculated: 340.84 kBq g^{-1} μA^{-1} at $t_W = 2.13$ mm
⇒ Greatest $S_{\text{Au-196}}(50\,\text{MeV})$ measured: 324.15 kBq g^{-1} μA^{-1} at $t_W = 4.21$ mm

Table F.4 (p. 182)

The differences between the calculated and experimental activities were now factors of 1.47–1.83 in 20 MeV, 1.09–1.19 in 35 MeV, and 1.05–2.64 in 50 MeV, all of which are greater than those of the upstream Au foils. The factor 2.64 from the Au foil number 14, corresponding to the electron beam energy of 50 MeV and the W thickness of 2.13 mm (see Table 5.3), was the only calculation-experiment difference factor that was greater than 2 among the ^{196}Au results.

[48] S. Sekimoto *et al. J. Radioanal. Nucl. Chem.* **311**, 1361–1366 (2017).

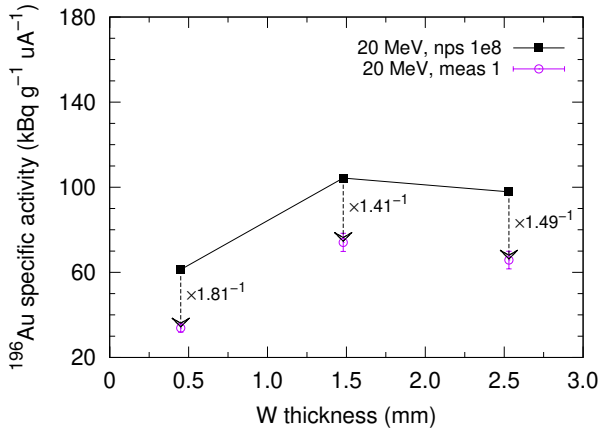

(a)

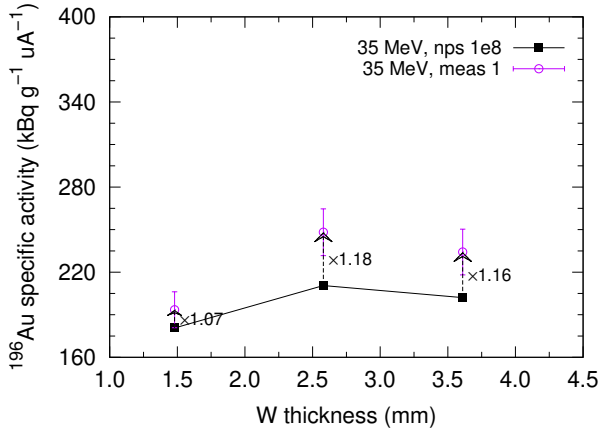

(b)

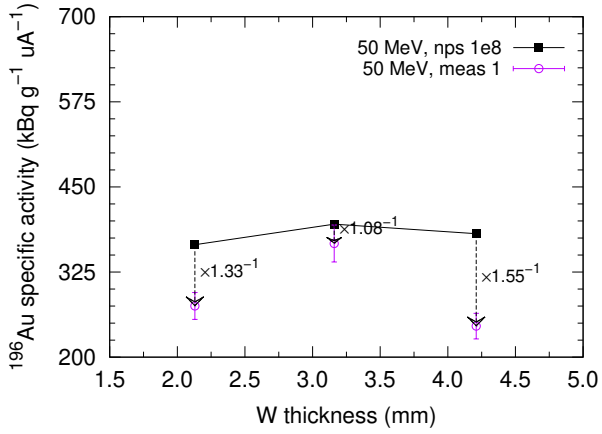

(c)

Fig. 5.18. Upstream ^{196}Au specific activities calculated (labeled with “nps”) and experimentally obtained (labeled with “meas”) for electron beams of (a) 20 MeV, (b) 35 MeV, and (c) 50 MeV. The irradiation times were 10 min in (a), and 5 min in (b) and (c). The exact values are listed in Table F.3.

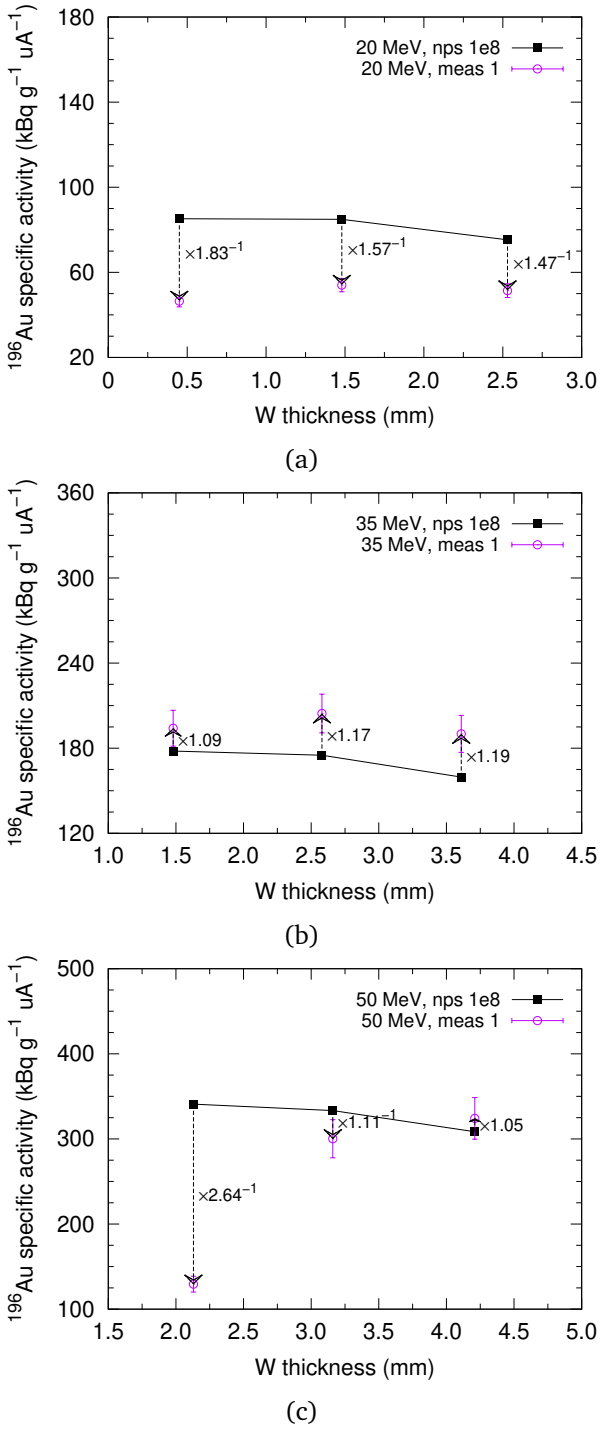

Fig. 5.19. Downstream ^{196}Au specific activities calculated (labeled with “nps”) and experimentally obtained (labeled with “meas”) for electron beams of (a) 20 MeV, (b) 35 MeV, and (c) 50 MeV. The irradiation times were 10 min in (a), and 5 min in (b) and (c). The exact values are listed in Table F.4.

Considering the overall agreement in the upstream Au foils and the overall discrepancy in the downstream Au foils, it is thought that the beam interactions within the MoO_3 targets could affect the $^{197}Au(\gamma,n)^{196}Au$ reactions in the downstream Au foils.

The agreeing W thicknesses of the MoO_3 results for 20 MeV and 35 MeV, together with the acceptably small differences in the overall calculation and experimental results, suggest that the parametric calculations of the optimal W thicknesses can be valid.

However, it should be noted that the above results hold only for the intertarget distance of our target holder (Fig. 5.8), or 13 mm, and for the beam sizes used in the experiments (Table 5.4): for a different set of an intertarget distance and a beam size, the contributions of the first and second terms of Eq. (5.2) to Γ_{MoO_3}, namely the primary and secondary hyperthreshold photons, are modified, and so is the balanced W thickness. Our program `phitar` (Sec. 2.2) can be used in such cases, which can calculate targetry- and beam-specific optimal thicknesses of W and other converter materials.

5.4 Summary

As part of the parametric analysis of ^{99}Mo production targetry, we investigated optimal W thicknesses for electron beam energies of 20–50 MeV at the interval of 15 MeV. The calculated results were compared with experimental results, and the overall results of MoO_3 targets and upstream Au foils agreed between calculations and experiments.

5.5 Acknowledgments

We are grateful to Prof. Ohtsuki, Dr. Sekimoto (KURNS, Kyoto Univ.), Prof. Kikunaga, and Prof. Kashiwagi (ELPH, Tohoku Univ.) for their guidance and support in conducting the converter experiments. We are also indebted to Dr. Tatenuma and Ms. Natori (Kaken) for their guidance and support in preparing MoO_3 targets, and to Mr. Kawakami (Kaken) and Dr. Inagaki (KURNS, Kyoto Univ.) for the help of gamma-ray spectrometry.

Chapter 6

Density change coefficient

Abstract

In all of the accelerator ^{99}Mo/^{99m}Tc production methods introduced in Chap. 1, the use of enriched ^{100}Mo is preferable or even necessary: in the ^{100}Mo(γ,n)^{99}Mo and ^{100}Mo(n,2n)^{99}Mo reaction routes, using 99%-enriched ^{100}Mo can increase the yield and specific yield of ^{99}Mo by a factor of approximately 10. In the ^{100}Mo(p,2n)^{99m}Tc reaction route, the use of enriched ^{100}Mo is required not only to increase the ^{99m}Tc yield, but also to minimize the yields of Tc impurities.

In order to facilitate determining the ^{100}Mo enrichment level and the depletion levels of $^{92,94–98}$Mo, we defined a figure of merit called density change coefficient, and developed its calculation program. The theoretical basis, calculation results, and applications of the density change coefficient will be presented.

6.1 Declaration

This chapter is based on our publication[15], which is licensed under CC BY 3.0[105]. The CC BY 3.0 license permits the contents of the article, including the text and figures, to be reused provided that the license terms are fully adhered to.

6.2 Introduction

In naturally occurring Mo, ^{100}Mo accounts for only 9.74% of the Mo isotopes[8,96], resulting in low production yields of ^{99}Mo/^{99m}Tc. The other, and more serious,

[15] J. Jang *et al. J. Phys. Commun.* **3**, 055015 (2019).
[105] Creative Commons. Attribution 3.0 Unported (CC BY 3.0).
[8] J. Meija *et al. Pure Appl. Chem.* **88**, 293–306 (2016).
[96] A. J. Mayer *et al. J. Anal. At. Spectrom.* **29**, 85–94 (2014).

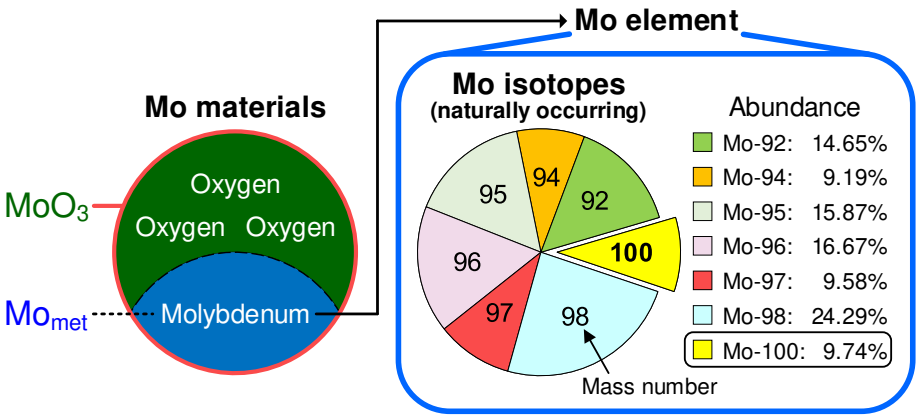

Fig. 6.1. Mo entities related to ^{99}Mo/^{99m}Tc production. Figure reproduced from our publication [15] which is licensed under CC BY 3.0.

problem of natural Mo is that all of the Mo isotopes other than ^{100}Mo, namely $^{92,94–98}$Mo, can react with incident particles and can lead to production of various impurity nuclides (see Appendix B). Among the impurity nuclides, niobium (Nb) radioisotopes greatly increase the dose rate around targetry, complicating the handling of Mo targets during and after irradiation. On the other hand, Tc isotopes reduce the specific activity and radioactive concentration of ^{99m}Tc, which can then become insufficient for conventional imaging protocols. For these reasons, using enriched ^{100}Mo is necessary in the ^{100}Mo-based ^{99}Mo/^{99m}Tc production reactions, namely ^{100}Mo(γ,n)^{99}Mo, ^{100}Mo(n,2n)^{99}Mo, and ^{100}Mo(p,2n)^{99m}Tc (Sec. 1.3).

The specific level of ^{100}Mo enrichment can be determined based on (i) the goal yields of ^{99}Mo/^{99m}Tc and (ii) the goal radionuclidic and isotopic purities of ^{99m}Tc. To facilitate determining the ^{100}Mo enrichment level, we defined a figure of merit for Mo targets called density change coefficient, which can evaluate the items (i) and (ii) above.

6.3 Theory

6.3.1 Molybdenum hierarchy

According to the hierarchical level, Mo can be grouped into Mo materials, Mo element, and Mo isotopes (Fig. 6.1). Based on this classification, we will explain the theoretical basis of the density change coefficient. Mo metal (Mo_{met}) and Mo(VI) oxide (MoO_3), the two widely used Mo target materials (Sec. 4.4.2), will be investigated as the Mo material group.

6.3.2 Amount fraction, mass fraction, and enrichment level

For a substance i that is the constituent of a mixture k, the amount fraction (mole fraction) is given by

$$x_i = \frac{n_i}{n_i + \sum_{j\neq i} n_j} = \frac{n_i}{n_{\text{tot}}} \neq \frac{n_i}{n_k}, \tag{6.1}$$

where n denotes the amount of substance (number of moles) in k, j all the constituents except i, and the subscript tot indicates a total quantity.

Similarly, the mass fraction of i is defined as

$$w_i = \frac{m_i}{m_i + \sum_{j\neq i} m_j} = \frac{n_i M_i}{n_i M_i + \sum_{j\neq i} n_j M_j} = \frac{m_i}{m_{\text{tot}}} = \frac{m_i}{m_k}, \tag{6.2}$$

where m and M signify the mass and molar mass, respectively.

Plugging Eq. (6.1) into Eq. (6.2), the mass fraction and amount fraction are related by

$$w_i = \frac{x_i M_i}{x_i M_i + \sum_{j\neq i} x_j M_j}. \tag{6.3}$$

On top of that, the weighted-average molar mass of k can be expressed as

$$\begin{aligned} \bar{M}_k &= x_i M_i + \sum_{j\neq i} x_j M_j \\ &= \frac{w_i + \sum_{j\neq i} w_j}{\frac{w_i}{M_i} + \sum_{j\neq i} \frac{w_j}{M_j}} = \frac{1}{\frac{w_i}{M_i} + \sum_{j\neq i} \frac{w_j}{M_j}}, \end{aligned} \tag{6.4}$$

by which Eq. (6.3) becomes

$$w_i = x_i \frac{M_i}{\bar{M}_k}. \tag{6.5}$$

The amount fraction of ^{100}Mo in naturally occurring Mo is $x_{\text{Mo-100}} = 0.09744$, while the corresponding mass fraction is $w_{\text{Mo-100}} = (0.09744)\left(\frac{99.907\,\text{g mol}^{-1}}{95.949\,\text{g mol}^{-1}}\right) \approx 0.1015$ (Fig. 6.2). As a result, the enrichment level of ^{100}Mo could, unless otherwise stated, mean any of the two fraction quantities. To avoid confusion and to conform to the conventions of enriched ^{100}Mo vendors[106,107], we will assume that the ^{100}Mo *amount* fraction represents the ^{100}Mo enrichment level. On the other hand, the ^{100}Mo *mass* fraction will be used in explaining the influence of enriched ^{100}Mo on the Mo entities, as can provide a clearer understanding of the density change coefficient.

Enrichment levels are juxtaposed with natural abundances[106,107], which are amount (mole) fractions.

[106] ISOFLEX. Stable isotopes of molybdenum available from ISOFLEX (2019).
[107] Trace Sciences International. Molybdenum Isotopes (2019).

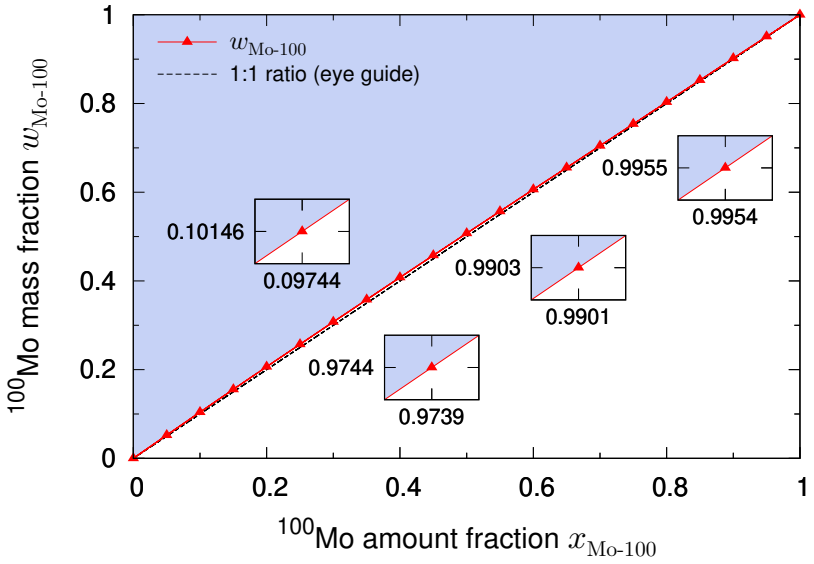

Fig. 6.2. Variation of the ^{100}Mo mass fraction with the ^{100}Mo amount fraction. Eqs. (6.4) and (6.5) were used for the calculation. Assuming that ^{100}Mo is enriched using gas centrifuges, $^{92,94–98}$Mo isotopes were depleted in ascending order of their mass numbers. The eye-guiding dashed line, whose slope is 1, and the upper region of $w_{\text{Mo-100}}$, shaded in light blue, clarify the relation $w_{\text{Mo-100}} \geq x_{\text{Mo-100}}$. Figure reproduced from our publication [15] which is licensed under CC BY 3.0.

6.3.3 Mass fraction of Mo element

Using Eq. (6.2) and Eq. (6.4), the mass fraction of Mo element in a Mo target can be expressed as a function of the ^{100}Mo mass fraction:

$$\begin{aligned} w_{\text{Mo}}(w_{\text{Mo-100}}) &= \frac{n_{\text{Mo}}\bar{M}_{\text{Mo}}}{n_{\text{Mo}}\bar{M}_{\text{Mo}} + n_{\text{O}}\bar{M}_{\text{O}}} \\ &= \left(\frac{n_{\text{Mo}}}{\frac{w_{\text{Mo-100}}}{M_{\text{Mo-100}}} + \sum_{A\neq 100} \frac{w_{\text{Mo-}A}}{M_{\text{Mo-}A}}} \right) \\ &\quad \times \left(\frac{n_{\text{Mo}}}{\frac{w_{\text{Mo-100}}}{M_{\text{Mo-100}}} + \sum_{A\neq 100} \frac{w_{\text{Mo-}A}}{M_{\text{Mo-}A}}} + \frac{n_{\text{O}}}{\sum_A \frac{w_{\text{O-}A}}{M_{\text{O-}A}}} \right)^{-1}, \end{aligned} \tag{6.6}$$

where, instead of molar masses, weighted-average molar masses are used, as the chemical elements themselves are mixtures of their isotopes. The symbol A represents the mass number.

For a target of nonenriched MoO_3, Eq. (6.6) is calculated to be

$$w_{\text{Mo}}(0.1015) = \frac{(1)(95.949\,\text{g mol}^{-1})}{(1)(95.949\,\text{g mol}^{-1}) + (3)(15.999\,\text{g mol}^{-1})} \approx 0.66656\,.$$

If the MoO_3 target is enriched to 99.00% by mass in ^{100}Mo, the value of w_{Mo} will increase to

$$w_{\text{Mo}}(0.9900) = \frac{(1)(99.887\,\text{g mol}^{-1})}{(1)(99.887\,\text{g mol}^{-1}) + (3)(15.999\,\text{g mol}^{-1})} \approx 0.67544\,,$$

meaning that the mass of Mo element per mass of MoO_3 will increase by a factor of

$$\frac{w_{\text{Mo}}(0.9900)}{w_{\text{Mo}}(0.1015)} = \frac{0.67544}{0.66656} \approx 1.0133\,. \tag{6.7}$$

In contrast, w_{Mo} in a Mo_{met} target is immune to the associated ^{100}Mo mass fraction:

$$\frac{w_{\text{Mo}}(0.9900)}{w_{\text{Mo}}(0.1015)} = \frac{\frac{(1)(99.887\,\text{g mol}^{-1})}{(1)(99.887\,\text{g mol}^{-1})+(0)(15.999\,\text{g mol}^{-1})}}{\frac{(1)(95.949\,\text{g mol}^{-1})}{(1)(95.949\,\text{g mol}^{-1})+(0)(15.999\,\text{g mol}^{-1})}} = 1.0000\,. \tag{6.8}$$

Fig. 6.3 plots Eqs. (6.7) and (6.8) in the range of $w_{\text{Mo-100}} = 0.0000$–$1.0000$. The increasing w_{Mo} in MoO_3 means that the Mo mass density ρ_{Mo} increases with $w_{\text{Mo-100}}$. On top of that, because of the relation $\rho_{\text{Mo-100}} \propto \rho_{\text{Mo}}$, the ^{100}Mo mass density $\rho_{\text{Mo-100}}$ is increased by the ρ_{Mo} increasing with $w_{\text{Mo-100}}$, in addition to by the sheer increase of $w_{\text{Mo-100}}$.

6.3.4 Density change coefficient

Using Eq. (6.2), the ^{100}Mo mass density can be written as

$$\begin{aligned}\rho_{\text{Mo-100}}(w_{\text{Mo-100}}) &= w_{\text{Mo-100}}\rho_{\text{Mo}} \\ &= w_{\text{Mo-100}} w_{\text{Mo}}(w_{\text{Mo-100}})\,\xi\rho_{\text{Mo-mat}},\end{aligned} \tag{6.9}$$

where $\xi \leq 1$ is the density ratio (Eq. (2.2)), and the subscript Mo-mat stands for a Mo material. Here $\rho_{\text{Mo-mat}}$ is the known mass density, $\rho_{\text{MoO}_3} = 4.69\,\text{g cm}^{-3}$ for example. Because the density interdependence is target-independent, we can assume that $\xi = 1$.

For a nonenriched MoO_3 target, Eq. (6.9) is calculated as

$$\rho_{\text{Mo-100}}(0.1015) = (0.1015)(0.66656)(4.690\,\text{g cm}^{-3}) \approx 0.3173\,\text{g cm}^{-3}.$$

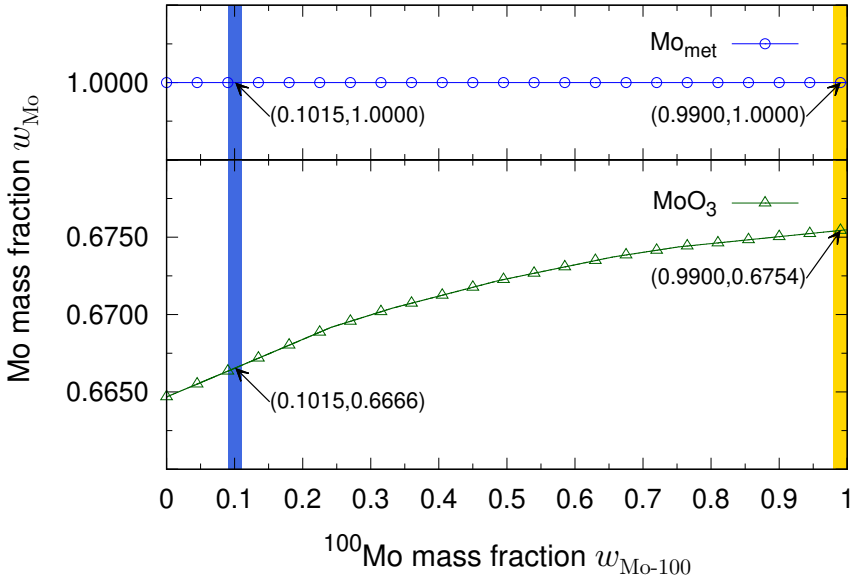

Fig. 6.3. Relation between the mass fraction of Mo element and the mass fraction of ^{100}Mo. Figure reproduced from our publication [15] which is licensed under CC BY 3.0.

If the MoO_3 target is enriched to 99.00% by mass in ^{100}Mo, the mass density of ^{100}Mo will become

$$\rho_{\text{Mo-100}}(0.9900) = (0.9900)(0.67544)(4.690\,\mathrm{g\,cm^{-3}}) \approx 3.136\,\mathrm{g\,cm^{-3}},$$

leading to a ^{100}Mo mass density increment of

$$\frac{\rho_{\text{Mo-100}}(0.9900)}{\rho_{\text{Mo-100}}(0.1015)} = \frac{3.136\,\mathrm{g\,cm^{-3}}}{0.3173\,\mathrm{g\,cm^{-3}}} \approx 9.884\,. \tag{6.10}$$

If the change in w_{Mo} by $w_{\text{Mo-100}}$ had been disregarded, Eq. (6.10) would have been

$$\frac{(0.9900)(0.66656)(4.690\,\mathrm{g\,cm^{-3}})}{(0.1015)(0.66656)(4.690\,\mathrm{g\,cm^{-3}})} = \frac{3.095\,\mathrm{g\,cm^{-3}}}{0.3173\,\mathrm{g\,cm^{-3}}} \approx 9.754\,, \tag{6.11}$$

leading to an underestimation. Also, note that Eq. (6.10) is actually the product of Eqs. (6.7) and (6.11):

$$\left(\frac{0.67544}{0.66656}\right)\left[\frac{(0.9900)(0.66656)(4.690\,\mathrm{g\,cm^{-3}})}{(0.1015)(0.66656)(4.690\,\mathrm{g\,cm^{-3}})}\right] = (1.0133)(9.754) \approx 9.884\,,$$

which clearly shows the role of Eq. (6.6).

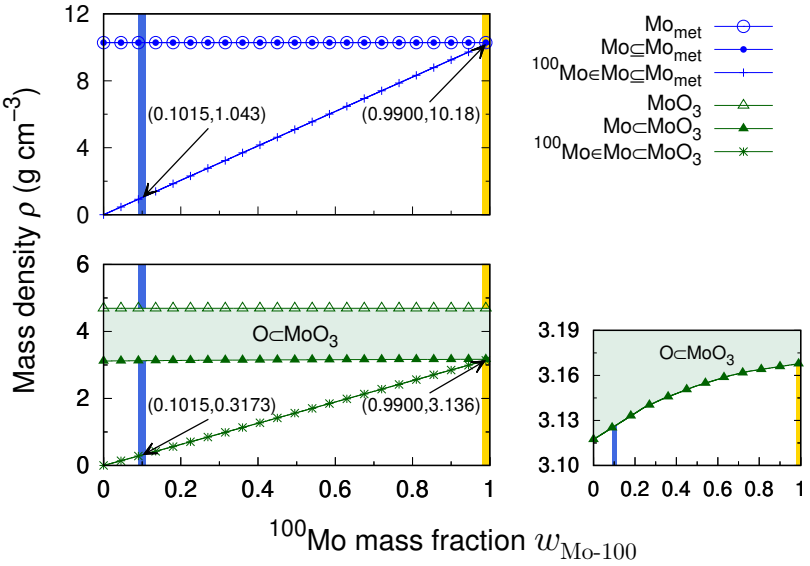

Fig. 6.4. Mass densities of Mo targets, Mo elements, and ^{100}Mo nuclides, as functions of ^{100}Mo mass fraction. Figure reproduced from our publication [15] which is licensed under CC BY 3.0.

As shown in Eq. (6.8), w_{Mo} in a Mo_{met} target is unaffected by $w_{\text{Mo-100}}$. Therefore, the increment of ^{100}Mo mass density is dictated only by $w_{\text{Mo-100}}$:

$$\frac{\rho_{\text{Mo-100}}(0.9900)}{\rho_{\text{Mo-100}}(0.1015)} = \frac{(0.9900)(1.0000)(10.28\,\text{g cm}^{-3})}{(0.1015)(1.0000)(10.28\,\text{g cm}^{-3})} \approx 9.754\,. \tag{6.12}$$

Eqs. (6.10) and (6.12) are plotted in Fig. 6.4, and the interpretations are as follows.

First, because the absolute mass density of Mo_{met} is greater than that of MoO_3, the ^{100}Mo mass density grows at a faster rate in Mo_{met} than in MoO_3.

Second, it should be noted that although slowly, the mass density of Mo element in MoO_3 increases with the ^{100}Mo mass fraction. This increase can also be seen in Eq. (6.6). Because the mass density of ^{100}Mo depends not only on (i) its mass fraction but also on (ii) the mass density of the associated Mo element (see Eq. (6.9)), the ^{100}Mo mass density increases more rapidly than the sole influence of the item (i) above.

Lastly, the largest difference between the pre- and post-enrichment ^{100}Mo mass densities is found from MoO_3, attributed to its oxygen constituents (see Eq. (6.6)). This means that when enriched in ^{100}Mo, MoO_3 can have a greater ^{100}Mo mass density increment than Mo_{met}. It should, however, be noted that the absolute ^{100}Mo mass density is always greater in Mo_{met} than in MoO_3, regardless of the ^{100}Mo enrichment

level:

$$\frac{\rho_{\text{Mo-100}}(0.1015)\text{ in Mo}_{\text{met}}}{\rho_{\text{Mo-100}}(0.1015)\text{ in MoO}_3} = \frac{(0.1015)(1.0000)(10.28\,\text{g cm}^{-3})}{(0.1015)(0.66656)(4.690\,\text{g cm}^{-3})} \approx 3.288\,,$$

$$\frac{\rho_{\text{Mo-100}}(0.9900)\text{ in Mo}_{\text{met}}}{\rho_{\text{Mo-100}}(0.9900)\text{ in MoO}_3} = \frac{(0.1015)(1.0000)(10.28\,\text{g cm}^{-3})}{(0.1015)(0.67544)(4.690\,\text{g cm}^{-3})} \approx 3.245\,.$$

Next, we move on to the number densities of Mo entities. For a substance i, the number density and mass density are related by

$$\mathcal{N}_i = \frac{\rho_i}{M_i} N_{\text{A}}, \tag{6.13}$$

where N_{A} is the Avogadro constant. Plugging Eq. (6.9) into Eq. (6.13), the number density of ^{100}Mo can be expressed as

$$\mathcal{N}_{\text{Mo-100}}(w_{\text{Mo-100}}) = \frac{w_{\text{Mo-100}} w_{\text{Mo}}(w_{\text{Mo-100}})\,\rho_{\text{Mo-mat}}}{M_{\text{Mo-100}}} N_{\text{A}}. \tag{6.14}$$

In terms of the amount fraction, Eq. (6.14) is written as

$$\begin{aligned}\mathcal{N}_{\text{Mo-100}}(x_{\text{Mo-100}}) &= x_{\text{Mo-100}} x_{\text{Mo}} \mathcal{N}_{\text{Mo-mat}}(x_{\text{Mo-100}}) \\ &= x_{\text{Mo-100}} x_{\text{Mo}} \frac{\rho_{\text{Mo-mat}}}{M_{\text{Mo-mat}}(x_{\text{Mo-100}})} N_{\text{A}},\end{aligned}$$

or

$$\mathcal{N}_{\text{Mo-100}}(x_{\text{Mo-100}}) = x_{\text{Mo-100}} \frac{\rho_{\text{Mo-mat}}}{M_{\text{Mo-mat}}(x_{\text{Mo-100}})} N_{\text{A}}, \tag{6.15}$$

provided that the Mo target is Mo$_{\text{met}}$ or MoO$_3$, both of which have $x_{\text{Mo}} = 1$. Note that while the denominator in Eq. (6.14) is the molar mass of ^{100}Mo, the denominator in Eq. (6.15) is the molar mass of a Mo target; care should be taken when calculating them.

Eqs. (6.13) and (6.14) calculated for Mo$_{\text{met}}$ and MoO$_3$ are graphed in Fig. 6.5. Because ^{100}Mo is the heaviest isotope among $^{92,94\text{–}98,100}$Mo, increasing the ^{100}Mo fraction in a Mo element is accompanied by increased $\bar{M}_{\text{Mo}}$ and thereby increased $M_{\text{Mo-mat}}$. Consequently, $\mathcal{N}_{\text{Mo}}$ and $\mathcal{N}_{\text{Mo-mat}}$ decrease with increasing $w_{\text{Mo-100}}$ (see Eq. (6.13)). The resulting dependence of $\mathcal{N}_{\text{Mo-100}}$ on $w_{\text{Mo-100}}$ is shown at the bottom panel.

Eventually, the ^{100}Mo number density dictates the yield of a ^{100}Mo reaction by affecting its macroscopic cross section:

$$\Sigma_{pe}(E_p, w_{\text{Mo-100}}) = \sigma_{pe}(E_p)\,\mathcal{N}_{\text{Mo-100}}(w_{\text{Mo-100}})\,, \tag{6.16}$$

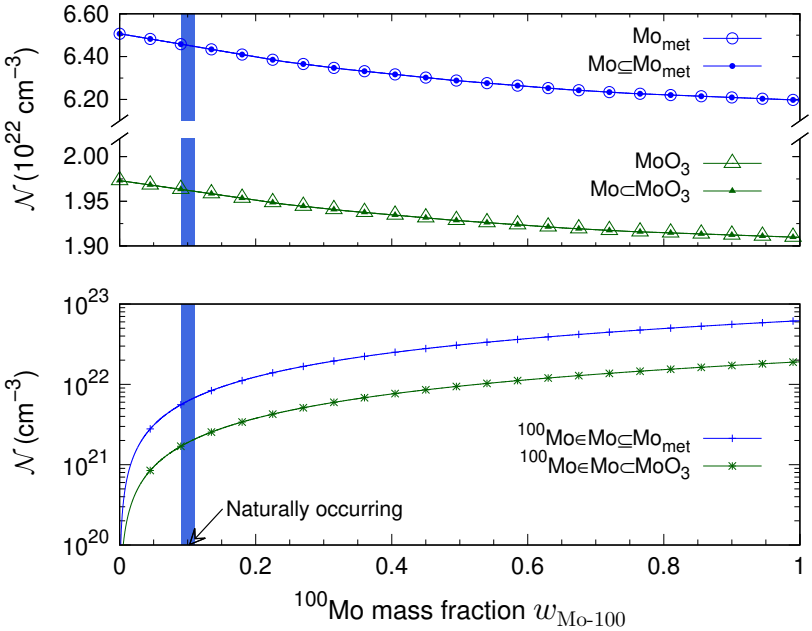

Fig. 6.5. Number densities of Mo materials, Mo elements, and ^{100}Mo nuclides, as functions of ^{100}Mo mass fraction. Figure reproduced from our publication [15] which is licensed under CC BY 3.0.

where p and e represent the projectile and ejectiles of the ^{100}Mo reaction in question, respectively, E_p the energy of the projectile, and σ_{pe} the corresponding microscopic cross section. Figs. 6.6(a), 6.6(b), and 6.6(c) plot $\Sigma_{pe}(E_p, 0.1015)$ and $\Sigma_{pe}(E_p, 0.9900)$ for $pe = \gamma$n, n2n, and p2n, respectively. These macroscopic cross sections were obtained using Eqs. (6.14) and (6.16), and TENDL-2017[24] presented in Fig. 1.4(b) and Appendix C.

The influence of $w_{\text{Mo-100}}$ on $\rho_{\text{Mo-100}}$ and $\mathcal{N}_{\text{Mo-100}}$ explained so far is generalized as follows. Denoting the mass fraction of ^{100}Mo before and after its enrichment as $w^{\text{bef}}_{\text{Mo-100}}$ and $w^{\text{aft}}_{\text{Mo-100}}$, respectively, and expressing ^{100}Mo as a Mo isotope, we define a figure of merit that relates Mo reaction yields to ^{100}Mo enrichment levels, called the density change coefficient (DCC):

$$\begin{aligned} D_{\text{Mo-}A}\left(w^{\text{bef}}_{\text{Mo-100}}, w^{\text{aft}}_{\text{Mo-100}}\right) &\equiv \frac{\rho_{\text{Mo-}A}\left(w^{\text{aft}}_{\text{Mo-100}}\right)}{\rho_{\text{Mo-}A}\left(w^{\text{bef}}_{\text{Mo-100}}\right)} = \frac{\mathcal{N}_{\text{Mo-}A}\left(w^{\text{aft}}_{\text{Mo-100}}\right)}{\mathcal{N}_{\text{Mo-}A}\left(w^{\text{bef}}_{\text{Mo-100}}\right)} \\ &= \frac{w_{\text{Mo-}A}\left(w^{\text{aft}}_{\text{Mo-100}}\right)}{w_{\text{Mo-}A}\left(w^{\text{bef}}_{\text{Mo-100}}\right)} \frac{w_{\text{Mo}}\left(w^{\text{aft}}_{\text{Mo-100}}\right)}{w_{\text{Mo}}\left(w^{\text{bef}}_{\text{Mo-100}}\right)}, \end{aligned} \tag{6.17}$$

[24] A. J. Koning *et al.* *Nucl. Data Sheets* **113**, 2841–2934 (2012).

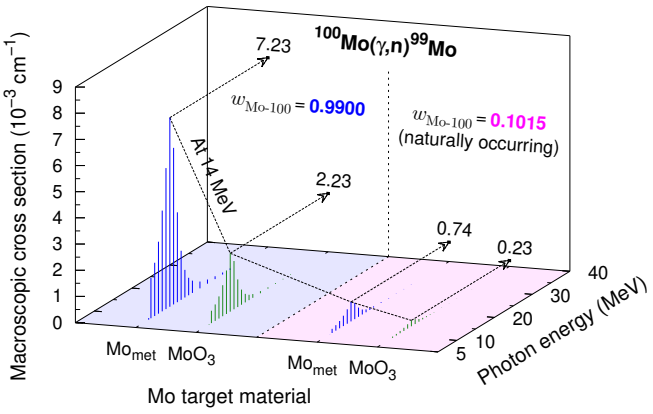

(a)

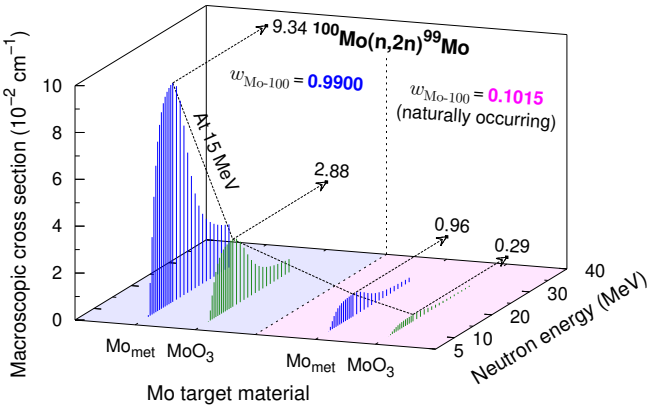

(b)

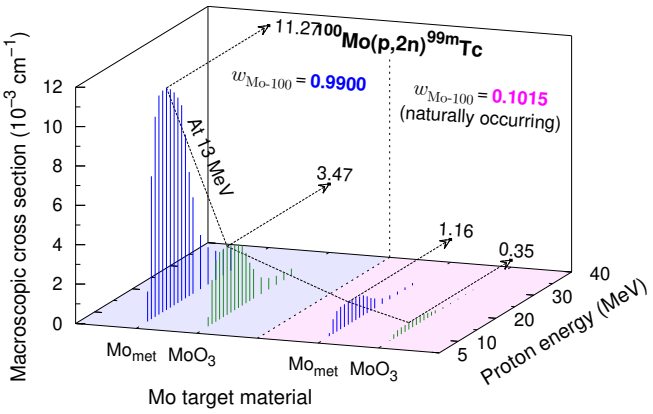

(c)

Fig. 6.6. Macroscopic cross sections for (a) ^{100}Mo(γ,n)^{99}Mo, (b) ^{100}Mo(n,2n)^{99}Mo, and (c) ^{100}Mo(p,2n)^{99m}Tc, generated using the excitation functions contained in TENDL-2017 [24] and the number densities calculated from Eq. (6.14).

where the ratio $\frac{w_{\text{Mo}}\left(w^{\text{aft}}_{\text{Mo-100}}\right)}{w_{\text{Mo}}\left(w^{\text{bef}}_{\text{Mo-100}}\right)}$, effectively representing Eqs. (6.7) and (6.8), is dependent on the chemical composition of a Mo target. Accordingly, Eq. (6.17) should be calculated separately for Mo_{met} and MoO_3.

In practice, the pre-enrichment ^{100}Mo mass fraction is fixed to its nonenriched state (Sec. 6.3.2), reducing one independent variable of Eq. (6.17):

$$D_{\text{Mo-}A}\left(w^{\text{aft}}_{\text{Mo-100}}\right) = \frac{w_{\text{Mo-}A}\left(w^{\text{aft}}_{\text{Mo-100}}\right)}{w_{\text{Mo-}A}(0.1015)} \frac{w_{\text{Mo}}\left(w^{\text{aft}}_{\text{Mo-100}}\right)}{w_{\text{Mo}}(0.1015)}. \tag{6.18}$$

By using Eq. (6.15), the DCC can also be defined in terms of the ^{100}Mo amount fraction:

$$\begin{aligned} D_{\text{Mo-}A}\left(x^{\text{bef}}_{\text{Mo-100}}, x^{\text{aft}}_{\text{Mo-100}}\right) &\equiv \frac{\mathcal{N}_{\text{Mo-}A}\left(x^{\text{aft}}_{\text{Mo-100}}\right)}{\mathcal{N}_{\text{Mo-}A}\left(x^{\text{bef}}_{\text{Mo-100}}\right)} \\ &= \frac{x_{\text{Mo-}A}\left(x^{\text{aft}}_{\text{Mo-100}}\right)}{x_{\text{Mo-}A}\left(x^{\text{bef}}_{\text{Mo-100}}\right)} \frac{M_{\text{Mo-mat}}\left(x^{\text{bef}}_{\text{Mo-100}}\right)}{M_{\text{Mo-mat}}\left(x^{\text{aft}}_{\text{Mo-100}}\right)}, \end{aligned}$$

which, with the $x^{\text{bef}}_{\text{Mo-100}}$ fixed as the ^{100}Mo natural abundance, reduces to

$$D_{\text{Mo-}A}\left(x^{\text{aft}}_{\text{Mo-100}}\right) = \frac{x_{\text{Mo-}A}\left(x^{\text{aft}}_{\text{Mo-100}}\right)}{x_{\text{Mo-}A}(0.0974)} \frac{M_{\text{Mo-mat}}(0.0974)}{M_{\text{Mo-mat}}\left(x^{\text{aft}}_{\text{Mo-100}}\right)}. \tag{6.19}$$

6.3.5 DCC calculation

Calculation program

Depending on the fraction quantity denoting the enrichment level, Eq. (6.18) or Eq. (6.19) is used for DCC calculation. Despite the concise forms of the two equations, however, calculating DCCs can be error-prone and time-consuming, because all the fractions of $^{92,94\text{–}98,100}$Mo isotopes must always be redistributed beforehand. To automate the whole calculation processes and to prevent errors, we developed the DCC calculation program `enrimo` introduced in Sec. 2.3.

As of `enrimo` v1.05, the following parameters can be specified by the user: (i) Mo materials, (ii) Mo isotope to be enriched, (iii) the fraction quantity to represent the enrichment level, (iv) range of enrichment levels to be examined, (v) minimum depletion levels of Mo isotopes, (vi) depletion order of Mo isotopes, (vii) calculation precision, and (viii) particles whose reactions on Mo isotopes will be associated with

the calculated DCCs.

To facilitate data exchange and analysis, `enrimo` has been designed to support multiple output formats, which include: columnar data (`.dat`), LaTeX 2_ε tabular environment (`.tex`), comma-separated values (`.csv`), MS EXCEL (`.xlsx`), JAVASCRIPT Object Notation (`.json`), and YAML (`.yaml`).

Calculation conditions

DCCs can be calculated for both theoretical and practical cases. Theoretical calculations are performed for a range of arbitrary mass or amount fractions of ^{100}Mo, and can be useful in understanding the physical meaning of DCC. Several sets of theoretical DCCs will be presented in the subsequent result section.

Practical DCCs, or simply DCCs, represent the DCCs that will be used in actual ^{99}Mo/^{99m}Tc production runs. Accordingly, DCCs must be calculated for existing enriched ^{100}Mo products; we calculated DCCs for nine commercial enriched ^{100}Mo products listed in Table 6.1. The two vendors mentioned in the table supply enriched ^{100}Mo products using gas centrifuges[108,109], which should be taken into account as follows.

Note that the actual force that separates gaseous isotopes is the centripetal force generated by a centrifuge.

When gaseous [$^{92,94–98,100}$Mo]Mo(VI) fluoride is fed into a chain of centrifuges, the light stream containing $^{92,94–98}$Mo are left behind in the centrifuges, and the heavy stream containing ^{100}Mo continues to travel through the centrifuge chain. Therefore, enrichment of ^{100}Mo means that the light stream is treated as the waste stream, and the heavy stream as the product stream. The degree to which the heavy and light streams are separated differs by the centrifugal conditions, leading to different $^{92,94–98}$Mo depletion levels and different ^{100}Mo enrichment levels in the ^{100}Mo product lines. To emulate such centrifugal enrichment of ^{100}Mo, our DCC calculation assumed that the $^{92,94–98}$Mo isotopes are depleted in ascending order of their mass numbers.

6.4 Results and discussion

Theoretical ^{100}Mo DCCs are presented in Fig. 6.7, where the dependence of ^{100}Mo DCC on the ^{100}Mo enrichment level is quantitatively described. Also, theoretical $^{92,94–98,100}$Mo DCCs are plotted in Figs. 6.8 and 6.9, showing the overall dependence of Mo DCCs on the ^{100}Mo enrichment level.

[108] Trace Sciences International. Modes of Production (2019).
[109] ISOFLEX. Stable isotopes produced in gas centrifuges (2019).

Table 6.1. Isotopic compositions of commercial enriched ^{100}Mo products used for DCC calculations. Table reproduced from our publication [15] which is licensed under CC BY 3.0.

Vendor	Reference	Amount percentage (%)						
		^{92}Mo	^{94}Mo	^{95}Mo	^{96}Mo	^{97}Mo	^{98}Mo	^{100}Mo
Trace[1]	[29]	0.005	0.005	0.005	0.005	0.01	2.58	97.39
	[31]	0.53	0.18	0.29	0.34	0.28	0.96	97.42
ISOFLEX[2]	[29]	0.09	0.06	0.1	0.11	0.08	0.55	99.01
	[49]	0.08	0.07	0.09	0.11	0.08	0.54	99.03
	[32]	0.08	0.05	0.1	0.11	0.07	0.54	99.05
	[30]	0.06	0.03	0.04	0.05	0.08	0.47	99.27
	[29]	0.006	0.0051	0.0076	0.0012	0.0016	0.41	99.54
	[35]	0.003	0.003	0.003	0.003	0.003	0.17	99.815
	[36]	0.005	0.005	0.005	0.005	0.005	0.115	99.86

[1] Trace Sciences International [107].
[2] ISOFLEX USA [106].

In its most basic sense, the DCC of a Mo isotope is the factor by which the amount of the Mo isotope in a given Mo target is modified as a result of a change of the ^{100}Mo enrichment level. One can, therefore, use a Mo DCC to estimate the degrees of changes in Mo reaction yields when an enriched ^{100}Mo is used. For instance, a ^{100}Mo DCC of $>$1.0 resulting from ^{100}Mo enrichment is a sign that the yields of the involved ^{100}Mo reactions will increase, and a ^{95}Mo DCC of $<$1.0 is a sign that the ^{95}Mo reaction yields will decrease. Generally speaking, high ^{100}Mo DCCs and low $^{92,94–98}$Mo DCCs are preferable in the ^{100}Mo-based ^{99}Mo/^{99m}Tc production reactions (Sec. 1.3).

Table 6.2 and Fig. 6.10 show the DCCs calculated for nine commercial enriched ^{100}Mo products. In Sec. 6.3.4, we explained that the ^{100}Mo density increment is higher in MoO_3 than in Mo_{met}. The same result was obtained in the DCC calculations: the ^{100}Mo DCCs were calculated to be greater in MoO_3 than in Mo_{met}. On the other hand, the $^{92,94–98}$Mo DCCs were almost the same in the two target materials.

The roles and importance of $^{92,94–98,100}$Mo DCCs differ by the ^{99}Mo/^{99m}Tc production methods. In both the ^{100}Mo(γ,n)^{99}Mo and ^{100}Mo(n,2n)^{99}Mo reaction routes, the major impurity radionuclides are Nb isotopes resulting from $^{92,94–98}$Mo[20,45,48,51]. Because Nb isotopes can be removed from ^{99}Mo/^{99m}Tc by chemical means[48,110], the

[20] K. Tsukada *et al. J. Phys. Soc. Jpn.* **87**, 043201 (2018).
[45] K. Mang'era *et al. J. Radioanal. Nucl. Chem.* **305**, 79–85 (2015).
[48] S. Sekimoto *et al. J. Radioanal. Nucl. Chem.* **311**, 1361–1366 (2017).
[51] T. Takeda *et al. J. Radioanal. Nucl. Chem.* **318**, 811–821 (2018).
[110] K. Ueno *et al. J. Nucl. Sci. Technol.* **6**, 203–206 (1969).

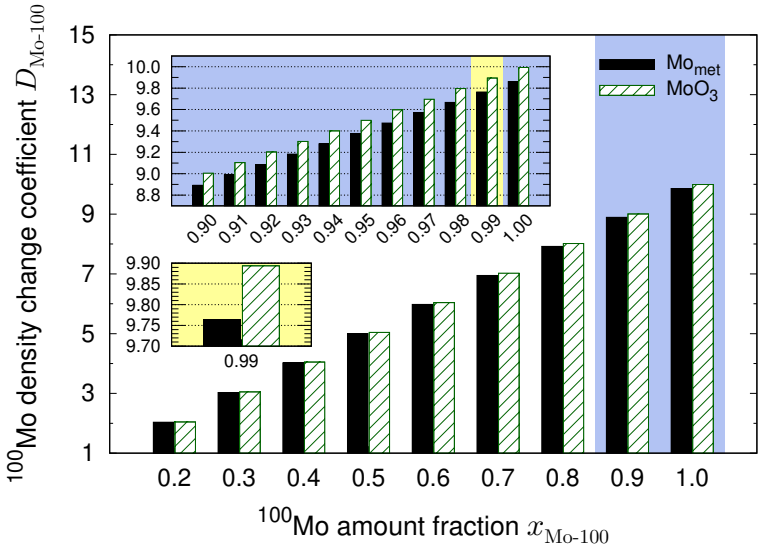

Fig. 6.7. Theoretical ^{100}Mo DCCs calculated for ^{100}Mo enrichment levels of 0.90–1.00.

^{99}Mo production routes can focus on ^{100}Mo DCCs.

^{100}Mo DCCs can be used as follows. If the ^{99}Mo yield of a nonenriched Mo$_{\text{met}}$ target obtained via the ^{100}Mo(γ,n)^{99}Mo reaction was

$$Y_{\text{Mo-99}}(0.0974) = 100.00\,\text{GBq},$$

the corresponding ^{99}Mo yield of 99.01% enriched ^{100}Mo can be simply calculated as

$$\begin{aligned} Y_{\text{Mo-99}}(0.9901) &= D_{\text{Mo-100}}(0.9901)\, Y_{\text{Mo-99}}(0.0974) \\ &= 9.7658 \times 100.00\,\text{GBq} = 976.58\,\text{GBq}. \end{aligned}$$

Similarly, if the ^{99}Mo specific yield of a nonenriched MoO$_3$ target was

$$S_{\text{Mo-99}}(0.0974) = 10.000\,\text{GBq Mo-g}^{-1},$$

using 99.54% enriched ^{100}Mo will lead to

$$\begin{aligned} S_{\text{Mo-99}}(0.9954) &= D_{\text{Mo-100}}(0.9954)\, S_{\text{Mo-99}}(0.0974) \\ &= 9.9468 \times 10.000\,\text{GBq Mo-g}^{-1} = 99.468\,\text{GBq Mo-g}^{-1}. \end{aligned}$$

The above examples suggest that a possible application of the DCC is to scale ^{99}Mo yields which have been (i) calculated or (ii) obtained from experiments using nonenriched Mo targets (Fig. 6.11). The option (ii) can be particularly useful: be-

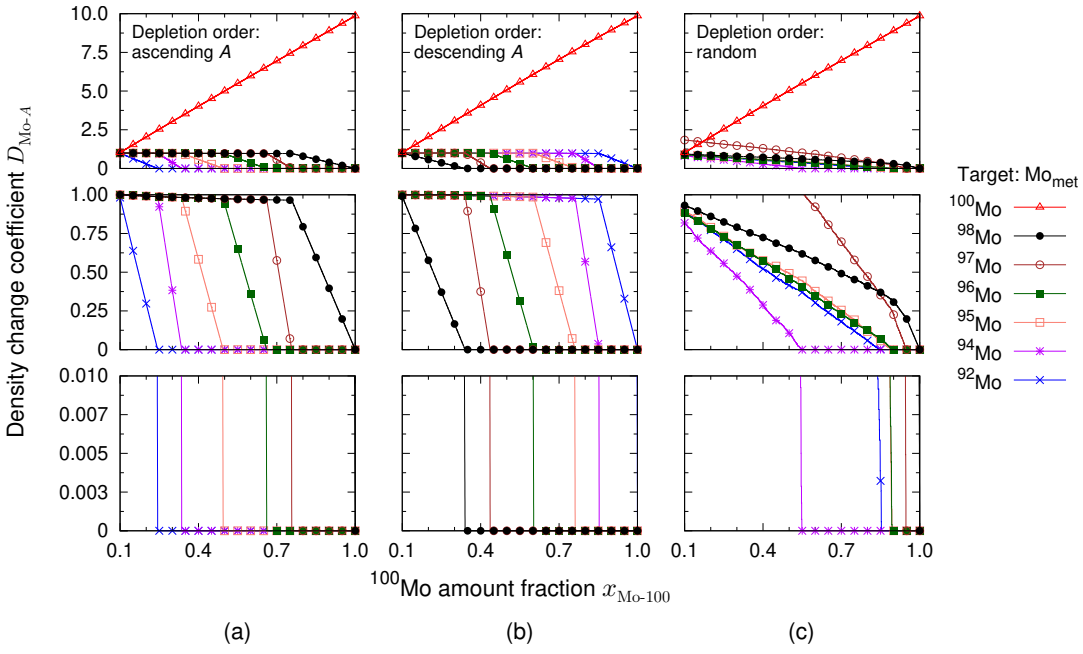

Fig. 6.8. Theoretical DCCs of $^{92,94–98,100}$Mo in Mo$_{\text{met}}$. The $^{92,94–98}$Mo isotopes were depleted in (a) ascending order of mass number, (b) descending order of mass number, and (c) random order.

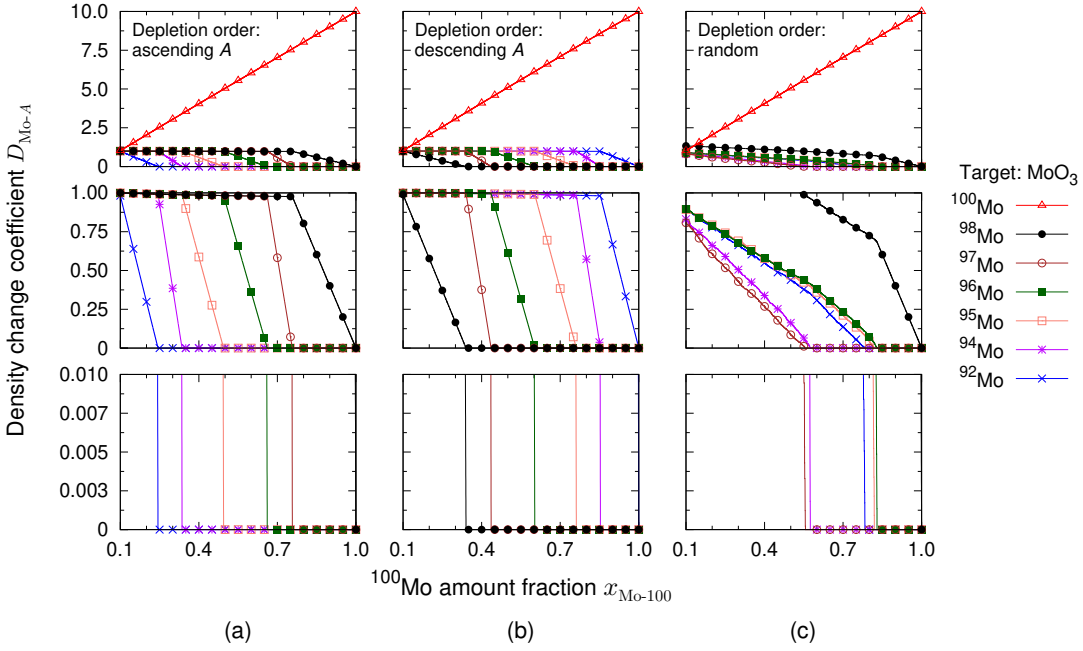

Fig. 6.9. Theoretical DCCs of $^{92,94–98,100}$Mo in MoO$_3$. The $^{92,94–98}$Mo isotopes were depleted in (a) ascending order of mass number, (b) descending order of mass number, and (c) random order.

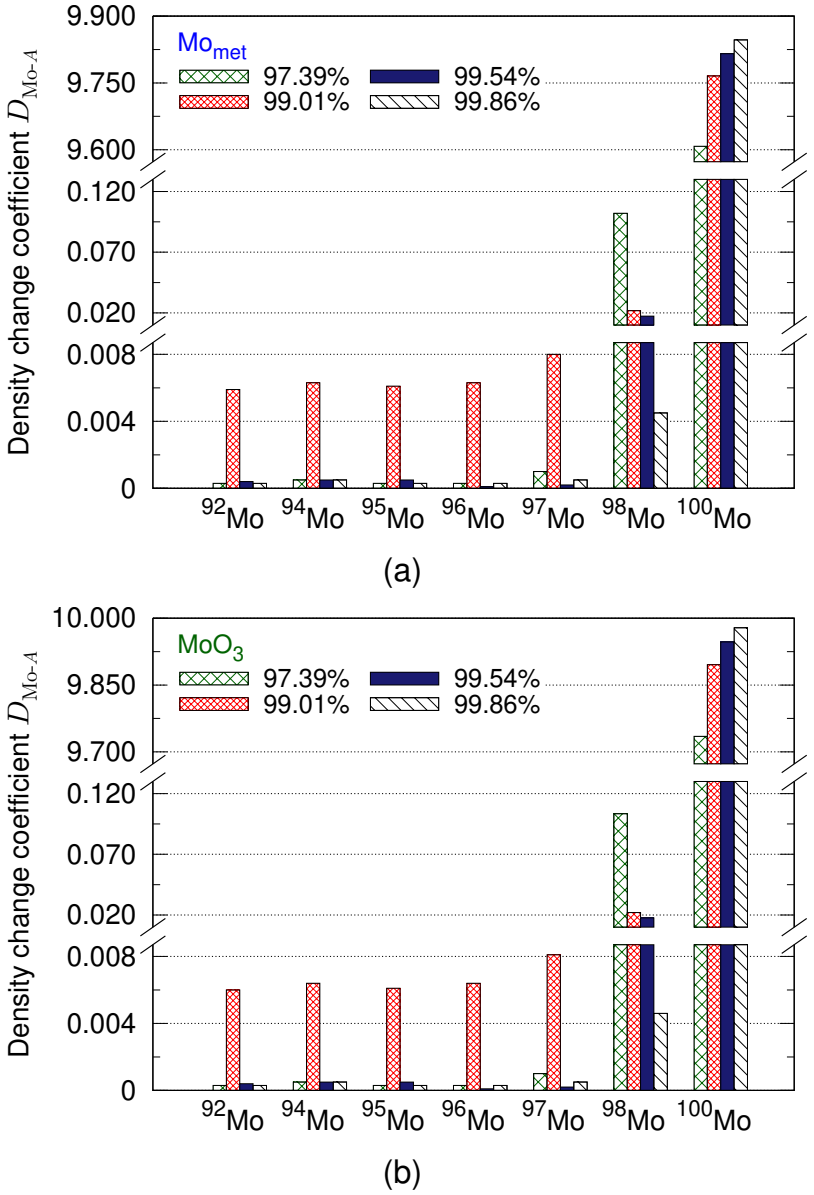

Fig. 6.10. DCCs of $^{92,94–98,100}$Mo in (a) Mo_{met} and (b) MoO_3. The percentages indicate ^{100}Mo enrichment levels. Note that the *y*-axes are not uniformly scaled in order to accommodate ^{98,100}Mo exhibiting relatively high DCCs. Figure reproduced from our publication [15] which is licensed under CC BY 3.0.

Table 6.2. DCCs of $^{92,94–98,100}$Mo calculated for the commercial enriched ^{100}Mo products listed in Table 6.1. Table reproduced from our publication [15] which is licensed under CC BY 3.0.

% $x^{\text{aft}}_{\text{Mo-100}}$	Density change coefficient						
	^{92}Mo	^{94}Mo	^{95}Mo	^{96}Mo	^{97}Mo	^{98}Mo	^{100}Mo
Trace, Mo target material: Mo_{met}							
97.39	0.0003	0.0005	0.0003	0.0003	0.0010	0.1021	9.6079
97.42	0.0348	0.0188	0.0176	0.0196	0.0281	0.0380	9.6162
ISOFLEX, Mo target material: Mo_{met}							
99.01	0.0059	0.0063	0.0061	0.0063	0.0080	0.0218	9.7658
99.03	0.0052	0.0073	0.0054	0.0063	0.0080	0.0214	9.7677
99.05	0.0052	0.0052	0.0061	0.0063	0.0070	0.0214	9.7695
99.27	0.0039	0.0031	0.0024	0.0029	0.0080	0.0186	9.7903
99.54	0.0004	0.0005	0.0005	0.0001	0.0002	0.0173	9.8157
99.815	0.0002	0.0003	0.0002	0.0002	0.0003	0.0067	9.8383
99.86	0.0003	0.0005	0.0003	0.0003	0.0005	0.0045	9.8466
Trace, Mo target material: MoO_3							
97.39	0.0003	0.0005	0.0003	0.0003	0.0010	0.1034	9.7348
97.42	0.0352	0.0191	0.0178	0.0199	0.0285	0.0385	9.7415
ISOFLEX, Mo target material: MoO_3							
99.01	0.0060	0.0064	0.0061	0.0064	0.0081	0.0220	9.8955
99.03	0.0053	0.0074	0.0055	0.0064	0.0081	0.0216	9.8974
99.05	0.0053	0.0053	0.0061	0.0064	0.0071	0.0216	9.8993
99.27	0.0040	0.0032	0.0025	0.0029	0.0081	0.0188	9.9207
99.54	0.0004	0.0005	0.0005	0.0001	0.0002	0.0176	9.9468
99.815	0.0002	0.0003	0.0002	0.0002	0.0003	0.0068	9.9698
99.86	0.0003	0.0005	0.0003	0.0003	0.0005	0.0046	9.9784

cause nonenriched Mo materials are easy to obtain, irradiation experiments can be repeatedly conducted so that statistically useful ^{99}Mo yield data can be accumulated. The experimental ^{99}Mo yield data can then be scaled for various ^{100}Mo enrichment levels using DCCs, which can in turn be used as the basis of selecting the actual ^{100}Mo enrichment level. This approach can be suitable in the ^{100}Mo(γ,n)^{99}Mo and ^{100}Mo(n,2n)^{99}Mo reaction routes, where the yields and specific yields of ^{99}Mo are the primary concern.

On the other hand, the $^{92,94–98}$Mo DCCs as well as the ^{100}Mo DCC must be considered in the ^{100}Mo(p,2n)^{99m}Tc reaction route. As shown in Table B.3, proton reactions on $^{92,94–98}$Mo isotopes result in production of Tc isotopes. Because the chemistries of Tc isotopes are almost identical to each other, ^{99m}Tc cannot be isolated from the

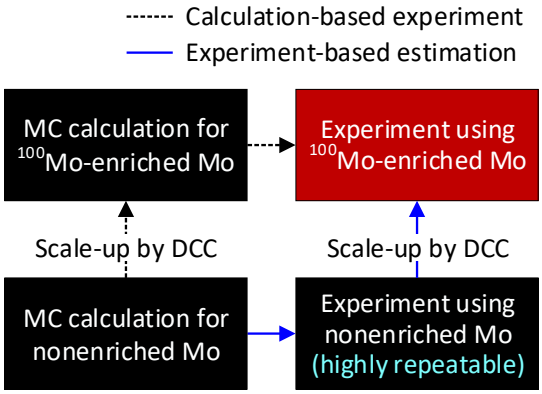

Fig. 6.11. A diagram for activity scale-ups using DCCs.

impurity Tc isotopes by chemical means. Especially undesirable Tc isotopes are the radioactive ones, which unnecessarily increase patient dose[29] and degrade image quality[34]. For these reasons, enriched ^{100}Mo products having low $^{92,94–98}$Mo DCCs as well as high ^{100}Mo DCCs are required in the ^{100}Mo(p,2n)^{99m}Tc reaction route.

The $^{94–97}$Mo DCCs are particularly important for proton beam energies of $<$20 MeV. In this energy range, the major reactions on $^{94–97}$Mo are their (p,n) and (p,2n) reactions, which lead to production of $^{93–96}$Tc (including their metastable isomers; see Table B.3). The $^{94–96}$Tc radioisotopes are especially harmful, as they exhibit half-lives of similar to or slightly longer than that of ^{99m}Tc. Indeed, studies of patient dose and image quality[29,34] reported that with $<$20 MeV proton beams used, the amounts of $^{94–97}$Mo isotopes contribute more than the amount of ^{98}Mo isotope to the dose increase and image quality degradation. Comparable results have also been reported by recent studies[37,38].

Based on the $^{94–96}$Tc production discussed above, we explain how $^{94–97}$Mo DCCs can be used in selecting an enriched ^{100}Mo product. Table 6.2 shows that all the $^{94–97}$Mo DCCs of the 97.39% enriched ^{100}Mo product are lower than those of the 97.42%, 99.01%, 99.03%, 99.05%, and 99.27% ones. This means that by using the 97.39% product, the amounts of $^{94–96}$Tc impurities can be reduced, even though the ^{99m}Tc yield will be slightly reduced. To be more specific, the ^{95}Mo DCC of the 97.39% product in the form of Mo_{met} is smaller than those of the 97.42%, 99.01%, 99.03%, 99.05%, and 99.27% products by factors of 8–58.7, while the ^{100}Mo DCCs differ only by factors of 1.001–1.019. This means that while the ^{99m}Tc yield remains almost unaffected, the

[29] X. Hou *et al. Phys. Med. Biol.* **57**, 1499–1515 (2012).
[34] X. Hou *et al. Phys. Med. Biol.* **61**, 8199–8213 (2016).
[37] N. M. Uzunov *et al. Phys. Med. Biol.* **63**, 185021 (2018).
[38] L. Meléndez-Alafort *et al. Med. Phys.* **46**, 1437–1446 (2019).

yields of proton reactions on ^{95}Mo, for example ^{95}Mo(p,2n)^{94}Tc and ^{95}Mo(p,n)^{95}Tc, can be reduced by factors of 8–58.7. The same is true for the ^{94,96,97}Mo reactions. The low $^{94–97}$Mo DCCs of 97.39% enriched ^{100}Mo can also be seen in Fig. 6.10.

The ^{98}Mo DCC should also be taken into account for proton beams of $\geq$20 MeV, at which the ^{98}Mo(p,3n)^{96}Tc and ^{98}Mo(p,3n)^{96m}Tc reaction channels open[24,28]. ^{96m}Tc deexcites to ^{96}Tc with 98% probability[111], and ^{96}Tc is one of the major impurities affecting the radiation dose and image quality[29,34,37,38]. Therefore, the 99.815% and 99.86% enriched ^{100}Mo products, whose ^{98}Mo DCCs as well as $^{92,94–97}$Mo DCCs are significantly lower than the other enriched ^{100}Mo products, are preferable for $\geq$20 MeV proton beams.

6.5 Summary and conclusion

In order to facilitate determining the enrichment level of ^{100}Mo and the depletion levels of $^{92,94–98}$Mo, we defined a figure of merit called the DCC. As a dimensionless and multiplicative factor, the DCC can be used to estimate Mo reaction yields as functions of the ^{100}Mo enrichment level. DCC calculations can be automatically performed using the dedicated program `enrimo` (Sec. 2.3).

In the ^{100}Mo(γ,n)^{99}Mo and ^{100}Mo(n,2n)^{99}Mo reaction paths, the advantage of using enriched ^{100}Mo is literally the increment of the ^{100}Mo content, whereas in the ^{100}Mo(p,2n)^{99m}Tc reaction path, the value of using enriched ^{100}Mo lies in the depletion of $^{92,94–98}$Mo as well as in the increment of ^{100}Mo. This is because in the ^{100}Mo(p,2n)^{99m}Tc reaction route, chemically inseparable Tc impurities originating from the $^{92,94–98}$Mo isotopes must be minimized. In both ^{99}Mo production and ^{99m}Tc production routes, the use of DCCs provides an easy and quantitative means of investigating the influence of enriched ^{100}Mo, which can be useful in selecting the ^{100}Mo product.

[28] A. Celler *et al. Phys. Med. Biol.* **56**, 5469–5484 (2011).
[111] National Nuclear Data Center. NuDat 2.7.

Chapter
7

Parameterized radioactive concentration

Abstract

The inability to use an alumina ^{99m}Tc generator with low specific activity ^{99}Mo stems from the resulting low radioactive concentration of ^{99m}Tc. Conversely, it is the ^{99m}Tc radioactive concentration that determines if a ^{99m}Tc generator can be used for medical imaging. To enable calculation of radioactive concentration with the issue of low specific activity ^{99}Mo considered, we parameterized the radioactive concentrations of alumina and activated carbon ^{99m}Tc generators, the latter of which was experimentally verified.

7.1 Introduction

As explained in Sec. 1.1, conventional ^{99m}Tc is supplied in the form of a chromatographic device referred to as a ^{99m}Tc generator. A ^{99m}Tc generator houses a column of acidic Al_2O_3, onto which fission-produced $[^{99}Mo]MoO_4^{2-}$ and its decay product $[^{99m}Tc]TcO_4^-$ are loaded. Exhibiting a weaker affinity for the Al_2O_3 column than that of $[^{99}Mo]MoO_4^{2-}$, the $[^{99m}Tc]TcO_4^-$ ions can be eluted by passing normal saline (0.9% w/v NaCl) through the Al_2O_3 column. If the ^{99}Mo-loaded Al_2O_3 column is immersed in saline, the ^{99m}Tc generator is called a wet-type generator. If, on the other hand, the Al_2O_3 column is dried and saline is passed from outside the generator, the generator is called a dry-type generator (Fig. 7.1).

The affinity difference between MoO_4^{2-} and TcO_4^-, however, is sufficient only for high specific activity (HSA) ^{99}Mo, which can only be obtained via the ^{235}U(n,f)^{99}Mo reaction (Fig. 1.2). The ^{100}Mo(γ,n)^{99}Mo reaction, on the other hand, unavoidably leads to low specific activity (LSA) ^{99}Mo, for which Al_2O_3 is no longer effective in

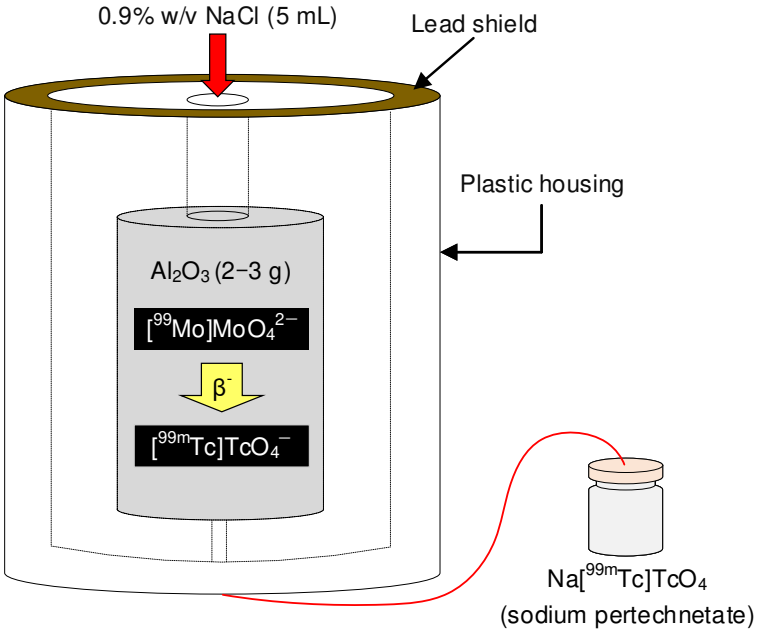

Fig. 7.1. An illustration of a dry-type alumina ^{99m}Tc generator. Figure adapted from our previous thesis [60].

separating ^{99}Mo/^{99m}Tc. Therefore, our ^{99}Mo/^{99m}Tc production system uses activated carbon (AC) as the alternative adsorbent.

It is the radioactive concentration (RAC) of ^{99m}Tc in which the root cause of the LSA issue lies, and that represents if a novel ^{99m}Tc generator, including the AC chromatographic device, can be used for medical imaging. To calculate the ^{99m}Tc RAC with the issue of LSA ^{99}Mo taken into account, we parameterized the ^{99m}Tc RAC of alumina and AC chromatography. By delving into the LSA issue, we will derive the parameterized RAC in the following section. A description of the AC chromatographic device and experimental verification of its parameterized RAC will follow.

7.2 The LSA issue: Revisited

Two figures of merit are important in addressing the issue of LSA ^{99}Mo. The first one is the specific activity of ^{99}Mo itself, which can be expressed as

$$S_{\text{Mo-99}}(t_{\text{irr}}, E_{\text{e}-}) \equiv \frac{A_{\text{Mo-99}}(t_{\text{irr}}, E_{\text{e}-})}{m_{\text{Mo}\ni\text{Mo-99}}} \neq \frac{A_{\text{Mo-99}}(t_{\text{irr}}, E_{\text{e}-})}{m_{\text{Mo-tar}\supset\text{Mo}\ni\text{Mo-99}}}, \tag{7.1}$$

where $A_{\text{Mo-99}}$ is the ^{99}Mo activity, m_{Mo} the mass of a Mo element, and $m_{\text{Mo-tar}}$ the mass of a Mo target.

Eq. (7.1) shows that the larger the amounts of Mo isotopes other than ^{99}Mo (see Fig. 6.1) are involved in the Mo element, the lower the specific activity of ^{99}Mo will be. In the fission reaction ^{235}U(n,f)^{99}Mo, the Mo element consists mostly of ^{99}Mo, and the absolute value of $A_{\text{Mo-99}}$ is large. Therefore, the specific activity of fission ^{99}Mo can be as high as 1.85×10^5 GBq Mo-g^{-1}[54], and is referred to as HSA ^{99}Mo. By contrast, the photonuclear reaction ^{100}Mo(γ,n)^{99}Mo is associated with (i) various Mo isotopes and (ii) small $A_{\text{Mo-99}}$ compared with the ^{235}U(n,f)^{99}Mo reaction (see Fig. 1.4(b) for their cross section differences). Thus, the ^{99}Mo specific activity of ^{100}Mo(γ,n)^{99}Mo is smaller than that of ^{235}U(n,f)^{99}Mo by 2–3 orders of magnitude[54,87], and is referred to as LSA ^{99}Mo.

The second figure of merit important in the LSA issue is the RAC of a [^{99m}Tc]TcO_4^- eluate, which is defined as[112]

$$C_{\text{Tc-99m}} \equiv \frac{A_{\text{Tc-99m}}}{\mathcal{V}_{\text{liq}}}, \tag{7.2}$$

where $\mathcal{V}_{\text{liq}}$ is the volume of a liquid solution in which [^{99m}Tc]TcO_4^-(l) is contained. Here, it must be noted that the $A_{\text{Tc-99m}}$ of Eq. (7.2) is the activity of a TcO_4^- eluate, which differs from the activity of TcO_4^- *within* the adsorbent column. The two ^{99m}Tc activities are related by the elution efficiency (Eq. (3.35)):

$$A_{\text{Tc-99m,eluate}} = \zeta A_{\text{Tc-99m,column}}, \tag{7.3}$$

by which Eq. (7.2) can be rewritten as

$$C_{\text{Tc-99m}} = \frac{\zeta A_{\text{Tc-99m,column}}}{\mathcal{V}_{\text{liq}}},$$

or

$$C_{\text{Tc-99m}} = \frac{\zeta A_{\text{Tc-99m,column}}}{\mathcal{V}_{\text{NaCl(aq)}} + \mathcal{V}_{MoO_4^{2-}\text{(l)}} + \mathcal{V}_{TcO_4^-\text{(l)}}}. \tag{7.4}$$

Denoting the ratio of $A_{\text{Tc-99m,column}}$ to $A_{\text{Mo-99,column}}$ as $r^{\text{column}}_{\text{Tc-99m/Mo-99}}$, and using

[54] International Atomic Energy Agency. *Non-HEU Production Technologies for Molybdenum-99 and Technetium-99m* (2013).
[87] J. Jang *et al.* Photonuclear production of Mo-99/Tc-99m using molybdenum trioxide and activated carbon (2017).
[112] J. J. M. de Goeij *et al. J. Radioanal. Nucl. Chem.* **263**, 13–18 (2005).

Eq. (7.3), we further modify Eq. (7.4) as

$$C_{\text{Tc-99m}} = \frac{\zeta r^{\text{column}}_{\text{Tc-99m/Mo-99}} A_{\text{Mo-99,column}}}{\mathcal{V}_{\text{NaCl(aq)}} + \mathcal{V}_{{\text{MoO}_4}^{2-}\text{(l)}} + \mathcal{V}_{{\text{TcO}_4}^{-}\text{(l)}}}. \tag{7.5}$$

In general, $\mathcal{V}_{{\text{MoO}_4}^{2-}\text{(l)}}$ and $\mathcal{V}_{{\text{TcO}_4}^{-}\text{(l)}}$ are much smaller than $\mathcal{V}_{\text{NaCl(aq)}}$ and, ideally, $\mathcal{V}_{{\text{MoO}_4}^{2-}\text{(l)}}$ is marginal compared with $\mathcal{V}_{{\text{TcO}_4}^{-}\text{(l)}}$. That is, it should hold that $\mathcal{V}_{\text{NaCl(aq)}} \gg \mathcal{V}_{{\text{TcO}_4}^{-}\text{(l)}} \gg \mathcal{V}_{{\text{MoO}_4}^{2-}\text{(l)}}$. Besides, for ^{99}Mo/$^{99\text{m}}$Tc where the transient equilibrium has been achieved, $r^{\text{column}}_{\text{Tc-99m/Mo-99}}$ becomes equal to the ^{99}Mo-to-$^{99\text{m}}$Tc branching fraction B (Eq. (3.32)).

Plugging Eq. (7.1) into Eq. (7.5), we obtain the parameterized RAC of conventional alumina chromatography:

$$C_{\text{Tc-99m}} = \frac{\zeta r^{\text{column}}_{\text{Tc-99m/Mo-99}} S_{\text{Mo-99}} m_{\text{Mo}}}{\mathcal{V}_{\text{NaCl(aq)}} + \mathcal{V}_{{\text{MoO}_4}^{2-}\text{(l)}} + \mathcal{V}_{{\text{TcO}_4}^{-}\text{(l)}}}, \tag{7.6}$$

which can now explain the root cause of the inability to use Al_2O_3 in ^{99}Mo/$^{99\text{m}}$Tc separation. The explanation is as follows.

(1) The amount of ${MoO_4}^{2-}$ that can be loaded onto a column of Al_2O_3, or the adsorption capacity of an Al_2O_3 column, is fixed, and so is m_{Mo}: typical acidic Al_2O_3 exhibits adsorption capacities of 2–20 mg ${MoO_4}^{2-}$ per g Al_2O_3[7,18], and a typical $^{99\text{m}}$Tc generator contains 2–3 g of acidic Al_2O_3[54]. Therefore, a typical alumina generator contains 4–60 mg of [^{99}Mo]${MoO_4}^{2-}$, or m_{Mo} = 2.4–36 mg.

(2) As explained, $S_{\text{Mo-99}}$ of ^{100}Mo(γ,n)^{99}Mo is smaller than that of ^{235}U(n,f)^{99}Mo by 2–3 orders of magnitude.

(3) Because of the two terms m_{Mo} and $S_{\text{Mo-99}}$ explained above, $C_{\text{Tc-99m}}$ of the ^{100}Mo(γ,n)^{99}Mo is fundamentally small compared with that of ^{235}U(n,f)^{99}Mo.

(4) The activity of $^{99\text{m}}$Tc eluate $A_{\text{Tc-99m,eluate}}$ (= $A_{\text{Tc-99m}}$ in Eq. (7.2)) itself can be increased by increasing the amount of Al_2O_3 per column and thereby m_{Mo}. This will, however, increase the elution volume, or $\mathcal{V}_{\text{NaCl(aq)}}$, and such increased $\mathcal{V}_{\text{NaCl(aq)}}$ will overtake increased $A_{\text{Tc-99m,eluate}}$, decreasing the $C_{\text{Tc-99m}}$ after all.

Consequently, as long as the conventional acidic alumina is used, $C_{\text{Tc-99m}}$ will remain low. Low $C_{\text{Tc-99m}}$, in turn, precludes the medical use of the [$^{99\text{m}}$Tc]${TcO_4}^{-}$: because conventional $^{99\text{m}}$Tc radiopharmaceuticals (Table 1.1) have been designed to react with certain volumes of ${TcO_4}^{-}$(l), typically 1–9 mL, low $C_{\text{Tc-99m}}$ will result in low $A_{\text{Tc-99m}}$ of $^{99\text{m}}$Tc radiopharmaceuticals. A $^{99\text{m}}$Tc radiopharmaceutical with low $^{99\text{m}}$Tc activity

[7] V. J. Molinski. *Int. J. Appl. Radiat. Isot.* **33**, 811–819 (1982).
[18] A. Dash *et al. Nucl. Med. Biol.* **40**, 167–176 (2013).

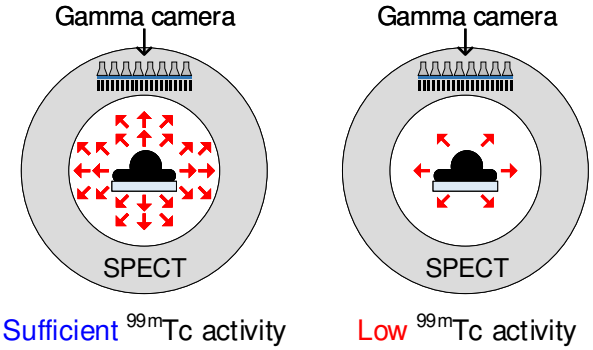

Fig. 7.2. An illustration of sufficient and low ^{99m}Tc activities of ^{99m}Tc radiopharmaceuticals.

means that its gamma-ray intensity emitted from the patient body will be insufficient for generating diagnostic images (Fig. 7.2).

For instance, if we have $C_{\text{Tc-99m}} = 148\,\text{MBq}\,\text{mL}^{-1}$, labeling a pharmaceutical using 5 mL of the $[^{99m}\text{Tc}]\text{TcO}_4^-$(l) will result in $(148\,\text{MBq}\,\text{mL}^{-1})(5\,\text{mL}) = 740\,\text{MBq}$. This 740 MBq will be the activity of the ^{99m}Tc radiopharmaceutical, and will generate sufficient radiation signals. If, on the other hand, the RAC was only $C_{\text{Tc-99m}} = 0.148\,\text{MBq}\,\text{mL}^{-1}$ and 5 mL of it was used for labeling, the resulting activity of the ^{99m}Tc radiopharmaceutical will be 0.74 MBq, which is insufficient for generating nuclear diagnostic images.

Three methods can solve the LSA issue, the first of which is to increase $S_{\text{Mo-99}}$ (Eq. (7.6)). This can be achieved by increasing $Y_{\text{Mo-99}}$ (Eqs. (2.1) and (3.5)) via a high beam energy (Chap. 3), high beam current (Chap. 3), long irradiation time (Chap. 3), geometric design of the targetry (Chaps. 4 and 5), and use of enriched ^{100}Mo (Chap. 6), all of which have been addressed in this dissertation.

The second option is to develop adsorbents having higher adsorption capacities than conventional acidic Al_2O_3, and thereby increasing m_{Mo} per column[113,114].

The last method is to directly increase the RAC of a $[^{99m}\text{Tc}]\text{TcO}_4^-$ eluate by $[^{99m}\text{Tc}]\text{TcO}_4^-$ concentration. The concentration can be performed either before or after[115–117] the final elution of $[^{99m}\text{Tc}]\text{TcO}_4^-$, the former of which is addressed in this dissertation. In such pre-elution ^{99m}Tc concentration, $[^{99m}\text{Tc}]\text{TcO}_4^-$ ions are concentrated in a special column *before* the final elution of ^{99m}Tc, and therefore

[113] M. Tanase *et al. Appl. Radiat. Isot.* **48**, 607–611 (1997).
[114] R. Chakravarty *et al. Nucl. Med. Biol.* **39**, 916–922 (2012).
[115] S. K. Sarkar *et al. Appl. Radiat. Isot.* **55**, 561–567 (2001).
[116] S. Chattopadhyay *et al. Appl. Radiat. Isot.* **66**, 1295–1299 (2008).
[117] T. H. Bokhari *et al. J. Radioanal. Nucl. Chem.* **279**, 281–285 (2009).

$A_{\text{Tc-99m,column}}$ is increased (Eq. (7.4)). In this case, $A_{\text{Tc-99m,column}}$ is no longer dictated by $A_{\text{Mo-99,column}}$, but by the efficiency of ^{99m}Tc concentration ψ_{conc}:

$$\begin{aligned} A_{\text{Tc-99m,column}} &= \sum_n A_{\text{Tc-99m,column},n} \\ &= \psi_{\text{conc}} \sum_n A_{\text{Tc-99m,solution},n}, \end{aligned} \tag{7.7}$$

where $A_{\text{Tc-99m,solution},n}$ is the ^{99m}Tc activity exists in the $[^{99}\text{Mo}]\text{MoO}_4^{2-}$ solution at a concentration run n.

Eq. (7.7) signifies that regardless of the ^{99}Mo specific activity of a $[^{99}\text{Mo}]\text{MoO}_4^{2-}$ solution, most of the associated ^{99m}Tc activity can be transferred to a $[^{99m}\text{Tc}]\text{TcO}_4^-$ concentration column, by increasing ψ_{conc} or n. Once the $[^{99m}\text{Tc}]\text{TcO}_4^-$ concentration is completed, the column ^{99m}Tc activity can be extracted by chemical treatment. Consequently, the RAC of a ^{99m}Tc eluate obtained from a pre-elution concentrator can be expressed as

$$C_{\text{Tc-99m}} = \frac{\zeta \psi_{\text{conc}} \sum_n A_{\text{Tc-99m,solution},n}}{\mathcal{V}_{\text{liq}}}, \tag{7.8}$$

which can be obtained by inserting Eq. (7.7) into Eq. (7.4).

Novel ^{99m}Tc generators using the aqueous biphasic extraction chromatographic (ABEC) resin[118–124] and AC[48,86,87,125] are essentially pre-elution ^{99m}Tc concentrators integrated with the subsequent ^{99m}Tc elution modules, and our ^{99}Mo/^{99m}Tc production system uses the AC method. The following section will explain the process of AC chromatography and its parameterized RAC.

7.3 AC chromatography

When given a solution of $[^{99}\text{Mo}]\text{MoO}_4^{2-}$ and $[^{99m}\text{Tc}]\text{TcO}_4^-$, a column of AC selectively captures $[^{99m}\text{Tc}]\text{TcO}_4^-$ ions in its surfaces (Fig. 7.3(a)). Discovering and utilizing this phenomenon, Kaken Inc., one of our collaborators, has developed an

[118] R. D. Rogers *et al.* *Appl. Radiat. Isot.* **47**, 497–499 (1996).
[119] R. Rogers *et al.* US5603834 (1997).
[120] R. D. Rogers *et al.* *Sep. Sci. Technol.* **32**, 867–882 (1997).
[121] R. D. Rogers *et al.* *Solvent Extr. Ion Exch.* **15**, 547–562 (1997).
[122] E. P. Horwitz *et al.* US6998052 (2006).
[123] D. R. McAlister *et al.* *Appl. Radiat. Isot.* **67**, 1985–1991 (2009).
[124] P. Tkac *et al.* *J. Radioanal. Nucl. Chem.* **308**, 205–212 (2016).
[48] S. Sekimoto *et al.* *J. Radioanal. Nucl. Chem.* **311**, 1361–1366 (2017).
[86] K. Tatenuma *et al.* *RADIOISOTOPES* **63**, 501–513 (2014).
[125] K. Tatenuma *et al.* US9236153 (2016).

AC chromatographic device called Technetium Master Milker (TcMM)[48,86,87,125]. A prototype device is shown in Fig. 7.3(b).

7.3.1 $[^{99m}Tc]TcO_4^-$ concentration and elution

The $[^{99m}Tc]TcO_4^-$ concentration and elution of the TcMM are performed in the following seven steps[48,86].

① *Adsorption of $[^{99m}Tc]TcO_4^-$ on AC.* A solution containing $[^{99}Mo]MoO_4^{2-}$ and $[^{99m}Tc]TcO_4^-$ is passed through an AC column at a rate of 50–200 mL min^{-1}. As a result, the $[^{99m}Tc]TcO_4^-$ ions adsorb onto the AC surfaces, while the $[^{99}Mo]MoO_4^{2-}$ ions pass through the AC column without adsorption. The selective adsorption of $[^{99m}Tc]TcO_4^-$ on the AC column is attributed to their hydrophobicity. The $[^{99}Mo]MoO_4^{2-}$ solution is then collected into a separate vessel, which is repassed through a new AC column after a sufficient amount of ^{99m}Tc has been generated from the decay of ^{99}Mo.

② *Removal of $[^{99}Mo]MoO_4^{2-}$ from AC.* In the step ① above, a small fraction of the $[^{99}Mo]MoO_4^{2-}$ ions are retained together with the $[^{99m}Tc]TcO_4^-$ ions in the AC surfaces. To minimize the Mo breakthrough in the final ^{99m}Tc eluate, the remnant $[^{99}Mo]MoO_4^{2-}$ ions are removed by passing 50-mL distilled water through the AC column. The flow rate is 50 mL min^{-1}.

③ *Alkalinization of AC.* To enable $[^{99m}Tc]TcO_4^-$ elution from the AC column, the AC column is impregnated with 15 mL of 6-*M* NaOH. The flow rate of NaOH is 10 mL min^{-1}.

④ *Removal of excessive alkali from $[^{99m}Tc]TcO_4^-$.* By passing distilled water through the AC column, where $[^{99m}Tc]TcO_4^-$ ions are retained, the excessive OH^- ions in the $[^{99m}Tc]TcO_4^-$ solution resulting from the step ③ above are removed. 9 mL of distilled water is passed at a flow rate of 10 mL min^{-1}.

⑤ *$[^{99m}Tc]TcO_4^-$ elution from AC and adsorption to AA.* Now that the AC has been alkalinized by NaOH in the step ③ above, the $[^{99m}Tc]TcO_4^-$ ions can be eluted from the AC column using distilled water. 50-mL distilled water is passed through the AC column at a rate of 10 mL min^{-1}, by which a weak alkaline solution of $[^{99m}Tc]TcO_4^-$ is eluted from the AC column and is subsequently passed through the columns of strong acidic IER and weak acidic AA. Consequently, the $[^{99m}Tc]TcO_4^-$ solution is neutralized by the acidic IER, and the $[^{99m}Tc]TcO_4^-$ ions are weakly bound to the surfaces of acidic AA. The remnant $[^{99}Mo]MoO_4^{2-}$ ions and Nb impurities are also trapped by the AA column.

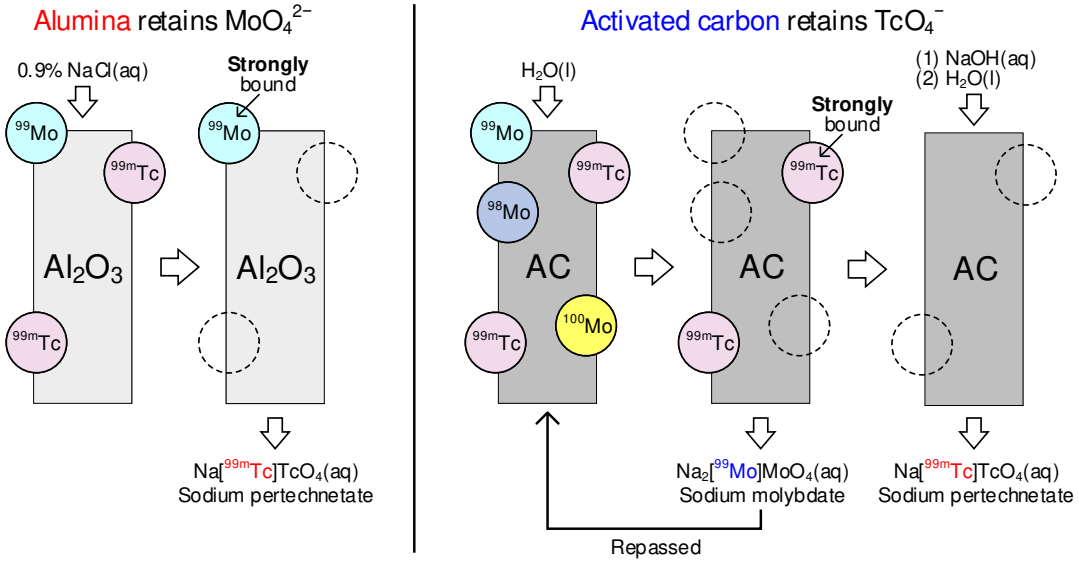

(a)

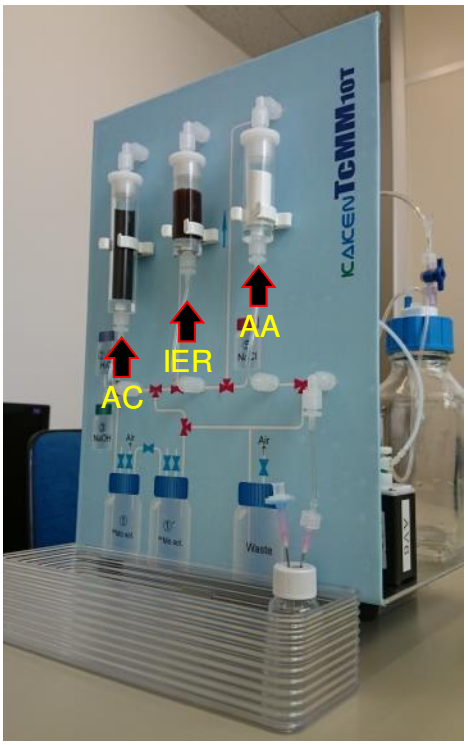

(b)

Fig. 7.3. (a) ^{99}Mo/^{99m}Tc adsorption characteristics of alumina and activated carbon. (b) A prototype AC chromatographic device. AC: activated carbon; IER: ion exchange resin; and AA: activated alumina. Figure (b) courtesy of Kaken Inc., Japan.

⑥ *AA rinsing*. Because the first 2 mL of a saline eluent does not elute $[^{99m}\mathrm{Tc}]\mathrm{TcO_4}^-$ from the AA column, 2 mL of 1.0% w/v NaCl is passed through the AA column at a rate of 10 mL min^{-1} and is discarded. Through this step, the RAC of the final ^{99m}Tc eluate can be increased.

⑦ *$[^{99m}Tc]TcO_4^-$ elution from AA*. Finally, 10 mL of 1.0% w/v NaCl is passed through the AA column at a rate of 10 mL min^{-1}, eluting ^{99m}Tc in the form of $\mathrm{Na}[^{99m}\mathrm{Tc}]\mathrm{TcO_4(aq)}$. By the use of 1.0% w/v saline, the salinity of the final ^{99m}Tc eluate is adjusted to 0.9% w/v. A variation run is to perform ⑥ and ⑦ simultaneously; that is, passing 12 mL of 1.0% saline through the AA column is also an option.

As a result, a $[^{99m}\mathrm{Tc}]\mathrm{TcO_4}^-$ solution of neutral pH and of 0.9% salinity is obtained. The time required for the steps ①–⑦ above is 20–30 min.

In addition, the used column packing materials are as follows.

(i) *Activated carbon*. 4.5 g of coconut shell-based AC having particle sizes of 0.300–0.850 mm (SHIRASAGI, Osaka Gas Chemicals Co. Ltd., Japan) is used.

(ii) *Ion exchange resin*. A strong acidic IER is obtained by acidifying IER with HCl. The particle size and amount of the IER are 0.15 mm and 6 g, respectively.

(iii) *Activated alumina*. Weak acidic (pH 4.3) AA is used. The particle size and amount of the AA are 0.063–0.20 mm and 6 g, respectively. By doubling the amount of AA, the use of IER can be omitted.

7.3.2 Parameterized RAC of AC chromatography

Because of its large $\mathrm{TcO_4}^-$ selectivity, the ^{99m}Tc concentration efficiency of AC can be approximated to 100%, or $\psi_{\mathrm{conc}} \approx 1$. Only one cycle of pre-elution ^{99m}Tc concentration will then suffice, by which Eq. (7.8) reduces to

$$C_{\text{Tc-99m}} = \frac{\zeta A_{\text{Tc-99m,solution}}}{\mathcal{V}_{\text{liq}}}. \tag{7.9}$$

A comparison of Eqs. (7.4) and (7.9) suggests that by combining its one-time ^{99m}Tc concentration and the subsequent ^{99m}Tc elution (Sec. 7.3.1), AC chromatography can be used much like the conventional alumina chromatography.

In order to verify the parameterized RAC of AC chromatography, or Eq. (7.9), we conducted ^{99m}Tc elution experiments.

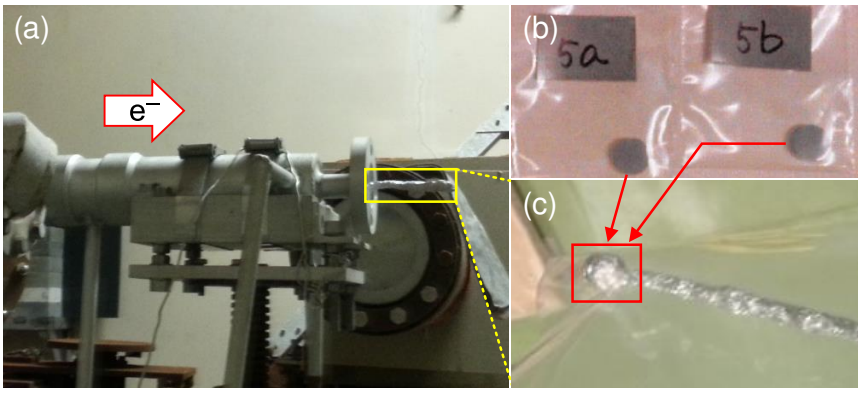

Fig. 7.4. MoO_3 targets (a) set at the beam exit, and (b) before and (c) after irradiation.

7.4 Experimental verification

The experiments of AC chromatography were conducted in collaboration with Kaken Inc. The experimental steps were much the same as the ones we used in Sec. 5.3; the biggest difference was that prior to gamma-ray spectrometry, $[^{99m}Tc]TcO_4^-$ ions were separated from $[^{99}Mo]MoO_4^{2-}$ solutions using AC chromatography.

7.4.1 Materials and methods

MoO_3 targets

As in Sec. 5.3.1, MoO_3 targets were prepared using nonenriched MoO_3 powder (99.99% purity, Kojundo Chemical Laboratory Co., Ltd., Japan) and a PECS machine. Six cylindrical MoO_3 targets of 10.2–10.3 mm in diameter and 2.9–3.0 mm in thickness were prepared. The density ratios of the MoO_3 targets (Eq. (2.2)) were $\xi = 0.781$–0.918.

Irradiation

The MoO_3 targets were irradiated using an L-band electron linac (Fig. 7.4(a)) at the KURNS, the then Kyoto University Research Reactor Institute (KURRI).

The electron beam energies and irradiation times were 35 MeV and 10 min, respectively, for all the six MoO_3 targets.

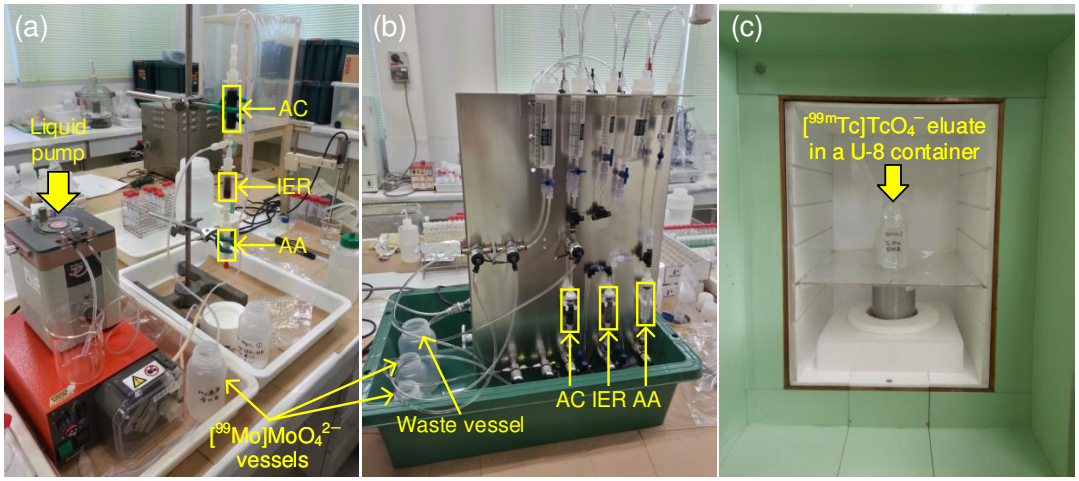

Fig. 7.5. (a) Manually operated and (b) automatic AC chromatographic devices, and (c) one of the obtained $[^{99m}\mathrm{Tc}]\mathrm{TcO_4}^-$ eluates placed in a germanium detector.

Postirradiation processing

The same processing shown in Fig. 5.15 was performed for gamma-ray spectrometry: namely, irradiated MoO_3 targets were dissolved using 6-*M* NaOH solutions, and the resulting $MoO_4{}^{2-}$ solutions were diluted to reduce the dead time t_{dead} and to reduce the worker dose.

Manual and automatic AC chromatographic devices

Manual and automatic AC chromatographic devices were tested (Fig. 7.5), both of which had the same procedures as the ones explained in Sec. 7.3.1.

Gamma-ray spectrometry

The gamma rays of $MoO_4{}^{2-}$, $TcO_4{}^-$, liquid residues, and the columns and their rinsings were measured using a germanium detector (Fig. 7.5(c)) for live times of $t_{\mathrm{live}} = 300$–$600\,\mathrm{s}$. The measured gamma counts were subsequently converted to activities using the efficiency curve of the detector.

7.4.2 Results and discussion

Parts of the gamma-ray spectra obtained from the manually operated AC chromatography are presented in Figs. 7.6 and 7.7, and those obtained from the automatic AC chromatography in Figs. 7.8 and 7.9.

During the AC chromatography, not only the $[^{99}\text{Mo}]\text{MoO}_4^{2-}$ ions, but also Nb radioisotopes such as ^{92m,95,95m,96}Nb (Table B.1) were removed from the $[^{99m}\text{Tc}]\text{TcO}_4^-$ eluate. The resulting high radionuclidic purities are clearly shown in Fig. 7.6(c) and Fig. 7.8(c). Also, Fig. 7.6(b) shows that the first 2 mL of 1% saline eluent did not contain $[^{99m}\text{Tc}]\text{TcO}_4^-$, as explained in Sec. 7.3.1.

The average ^{99m}Tc elution efficiency was 85.0% in the manual AC chromatography, and 81.2% in the automatic one. The decreased elution efficiency is attributed to reduced elution times: the manual runs took 40 min on average, whereas the automatic ones took 20 min on average. On top of that, because the volumes of $[^{99m}\text{Tc}]\text{TcO}_4^-$ eluates were 10 mL in the manual runs and 12 mL in the automatic runs, Eq. (7.9) can be used as

$$C_{\text{Tc-99m}} = \frac{0.850 A_{\text{Tc-99m,solution}}}{10\,\text{mL}}, \qquad C_{\text{Tc-99m}} = \frac{0.812 A_{\text{Tc-99m,solution}}}{12\,\text{mL}},$$
$$C_{\text{Tc-99m}} = \frac{0.0850 A_{\text{Tc-99m,solution}}}{\text{mL}}, \qquad C_{\text{Tc-99m}} = \frac{0.0677 A_{\text{Tc-99m,solution}}}{\text{mL}}. \tag{7.10}$$

$A_{\text{Tc-99m}}$ can be calculated from $A_{\text{Mo-99}}$; see Eq. (3.34).

Using Eq. (7.10), the ^{99m}Tc RAC of can be calculated immediately when either $A_{\text{Tc-99m}}$ or $A_{\text{Mo-99}}$ becomes known. For example, one of the $[^{99m}\text{Tc}]\text{TcO}_4^-$ eluates obtained from the manual AC chromatography had a measured activity of $A_{\text{Tc-99m,solution}} = 6.76$ kBq at the time of elution, of which the RAC can be calculated as

$$C_{\text{Tc-99m}} = \frac{(0.0850)(6.76\,\text{kBq})}{\text{mL}} = 0.575\,\text{kBq}\,\text{mL}^{-1},$$

which agrees well with our empirical data.

Providing a means of immediate calculation of ^{99m}Tc RAC with the LSA issue considered, the parameterized RAC can be useful in setting the irradiation conditions of electron linac production of ^{99}Mo/^{99m}Tc.

7.5 Summary

In this chapter, we parameterized the $[^{99m}\text{Tc}]\text{TcO}_4^-$ RAC of alumina chromatography (Eq. (7.6)), pre-elution ^{99m}Tc concentrator (Eq. (7.8)), and AC chromatography (Eq. (7.9)). Used simultaneously, the two types of parameterized RAC can be useful in addressing the LSA issue.

As can be seen in Eqs. (7.8) and (7.9), the parameterized RAC of a pre-elution ^{99m}Tc concentrator is free of the ^{99}Mo specific activity and free of the amount of $[^{99}\text{Mo}]\text{MoO}_4^{2-}$ adsorbate, signifying that the LSA problem can be circumvented by

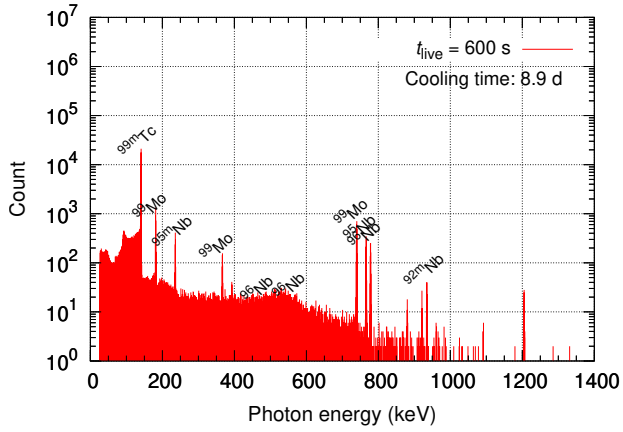

(a)

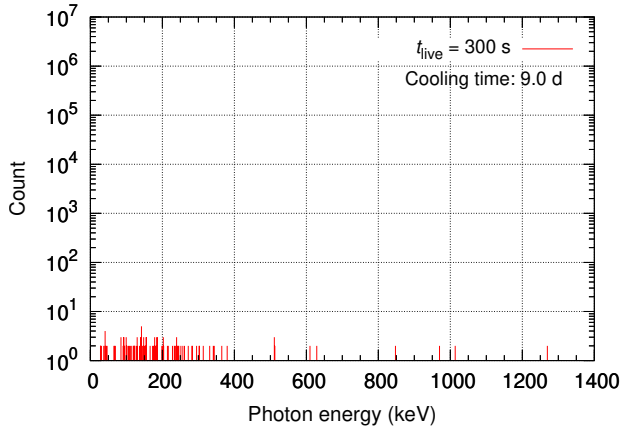

(b)

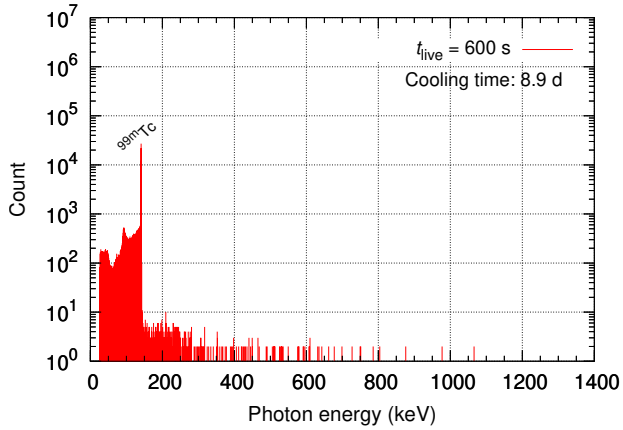

(c)

Fig. 7.6. Gamma-ray spectra for manually operated AC chromatography (see Sec. 7.3.1). (a) $[^{99}\mathrm{Mo}]MoO_4^{2-}$ solution before $[^{99m}\mathrm{Tc}]TcO_4^-$ elution; (b) step ⑥ ··· 2-mL saline rinsings of the AA column; and (c) step ⑦ ··· 10-mL $[^{99m}\mathrm{Tc}]TcO_4^-$ eluate.

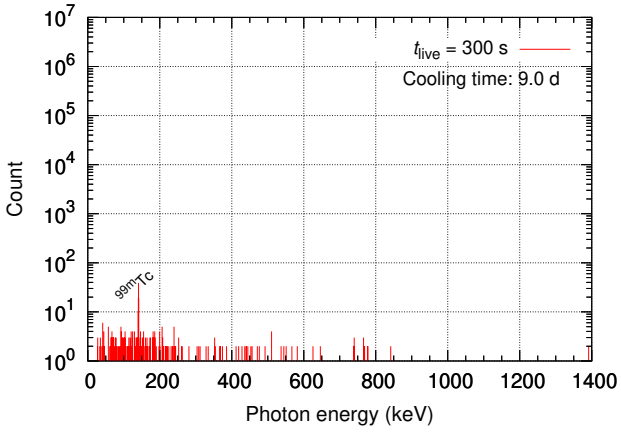

(a)

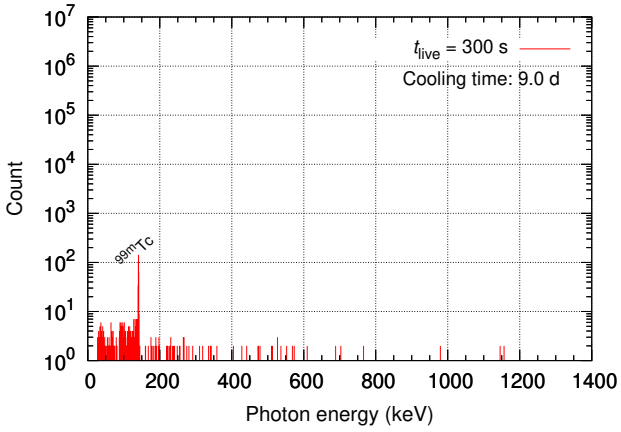

(b)

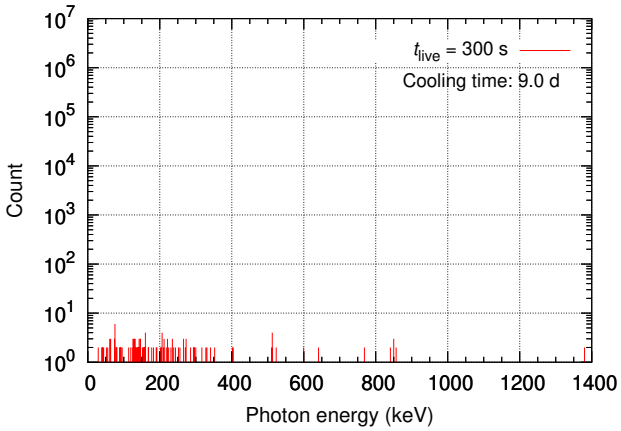

(c)

Fig. 7.7. Gamma-ray spectra for manually operated AC chromatography. (a) Step ③ ··· residue of NaOH used for AC alkalinization; (b) step ④ ··· distilled water used for OH^- removal from $[^{99m}Tc]TcO_4^-$; and (c) step ⑤ ··· distilled water used for $[^{99m}Tc]TcO_4^-$ elution from the AC column.

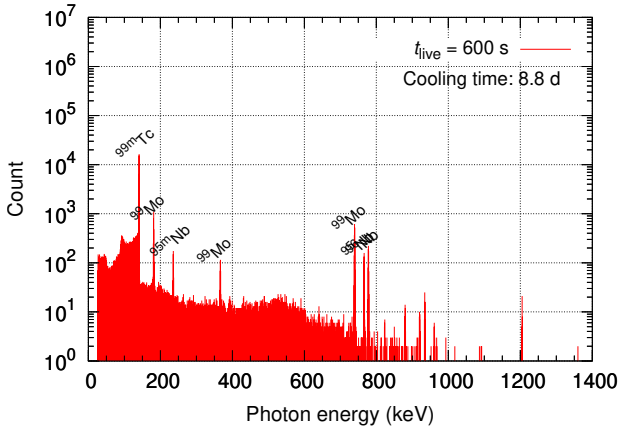

(a)

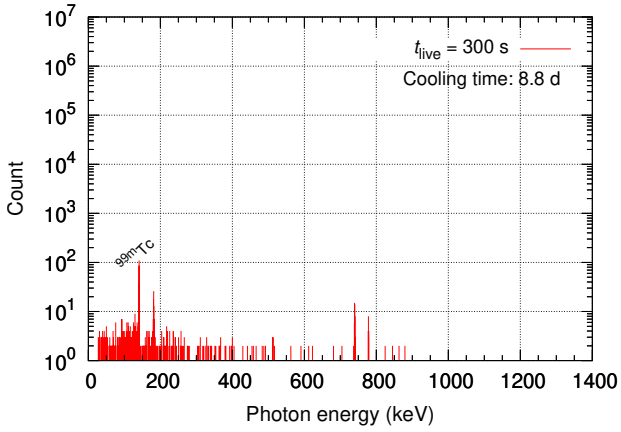

(b)

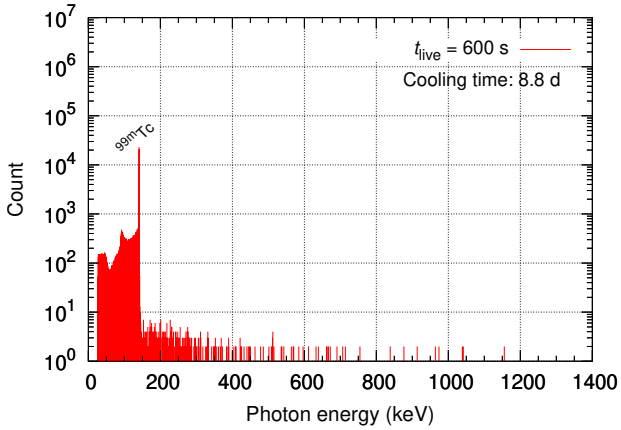

(c)

Fig. 7.8. Gamma-ray spectra for automatic AC chromatography (see Sec. 7.3.1). (a) $[^{99}\mathrm{Mo}]MoO_4^{2-}$ solution before $[^{99m}\mathrm{Tc}]TcO_4^-$ elution; (b) step ② ··· distilled water used for MoO_4^{2-} removal from the AC column; and (c) steps ⑥ and ⑦ combined ··· 12-mL $[^{99m}\mathrm{Tc}]TcO_4^-$ eluate.

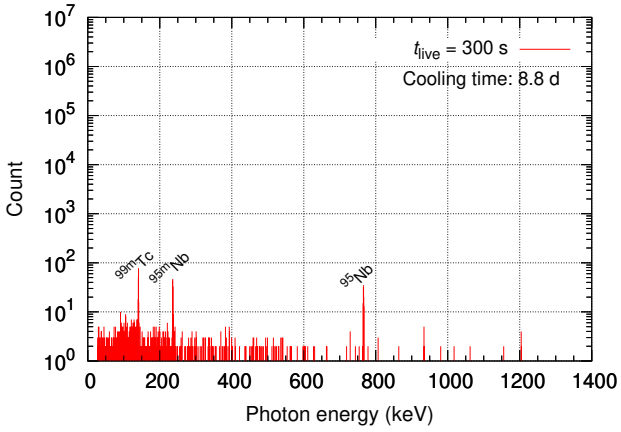

(a)

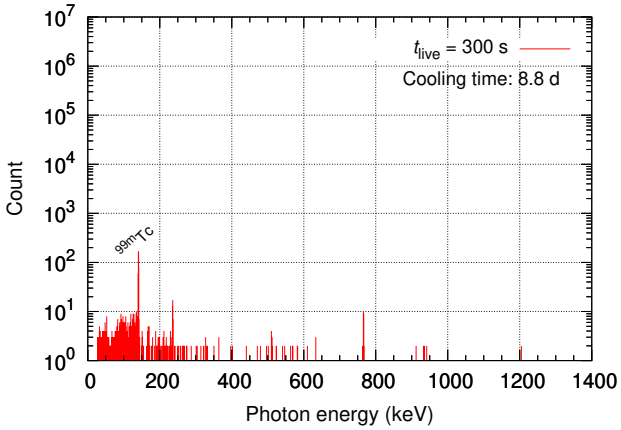

(b)

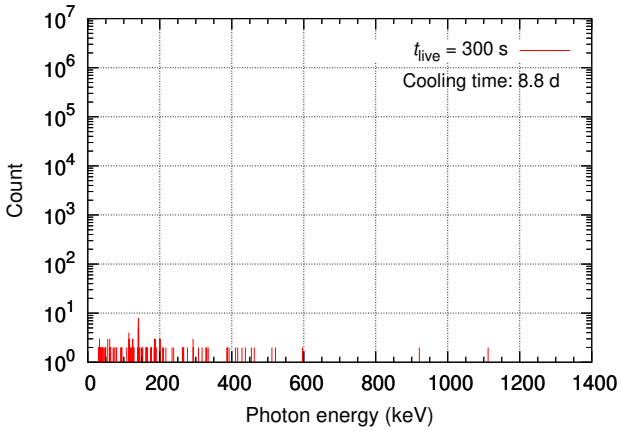

(c)

Fig. 7.9. Gamma-ray spectra for automatic AC chromatography. (a) Step ③ ··· residue of NaOH used for AC alkalinization; (b) step ④ ··· distilled water used for OH^- removal from $[^{99m}Tc]TcO_4^-$; and (c) step ⑤ ··· distilled water used for $[^{99m}Tc]TcO_4^-$ elution from the AC column.

using pre-elution ^{99m}Tc concentrators such as the ABEC and AC ^{99m}Tc generators.

The experimental verification of Eq. (7.9) showed that the parameterized RAC of AC chromatography can correctly describe its ^{99m}Tc RAC, and can provide a means of direct calculation of ^{99m}Tc RAC.

7.6 Acknowledgments

We would like to express our appreciation to Dr. Tatenuma and Mr. Tsuguchi (Kaken) for their guidance and support in conducting the chromatographic experiments.

Chapter
8

Beyond parametric analyses: Biodistribution studies

Abstract

Preclinical testing of linac-derived ^{99m}Tc can be useful in verifying its radiopharmaceutical quality, and is an important step in advancing the overall research of electron linac production of ^{99}Mo/^{99m}Tc. As part of the preclinical testing, biodistribution studies were conducted on laboratory mice using fission- and linac-derived [^{99m}Tc]TcO_4^-. Comparison of the two results showed that linac-derived ^{99m}Tc is comparable to that of reactor-derived ^{99m}Tc.

8.1 Declaration

The animal experiments presented in this chapter were carried out in accordance with the University of Tokyo Conduct No. 129 “University of Tokyo Code of Practice for Animal Experiments”, and were subject to the authorization by the Life Science Research Support and Research Ethics Review, conducted by the Environmental Health and Safety Office, School of Engineering and Graduate School of Information Science and Technology, University of Tokyo.

8.2 Overview

We have so far addressed the parametric studies of a ^{99}Mo production electron linac (Chap. 3) and its targetry (Chap. 4), optimal converter thicknesses (Chap. 5), density change coefficient (Chap. 6), and parameterized RAC (Chap. 7). All of these subjects addressed physical or chemical problems, or combination of the two, and were focused on increasing the yields of ^{99}Mo/^{99m}Tc and increasing the RAC of ^{99m}Tc.

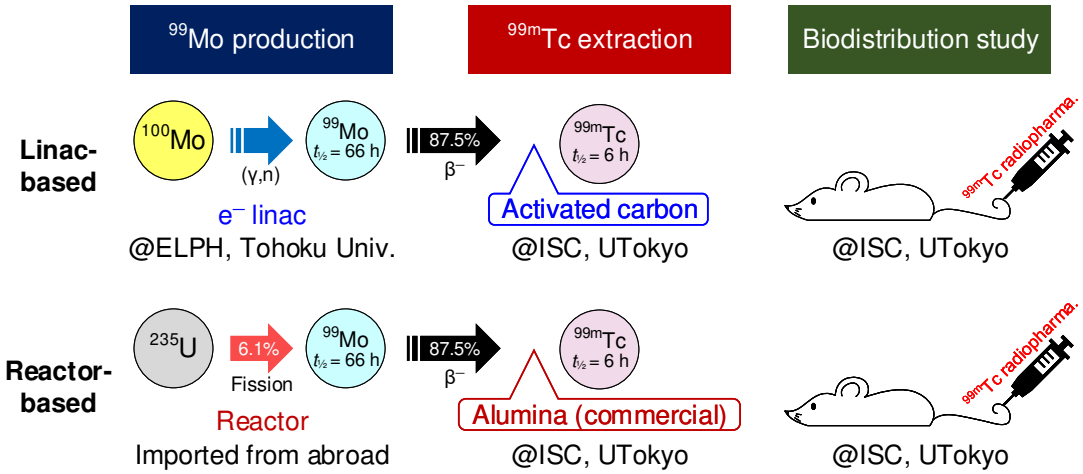

Fig. 8.1. The experimental schematic of biodistribution studies.

As we mentioned in Sec. 1.4.3 (Fig. 1.6), the research task after the physical and chemical steps is to test the pharmaceutical quality of linac-derived ^{99m}Tc. This biomedical research is necessary to verify and ensure the clinical value of linac-derived ^{99m}Tc. At the preclinical phase, testing is performed on small animals, and can be extended to medium-sized and large animals.

Following the parametric analyses, we conducted biodistribution studies on ICR mice. The experimental schematic is illustrated in Fig. 8.1. ^{99}Mo was produced using the S-band high-intensity electron linac at the ELPH, Tohoku University (the same one used in Chap. 5), and ^{99m}Tc was extracted from the ^{99}Mo using an automatic AC chromatography device (the same one used in Chap. 7) at the Isotope Science Center (ISC), University of Tokyo. The linac-derived [^{99m}Tc]TcO_4^- was then used for biodistribution studies at the ISC. The same type of experiments was carried out using a commercial alumina ^{99m}Tc generator, or reactor-derived ^{99m}Tc. Finally, the biodistribution results of the linac- and reactor-derived ^{99m}Tc were compared.

8.3 Materials and methods

8.3.1 ^{99}Mo production

^{99}Mo was obtained by irradiating two MoO_3 targets prepared in Sec. 5.3.1. A series of three 1-mm thick Ta plates was used as the converter. To obtain 5 MBq of ^{99}Mo at the end of irradiation, average beam currents of 20–30 μA and irradiation times of 36–45 min were necessary (Table 8.1). These relatively high currents and long

Table 8.1. MoO_3 targets irradiated for the biodistribution studies.

Target No.	Mass (g)	Volume (cm^3)	Density ratio[1]	Irradiation conditions
181213-10	1.3573	0.3787	0.7642	50 MeV, 30 μA, 36 min
181213-11	1.5991	0.3948	0.8636	50 MeV, 20 μA, 45 min

[1] The ratio to the material density of MoO_3, 4.69 g cm^{-3}. See Eq. (2.2).

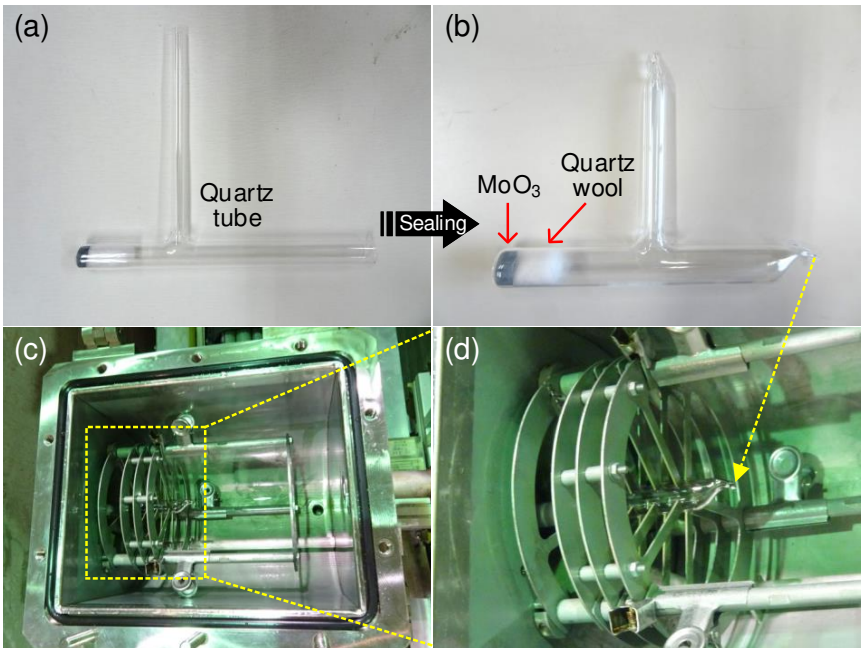

Fig. 8.2. An encapsulated MoO_3 target irradiated for the biodistribution studies. The MoO_3 target (a) before and (b) after its sealing, and (c) in a water-cooled target holder and its (d) enlarged view.

irradiation times (compare Table 8.1 with Table 5.4) required the use of a water-cooled target holder (Fig. 8.2(c)), for which the MoO_3 targets were encapsulated in quartz tubes under a helium atmosphere (Fig. 8.2(b)).

After irradiation, the MoO_3 targets were transported to the ISC, University of Tokyo, using excepted packages (UN 2910; L-type package in Japan).

8.3.2 ^{99m}Tc extraction using AC chromatography

As in Sec. 5.3.3, the two MoO_3 targets were dissolved separately using 6-*M* NaOH (Eq. (4.2)) on a hot plate with heating temperature of 80°C. Table 8.2 summarizes the dissolution conditions. The target 181213-10 was put on the hot plate for 60 min (Fig. 8.3), and the target 181213-11 for 120 min.

Table 8.2. MoO_3 target dissolution conditions.

	MoO_3		NaOH	
Target No.	Mass (g)	Amount (mmol)	Amount (mmol)	Volume, 6 M (mL)
181213-10	1.3573	9.429	18.858	3.143
181213-11	1.5991	11.109	22.218	3.703

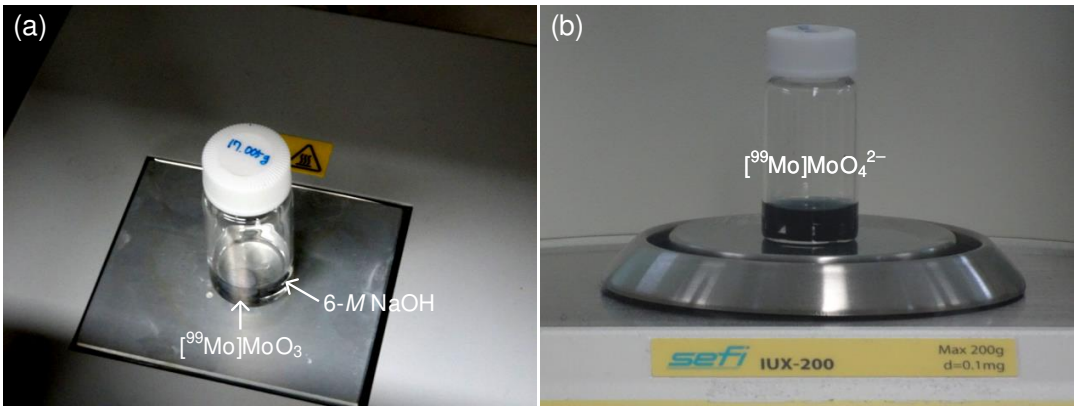

Fig. 8.3. The $[^{99}Mo]MoO_3$ target 181213-10 (a) before and (b) after its dissolution. The number written on the vial cap in (a) is the mass of the empty vial.

The dissolution of $[^{99}Mo]MoO_3$ targets resulted in $[^{99}Mo]MoO_4{}^{2-}$, which contained its decay product $[^{99m}Tc]TcO_4{}^-$. The ^{99m}Tc oxyanions were then extracted from the ^{99}Mo ones using an AC chromatographic device (Fig. 8.4). The ^{99m}Tc concentration and elution processes were the same as the ones explained in Sec. 7.3.1.

8.3.3 Preparation of reactor-derived ^{99m}Tc

Reactor-derived ^{99m}Tc was prepared using a commercial wet-type alumina ^{99m}Tc generator (Ultra-Techne Kow, FUJIFILM Toyama Chemical Co., Ltd., Japan). The $[^{99m}Tc]TcO_4{}^-$ elution was performed according to the instruction manual enclosed with the generator.

8.3.4 ^{99m}Tc radiopharmaceutical

$[^{99m}Tc]TcO_4{}^-$, or ^{99m}Tc-pertechnetate, is the most important radiopharmaceutical in testing the radiopharmaceutical quality of linac-derived ^{99m}Tc. This is because, in addition to its standalone use in thyroid imaging, $TcO_4{}^-$ is always the starting ionic compound with which ^{99m}Tc radiopharmaceuticals (see Table 1.1) are formu-

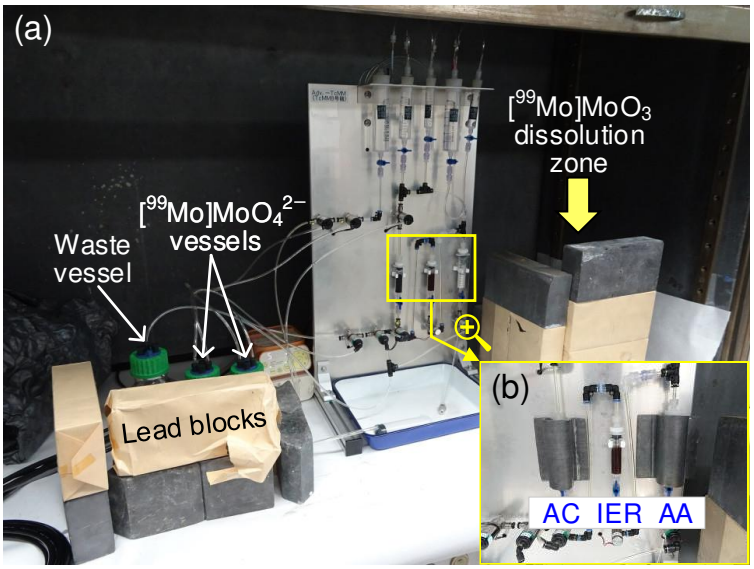

Fig. 8.4. The AC chromatographic device (Kaken Inc, Japan) used for the biodistribution studies. (a) The device set up in a fume hood and (b) its three main columns. AC: activated carbon, IER: ion exchange resin, and AA: activated alumina (see also Fig. 7.5). In (b), the AC and AA columns are covered with lead plates for radiation shielding.

lated. When used alone, TcO_4^- itself is uptaken by tissues bearing the sodium-iodide symporter (NIS), such as the thyroid, salivary gland, and gastric mucosa[126–129], thereby playing the role of a thyroid imaging agent. For these reasons, we conducted biodistribution studies using $[^{99m}Tc]TcO_4^-$.

8.3.5 Biodistribution studies

Ten healthy female ICR mice weighing 25.7–30.3 g (Sankyo Labo Service Corp., Inc., Japan) were studied (Table 8.3). The mice were cared and handled in accordance with the corresponding regulations set by the University of Tokyo (Sec. 8.1).

The biodistribution studies were conducted in the following order.

① An ICR mouse, hereafter referred to simply as a mouse, was anesthetized using isoflurane administered via an anesthetic device (Anes II, Biomachinery, Japan).

② After weighed, the mouse was administered with 0.2–0.3 mL of $[^{99m}Tc]TcO_4^-$ via tail vein injection, and kept on a heating pad in a prone position for 30 min.

Isoflurane is a common inhalation anesthetic.

[126] F. Boschi *et al. J. Biomed. Opt.* **18**, 076005 (2013).
[127] L. S. Zuckier *et al. J. Nucl. Med.* **45**, 500–507 (2004).
[128] P. R. Franken *et al. Thyroid* **20**, 519–526 (2010).
[129] M. L. Schipper *et al. Eur. J. Nucl. Med. Mol.* **34**, 638–650 (2007).

Table 8.3. Information of the ICR mice.

	Type of $[^{99m}Tc]TcO_4^-$	
	Reactor-derived	Linac-derived
Strain	Slc:ICR	
Modification	None (healthy)	
Number n	4	6
Gender	Female	
Age (wk)	6	6–7
Weight (g)	25.7–27.9	26.6–30.3

The purpose of the 30-min waiting time was to allow sufficient uptake of the $[^{99m}Tc]TcO_4^-$ ions by the NIS-expressing tissues.

③ The mouse was sacrificed, and the organs of interest were extracted and put into respective preweighed test tubes. The collected organs were: (i) 100 μL of whole blood for checking the blood clearance of $[^{99m}Tc]TcO_4^-$, (ii) the heart, liver, and kidneys as NIS-free or cold organs, and (iii) the thyroid and salivary gland as the NIS-bearing or hot organs. Subsequently, the weights of the organs were determined by using the preweighted test tube weights.

Here, the words "cold" and "hot" are used in radioactivity context.

④ The gamma-ray intensities of the organs were measured using a gamma counter (Packard Cobra Quantum 5003).

8.3.6 Calculation of %ID/g

In biodistribution studies, a figure of merit called percent injected dose (%ID) is used to represent the uptake of a radiopharmaceutical by its target organ. %ID is calculated as

$$\%\text{ID} \equiv \frac{D_{\text{org}}}{D_{\text{tot}}} \times 100\,(\%), \tag{8.1}$$

In biodistribution context, the dose is the activity of a radiopharmaceutical, not the absorbed dose.

where D_{org} and D_{tot} denote the dose of the organ in question and the total dose administered to the subject, respectively. When low activities are used in small-animal biodistribution studies, the dose can be measured using a gamma counter in the unit of count per minute (cpm). For high activities, a calibrated well counter can be a suitable measurement device.

Because, however, %ID does not take into account the size or density of organs, another figure of merit called %ID/g is used in practice. %ID/g is simply %ID divided

by the weight of the organ under consideration:

$$\%\mathrm{ID/g} \equiv \frac{\%\mathrm{ID}}{m_{\mathrm{org}}} = \frac{D_{\mathrm{org}}}{D_{\mathrm{tot}} m_{\mathrm{org}}} \times 100\,(\%). \tag{8.2}$$

In calculating Eqs. (8.1) and (8.2), both D_{org} and D_{tot} must represent activities at the same time point; the %ID and %ID/g presented in this chapter were all decay-corrected to the respective administration times.

8.4 Results and discussion

The %ID and %ID/g results are plotted in Figs. 8.5(a) and 8.5(b), respectively. As shown in Fig. 8.5(a), %ID alone is insufficient for representing the radiopharmaceutical uptake.

In Fig. 8.5(b), the %ID/g of the thyroid and the %ID/g of the salivary gland show similar values between reactor- and linac-derived [$^{99\mathrm{m}}$Tc]$\mathrm{TcO_4}^-$, suggesting that the two $^{99\mathrm{m}}$Tc radiopharmaceuticals exhibited the same pharmacokinetics.

Although the standard deviation of the thyroid %ID/g was greater than those of the other organs, this much dispersion is deemed acceptable considering the thyroid %ID/g of other papers[127,129].

8.5 Summary

In order to verify the pharmaceutical quality of linac-derived $^{99\mathrm{m}}$Tc, we conducted biodistribution studies on ICR mice using linac- and reactor-derived [$^{99\mathrm{m}}$Tc]$\mathrm{TcO_4}^-$. The linac-derived $^{99\mathrm{m}}$Tc was prepared by producing ^{99}Mo using an electron linac, and subsequently by extracting $^{99\mathrm{m}}$Tc using an AC chromatographic device. On the other hand, the reactor-derived $^{99\mathrm{m}}$Tc was prepared using a commercial wet-type $^{99\mathrm{m}}$Tc generator.

Comparison of the two %ID/g results showed that the linac-derived $^{99\mathrm{m}}$Tc can exhibit the same pharmacokinetics as the reactor-derived one, corroborating that electron linacs can become an alternative to the aging reactors in ^{99}Mo/$^{99\mathrm{m}}$Tc production.

8.6 Acknowledgments

We would like to express our gratitude to Prof. Kumakura (SMC, Saitama Medical Univ.), Prof. Wada, and Prof. Akimitsu (ISC, UTokyo), for their guidance and valuable

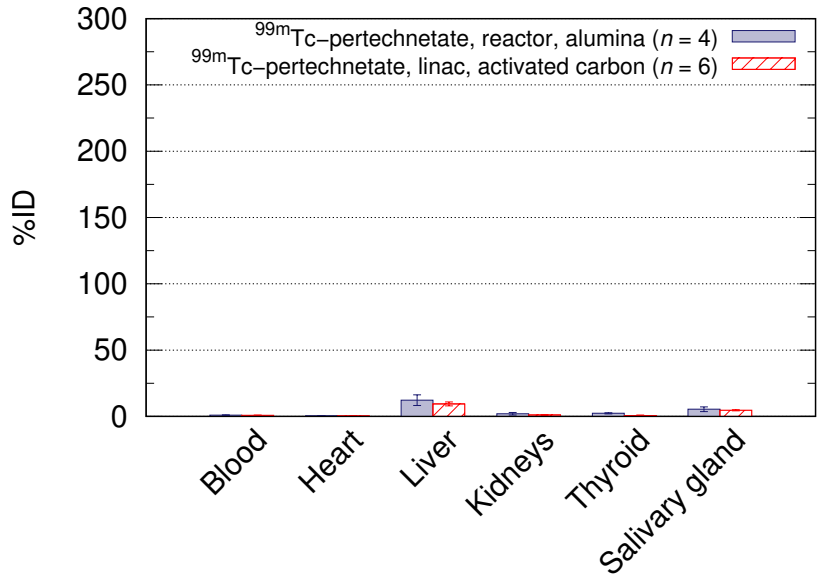

(a)

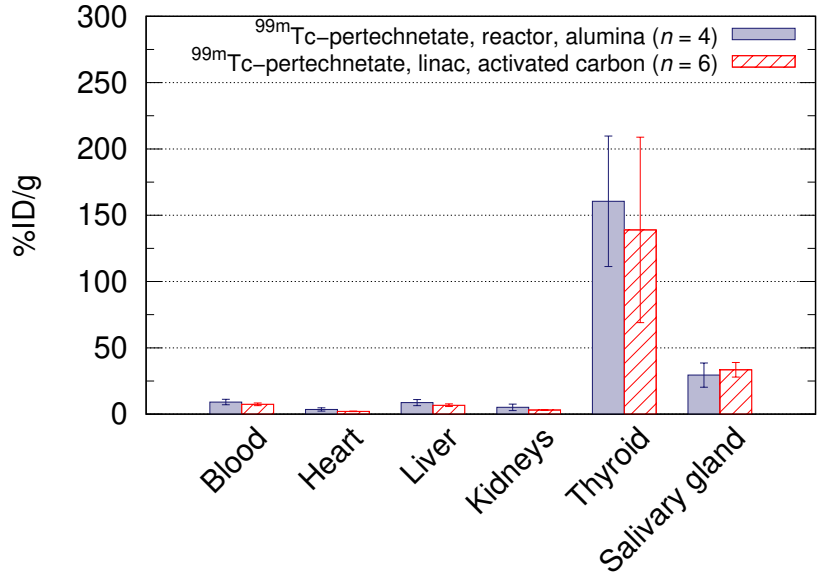

(b)

Fig. 8.5. (a) %ID and (b) %ID/g results of the $[^{99m}Tc]TcO_4^-$ biodistribution studies. The data are represented as mean±standard deviation.

discussions on the biodistribution studies. Also, we are deeply indebted to Dr. Ozeki (Nakanishi) and Ms. Shiizu (ISC, UTokyo) for the assistance of mouse handling.

We are grateful to Prof. Kikunaga (ELPH, Tohoku Univ.) for his guidance in the use of the water-cooled target holder and the transport of irradiated MoO_3 targets to the ISC, UTokyo.

Special thanks go to Dr. Tatenuma and Mr. Tsuguchi (Kaken) for providing us with the opportunity to use their AC chromatographic device, TcMM. It was their generous support and guidance that made possible the first (to the best of our knowledge) biodistribution studies of linac- and AC-derived ^{99m}Tc.

Chapter
9

Conclusion and future work

9.1 Summary and conclusion

In an attempt to find reasonable values of the parameters associated with electron linac production of ^{99}Mo/^{99m}Tc, we solved various parameter problems through theoretical investigations, calculations, and analyses. Experiments were also carried out for some of the parametric problems.

Three programs dedicated to parametric analyses were developed and used throughout this dissertation: Chap. 2

(i) `phitar`, for the parametric analysis and design of ^{99}Mo production targetry
⇒ Used in Chaps. 3, 4, and 5

(ii) `enrimo`, for investigating the influence of enriched ^{100}Mo on the production yields of ^{99}Mo/^{99m}Tc and on the radionuclidic and isotopic purities of ^{99m}Tc
⇒ Used in Chap. 6

(iii) `actdyn`, for simulating our modeled ^{99}Mo/^{99m}Tc activities
⇒ Used in Chap. 3

The first set of analyses was performed on the accelerator and beam parameters of a ^{99}Mo production electron linac, of which the findings were as follows. Chap. 3

(1) In designing or purchasing a ^{99}Mo production linac, an X-band RF and an SW structure, or an SCS in particular, can be preferable if downsizing of the linac is necessary. If, on the other hand, cost reduction and a high beam current are prioritized, using an S-band RF and a TW structure can be a reasonable choice.

(2) An electron beam energy of 35 MeV was found to result in sufficient ^{99}Mo yields with a moderate degree of beam loading.

(3) A high average beam current is preferable to increase the ^{99}Mo yield. However, the average beam current is essentially dictated by the average power of the RF source which, in turn, is determined by the available budget. A compromise should be made accordingly.

(4) A transverse beam size of >2 mm in FWHM, for example 4.5-mm FWHM, can alleviate focused heat load on a Mo target.
(5) The beam emittance need not be small, but should be designed such that the beam stability is unaffected.
(6) The modeled ^{99}Mo/^{99m}Tc activities simulated using `actdyn` showed that 11 of 35 MeV and 260 μA electron linacs can meet one million ^{99m}Tc scans per year.

Chap. 4

Subsequently, the geometrical and material parameters of targetry components were analyzed, where we found that:

(7) Use of a separated target system can reduce the heat load and radiation damage of a Mo target.
(8) Candidate converter materials include Ta, W, Ir, Pt, and Au. PHITS simulations performed via `phitar` showed that these materials do not exhibit significant differences in the bremsstrahlung generation efficiency. Considering other properties such as the melting point and thermal conductivity, W can be an appropriate converter material.
(9) Both Mo metal (Mo_{met}) and trioxide (MoO_3) can be used as a Mo target. Mo_{met} has advantages of a higher melting point, higher thermal conductivity, and higher mass density. MoO_3, on the other hand, can be useful because of its relatively simple dissolution reaction.
(10) We experimentally confirmed that the dissolution of MoO_3(s) in NaOH(aq) is a weak acid-strong base reaction.

Chap. 5

For validating the results of parametric studies on converter thicknesses, we conducted irradiation experiments. The overall parametric calculations were in agreement with the experimental results: for an intertarget distance of 13 mm and Gaussian transverse beam sizes of around 4.5 mm, the optimal W thicknesses were found to be 1.48 mm for E_{e^-} = 20 MeV, and 2.58 mm for E_{e^-} = 35 MeV. Our program `phitar` can be used to find such optimal converter thicknesses.

Chap. 6

As part of the parametric analysis, a figure of merit called density change coefficient (DCC) was defined and its calculation program `enrimo` was developed. The DCC is applicable to all of the ^{100}Mo(γ,n)^{99}Mo, ^{100}Mo(n,2n)^{99}Mo, ^{100}Mo(p,2n)^{99m}Tc reaction routes, and can be useful in setting the goal ^{100}Mo enrichment level and the goal $^{92,94–98}$Mo depletion levels. For instance, we found that for the ^{100}Mo(p,2n)^{99m}Tc reaction route, a 97.39% enriched ^{100}Mo product can be preferable to the 97.42%, 99.01%, 99.03%, 99.05%, and 99.27% ones.

Chap. 7

The radioactive concentration (RAC) of ^{99m}Tc is the quantity that determines whether or not a ^{99m}Tc generator can be used with LSA ^{99}Mo. To calculate RAC

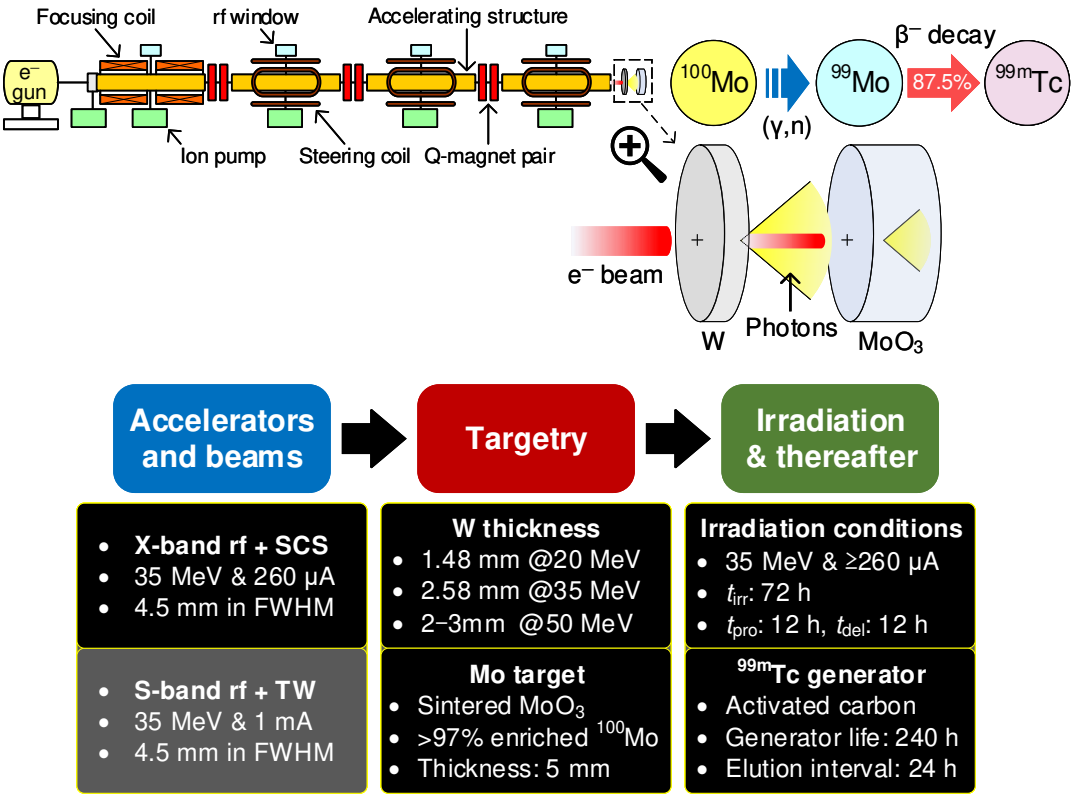

Fig. 9.1. Summary of parameter values investigated in this dissertation.

with the LSA issue considered, we parameterized the RAC of alumina ^{99m}Tc generators and the RAC of pre-elution ^{99m}Tc concentrators, the latter of which was experimentally verified. The parameterized RAC can be useful in addressing the LSA issue and provides a direct means of RAC calculation.

In order to verify the pharmaceutical quality of linac-derived ^{99m}Tc, we carried out biodistribution studies on laboratory mice. The resulting values of %ID/g were similar between fission-derived and linac-derived [^{99m}Tc]TcO_4^-, corroborating that electron linacs can become an alternative source of ^{99}Mo/^{99m}Tc. Chap. 8

This dissertation identified and analyzed several important parameters involved in the linac production of ^{99}Mo/^{99m}Tc, and found reasonable ranges of the parameter values (Fig. 9.1). The characteristic approach of this dissertation was the writing and use of dedicated analysis programs, which enabled us to conduct a wide spectrum of parametric studies. In addition, new parameters such as the DCC and parameterized RAC were defined to improve ^{99}Mo/^{99m}Tc production processes and efficiencies. We expect that by using the parameter values and the computational approaches of the dissertation, the yields of ^{99}Mo/^{99m}Tc and the RAC of ^{99m}Tc can be significantly

improved, which in turn can contribute to the realization of linac production of ^{99}Mo/^{99m}Tc.

9.2 Future research

9.2.1 Program upgrades

Development of graphical user interfaces

The three PERL programs developed in this dissertation, namely `phitar`, `enrimo`, and `actdyn` (Chap. 2), have all been written to run on command-line interfaces (CLIs). While CLIs provide means of batch processing and automation, users having no experience of CLIs or preferring graphical user interfaces (GUIs) may feel difficult to use our CLI-driven programs. Therefore, we are planning to upgrade the programs to support GUIs as auxiliary running environments, while maintaining the CLIs as the primary interfaces.

Adding an energy distribution setter in `phitar`

As of v1.03[56], `phitar` can designate only monoenergetic electron beams via the `e0` command of PHITS[59]. As pointed out in Sec. 5.3.4, however, the actual electron beams exhibit energy spread and, depending on the degree of the spread, significant differences between MC calculations and experimental data can be induced. Therefore, one of the future upgrades of `phitar` is to make the `e-type` command of PHITS available in `phitar`, which will then allow the user to specify the beam energy distribution.

9.2.2 Determination of targetry cooling time

As shown in Table B.1 and Appendix E, various impurity radionuclides are produced along with ^{99}Mo during photon irradiation. This is because naturally occurring Mo consists of seven Mo isotopes, namely $^{92,94–98,100}$Mo, of which ^{100}Mo has natural abundance of only 9.74% (Fig. 6.1). The diverse impurity radionuclides then complicate the dose rate around targetry, making it difficult to determine the appropriate target cooling time t_{cool} (see Sec. 5.3.3). To provide a quantitative means of cooling time calculation, a mathematical model that can describe photonuclear reaction cascades

[56] J. Jang. `phitar` - A PHITS wrapper for targetry design (v1.03) (2019).
[59] T. Sato *et al. J. Nucl. Sci. Technol.* **55**, 684–690 (2018).

and the resultant decay chains needs to be developed. Eventually, such a model should be able to calculate the minimum required target cooling times as functions of irradiation parameters, such as the beam energy, irradiation time, ^{100}Mo enrichment level, and $^{92,94–98}$Mo depletion levels.

9.2.3 Intertarget distances and beam sizes

In the order-made target holder used in the converter experiments (Fig. 5.8), the distance between a converter and a Mo target, or the intertarget distance, was fixed to be 13 mm. For other target holders having different intertarget distances, the W thicknesses addressed in Sec. 5.3.4 are no longer optimal for ^{99}Mo production. This is because the amount of photons entering a Mo target is greatly affected by the intertarget distance, which is further affected by the electron beam size. At present, therefore, finding optimal converter thicknesses should be carried out for individual sets of intertarget distances and electron beam sizes, requiring a large number of simulation runs and analyses. To reduce the number of simulation studies and to provide a general understanding of optimal converter thicknesses, developing a physical model that can quantitatively explain the relations between intertarget distances, beam sizes, and photon distributions is necessary.

Appendix

A

Program usage instructions

A.1 Usage of `phitar`

The usage instructions of `phitar`[56] is presented in Listing A.1.

```
NAME
    phitar - A PHITS wrapper for targetry design

SYNOPSIS
        perl phitar.pl [run_mode] [-rpt_subdir=dname] [-rpt_fmts=ext ...]
                       [-rpt_flag=str] [-nofm] [-nopause]

DESCRIPTION
        phitar is a PHITS wrapper written in Perl, intended for the design
    of
        bremsstrahlung converters and Mo targets. phitar can:
          - examine a range of targetry dimensions and beam parameters
            according to user specifications
          - generate MAPDL table and macro files
          - collect information from PHITS tally outputs and generate
            report files
          - collect information from PHITS general outputs and generate
            report files
          - modify ANGEL inputs and outputs
          - calculate yields and specific yields of Mo-99 and Au-196
          - convert ANGEL-generated .eps files to various image formats
          - generate animations using the converted rasters

OPTIONS
        run_mode
            file
```

[56] J. Jang. `phitar` - A PHITS wrapper for targetry design (v1.03) (2019).

```
26              An input file specifying simulation conditions.
27              Refer to 'args.phi' for the syntax.
28          -d
29              Run simulations with the default settings.
30          -dump_src=particle
31                  electron
32                  photon
33                  neutron
34              Run simulations using a dump source.
35              (as of v1.03, particles entering a Mo target are used
36              as the dump source)
37
38      -rpt_subdir=dname (short: -subdir, default: reports)
39          Name of subdirectory to which report files will be stored.
40
41      -rpt_fmts=ext ... (short: -fmts, default: dat,xlsx)
42          Output file formats. Multiple formats are separated by the
    comma (,).
43          all
44              All of the following ext's.
45          dat
46              Plain text
47          tex
48              LaTeX tabular environment
49          csv
50              comma-separated value
51          xlsx
52              Microsoft Excel 2007
53          json
54              JavaScript Object Notation
55          yaml
56              YAML
57
58      -rpt_flag=str (short: -flag)
59          str is appended to the report filenames followed by an
    underscore.
60          Use this option when different materials are simulated
61          in the same batch.
62
63      -nofm
64          The front matter will not be displayed at the beginning of
    program.
65
66      -nopause
67          The shell will not be paused at the end of program.
```

```
68              Use it for a batch run.
69
70  EXAMPLES
71          perl phitar.pl args.phi
72          perl phitar.pl -d
73          perl phitar.pl -dump=electron -rpt_flag=elec_dmp args.phi
74          perl phitar.pl args.phi > phitar.log -nopause
75          perl phitar.pl -rpt_flag=au args.phi
76          perl phitar.pl -rpt_flag=moo3 args_moo3.phi
77
78  REQUIREMENTS
79          Perl 5
80              Moose, namespace::autoclean
81              Text::CSV, Excel::Writer::XLSX, JSON, YAML
82          PHITS, Ghostscript, Inkscape, ImageMagick, FFmpeg, gnuplot
83          (optional) ANSYS MAPDL
84
85  SEE ALSO
86      phitar on GitHub <https://github.com/jangcom/phitar>
87
88  AUTHOR
89      Jaewoong Jang <jangj@korea.ac.kr>
90
91  COPYRIGHT
92      Copyright (c) 2018-2019 Jaewoong Jang
93
94  LICENSE
95      This software is available under the MIT license; the license
96      information is found in 'LICENSE'.
```

Listing A.1: Usage instructions of phitar.

A.2 Usage of `enrimo`

This is the manual page of `enrimo` v1.05 with some mistyped words corrected and publication information added.

The usage instructions of `enrimo`[57] is presented in Listing A.2.

```
NAME
    enrimo - Investigate the influence of an enriched Mo isotope

SYNOPSIS
        perl enrimo.pl [-materials=mo_mat ...] [-isotope=mo_isot]
                       [-enri_lev_type=frac_type] [-enri_lev_range=
    frac_range]
                       [-min_depl_lev_global=enri_lev] [-depl_order=option
    ]
                       [-inp=fname] [-out_path=path] [-out_fmts=ext ...]
                       [-projectiles=particle ...]
                       [-verbose] [-nofm] [-nopause]

DESCRIPTION
        This Perl program generates datasets for investigating the
    influence of
        an enriched Mo isotope on its associated Mo material, Mo element,
        and companion isotopes.
        The following quantities, as functions of the enrichment level of
        the Mo isotope to be enriched, are calculated for a Mo material:
        - Amount fractions and mass fractions of Mo and O isotopes
        - Mass fractions of Mo and O elements
        - Mass and number densities of the Mo material, Mo and O elements,
          and their isotopes
        - Density change coefficients (DCCs) of Mo and O isotopes

OPTIONS
        Multiple values are separated by the comma (,).

        -materials=mo_mat ... (short: -mats, default: momet)
            all
                All of the following mo_mat's.
            momet
                Mo metal
            moo2
                Mo(IV) oxide (aka Mo dioxide)
            moo3
                Mo(VI) oxide (aka Mo trioxide)

```

[57] J. Jang. `enrimo` - Investigate the influence of an enriched Mo isotope (v1.05) (2019).

```
37      -isotope=mo_isot (short: -isot, default: mo100)
38          Mo isotope to be enriched.
39          mo92
40          mo94
41          mo95
42          mo96
43          mo97
44          mo98  <= Mo-98(n,g)Mo-99
45          mo100 <= Mo-100(g,n)Mo-99, Mo-100(n,2n)Mo-99, Mo-100(p,2n)Tc
    -99m
46
47      -enri_lev_type=frac_type (short: -type, default: amt_frac)
48          The fraction type to refer to the enrichment level.
49          amt_frac
50          mass_frac
51
52      -enri_lev_range=frac_range (short: -range, default: 0,0.0001,1)
53          The range of enrichment levels to be examined.
54          e.g. 0.1,0.5     (beg,end; incre is automatically determined)
55          e.g. 0,0.001,1   (beg,incre,end)
56          e.g. 0,0.00001,1 (beg,incre,end)
57
58      -min_depl_lev_global=enri_lev (short: -global, default: 0.0000)
59          The minimum depletion level that applies to all the nuclides
60          associated with the designated Mo materials. Overridden, if
    given,
61          by nuclide-specific minimum depletion levels.
62          e.g. 0.0007
63
64      -depl_order=option (short: -order, default: ascend)
65          The order in which the Mo isotopes other than the to-be-
    enriched one
66          will be depleted.
67          ascend (short: asc)
68              Ascending order of mass number
69          descend (short: desc)
70              Descending order of mass number
71          random (short: rand, alt: shuffle)
72              Random order
73
74      -inp=fname (short: -i)
75          An input file specifying the nuclide-specific minimum
    depletion levels
76          and the calculation precision. See the sample input file for
    the syntax.
```

```
77          e.g. 0p9739.enr
78
79      -out_path=path (short: -path, default: the value of -isotope)
80          Path for the output files.
81
82      -out_fmts=ext ... (short: -o, default: dat,xlsx)
83          Output file formats.
84          all
85              All of the following ext's.
86          dat
87              Plain text
88          tex
89              LaTeX tabular environment
90          csv
91              comma-separated value
92          xlsx
93              Microsoft Excel 2007
94          json
95              JavaScript Object Notation
96          yaml
97              YAML
98
99      -projectiles=particle ... (short: -projs, default: none)
100         Reaction projectiles for associating the product nuclides with
    DCCs.
101         If designated, the relevant reporting files are generated
102         in addition to the default output files.
103         all
104             All of the following particles.
105         g
106             Photon <= Mo-100(g,n)Mo-99
107         n
108             Neutron <= Mo-98(n,g)Mo-99, Mo-100(n,2n)Mo-99
109         p
110             Proton <= Mo-100(p,2n)Tc-99m
111
112     -verbose (short: -verb)
113         Display the calculation process in real time. This will pause
114         the shell each time a core calculation routine is called; use
    it
115         only when debugging or checking part of the calculation
    process.
116
117     -nofm
```

```
118             The front matter will not be displayed at the beginning of
    program.
119
120         -nopause
121             The shell will not be paused at the end of program.
122             Use it for a batch run.
123
124 EXAMPLES
125         perl enrimo.pl -type=mass_frac -range=0,0.00001,1
126         perl enrimo.pl -mats=moo3 -global=0.0005 -verb
127         perl enrimo.pl -mats=momet,moo3 -range=0.0974,0.0001,0.9739 -inp=0
    p9739.enr
128
129 REQUIREMENTS
130         Perl 5
131             Text::CSV, Excel::Writer::XLSX, JSON, YAML
132
133 SEE ALSO
134     enrimo on GitHub <https://github.com/jangcom/enrimo>
135
136     enrimo on Zenodo <https://doi.org/10.5281/zenodo.2628760>
137
138     enrimo in a paper: *J. Phys. Commun.* 3, 055015
139     <https://iopscience.iop.org/article/10.1088/2399-6528/ab1d6b>
140
141 AUTHOR
142     Jaewoong Jang <jangj@korea.ac.kr>
143
144 COPYRIGHT
145     Copyright (c) 2018-2019 Jaewoong Jang
146
147 LICENSE
148     This software is available under the MIT license; the license
149     information is found in 'LICENSE'.
```

Listing A.2: Usage instructions of enrimo.

A.3 Usage of `actdyn`

The usage instructions of `actdyn`[58] is presented in Listing A.3.

```
NAME
    actdyn – A Mo–99/Tc–99m activity dynamics simulator

SYNOPSIS
        perl actdyn.pl [–i|–d] [–nofm] [–verbose] [–nopause]

DESCRIPTION
        actdyn calculates and generates data of the activity dynamics of
        Mo–99/Tc–99m produced via the Mo–100(g,n)Mo–99 reaction.
        Parameters that can be specified via the interactive mode include:
            – Fluence data: directory name, filename rules, and beam
    energy range
            – Cross section data
            – Mo target materials (options: metallic Mo, MoO2, MoO3)
            – Mo–100 mass fraction
            – The beam energy for which Mo–99/Tc–99m activity dynamics
    data
              will be calculated
            – Average beam current
            – Time frames: time of irradiation, time of postirradiation
    processing,
              and time of Tc–99m generator delivery
            – The fractions of Mo–99 and Tc–99m activities
              lost during postirradiation processing
            – Tc–99m elution conditions: elution efficiency, whether to
    discard
              the first eluate, elution intervals, and Tc–99m generator
    shelf–life
        The generated data files (.dat) follow the gnuplot data structure
        (data block and dataset).

OPTIONS
        –i
            Run on the interactive mode.

        –d
            Run on the default mode.

        –nofm
```

[58] J. Jang. `actdyn` - A Mo-99/Tc-99m activity dynamics simulator (v2.31) (2019).

```
35              The front matter will not be displayed at the beginning of the
     program.
36
37          -verbose (short form: -verb)
38              Calculation processes will be displayed.
39
40          -nopause
41              The shell will not be paused at the end of the program.
42              Use it for a batch run.
43
44 EXAMPLES
45          perl actdyn.pl -d -nopause
46          perl actdyn.pl -verbose
47
48 REQUIREMENTS
49          Perl 5
50              Excel::Writer::XLSX
51          PHITS
52              Please note that since only licensed users are allowed to use
     PHITS,
53              I opted not to upload PHITS-generated photon fluence files
54              which are necessary to run actdyn.
55              If you already have the license, please obtain T-Track files
56              with axis=eng used, and name the tally files in sequential
     order.
57              You can specify the naming rules of the fluence files and
     their
58              directory via the interactive input.
59
60 SEE ALSO
61      actdyn on GitHub <https://github.com/jangcom/actdyn>
62
63      actdyn-generated data in a paper: *Phys. Rev. Accel. Beams* 20, 104701
64      (Figs. 4, 5, 12, and 13)
65      <https://link.aps.org/doi/10.1103/PhysRevAccelBeams.20.104701>
66
67 AUTHOR
68      Jaewoong Jang <jangj@korea.ac.kr>
69
70 COPYRIGHT
71      Copyright (c) 2016-2019 Jaewoong Jang
72
73 LICENSE
74      This software is available under the MIT license; the license
```

```
75     information is found in 'LICENSE'.
```

Listing A.3: Usage instructions of `actdyn`.

Appendix

B

Nuclear reactions on ^{nat}Mo

This section tabulates photon-, neutron-, and proton-induced nuclear reactions on naturally occurring Mo isotopes[111] with the following listing conditions:

(i) The TENDL-2017 [24] peak cross section of the reaction is greater than 0.1 mb. The upper energy limits of excitation functions are mentioned in table captions.

(ii) The product radionuclide has a half-life of 10 min $< t_{1/2} <$ 1 y.

Table B.1. Photon reactions on naturally occurring Mo isotopes. The upper energy limits of excitation functions are 35 MeV[1].

PRN[2]	Decay mode		Photonuclear reaction					
	$t_{1/2}$	DP[3]	^{92}Mo	^{94}Mo	^{96}Mo	^{97}Mo	^{98}Mo	^{100}Mo
^{87}Zr	1.7 h	^{87}Y	(γ,αn)					
^{88}Zr	83.4 d	^{88}Y	(γ,α)					
^{89}Zr	78.4 h	^{89}Y		(γ,αn)				
^{90}Nb	14.6 h	^{90}Zr	(γ,np)					
^{91m}Nb	60.9 d	^{91}Nb	(γ,p)					
^{92m}Nb	10.2 d	^{92}Zr		(γ,np)				
^{95}Nb	35.0 d	^{95}Mo			(γ,p)	(γ,np)		
^{95m}Nb	3.6 d	^{95}Nb			(γ,p)	(γ,np)		
^{96}Nb	23.4 h	^{96}Mo				(γ,p)	(γ,np)	
^{97}Nb	72.1 m	^{97}Mo					(γ,p)	
^{90}Mo	5.6 h	^{90}Nb	(γ,2n)					
^{91}Mo	15.5 m	^{91}Nb	(γ,n)					
^{93m}Mo	6.9 h	^{93}Mo		(γ,n)				
^{99}Mo	66.0 h	^{99m}Tc						(γ,n)

[1] The design beam energy of our electron linac [50].
[2] Product radionuclide.
[3] Decay product.

[111] National Nuclear Data Center. NuDat 2.7.

Table B.2. Neutron reactions on naturally occurring Mo isotopes. The upper energy limits of excitation functions are 40 MeV[1].

PRN	Decay mode		Neutron reaction						
	$t_{1/2}$	DP	^{92}Mo	^{94}Mo	^{95}Mo	^{96}Mo	^{97}Mo	^{98}Mo	^{100}Mo
^{88}Y	106.6 d	^{88}Sr	(n,αp)						
^{90}Y	64.1 h	^{90}Zr		(n,αp)					
^{90m}Y	3.2 h	^{90}Y		(n,αp)					
^{92}Y	3.5 h	^{92}Zr				(n,αp)			
^{88}Zr	83.4 h	^{88}Y	(n,αn)						
^{89}Zr	78.4 h	^{89}Y	(n,α)						
^{95}Zr	64.0 d	^{95}Nb						(n,α)	
^{97}Zr	16.7 h	^{97m}Nb							(n,α)
^{90}Nb	14.6 h	^{90}Zr	(n,t)						
^{91m}Nb	60.9 d	^{91}Nb	(n,np) (n,d)						
^{92m}Nb	10.2 d	^{92}Zr	(n,p)[2]	(n,t)					
^{95}Nb	35.0 d	^{95}Mo			(n,p)	(n,np) (n,d)	(n,t)		
^{95m}Nb	3.6 d	^{95}Nb			(n,p)	(n,np) (n,d)	(n,t)		
^{96}Nb	23.4 h	^{96}Mo				(n,p)	(n,np) (n,d)	(n,t)	
^{97}Nb	72.1 m	^{97}Mo					(n,p)	(n,np) (n,d)	
^{98m}Nb	51.3 m	^{98}Mo						(n,p)	(n,t)
^{90}Mo	5.6 h	^{90}Nb	(n,3n)						
^{91}Mo	15.5 m	^{91}Nb	(n,2n)						
^{93m}Mo	6.9 h	^{93}Mo	(n,γ)[3]	(n,2n)	(n,3n)				
^{99}Mo	66.0 h	^{99m}Tc						(n,γ)	(n,2n)
^{101}Mo	14.6 m	^{101}Tc							(n,γ)

[1] The deuteron beam energy of [19, 130].
[2] The excitation function is found in JENDL4.0 [131].
[3] The excitation function is found in JENDL/AD-2017 [132].

Table B.3. Proton reactions on naturally occurring Mo isotopes. The upper energy limits of excitation functions are 25 MeV[1]. Table reproduced from our publication [15] which is licensed under CC BY 3.0.

PRN	Decay mode		Proton reaction						
	$t_{1/2}$	DP	^{92}Mo	^{94}Mo	^{95}Mo	^{96}Mo	^{97}Mo	^{98}Mo	^{100}Mo
^{88}Zr	83.4 d	^{88}Y	(p,αp)						
^{89}Nb	2.0 h	^{89}Zr	(p,α)						
^{89m}Nb	66.0 m	^{89}Zr	(p,α)						
^{90}Nb	14.6 h	^{90}Zr		(p,αn)					
^{91m}Nb	60.9 d	^{91}Nb	(p,2p)	(p,α)[2]	(p,αn)	(p,α2n)			
^{92m}Nb	10.2 d	^{92}Zr			(p,α)[2]	(p,αn)	(p,α2n)		
^{95}Nb	35.0 d	^{95}Mo				(p,2p)		(p,α)	(p,α2n)
^{95m}Nb	3.6 d	^{95}Nb						(p,α)[2]	(p,α2n)
^{96}Nb	23.4 h	^{96}Mo					(p,2p)		(p,αn)
^{97}Nb	72.1 m	^{97}Mo							(p,α)
^{91}Mo	15.5 m	^{91}Nb	(p,pn) (p,d)						
^{93m}Mo	6.9 h	^{93}Mo		(p,pn) (p,d)	(p,t)				
^{99}Mo	66.0 h	^{99m}Tc							(p,pn) (p,d)
^{93}Tc	2.8 h	^{93}Mo	(p,γ)	(p,2n)	(p,3n)				
^{93m}Tc	43.5 m	^{93}Tc	(p,γ)[2]	(p,2n)	(p,3n)				
^{94}Tc	293.0 m	^{94}Mo		(p,n)	(p,2n)	(p,3n)			
^{94m}Tc	52.0 m	^{94}Mo		(p,n)	(p,2n)	(p,3n)			
^{95}Tc	20.0 h	^{95}Mo		(p,γ)	(p,n)	(p,2n)	(p,3n)		
^{95m}Tc	61.0 d	^{95}Mo		(p,γ)[2]	(p,n)	(p,2n)	(p,3n)		
^{96}Tc	4.3 d	^{96}Mo			(p,γ)	(p,n)	(p,2n)	(p,3n)	
^{96m}Tc	51.5 m	^{96}Tc				(p,n)	(p,2n)	(p,3n)	
^{97m}Tc	91.0 d	^{97}Tc					(p,n)	(p,2n)	
^{99m}Tc	6.0 h	^{99}Tc						(p,γ)[3]	(p,2n)
^{101}Tc	14.0 m	^{101}Ru							(p,γ)

[1] Above which Tc impurities multiply [39].
[2] The excitation function is found in [28].
[3] The excitation function is found in [33].

Appendix

C

Excitation functions

Table C.1. Excitation functions listed in this appendix.

Figure	Library	Reaction
C.1		^{235}U(n,f)^{99}Mo
C.2		^{100}Mo(γ,n)^{99}Mo
C.3	TENDL-2017	^{100}Mo(n,2n)^{99}Mo
C.4		^{100}Mo(p,2n)^{99m}Tc
C.5		^{197}Au(γ,n)^{196}Au

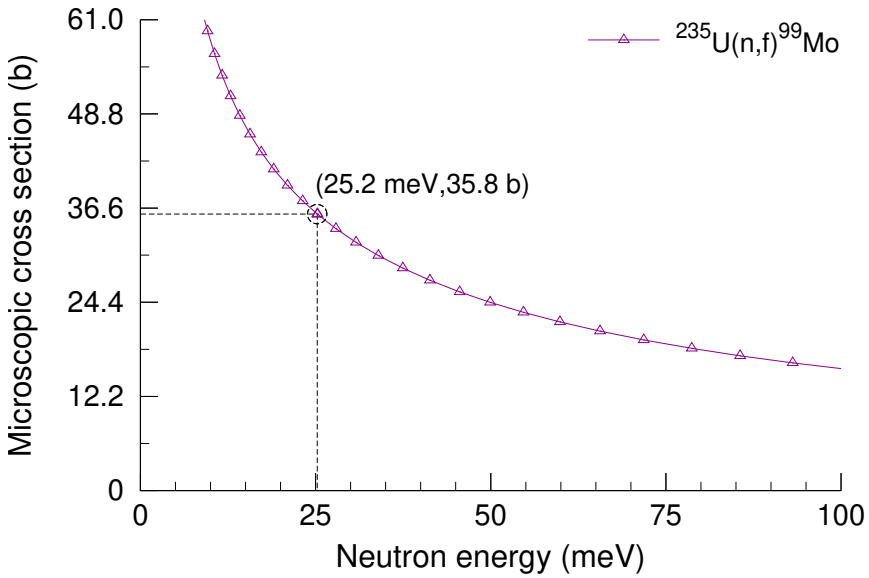

Fig. C.1. The ENDF/B-VIII.0 [25] excitation function for ^{235}U(n,f) multiplied by the 6.1% fission yield for ^{99}Mo.

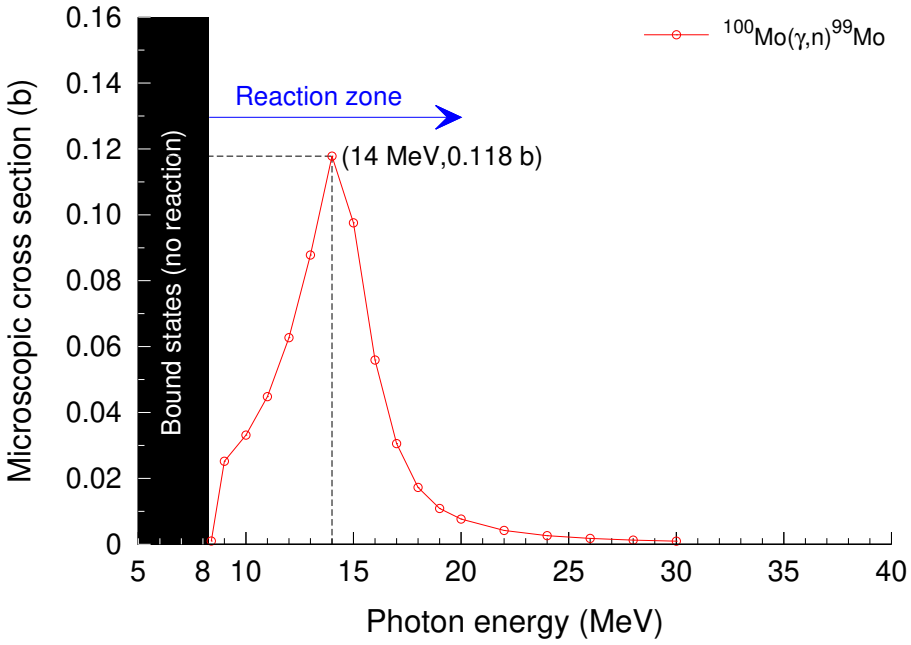

Fig. C.2. The TENDL-2017 excitation function [24] for ^{100}Mo(γ,n)^{99}Mo.

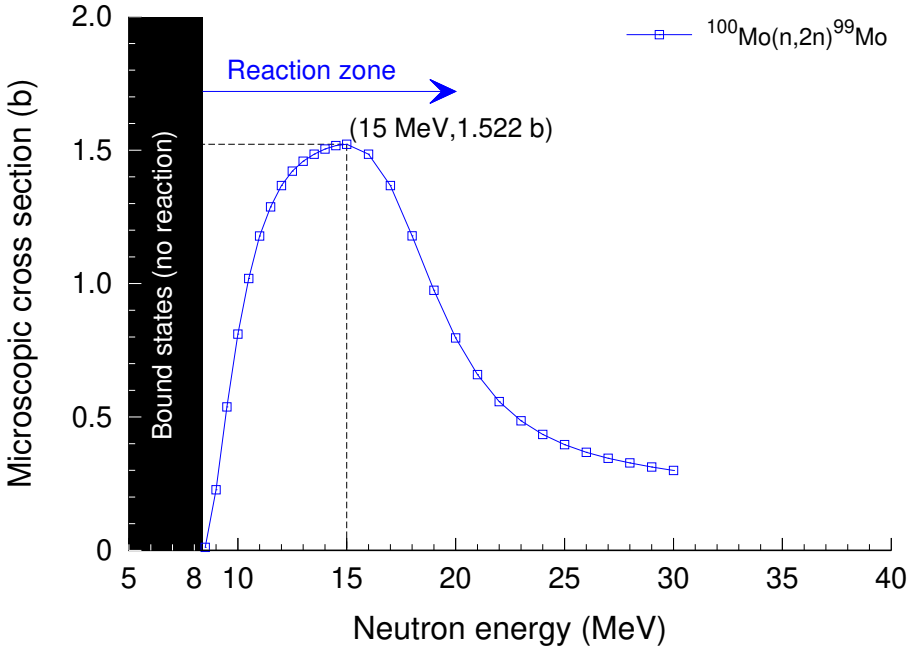

Fig. C.3. The TENDL-2017 excitation function for ^{100}Mo(n,2n)^{99}Mo.

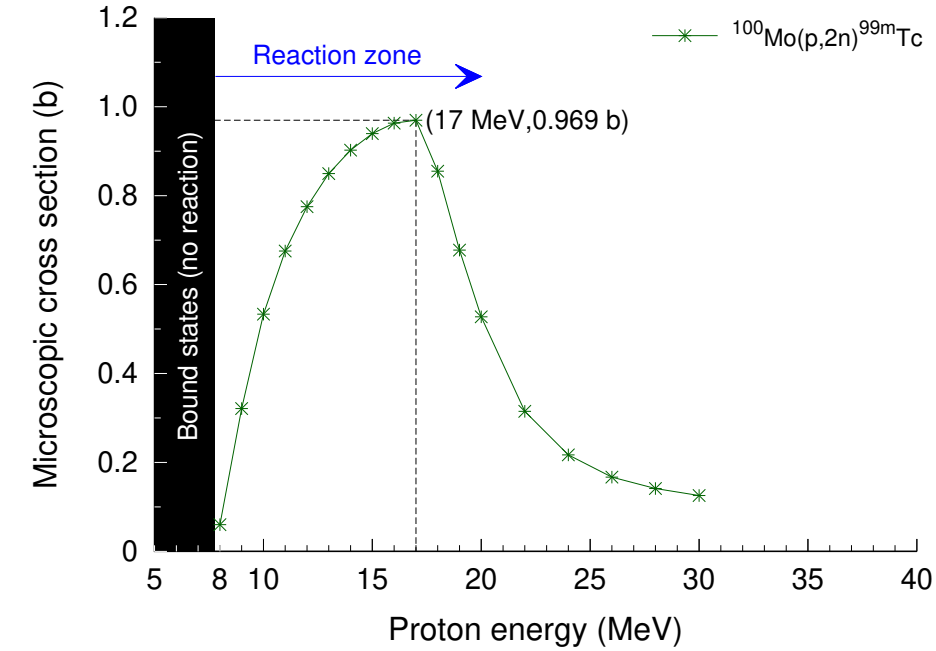

Fig. C.4. The TENDL-2017 excitation function for ^{100}Mo(p,2n)^{99m}Tc.

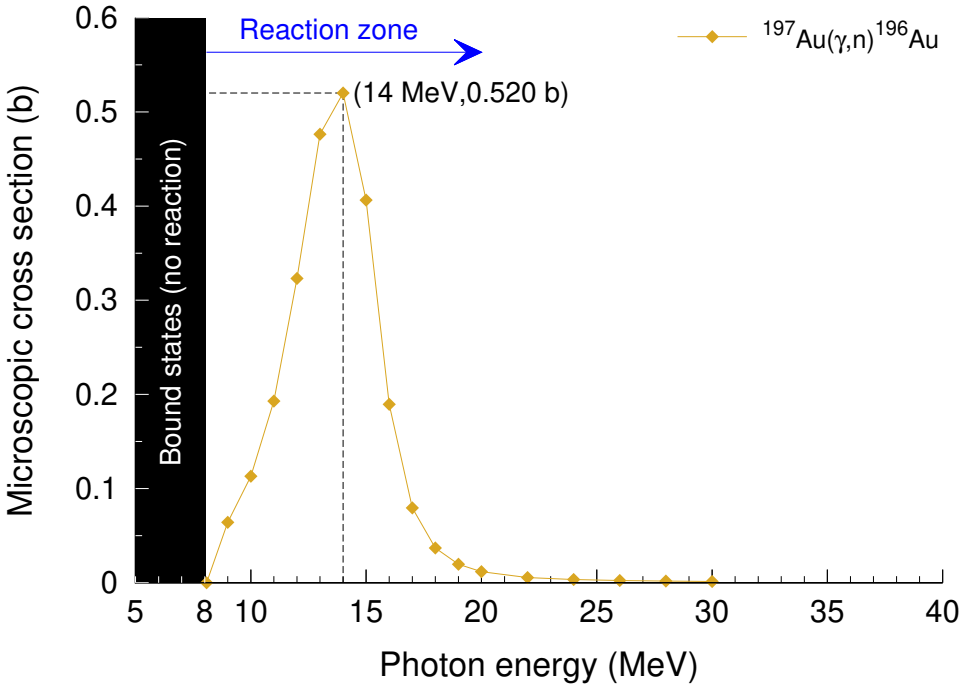

Fig. C.5. The TENDL-2017 excitation function for ^{197}Au(γ,n)^{196}Au.

Appendix

D

Efficiency curves

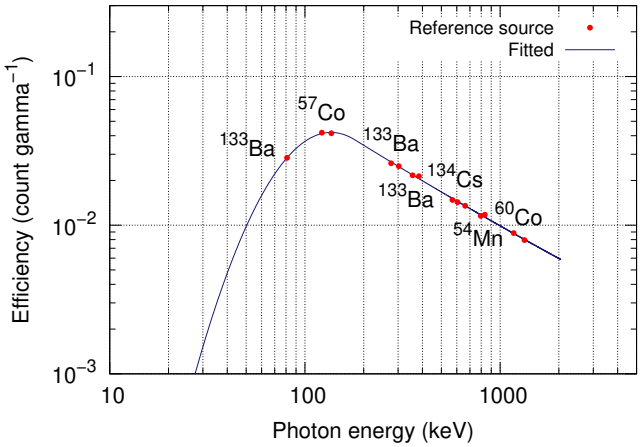

(a)

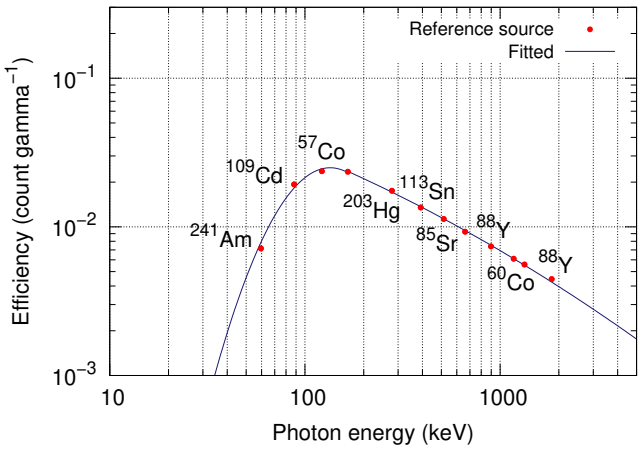

(b)

Fig. D.1. Efficiency curves of the germanium detectors used for (a) irradiated MoO_3 targets and (b) irradiated Au foils.

Appendix

E

Gamma-ray spectra

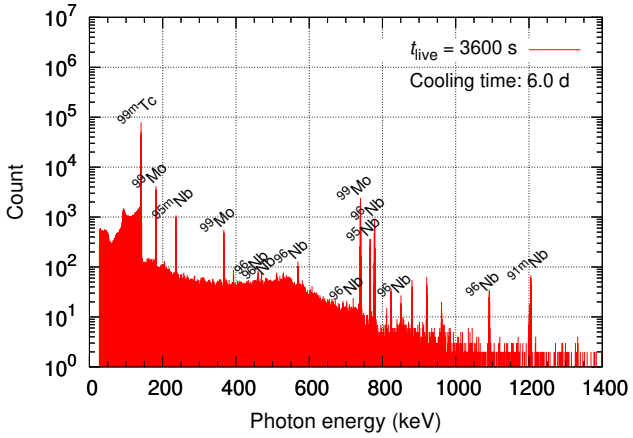

(a)

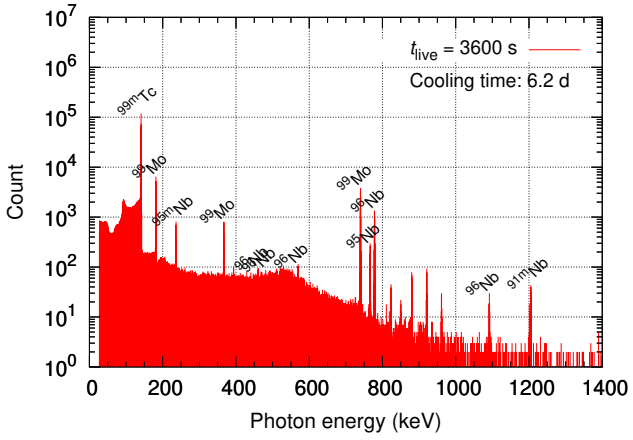

(b)

Fig. E.1. Gamma-ray spectra of irradiated MoO_3 for the irradiation runs of (a) 1 and (b) 3 (Table 5.4). Radionuclides having $\geq$20 counts are annotated. The corresponding spectra for the irradiation number 2 is found in Fig. 5.16(a).

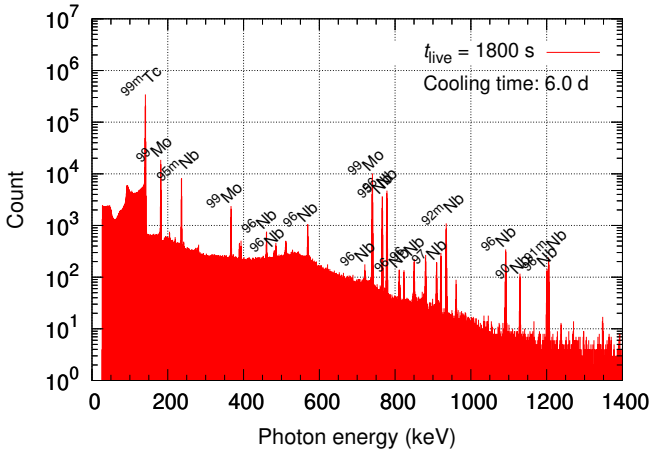

(a)

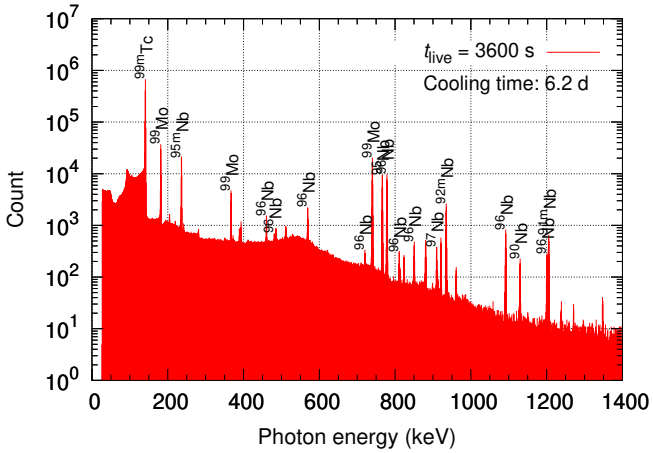

(b)

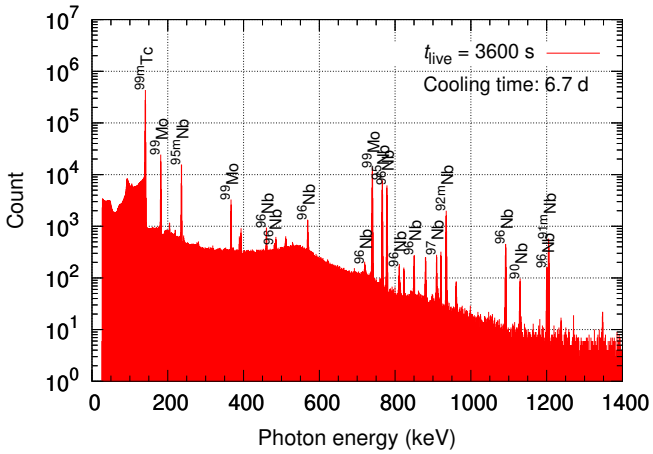

(c)

Fig. E.2. Gamma-ray spectra of irradiated MoO_3 for the irradiation runs of (a) 4, (b) 5, and (c) 6 (Table 5.4). Radionuclides having ≥20 counts are annotated.

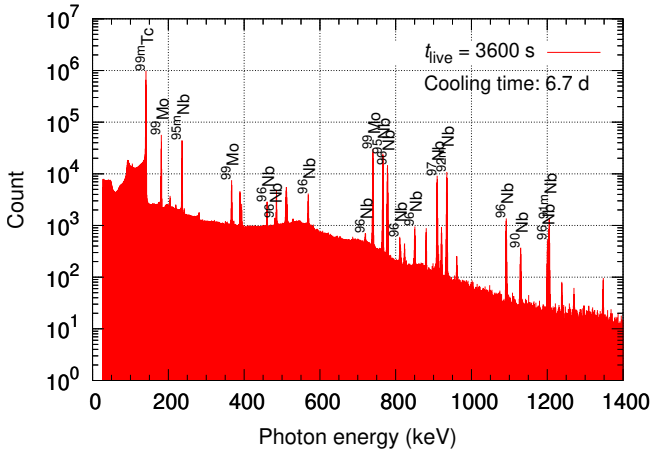

(a)

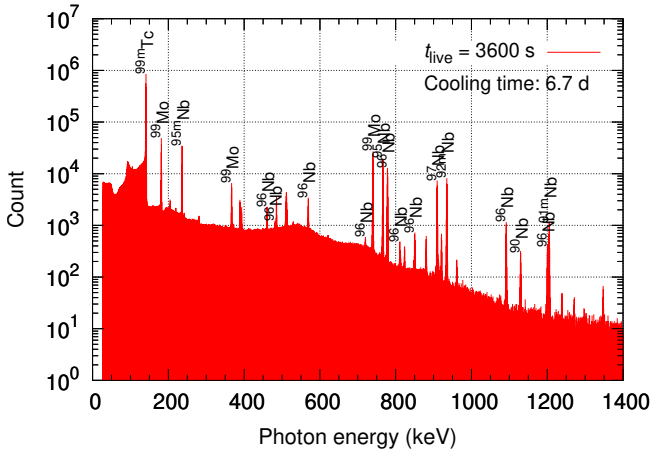

(b)

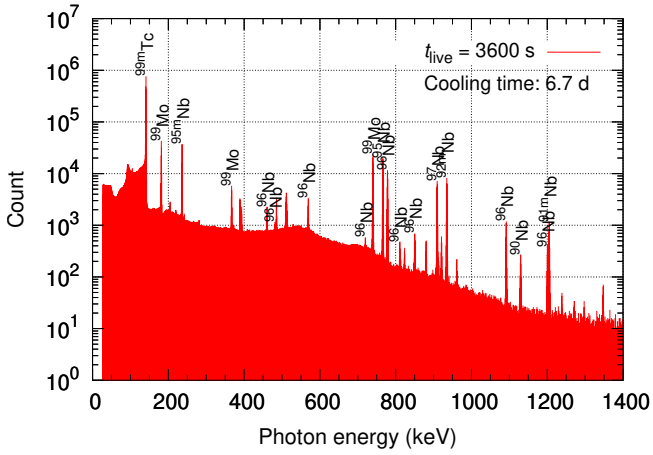

(c)

Fig. E.3. Gamma-ray spectra of irradiated MoO_3 for the irradiation runs of (a) 7, (b) 8, and (c) 9 (Table 5.4). Radionuclides having $\geq$20 counts are annotated.

Appendix

F

Records of specific activities

This appendix is an archive of the specific activities of ^{99}Mo and ^{196}Au addressed in Chap. 5 (Table F.1). The greatest specific activities at respective beam energies are highlighted as `<number>` in Tables F.2, F.3, and F.4.

Table F.1. Tables in this appendix and the corresponding figures in Chap. 5.

Material	Table in this appendix	Figure in Chap. 5
MoO_3 target	Table F.2	Fig. 5.17
Upstream Au foil	Table F.3	Fig. 5.18
Downstream Au foil	Table F.4	Fig. 5.19

Table F.2. Calculation and experimental results of [^{99}Mo]MoO_3 targets.

Beam energy (MeV)	W thickness (mm)	^{99}Mo specific activity (kBq g^{-1} μA^{-1})	
		Calculation	Experiment
20	0.45	10.58	4.23±0.27
	1.48	12.91	6.14±0.30
	2.53	11.70	6.03±0.31
35	1.48	25.22	31.26±0.77
	2.58	26.80	32.29±0.57
	3.61	24.97	24.20±0.49
50	2.13	49.50	52.25±0.70
	3.16	50.50	45.69±0.67
	4.21	47.74	43.27±0.63

Table F.3. Calculation and experimental results of upstream [^{196}Au]Au foils.

Beam energy (MeV)	W thickness (mm)	^{196}Au specific activity (kBq g^{-1} μA^{-1})	
		Calculation	Experiment
20	0.45	61.29	33.84±1.98
	1.48	104.34	74.08±4.27
	2.53	97.85	65.77±4.12
35	1.48	180.65	193.51±12.67
	2.58	210.60	248.18±16.47
	3.61	202.07	234.23±16.11
50	2.13	365.18	275.15±19.73
	3.16	395.38	366.92±27.09
	4.21	381.27	245.56±18.76

Table F.4. Calculation and experimental results of downstream [^{196}Au]Au foils.

Beam energy (MeV)	W thickness (mm)	^{196}Au specific activity (kBq g^{-1} μA^{-1})	
		Calculation	Experiment
20	0.45	85.21	46.47±2.68
	1.48	84.93	54.00±3.14
	2.53	75.31	51.39±3.22
35	1.48	178.01	194.06±12.67
	2.58	175.05	204.45±13.63
	3.61	159.64	190.07±13.02
50	2.13	340.84	129.33± 9.28
	3.16	333.38	300.21±22.40
	4.21	308.48	324.15±24.44

Bibliography

[1] F. A. Mettler and M. J. Guiberteau. *Essentials of Nuclear Medicine Imaging*. 6th ed. Philadelphia, PA: Saunders, 2012. ISBN: 978-1-4557-0104-9 (cit. on p. 1).

[2] W. C. Eckelman. Unparalleled contribution of technetium-99m to medicine over 5 decades. *JACC: Cardiovascular Imaging* **2**, 364–368 (2009). DOI: 10.1016/j.jcmg.2008.12.013 (cit. on pp. 1, 2).

[3] OECD Nuclear Energy Agency. *The Supply of Medical Radioisotopes: 2018 Medical Isotope Demand and Capacity Projection for the 2018-2023 Period*. Supply of Medical Radioisotopes series. Paris: OECD, 2018 (cit. on pp. 1, 4).

[4] E. Browne and J. K. Tuli. Nuclear Data Sheets for A=99. *Nuclear Data Sheets* **145**, 25–340 (2017). DOI: 10.1016/j.nds.2017.09.002 (cit. on p. 2).

[5] T. P. Sanders, T. D. Sanders, and D. E. Kuhl. Optimizing the window of an Anger camera for ^{99m}Tc. *Journal of Nuclear Medicine* **12**, 703–706 (1971). URL: http://jnm.snmjournals.org/content/12/11/703 (cit. on p. 2).

[6] S. Liu and D. S. Edwards. ^{99m}Tc-labeled small peptides as diagnostic radiopharmaceuticals. *Chemical Reviews* **99**, 2235–2268 (1999). DOI: 10.1021/cr9804361 (cit. on p. 2).

[7] V. J. Molinski. A review of ^{99m}Tc generator technology. *The International Journal of Applied Radiation and Isotopes* **33**, 811–819 (1982). DOI: 10.1016/0020-708X(82)90122-3 (cit. on pp. 2, 126).

[8] J. Meija *et al.* Isotopic compositions of the elements 2013 (IUPAC Technical Report). *Pure and Applied Chemistry* **88**, 293–306 (2016). DOI: 10.1515/pac-2015-0503 (cit. on pp. 3, 73, 103).

[9] National Academies of Sciences, Engineering, and Medicine. *Molybdenum-99 for Medical Imaging*. Washington, DC: National Academies Press, 2016. DOI: 10.17226/23563 (cit. on pp. 3, 4).

[10] O. Reistad and S. Hustveit. HEU fuel cycle inventories and progress on global minimization. *The Nonproliferation Review* **15**, 265–287 (2008). DOI: 10.1080/10736700802117312 (cit. on p. 3).

[11] C. Hansell. Nuclear medicine's double hazard. *The Nonproliferation Review* **15**, 185–208 (2008). DOI: 10.1080/10736700802117270 (cit. on p. 4).

[12] C. Hansell. Practical steps toward a world without civilian HEU. *The Nonproliferation Review* **15**, 289–310 (2008). DOI: 10.1080/10736700802117320 (cit. on p. 4).

[13] B. Ponsard. Mo-99 supply issues: Status report and lessons learned. In *Proceedings of the 14th International Topical Meeting on Research Reactor Fuel Management, RRFM 2010*. Brussels, Belgium: European Nuclear Society, 2010. URL: https://inis.iaea.org/search/search.aspx?orig_q=RN:41064193 (cit. on p. 4).

[14] R. Van Noorden. Radioisotopes: The medical testing crisis. *Nature* **504**, 202–204 (2013). DOI: 10.1038/504202a (cit. on p. 4).

[15] J. Jang and M. Uesaka. Influence of enriched ^{100}Mo on Mo reaction yields. *Journal of Physics Communications* **3**, 055015 (2019). DOI: 10.1088/2399-6528/ab1d6b (cit. on pp. 4, 6, 7, 14, 18, 21, 73, 74, 103, 104, 106, 108, 109, 111, 115, 118, 119, 169).

[16] International Atomic Energy Agency. *Fission Molybdenum for Medical Use*. IAEA TECDOC Series 515. Vienna: International Atomic Energy Agency, 1989 (cit. on p. 5).

[17] National Research Council (US). *Medical Isotope Production Without Highly Enriched Uranium*. Washington, DC: National Academies Press, 2009. DOI: 10.17226/12569 (cit. on pp. 5, 52).

[18] A. Dash, F. F. R. Knapp Jr., and M. R. A. Pillai. ^{99}Mo/^{99m}Tc separation: An assessment of technology options. *Nuclear Medicine and Biology* **40**, 167–176 (2013). DOI: 10.1016/j.nucmedbio.2012.10.005 (cit. on pp. 5, 126).

[19] Y. Nagai *et al.* Generation of radioisotopes with accelerator neutrons by deuterons. *Journal of the Physical Society of Japan* **82**, 064201 (2013). DOI: 10.7566/jpsj.82.064201 (cit. on pp. 5, 168).

[20] K. Tsukada, Y. Nagai, K. Hashimoto, M. Kawabata, F. Minato, H. Saeki, S. Motoishi, and M. Itoh. ^{99}Mo yield using large sample mass of MoO_3 for sustainable production of ^{99}Mo. *Journal of the Physical Society of Japan* **87**, 043201 (2018). DOI: 10.7566/JPSJ.87.043201 (cit. on pp. 5, 115).

[21] K.-N. Leung, J. K. Leung, and G. Melville. Feasibility study on medical isotope production using a compact neutron generator. *Applied Radiation and Isotopes* **137**, 23–27 (2018). DOI: 10.1016/j.apradiso.2018.02.026 (cit. on p. 5).

[22] M. Capogni *et al.* 14 MeV neutrons for ^{99}Mo/^{99m}Tc production: Experiments, simulations and perspectives. *Molecules* **23**, 1872 (2018). DOI: 10.3390/molecules23081872 (cit. on p. 5).

[23] M. Ohta, S. Kwon, S. Sato, K. Ochiai, and H. Suzuki. Investigation of Mo-99 radioisotope production by d-Li neutron source. *Nuclear Materials and Energy* **15**, 261–266 (2018). DOI: 10.1016/j.nme.2018.05.017 (cit. on p. 5).

[24] A. J. Koning and D. Rochman. Modern nuclear data evaluation with the TALYS code system. *Nuclear Data Sheets* **113**, 2841–2934 (2012). DOI: 10.1016/j.nds.2012.11.002 (cit. on pp. 6, 34, 71, 84, 111, 112, 121, 167, 172).

[25] D. A. Brown *et al.* ENDF/B-VIII.0: The 8th major release of the nuclear reaction data library with CIELO-project cross sections, new standards and thermal scattering data. *Nuclear Data Sheets* **148**, 1–142 (2018). DOI: 10.1016/j.nds.2018.02.001 (cit. on pp. 6, 171).

[26] J. E. Beaver and H. B. Hupf. Production of ^{99m}Tc on a medical cyclotron: A feasibility study. *Journal of Nuclear Medicine* **12**, 739–741 (1971). DOI: 10.2967/jnumed.116.178509 (cit. on p. 5).

[27] T. Ruth. Accelerating production of medical isotopes. *Nature* **457**, 536–537 (2009). DOI: 10.1038/457536a (cit. on p. 7).

[28] A. Celler, X. Hou, F. Bénard, and T. Ruth. Theoretical modeling of yields for proton-induced reactions on natural and enriched molybdenum targets. *Physics in Medicine and Biology* **56**, 5469–5484 (2011). DOI: 10.1088/0031-9155/56/17/002 (cit. on pp. 7, 121, 169).

[29] X. Hou, A. Celler, J. Grimes, F. Bénard, and T. Ruth. Theoretical dosimetry estimations for radioisotopes produced by proton-induced reactions on natural and enriched molybdenum targets. *Physics in Medicine and Biology* **57**, 1499–1515 (2012). DOI: 10.1088/0031-9155/57/6/1499 (cit. on pp. 7, 115, 120, 121).

[30] K. Gagnon, J. S. Wilson, C. M. B. Holt, D. N. Abrams, A. J. B. McEwan, D. Mitlin, and S. A. McQuarrie. Cyclotron production of ^{99m}Tc: Recycling of enriched ^{100}Mo metal targets. *Applied Radiation and Isotopes* **70**, 1685–1690 (2012). DOI: 10.1016/j.apradiso.2012.04.016 (cit. on pp. 7, 115).

[31] K. Gagnon, J. S. Wilson, and S. A. McQuarrie. Experimental cross section measurements for the ^{100}Mo(p,x)^{101}Tc, ^{96}Nb, ^{97}Nb reactions in the energy range of 10 to 18MeV. *Nuclear Medicine and Biology* **39**, 923–925 (2012). DOI: 10.1016/j.nucmedbio.2012.05.005 (cit. on pp. 7, 115).

[32] J. Esposito, G. Vecchi, G. Pupillo, A. Taibi, L. Uccelli, A. Boschi, and M. Gambaccini. Evaluation of ^{99}Mo and ^{99m}Tc productions based on a high-performance cyclotron. *Science and Technology of Nuclear Installations* **2013**, 972381 (2013). DOI: 10.1155/2013/972381 (cit. on pp. 7, 115).

[33] S. M. Qaim, S. Sudár, B. Scholten, A. J. Koning, and H. H. Coenen. Evaluation of excitation functions of ^{100}Mo(p,d+pn)^{99}Mo and ^{100}Mo(p,2n)^{99m}Tc reactions: Estimation of long-lived Tc-impurity and its implication on the specific activity of cyclotron-produced ^{99m}Tc. *Applied Radiation and Isotopes* **85**, 101–113 (2014). DOI: 10.1016/j.apradiso.2013.10.004 (cit. on pp. 7, 169).

[34] X. Hou, J. Tanguay, M. Vuckovic, K. Buckley, P. Schaffer, F. Bénard, T. J. Ruth, and A. Celler. Imaging study of using radiopharmaceuticals labeled with cyclotron-produced ^{99m}Tc. *Physics in Medicine and Biology* **61**, 8199–8213 (2016). DOI: 10.1088/0031-9155/61/23/8199 (cit. on pp. 7, 120, 121).

[35] J. D. Andersson, B. Thomas, S. V. Selivanova, E. Berthelette, J. S. Wilson, A. J. B. McEwan, and K. Gagnon. Robust high-yield 1 TBq production of cyclotron based sodium [^{99m}Tc]pertechnetate. *Nuclear Medicine and Biology* **60**, 63–70 (2018). DOI: 10.1016/j.nucmedbio.2018.02.003 (cit. on pp. 7, 115).

[36] P. Martini *et al.* In-house cyclotron production of high-purity Tc-99m and Tc-99m radiopharmaceuticals. *Applied Radiation and Isotopes* **139**, 325–331 (2018). DOI: 10.1016/j.apradiso.2018.05.033 (cit. on pp. 7, 115).

[37] N. M. Uzunov *et al.* Radioisotopic purity and imaging properties of cyclotron-produced ^{99m}Tc using direct ^{100}Mo(p,2n) reaction. *Physics in Medicine and Biology* **63**, 185021 (2018). DOI: 10.1088/1361-6560/aadc88 (cit. on pp. 7, 120, 121).

[38] L. Meléndez-Alafort, G. Ferro-Flores, L. De Nardo, M. Bello, M. Paiusco, A. Negri, A. Zorz, N. Uzunov, J. Esposito, and A. Rosato. Internal radiation dose assessment of radiopharmaceuticals prepared with cyclotron-produced ^{99m}Tc. *Medical Physics* **46**, 1437–1446 (2019). DOI: 10.1002/mp.13393 (cit. on pp. 7, 120, 121).

[39] International Atomic Energy Agency. *Cyclotron Based Production of Technetium-99m*. IAEA Radioisotopes and Radiopharmaceuticals Reports 2. Vienna: International Atomic Energy Agency, 2017. ISBN: 978-92-0-102916-4 (cit. on pp. 7, 169).

[40] R. G. Bennett, J. D. Christian, D. A. Petti, W. K. Terry, and S. B. Grover. A system of ^{99m}Tc production based on distributed electron accelerators and thermal separation. *Nuclear Technology* **126**, 102–121 (1999). DOI: 10.13182/NT99-A2961 (cit. on pp. 7, 63).

[41] C. Ross, R. Galea, P. Saull, W. Davidson, P. Brown, D. Brown, J. Harvey, G. Messina, R. Wassenaar, and M. de Jong. Using the ^{100}Mo photoneutron reaction to meet Canada's requirement for ^{99m}Tc. *Physics in Canada* **66**, 19–24 (2010). URL: https://services.cap.ca/drupal/sites/cap.ca/files/article/1278/Jan10-Offprint-Ross.pdf (cit. on pp. 7, 9, 63).

[42] R. Galea, R. G. Wells, C. K. Ross, J. Lockwood, K. Moore, J. T. Harvey, and G. H. Isensee. A comparison of rat SPECT images obtained using ^{99m}Tc derived from ^{99}Mo produced by an electron accelerator with that from a reactor. *Physics in Medicine and Biology* **58**, 2737–2750 (2013). DOI: 10.1088/0031-9155/58/9/2737 (cit. on pp. 7, 9, 63).

[43] B. Szpunar, C. Rangacharyulu, S. Daté, and H. Ejiri. Estimate of production of medical isotopes by photo-neutron reaction at the Canadian Light Source. *Nuclear Instruments and Methods in Physics Research Section A: Accelerators, Spectrometers, Detectors and Associated Equipment* **729**, 41–50 (2013). DOI: 10.1016/j.nima.2013.06.106 (cit. on pp. 7, 9, 63, 80).

[44] V. N. Starovoitova, L. Tchelidze, and D. P. Wells. Production of medical radioisotopes with linear accelerators. *Applied Radiation and Isotopes* **85**, 39–44 (2014). DOI: 10.1016/j.apradiso.2013.11.122 (cit. on pp. 7, 9, 63).

[45] K. Mang'era, K. Ogbomo, R. Zriba, J. Fitzpatrick, J. Brown, E. Pellerin, J. Barnard, C. Saunders, and M. de Jong. Processing and evaluation of linear accelerator-produced ^{99}Mo/^{99m}Tc in Canada. *Journal of Radioanalytical and*

Nuclear Chemistry **305**, 79–85 (2015). DOI: 10.1007/s10967-015-3997-5 (cit. on pp. 7, 9, 115).

[46] N. P. Dikiy, A. N. Dovbnya, D. V. Fedorchenko, and M. A. Khazhmuradov. GEANT 4 simulation of ^{99}Mo photonuclear production in nanoparticles. *Applied Radiation and Isotopes* **114**, 7–13 (2016). DOI: 10.1016/j.apradiso.2016.04.022 (cit. on pp. 7, 9).

[47] A. Tsechanski, A. F. Bielajew, J. P. Archambault, and E. Mainegra-Hing. Electron accelerator-based production of molybdenum-99: Bremsstrahlung and photoneutron generation from molybdenum vs. tungsten. *Nuclear Instruments and Methods in Physics Research Section B: Beam Interactions with Materials and Atoms* **366**, 124–139 (2016). DOI: 10.1016/j.nimb.2015.10.057 (cit. on pp. 7, 61, 67).

[48] S. Sekimoto, K. Tatenuma, Y. Suzuki, A. Tsuguchi, A. Tanaka, T. Tadokoro, Y. Kani, Y. Morikawa, A. Yamamoto, and T. Ohtsuki. Separation and purification of ^{99m}Tc from ^{99}Mo produced by electron linear accelerator. *Journal of Radioanalytical and Nuclear Chemistry* **311**, 1361–1366 (2017). DOI: 10.1007/s10967-016-4959-2 (cit. on pp. 7, 9, 10, 52, 63, 74, 99, 115, 128, 129).

[49] T. M. Martin, T. Harahsheh, B. Munoz, Z. Hamoui, R. Clanton, J. Douglas, P. Brown, and G. Akabani. Production of ^{99}Mo/^{99m}Tc via photoneutron reaction using natural molybdenum and enriched ^{100}Mo: part 1, theoretical analysis. *Journal of Radioanalytical and Nuclear Chemistry* **314**, 1051–1062 (2017). DOI: 10.1007/s10967-017-5455-z (cit. on pp. 7, 9, 63, 115).

[50] J. Jang, M. Yamamoto, and M. Uesaka. Design of an X-band electron linear accelerator dedicated to decentralized ^{99}Mo/^{99m}Tc supply: From beam energy selection to yield estimation. *Physical Review Accelerators and Beams* **20**, 104701 (2017). DOI: 10.1103/PhysRevAccelBeams.20.104701 (cit. on pp. 7, 9, 14, 23, 27–30, 33–36, 39, 40, 42, 52–55, 63, 167).

[51] T. Takeda *et al.* ^{99m}Tc production via the (γ, n) reaction on natural Mo. *Journal of Radioanalytical and Nuclear Chemistry* **318**, 811–821 (2018). DOI: 10.1007/s10967-018-6078-8 (cit. on pp. 7, 9, 63, 115).

[52] D. V. Fedorchenko and A. Tsechanski. Photoneutronic aspects of the molybdenum-99 production by means of electron linear accelerators. *Nuclear Instruments and Methods in Physics Research Section B: Beam Interactions with Materials*

and Atoms **438**, 6–13 (2019). DOI: 10.1016/j.nimb.2018.10.018 (cit. on pp. 7, 9, 61, 67).

[53] A. H. Sullivan. *A guide to radiation and radioactivity levels near high energy particle accelerators*. Ashford, Kent, England: Nuclear Technology Publishing, 1992. ISBN: 1-870965-18-3 (cit. on p. 8).

[54] International Atomic Energy Agency. *Non-HEU Production Technologies for Molybdenum-99 and Technetium-99m*. IAEA Nuclear Energy Series NF-T-5.4. Vienna: International Atomic Energy Agency, 2013. ISBN: 978-92-0-137710-4 (cit. on pp. 10, 125, 126).

[55] H. Kawamura, K. Iimura, H. Izumo, N. Hori, K. Kato, Y. Natori, and K. Tatenuma. Method of manufacturing high-density and high-purity (n,γ)^{99}Mo (in Japanese). Jpn. Pat. 5569834. (2014) (cit. on pp. 10, 74).

[56] J. Jang. `phitar` - A PHITS wrapper for targetry design (v1.03). Zenodo. 2019. DOI: 10.5281/zenodo.3344971 (cit. on pp. 13, 17, 25, 60, 154, 157).

[57] J. Jang. `enrimo` - Investigate the influence of an enriched Mo isotope (v1.05). Zenodo. 2019. DOI: 10.5281/zenodo.2628760 (cit. on pp. 13, 21, 25, 60, 160).

[58] J. Jang. `actdyn` - A Mo-99/Tc-99m activity dynamics simulator (v2.31). Zenodo. 2019. DOI: 10.5281/zenodo.3233940 (cit. on pp. 13, 24, 25, 60, 164).

[59] T. Sato *et al.* Features of Particle and Heavy Ion Transport code System (PHITS) version 3.02. *Journal of Nuclear Science and Technology* **55**, 684–690 (2018). DOI: 10.1080/00223131.2017.1419890 (cit. on pp. 15, 33, 62, 80, 154).

[60] J. Jang. *Study on decentralized production of medical radionuclides by compact X-band electron linear accelerators*. Master's thesis. University of Tokyo, Tokyo, Japan (cit. on pp. 23, 29–33, 39, 40, 42, 52, 53, 124).

[61] Creative Commons. Attribution 4.0 International (CC BY 4.0). URL: https://creativecommons.org/licenses/by/4.0/ (cit. on p. 27).

[62] T. P. Wangler. *RF Linear Accelerators*. 2nd ed. Weinheim: Wiley-VCH, 2008. ISBN: 978-3-527-40680-7 (cit. on pp. 27, 28, 32, 38).

[63] D. H. Whittum. Microwave electron linacs for oncology. In *Reviews of Accelerator Science and Technology*. Ed. by A. W. Chao and W. Chou. Vol. 2. Singapore: World Scientific, 2009, 63–92. DOI: 10.1142/S1793626809000260 (cit. on pp. 28, 32).

[64] S. Takeda. Fundamentals of linear accelerators (in Japanese). KEK OHO Text. 1991. URL: http://accwww2.kek.jp/oho/OHOtxt/OHO-1990/txt-1990-%E2%85%A0.pdf (cit. on p. 28).

[65] M. Yamamoto. Examination of a high-power X-band accelerator system for nuclear medicine RI production (in Japanese). Report No. EM-15013B. Accuthera Inc., 2015 (cit. on p. 28).

[66] J. Jang, M. Uesaka, and M. Yamamoto. Development of a compact X-band electron linac for production of Mo-99/Tc-99m. In *Proceedings of the 7th International Particle Accelerator Conference, IPAC 2016*. Ed. by K. S. Kim, I. S. Ko, K. R. Kim, and V. R. W. Schaa. Geneva: JACoW, 2016, 1917–1920. DOI: 10.18429/JACoW-IPAC2016-TUPOY007 (cit. on pp. 29, 30, 52).

[67] J. Jang, M. Uesaka, and M. Yamamoto. Photonuclear production of self-targeting medical radionuclides using an X-band electron linear accelerator: A feasibility study. In *Proceedings of the 14th Annual Meeting of Particle Accelerator Society of Japan, PASJ 2017*. Tokyo: Particle Accelerator Society of Japan, 2017, 740–742. URL: http://www.pasj.jp/web_publish/pasj2017/proceedings/ (cit. on p. 29).

[68] J. H. Billen and L. M. Young. POISSON/SUPERFISH on PC compatibles. In *Proceedings of the 1993 Particle Accelerator Conference, PAC 1993*. New York: IEEE, 1993, 790–792. DOI: 10.1109/PAC.1993.308773 (cit. on p. 29).

[69] S. B. van der Geer and M. J. de Loos. General Particle Tracer: A 3D code for accelerator and beam line design. In *Proceedings of the 5th European Particle Accelerator Conference, EPAC 1996*. Ed. by S. Myers, A. Pacheco, R. Pascual, C. Petit-Jean-Genaz, and J. Poole. Bristol: IOP Publishing, 1996, 1245–1247. URL: http://www.pulsar.nl/gpt (cit. on p. 29).

[70] S. M. Hanna. Applications of X-band technology in medical accelerators. In *Proceedings of the 1999 Particle Accelerator Conference, PAC 1999*. Ed. by A. U. Luccio and W. W. MacKay. New York: IEEE, 1999, 2516–2518. URL: https://accelconf.web.cern.ch/accelconf/p99/PAPERS/WEP114.PDF (cit. on p. 29).

[71] M. I. Skolnik. An introduction to radar. In *Radar Handbook*. Ed. by M. I. Skolnik. 2nd ed. New York: McGraw-Hill, 1990 (cit. on pp. 29, 32).

[72] M. Uesaka *et al.* 950 keV, 3.95 MeV and 6 MeV X-band linacs for nondestructive evaluation and medicine. *Nuclear Instruments and Methods in Physics Research Section A: Accelerators, Spectrometers, Detectors and Associated Equipment* **657**, 82–87 (2011). DOI: 10.1016/j.nima.2011.07.026 (cit. on p. 29).

[73] S. Hanna. *RF Linear Accelerators for Medical and Industrial Applications*. Norwood, MA: Artech House, 2012. ISBN: 978-1-60807-090-9 (cit. on pp. 29, 30).

[74] J. Shao *et al.* Development of a C-band 6 MeV standing-wave linear accelerator. *Physical Review Special Topics - Accelerators and Beams* **16**, 090102 (2013). DOI: 10.1103/PhysRevSTAB.16.090102 (cit. on p. 29).

[75] T. Anno, Y. Okubo, and T. Tanaka. Development of the X-band 6 MW pulsed klystron (in Japanese). In *Proceedings of the 12th Annual Meeting of Particle Accelerator Society of Japan, PASJ 2015*. Tokyo: PASJ, 2015, 1129–1132. URL: http://www.pasj.jp/web_publish/pasj2015/proceedings/PDF/THP0/THP062.pdf (cit. on p. 30).

[76] R. Tomás. Overview of the compact linear collider. *Physical Review Special Topics - Accelerators and Beams* **13**, 014801 (2010). DOI: 10.1103/PhysRevSTAB.13.014801 (cit. on pp. 30, 38).

[77] H. Braun, L. Rinolfi, S. Weisz, A. Ferrari, R. Tomas, G. Geschonke, W. Wuensch, A. Grudiev, E. Jensen, and R. Corsini. CLIC 2008 parameters. Report No. CLIC-Note-764. CLIC Study Team, 2008. URL: http://cds.cern.ch/record/1132079/?ln=ja (cit. on p. 30).

[78] Y. Inoue. *Study on basic design of S-band electron linear accelerator system for $^{99}Mo/^{99m}Tc$ production (in Japanese)*. Master's thesis. University of Tokyo, Tokyo, Japan (cit. on pp. 32, 36).

[79] M. Yamamoto. Electron beam acceleration characteristics of AIST accelerating structures and examination of an accelerator system (in Japanese). Report No. EM-18034A. Accuthera Inc., 2018 (cit. on pp. 32, 36).

[80] R. H. Miller. Comparison of standing wave and traveling wave structures. In *Proceedings of the 1986 International Linac Conference*. Stanford, CA, 1986, 200–205. URL: http://inspirehep.net/record/230607/ (cit. on p. 32).

[81] E. A. Knapp, B. C. Knapp, and J. M. Potter. Standing wave high energy linear accelerator structures. *Review of Scientific Instruments* **39**, 979–991 (1968). DOI: 10.1063/1.1683583 (cit. on p. 32).

[82] H. Hirayama, Y. Namito, A. F. Bielajew, S. J. Wilderman, and W. R. Nelson. *The* EGS5 *code system*. SLAC-R-730 and 2005-8. SLAC National Accelerator Laboratory (USA) and High Energy Accelerator Research Organization (Japan), 2005 (cit. on pp. 33, 62, 80).

[83] J. Yang, T. Kondoh, K. Kan, and Y. Yoshida. Ultrafast pulse radiolysis. *Nuclear Instruments and Methods in Physics Research Section A: Accelerators, Spectrometers, Detectors and Associated Equipment* **629**, 6–10 (2011). DOI: 10.1016/j.nima.2010.11.109 (cit. on pp. 37, 38).

[84] E. Rutherford. *Radio-activity*. 2nd ed. Cambridge: University Press, 1905 (cit. on p. 39).

[85] H. Bateman. The solution of a system of differential equations occurring in the theory of radioactive transformations. *Proceedings of the Cambridge Philosophical Society* **15**, 423–427 (1910). URL: http://www.biodiversitylibrary.org/item/97262 (cit. on p. 39).

[86] K. Tatenuma *et al.* A mass-production process of a highly pure medical use ^{99m}Tc from natural isotopic Mo(n, γ)^{99}Mo without using uranium. *RADIOISOTOPES* **63**, 501–513 (2014). DOI: 10.3769/radioisotopes.63.501 (cit. on pp. 52, 75, 128, 129).

[87] J. Jang, M. Uesaka, K. Tatenuma, A. Tsuguchi, S. Sekimoto, and T. Ohtsuki. Photonuclear production of Mo-99/Tc-99m using molybdenum trioxide and activated carbon. 2017 Mo-99 Topical Meeting, Montréal, QC Canada, 2017, oral presentation S9-P3. 2017. URL: https://mo99.ne.anl.gov/2017/pdfs/presentations/S9-P3%20Jang%20Presentation.pdf (cit. on pp. 52, 125, 128, 129).

[88] Science Council of Japan. On the stable supply system of radioisotope in Japan (in Japanese). 60th Executive Board Meeting Material. 2008. URL: http://www.scj.go.jp/ja/info/kohyo/pdf/kohyo-20-t60-5.pdf (cit. on p. 55).

[89] T. Yamashita. Estimate of Japan's post-2016 demand for ^{99m}Tc. OECD-NEA HLG-MR Meeting. 2013. URL: http://www.jrias.or.jp/e/pdf/Y130710OECD.pdf (cit. on p. 55).

[90] International Atomic Energy Agency. *Radiological Safety Aspects of the Operation of Electron Linear Accelerators*. Technical Reports Series 188. Vienna:

International Atomic Energy Agency, 1979. ISBN: 92-0-125179-3 (cit. on p. 56).

[91] A. Fassò, K. Goebel, M. Höfert, G. Rau, H. Schönbacher, G. R. Stevenson, A. H. Sullivan, W. P. Swanson, and J. W. N. Tuyn. Radiation problems in the design of the large electron-positron collider (LEP). Report No. CERN 84-02. CERN, 1984. DOI: 10.5170/CERN-1984-002 (cit. on p. 56).

[92] G. H. McCall. Calculation of x-ray bremsstrahlung and characteristic line emission produced by a Maxwellian electron distribution. *Journal of Physics D: Applied Physics* **15**, 823–831 (1982). DOI: 10.1088/0022-3727/15/5/012 (cit. on p. 66).

[93] N. A. Dyson. The continuous x-ray spectrum from electron-opaque targets. *Proceedings of the Physical Society* **73**, 924–936 (1959). DOI: 10.1088/0370-1328/73/6/311 (cit. on p. 66).

[94] A. H. Compton and S. K. Allison. *X-Rays in Theory and Experiment*. 2nd ed. New York: D. Van Nostrand, 1967 (cit. on p. 66).

[95] J. K. Shultis and R. E. Faw. *Fundamentals of Nuclear Science and Engineering*. 3rd ed. Boca Raton: CRC Press, 2017. ISBN: 978-1-4987-6929-7 (cit. on p. 66).

[96] A. J. Mayer and M. E. Wieser. The absolute isotopic composition and atomic weight of molybdenum in SRM 3134 using an isotopic double-spike. *Journal of Analytical Atomic Spectrometry* **29**, 85–94 (2014). DOI: 10.1039/C3JA50164G (cit. on pp. 73, 103).

[97] L. Brewer and R. H. Lamoreaux. The Mo-O system (molybdenum-oxygen). *Bulletin of Alloy Phase Diagrams* **1**, 85–89 (1980). DOI: 10.1007/BF02881199 (cit. on p. 73).

[98] F. Predel. Phase diagram of Mo-O (molybdenum-oxygen) system. In *Phase Equilibria, Crystallographic and Thermodynamic Data of Binary Alloys*. Ed. by F. Predel. Berlin: Springer-Verlag, 2016, 81–81. DOI: 10.1007/978-3-642-24977-8_38 (cit. on p. 73).

[99] D. M. Hulbert, A. Anders, D. V. Dudina, J. Andersson, D. Jiang, C. Unuvar, U. Anselmi-Tamburini, E. J. Lavernia, and A. K. Mukherjee. The absence of plasma in "spark plasma sintering". *Journal of Applied Physics* **104**, 033305 (2008). DOI: 10.1063/1.2963701 (cit. on p. 74).

[100] Z. A. Munir, U. Anselmi-Tamburini, and M. Ohyanagi. The effect of electric field and pressure on the synthesis and consolidation of materials: A review of the spark plasma sintering method. *Journal of Materials Science* **41**, 763–777 (2006). DOI: 10.1007/s10853-006-6555-2 (cit. on p. 74).

[101] O. Guillon, J. Gonzalez-Julian, B. Dargatz, T. Kessel, G. Schierning, J. Räthel, and M. Herrmann. Field-assisted sintering technology/spark plasma sintering: Mechanisms, materials, and technology developments. *Advanced Engineering Materials* **16**, 830–849 (2014). DOI: 10.1002/adem.201300409 (cit. on p. 74).

[102] S. S. Zumdahl and S. A. Zumdahl. *Chemistry*. 9th ed. United States: Cengage Learning, 2014. ISBN: 978-1-133-61205-6 (cit. on p. 76).

[103] F. Hinode, S. Kashiwagi, K. Kanomata, Y. Shibasaki, K. Takahashi, I. Nagasawa, K. Nanbu, S. Miura, T. Muto, and H. Hama. Status of accelerator facility in Research Center for ELectron PHoton science at Tohoku University (in Japanese). In *Proceedings of the 15th Annual Meeting of Particle Accelerator Society of Japan*. Tokyo: Particle Accelerator Society of Japan, 2018, 1326–1328. URL: http://www.pasj.jp/web_publish/pasj2018/proceedings/PDF/FSP0/FSP017.pdf (cit. on p. 89).

[104] G. Gilmore. *Practical Gamma-ray Spectrometry*. 2nd ed. Chichester, England: Wiley, 2008. ISBN: 978-0-470-86196-7 (cit. on p. 92).

[105] Creative Commons. Attribution 3.0 Unported (CC BY 3.0). URL: https://creativecommons.org/licenses/by/3.0/ (cit. on p. 103).

[106] ISOFLEX. Stable isotopes of molybdenum available from ISOFLEX. accessed March 27, 2019. 2019. URL: https://www.isoflex.com/molybdenum-mo (cit. on pp. 105, 115).

[107] Trace Sciences International. Molybdenum Isotopes. accessed March 27, 2019. 2019. URL: http://www.tracesciences.com/mo.htm (cit. on pp. 105, 115).

[108] Trace Sciences International. Modes of Production. accessed March 2, 2019. 2019. URL: http://www.tracesciences.com/modesofproduction.html (cit. on p. 114).

[109] ISOFLEX. Stable isotopes produced in gas centrifuges. accessed March 2, 2019. 2019. URL: http://www.isoflex-russia.com/gas.html (cit. on p. 114).

[110] K. Ueno, M. Saeki, and T. Ishimori. Isolation of radioniobium from γ-irradiated molybdenum oxide. *Journal of Nuclear Science and Technology* **6**, 203–206 (1969). DOI: 10.1080/18811248.1969.9732867 (cit. on p. 115).

[111] National Nuclear Data Center. NuDat 2.7. accessed May 28, 2019. URL: https://www.nndc.bnl.gov/nudat2/ (cit. on pp. 121, 167).

[112] J. J. M. de Goeij and M. L. Bonardi. How do we define the concepts specific activity, radioactive concentration, carrier, carrier-free and no-carrier-added? *Journal of Radioanalytical and Nuclear Chemistry* **263**, 13–18 (2005). DOI: 10.1007/s10967-005-0004-6 (cit. on p. 125).

[113] M. Tanase, K. Tatenuma, K. Ishikawa, K. Kurosawa, M. Nishino, and Y. Hasegawa. A ^{99m}Tc generator using a new inorganic polymer adsorbent for (n, γ) ^{99}Mo. *Applied Radiation and Isotopes* **48**, 607–611 (1997). DOI: 10.1016/S0969-8043(96)00320-X (cit. on p. 127).

[114] R. Chakravarty, R. Ram, A. Dash, and M. R. A. Pillai. Preparation of clinical-scale ^{99}Mo/^{99m}Tc column generator using neutron activated low specific activity ^{99}Mo and nanocrystalline γ-Al_2O_3 as column matrix. *Nuclear Medicine and Biology* **39**, 916–922 (2012). DOI: 10.1016/j.nucmedbio.2012.03.010 (cit. on p. 127).

[115] S. K. Sarkar, G. Arjun, P. Saraswathy, and N. Ramamoorthy. Post-elution concentration of 99mTcO_4^- by a single anion exchanger column: I: Feasibility of extending the useful life of column chromatographic ^{99m}Tc generator. *Applied Radiation and Isotopes* **55**, 561–567 (2001). DOI: 10.1016/S0969-8043(00)00325-0 (cit. on p. 127).

[116] S. Chattopadhyay and M. K. Das. A novel technique for the effective concentration of ^{99m}Tc from a large alumina column loaded with low specific-activity (n,γ)-produced ^{99}Mo. *Applied Radiation and Isotopes* **66**, 1295–1299 (2008). DOI: 10.1016/j.apradiso.2008.02.085 (cit. on p. 127).

[117] T. H. Bokhari, A. Mushtaq, and I. U. Khan. Lead cation exchange and alumina columns for concentration of ^{99m}Tc-pertechnetate. *Journal of Radioanalytical and Nuclear Chemistry* **279**, 281–285 (2009). DOI: 10.1007/s10967-007-7264-2 (cit. on p. 127).

[118] R. D. Rogers, A. H. Bond, J. Zhang, and C. B. Bauer. Polyethylene glycol based-aqueous biphasic systems as technetium-99m generators. *Applied Radiation and Isotopes* **47**, 497–499 (1996). DOI: 10.1016/0969-8043(95)00335-5 (cit. on p. 128).

[119] R. Rogers, E. P. Horwitz, and A. H. Bond. Process for recovering pertechnetate ions from an aqueous solution also containing other ions. US5603834. (1997) (cit. on p. 128).

[120] R. D. Rogers, A. H. Bond, J. Zhang, and E. P. Horwitz. New technetium-99m generator technologies utilizing polyethylene glycol-based aqueous biphasic systems. *Separation Science and Technology* **32**, 867–882 (1997). DOI: 10.1080/01496399708003234 (cit. on p. 128).

[121] R. D. Rogers, S. T. Griffin, E. P. Horwitz, and H. Diamond. Aqueous biphasic extraction chromatography (ABEC^{TM}): uptake of pertechnetate from simulated Hanford tank wastes. *Solvent Extraction and Ion Exchange* **15**, 547–562 (1997). DOI: 10.1080/07366299708934493 (cit. on p. 128).

[122] E. P. Horwitz and A. H. Bond. Multicolumn selectivity inversion generator for production of ultrapure radionuclides. US6998052. (2006) (cit. on p. 128).

[123] D. R. McAlister and E. P. Horwitz. Automated two column generator systems for medical radionuclides. *Applied Radiation and Isotopes* **67**, 1985–1991 (2009). DOI: 10.1016/j.apradiso.2009.07.019 (cit. on p. 128).

[124] P. Tkac and G. F. Vandegrift. Recycle of enriched Mo targets for economic production of ^{99}Mo/^{99m}Tc medical isotope without use of enriched uranium. *Journal of Radioanalytical and Nuclear Chemistry* **308**, 205–212 (2016). DOI: 10.1007/s10967-015-4357-1 (cit. on p. 128).

[125] K. Tatenuma, T. Ueda, K. Kurosawa, K. Ishikawa, A. Tanaka, T. Noguchi, and Y. Arano. Method of recovering enriched radioactive technetium and system therefor. US9236153. (2016) (cit. on pp. 128, 129).

[126] F. Boschi, M. Pagliazzi, B. Rossi, M. P. Cecchini, G. Gorgoni, M. Salgarello, and A. E. Spinelli. Small-animal radionuclide luminescence imaging of thyroid and salivary glands with ^{99m}Tc-pertechnetate. *Journal of Biomedical Optics* **18**, 076005 (2013). DOI: 10.1117/1.JBO.18.7.076005 (cit. on p. 145).

[127] L. S. Zuckier, O. Dohan, Y. Li, C. J. Chang, N. Carrasco, and E. Dadachova. Kinetics of perrhenate uptake and comparative biodistribution of perrhenate, pertechnetate, and iodide by NaI symporter–expressing tissues in vivo. *Journal of Nuclear Medicine* **45**, 500–507 (2004). URL: http://jnm.snmjournals.org/content/45/3/500 (cit. on pp. 145, 147).

[128] P. R. Franken, J. Guglielmi, C. Vanhove, M. Koulibaly, M. Defrise, J. Darcourt, and T. Pourcher. Distribution and dynamics of ^{99m}Tc-pertechnetate uptake in the thyroid and other organs assessed by single-photon emission computed tomography in living mice. *Thyroid* **20**, 519–526 (2010). DOI: 10.1089/thy.2009.0213 (cit. on p. 145).

[129] M. L. Schipper, C. G. U. Riese, S. Seitz, A. Weber, M. Béhé, T. Schurrat, N. Schramm, B. Keil, H. Alfke, and T. M. Behr. Efficacy of ^{99m}Tc pertechnetate and ^{131}I radioisotope therapy in sodium/iodide symporter (NIS)-expressing neuroendocrine tumors in vivo. *European Journal of Nuclear Medicine and Molecular Imaging* **34**, 638–650 (2007). DOI: 10.1007/s00259-006-0254-8 (cit. on pp. 145, 147).

[130] F. Minato, K. Tsukada, N. Sato, S. Watanabe, H. Saeki, M. Kawabata, S. Hashimoto, and Y. Nagai. Measurement and estimation of the ^{99}Mo production yield by ^{100}Mo(n,2n)^{99}Mo. *Journal of the Physical Society of Japan* **86**, 114803 (2017). DOI: 10.7566/JPSJ.86.114803 (cit. on p. 168).

[131] K. Shibata *et al.* JENDL-4.0: A new library for nuclear science and engineering. *Journal of Nuclear Science and Technology* **48**, 1–30 (2011). DOI: 10.1080/18811248.2011.9711675 (cit. on p. 168).

[132] K. Shibata, N. Iwamoto, S. Kunieda, F. Minato, and O. Iwamoto. Activation cross-section file for decommissioning of LWRs. In *2015 Symposium on Nuclear Data*. Tokai, Japan, 2016, 47–52. DOI: 10.11484/jaea-conf-2016-004 (cit. on p. 168).